Atomistic Molecular Dynamics Simulations

of Polymer Melt Viscoelasticity

by

Vagelis A. Harmandaris

A dissertation submitted to the faculty of the University of Patras in partial fulfillment of the requirements for the degree of doctor of Philosophy in Chemical Engineering

PATRAS 2001

TABLE OF CONTENTS

APPENDIX

CHAPTER 1

INTRODUCTION

The ability to predict the key physical and chemical properties of polymers from their molecular structure is of great value in the design of polymers. Performance criteria, which must be satisfied for the technological applications of polymers, have become increasingly more stringent with the recent advances in many areas of technology. Consequently, the development of predictive computational schemes to evaluate candidates for specific applications has gained urgency.

To this direction, with the huge development of computers nowadays, computer simulation techniques have become valuable tools of fundamental and basic research in polymer science. Brownian dynamics, molecular dynamics and non-equilibrium dynamics are the main methods that are employed for the study of dynamic and viscoelastic properties of polymer liquids [1].

Polymers, however, are macromolecular systems characterized by a complex internal microstructure that gives rise to an enormous spectrum of length scales in their structure and a very wide spectrum of time scales in their molecular motion. Consequently the dynamic behavior of polymers is substantially different than those of a simple Newtonian liquid, exhibiting both liquidlike and solidlike characteristics [2],[3].

Even a single chain exhibits a much more complicated structure, than the simple atomic liquids, as it is shown in Fig. 1.1 [1]; from the scale of a single chemical bond (~ 1 Å) to the persistence statistical length (~ 10 Å) to the coil radius of the chain (~ 100 Å). Intramolecular correlations and local packing of chains in the bulk exhibit features on the length scale of bond lengths and atomic radiii. The statistical, Kuhn, segment length of a typical synthetic randomly coiled polymer is on the order of 10 Å and can be considerable larger for very stiff polymers. The radius of gyration of entire chains in the amorphous bulk scales as $N^{1/2}$ with the chain length N and is on the order of 100 Å for common molecular weights. On the other hand the smallest dimension of microphases

(lamelellae, cylinders, spheres) in microphase-separated block copolymer systems is of the order of 100 Å, while crustallite sizes in semicrystalline polymers and domain size in immiscible polymer blends can well be of the order of *μm*.
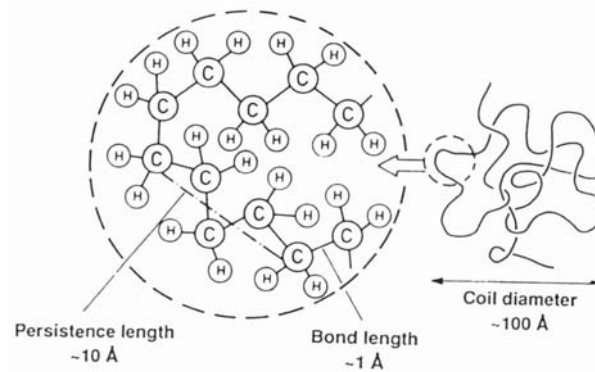
Figure 1.1 Length scales characterizing the structure of long polymer coil.

Huge in polymers is also the huge spread of time scales characterizing their dynamics. While in simple fluids at states far from phase transitions all fluctuations decay on time scales of a few picoseconds (10^{-12} sec), the behavior of polymers is substantial different, since motions occur on many very different time scales. For example fast motions such as vibrations of C-C bonds may tike times of the order of $\sim 10^{-14}$ sec or even less. However already the reorientation jumps in torsional potential are significantly slower: the average time between two jumps is typically of the order of $\sim 10^{-11}$ sec. On the other hand the global relaxation (maximum relaxation time) of a chain can be of the order of $\sim 10^{-6}$ sec for a chain in encountered in typical processing operations. The time scales for morphology development through nucleation and growth of spinodal decomposition processes typically is of the order of seconds, while the characteristic times for volume and enthalpy relaxation in a glassy polymer just a few degrees below the glass transition temperature are on the order of years.

Molecular simulations, on the other hand, particularly those of atomistic nature typically tracks, the evolution of model systems of length scale of about 100 Å for times up to a few tens of ns. Thus a straightforward application of the molecular dynamics (MD) simulations, for example, in order to extract the dynamic properties of polymers is at least problematic since it would require enormous computer time and would also

require stability of the integrator algorithms for very long times [4]. This is the well-known *problem of long relaxation times*.

To overcome the problem of long relaxation times in polymer systems a number of approaches have been proposed over the last years. The first is to develop new more efficient, clever algorithms for atomistic MD simulations. The range of length scales that can be simulated with MD simulations can be increased significantly by using a number of processors (nodes) and special parallelization techniques (such as the spatial or domain-decomposition, the force-decomposition or the replicated-data method). Concerning the time scale, recently new algorithms have been developed for the integration of equations of motion that involve a multiple time step approach and allow tracking the evolution of the systems longer times than the conventional algorithms [5].

A second approach, used traditionally, is to abandon chemical detail and replace it with a simpler model without loss of significant information. In coarse-grained models the study of polymer dynamics is restricted to the long wavelength properties, also called "universal" properties, since they do not depend on the detailed chemical structure of the polymer studied [1]. Unfortunately this characteristic does not permit a direct comparison with experimental data.

In order to bridge the many length and time scales present in polymeric systems, alternatively, a hierarchical approach may be followed which uses information of many different levels of abstraction and a combination of different methods of molecular simulations and theoretical approaches.

Such a hierarchical approach is followed in this thesis for the study of viscoelastic properties of polymer melts involving a combination of molecular simulation techniques with the ideas of the of mesoscopic theoretical models. The approach is a two-fold hierarchical methodology that involves state of the art atomistic Monte Carlo (MC) and MD simulations and a thorough mapping of the MD simulation data onto proper theoretical coarse-grained models.

Key in our hierarchical approach is the combination of both MC and MD atomistic simulations. First the simulated systems are equilibrated through a very powerful MC algorithm, the end-bridging Monte Carlo method. With this algorithm very long polymer melts have been fully equilibrated at all length scales. Then detailed atomistic MD simulations, incorporating the multiple time step algorithm, have been conducted to track the evolution of the simulated systems for very long times, up to a few hundreds of ns.

The MD technique predicts the evolution of a system in real time. Thus dynamic properties, such as the self-diffusion coefficient D, the mean square displacement of segments or the relaxation of the end-to-end distance, can be calculated directly from atomistic MD simulations. Viscoelastic properties, however, such as the zero-shear rate viscosity η_0, the friction coefficient ζ, or the stress relaxation modulus $G(t)$ can be calculated only indirect from the MD simulations through the use of an appropriate theoretical mesoscopic model. This concerns the other important characteristic of our hierarchical methodology, which involves the mapping of the atomistic MD data onto a mesoscopic model. The model we choose depends on the molecular weight of the simulated systems. For the small systems it was the Rouse model, whereas for the longer it was the reptation theory [6].

To study the flow properties of the polymeric systems the above methodology has been extended to systems under non-equilibrium (flowing) conditions. A new MC method has been developed for the application of a thermodynamic field, MD simulations conducted in a new statistical ensemble and the simulation data were mapped onto the proper expressions the mesoscopic model predicts for systems under the corresponding flowing conditions.

1.1   Thesis Overview

The present thesis is organized as follows:

Chapter 2 gives a rather detailed presentation of the molecular dynamics method, with particular emphasis in its implementation for polymeric systems.

Chapter 3 gives an overview of theoretical approaches to polymer melt dynamics and viscoelasticity. Particular emphasis is placed on two molecular theoretical models on which the present simulation data will be mapped, i.e. the Rouse model and the reptation theory.

The first results of the thesis are presented in chapter 4. There elements of the hierarchical methodology followed are introduced and results from atomistic MD simulations of short polyethylene (PE) melts in the unentangled regime are presented.

In the next chapter, i.e. chapter 5, the hierarchical methodology introduced in chapter 4, is extended to longer polymer melts in the crossover regime from unentangled (Rouse behavior) to entangled regime.

The short n-alkanes like regime, is studied in chapter 6 through atomistic MD simulations. In this regime extra free volume phenomena due to chain ends are very

important and are examined thoroughly. A direct calculation of the free volume within the system through a geometrical method is performed and compared with that of a free volume theory with emphasis in the chain ends, proposed by Bueche and von Meerwall predicts.

A study of chain self-diffusion in binary blends is presented in chapter 7. There atomistic MD simulations are performed into binary mixtures of *n*-alkane blends that have been obtained through a recently introduced very powerful MC scheme for the solubility of *n*-alkanes into a polymer matrix. A direct comparison with two different modifications of the free volume theory for the prediction of the self-diffusion of binary polymers systems is also presented in this chapter.

In chapters 4-7 all the systems studied are at equilibrium conditions. The extension of the hierarchical scheme for the study of dynamic and viscoelastic properties of non-equilibrium systems is given in chapter 8. First a novel MC approach that orients and/or deforms the systems by applying a thermodynamic is presented. Then MD simulations on the oriented configurations are performed in a new statistical ensemble. The MD data are then mapped onto the expressions that the Rouse mesoscopic model predicts for the system under the pertinent conditions. The methodology presented in this chapter is the atomistic modeling analogue of the stress relaxation experiment upon cessation of steady-state uniaxial elongational flow.

Chapter 9 presents the conclusions of the work of this thesis and recommendations for future plans.

CHAPTER 2

MOLECULAR DYNAMICS SIMULATIONS
OF POLYMERS

2.1 From Statistical Mechanics to Molecular Simulations

The study of atomic and molecular systems has a long and rich history, from both the theoretical and experimental standpoints. From early observations of Brownian motion to very recent neutron experiments, experimentalists have worked to improve the understanding of the structure and the particle dynamics that characterize the physical systems. At the same time, theoreticians have tried to construct analytical models, which explain how the physical systems behave. On the other hand computer simulations play a prohibiting role in the study of atomic or molecular systems, mainly the last years with the huge development of computers [4].

The first computer simulation was carried out almost 50 years ago by Metropolis *et al*. [7] and laid the foundations of modern Monte Carlo (MC) simulations. In the MC method, atoms are randomly chosen and randomly displaced to a nearby position. Energy considerations dictate whether the trial move will be accepted or not. MC proved to be a powerful tool for the equilibration of very complex systems because of their ability to overcome free energy barriers that limit the motion of these systems in configuration space.

A different technique, however, is required to obtain the dynamic properties of a many-particle systems. This is the Molecular Dynamics method, which is based on the solution of the classical equations of motion (Newton's equation) for every particle within a system. This method was first accomplished for a system of hard spheres by Alder and Wainright [8]. After these initial simulation works, conducted on atomic systems, computer simulations developed rapidly. Crystal systems, polymer, biological

systems, interfaces, copolymers, have all been subjects of study with molecular dynamics simulations [1],[5],[9].

Computer simulations can play a significant role providing essentially exact results for problems in statistical mechanics, that otherwise would be soluble only by approximate theories. From this sense computer simulations is a direct test of theories. From another point of view, the results of computer simulations may also be compared to those of real experiments. This has a dual character. On the one hand, it is a test of the model used in the computer simulations. On the other hand, if the model is proven to be a good one, the simulations can offer insights to the experimentalists and assist in the interpretation of new results. This dual role of the simulation, as a bridge between models and theoretical predictions on the one hand, and between models and experimental results on the other, is clearly illustrated in Fig. 2.1. Due to their connecting role, these techniques are often called "computer experiments".
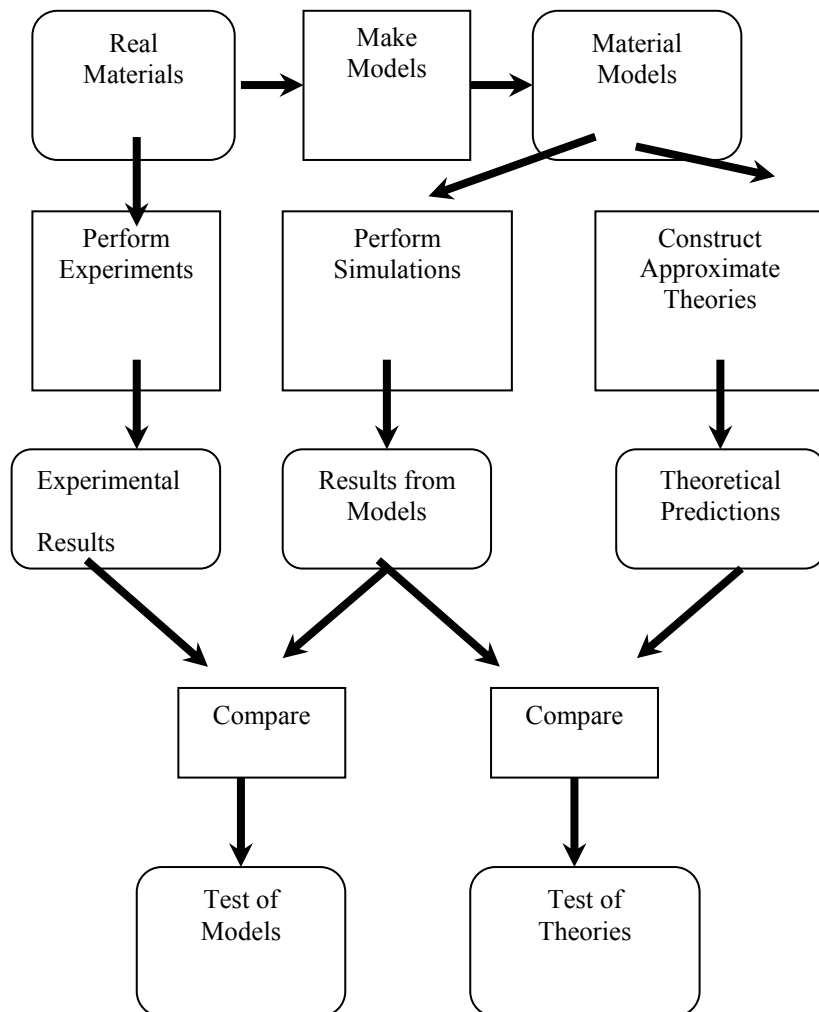
Figure 2.1 Connection between experiments, simulations and theories.

Schematically the inputs and outputs typically involved in "computer experiments" are shown in Fig. 2.2. The major limitation of simulations lies in their very heavy computational requirements, which do not allow their "brute-force" application for the study of large length-scale and long time-scale phenomena in real life materials. In many cases, introducing approximations, which are typically less drastic than those invoked in theories or special computational techniques, can alleviate this problem.

Geometry of molecules ⟶

Potentials of Interaction

MOLECULAR

SIMULATION

Macroscopic properties ⟶

External constraints
dynamics
Defining an ensemble (e.g. NVT)

Microscopic structure and

Macroscopic behavior
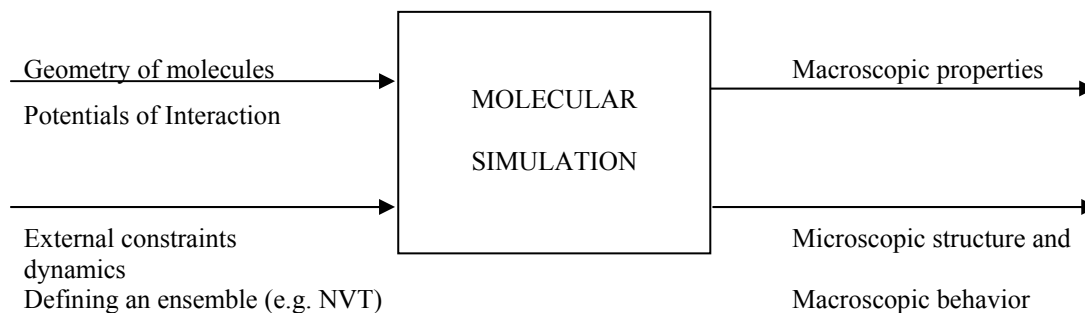
Figure 2.2 Inputs and outputs of a typical molecular simulation.

2.2   The Molecular Dynamics Technique

The Molecular Dynamics is a powerful technique to compute the equilibrium and dynamical properties of a classical many-body system. The heart of the technique is the solution of Newton's equations of motion. These can be integrated numerically to give information for the positions and velocities of atoms in a system [5].

Initial Configuration

Computer Forces on all particles within the system

Integrate Newton's equations of motion

N steps

Perform measurements every N_k steps

Collect averages, positions, …

End
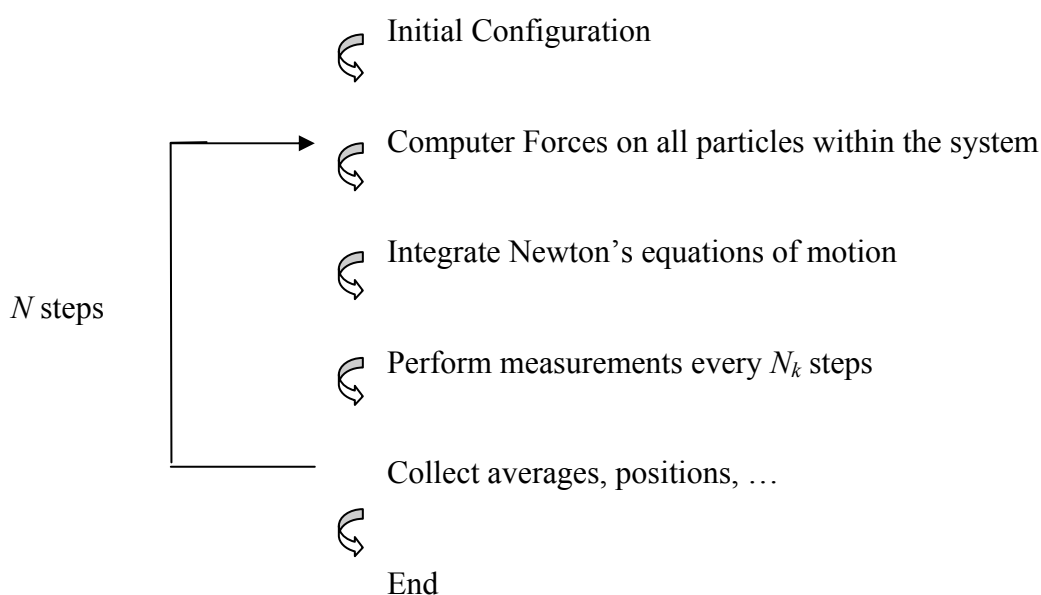
Figure 2.3 A simple flow diagram of the standard MD algorithm.

From many respects, Molecular Dynamics simulation is very similar to a real experiment. In a standard experiment, we first prepare a sample of the material that we wish to study. Then we use a measuring instrument (the experimental apparatus) to measure the property of interest during certain time intervals. In an analogous manner, in a MD simulation we first choose or develop a model system which represents a snapshot of the corresponding physical system. Then we compute the forces acting on all particles within the system and we solve the equations of motion with a proper integrator. Actual measurements are performed after the system has reached equilibration. A simple flow diagram of a standard MD algorithm is shown in Fig. 2.3.

2.2.1 Classical Equations of Motion

As it was also stated before the heart of an MD simulation is the solution of the classical equations of motion for the particular physical system. Consider a system consisting of N molecules interacting via a potential V. Let us denote as q_k and $\dot{q}_k$ the generalized coordinates and their time derivatives, respectively. The classical equations of motion for this system can be written in various ways [10]. In the Lagrangian formulations, the trajectory $\mathbf{q}(t)$ satisfies the set of differential equations:

$$\frac{\partial L}{\partial q_k} = \frac{d}{dt}\left(\frac{\partial L}{\partial \dot{q}_k}\right) \qquad (2.1)$$

where L is the Lagrangian function. This is defined in terms of the kinetic, K, and potential energies, V, as: $L = L(\mathbf{q},\dot{\mathbf{q}}_k,t) \equiv K - V$.

The generalized momenta p_k conjugated to the generalized coordinate q_k are defined as

$$p_k = \frac{\partial L}{\partial \dot{q}_k}. \qquad (2.2)$$

Alternatively one can adopt the Hamiltonian form, which considers generalized coordinates and momenta through

$$\dot{q}_k = \frac{\partial H}{\partial p_k}, \qquad \dot{p}_k = -\frac{\partial H}{\partial q_k} \qquad (2.3)$$

where H is the Hamiltonian of the system, defined through the equation

$$H(\mathbf{p},\mathbf{q}) = \sum_k \dot{q}_k p_k - L(\mathbf{p},\mathbf{q}) \qquad (2.4)$$

If the potential V is independent of velocities and time then H becomes equal to the total energy of the system: $H(\mathbf{p}, \mathbf{q}) = K(\mathbf{p}) + V(\mathbf{q})$ [10]. In Cartesian coordinates, Hamilton's equations of motion read as:

$$\dot{\mathbf{r}}_i = \frac{\mathbf{p}_i}{m_i}, \qquad \dot{\mathbf{p}}_i = -\frac{\partial V}{\partial \mathbf{r}_i} = \mathbf{F}_i \qquad (2.5)$$

or
$$m_i \ddot{\mathbf{r}}_i = \mathbf{F}_i \qquad (2.6)$$

where $\mathbf{F}_i$ is the force acting on atom i. The solution of equations of motion involves then the solution of the $3N$ second-order differential Eqs. (2.6).

There are some important characteristics of the classical equations of motion, the most important being the conservation law. If we assume that K and V do not depend explicitly on time then it is straightforward to verify that $\dot{H} = dH/dt$ is zero, i.e. the Hamiltonian is a constant of the motion. In actual calculations this conservation law is satisfied if there exist no explicitly time- or velocity-dependent forces acting on the system.

A second important point is that they are reversible in time. This means that if we change the signs of all the velocities, we will cause the molecules to retrace backwards their trajectories. The computer-generated trajectories should also posses this property.

There are many different methods for solving the ordinary differential equations of the form of Eq. (2.6). Criteria for the proper choice of an algorithm include the following:

- It must not require many forces evaluations per integration time step. Thus the common techniques for the solution of ordinary differential equations (such as the 4th order Runge-Kutta method) become inappropriate since they do not fulfill this criterion.

- It should satisfy the energy conservation law.

- It should permit the use of large time step dt.

- It should be *fast* and require *little memory*.

Concerning the solution of equations of motion for very long times it is clear that no algorithm provides an essentially exact solution. But this turns to be not a serious problem because the main object of the MD simulations is not to predict the exact configuration of a system after long time but rather is to predict the average behavior of the system and to calculate statistical predictions of the quantities we are interested in.

In the followings we describe the two most popular families of algorithms for the solution of classical equations of motion in MD simulations, i.e. the higher order methods and the Verlet algorithms.

A) Higher-Order Methods

The basic idea of the higher-order methods is to use information about positions and their n derivatives at time t in order to estimate positions and the n derivatives at time $t+dt$ [4]. If we consider the Taylor expansion of the position vectors of a given particle at time $t+dt$ and we include the 4th order terms

$$\mathbf{r}^p(t+dt) = \mathbf{r}(t) + dt\mathbf{v}(t) + \frac{dt^2}{2}\ddot{\mathbf{r}}(t) + \frac{dt^3}{6}\dddot{\mathbf{r}}(t) + \frac{dt^4}{24}\ddddot{\mathbf{r}}(t) + \dots \tag{2.7}$$

$$\mathbf{v}^p(t+dt) = \mathbf{v}(t) + dt\ddot{\mathbf{r}}(t) + \frac{dt^2}{2}\dddot{\mathbf{r}}(t) + \frac{dt^3}{6}\ddddot{\mathbf{r}}(t) + \dots \tag{2.8}$$

$$\ddot{\mathbf{r}}^p(t+dt) = \ddot{\mathbf{r}}(t) + dt\dddot{\mathbf{r}}(t) + \frac{dt^2}{2}\ddddot{\mathbf{r}}(t) + \dots \tag{2.9}$$

$$\dddot{\mathbf{r}}^p(t+dt) = \dddot{\mathbf{r}}(t) + dt\ddddot{\mathbf{r}}(t) + \dots \tag{2.10}$$

In the above equations the superscript p denotes "predicted" values. Eqs. (2.7)- (2.10) do not generate classical trajectories since we haven't introduced the eqs. of motion. To do this we estimate the size of the error, $\Delta\mathbf{x}$, by calculating the forces at the predicted positions

$$\Delta\mathbf{x} \equiv \ddot{\mathbf{r}}^{corrected}(t+dt) - \ddot{\mathbf{r}}^{predicted}(t+dt) \tag{2.11}$$

The error is account for and corrected in a "corrector" step, that is

$$\mathbf{r}^c(t+dt) = \mathbf{r}^p(t+dt) + c_0\Delta\mathbf{x} \tag{2.12}$$

$$\mathbf{v}^c(t+dt) = \mathbf{v}^p(t+dt) + c_1\Delta\mathbf{x} \tag{2.13}$$

$$\ddot{\mathbf{r}}^c(t+dt) = \ddot{\mathbf{r}}^p(t+dt) + c_2\Delta\mathbf{x} \tag{2.14}$$

$$\dddot{\mathbf{r}}^c(t+dt) = \dddot{\mathbf{r}}^p(t+dt) + c_3\Delta\mathbf{x} \tag{2.15}$$

where $c_i = 0,..,n$ are constants.

The general scheme of an algorithm based on the predictor-corrector method is as follows:

(a)   predict positions and their n derivatives at time $t+dt$ using the values of these quantities at time t.

(b)   compute forces from the new positions and the error $\Delta\mathbf{x}$

   (c)   correct the predicted positions and n derivatives using the quantity $\Delta\mathbf{x}$

B) Verlet Methods

This family of algorithms are simple, accurate and, as we will see later, time reversible. Thus, the Verlet methods are the most widely used methods for integrating the classical eqs. of motion. The initial form of Verlet equations [5] is obtained by using a Taylor expansion at time t-dt and t+dt

$$\mathbf{r}(t+dt) = \mathbf{r}(t) + dt\mathbf{v}(t) + \frac{dt^2}{2}\ddot{\mathbf{r}}(t) + \frac{dt^3}{6}\dddot{\mathbf{r}}(t) + \mathbb{Q}(dt^4) \tag{2.16}$$

$$\mathbf{r}(t-dt) = \mathbf{r}(t) - dt\mathbf{v}(t) + \frac{dt^2}{2}\ddot{\mathbf{r}}(t) - \frac{dt^3}{6}\dddot{\mathbf{r}}(t) + \mathbb{Q}(dt^4) \tag{2.17}$$

Summing these two equations, we obtain:

$$\mathbf{r}(t+dt) = 2\mathbf{r}(t) - \mathbf{r}(t-dt) + dt^2\ddot{\mathbf{r}}(t) + \mathbb{Q}(dt^4) \tag{2.18}$$

The calculations involved in one step of the algorithm as suggested by Eq. (2.18) are shown in Fig. 2.4a.

Two modifications of the Verlet scheme are of wide use. The first is the "leap-frog" algorithm [5] where positions and velocities are not calculated at the same time; velocities are evaluated every at half-integer time steps:

$$\mathbf{r}(t+dt) = \mathbf{r}(t) + dt\mathbf{v}(t+\frac{dt}{2}) \tag{2.19}$$

$$\mathbf{v}(t+\frac{dt}{2}) = \mathbf{v}(t-\frac{dt}{2}) + dt\ddot{\mathbf{r}}(t). \tag{2.20}$$

In order to calculate the Hamiltonian H at time t, we calculate the velocities at time t as the average of the values at $t + dt/2$ and $t - dt/2$ as

$$\mathbf{v}(t) = \frac{1}{2}\left(\mathbf{v}(t+\frac{dt}{2}) + \mathbf{v}(t-\frac{dt}{2})\right) \tag{2.21}$$

Fig. 2.4b shows the calculations involved in one step of the "leap-frog" algorithm.

The problem of defining the positions and velocities at the same time can be overcome by casting the Verlet algorithm in a different way. This is the velocity-Verlet algorithm [5], [11], according to which, positions are obtained by the usual Taylor expansion

$$\mathbf{r}(t+dt) = \mathbf{r}(t) + dt\mathbf{v}(t) + \frac{dt^2}{2}\ddot{\mathbf{r}}(t) \tag{2.22}$$

whereas the velocities are taken by

$$\mathbf{v}(t+dt) = \mathbf{v}(t) + \frac{dt}{2}\left[\ddot{\mathbf{r}}(t) + \ddot{\mathbf{r}}(t+dt)\right] \qquad (2.23)$$

To see how the velocity-Verlet algorithm is connected to the original Verlet method we note that

$$\mathbf{r}(t+2dt) = \mathbf{r}(t+dt) + dt\mathbf{v}(t+dt) + \frac{dt^2}{2}\ddot{\mathbf{r}}(t+dt) \qquad (2.24)$$

which means that if Eq. (2.22) written as

$$\mathbf{r}(t) = \mathbf{r}(t+dt) - dt\mathbf{v}(t) - \frac{dt^2}{2}\ddot{\mathbf{r}}(t) \qquad (2.25)$$

then by addition we get

$$\mathbf{r}(t+2dt) + \mathbf{r}(t) = 2\mathbf{r}(t+dt) + dt\left[\mathbf{v}(t+dt) - \mathbf{v}(t)\right] + \frac{dt^2}{2}\left[\ddot{\mathbf{r}}(t+dt) - \ddot{\mathbf{r}}(t)\right]. \qquad (2.26)$$

Substitution of Eq. (2.23) yields

$$\mathbf{r}(t+2dt) + \mathbf{r}(t) = 2\mathbf{r}(t+dt) + dt^2\ddot{\mathbf{r}}(t+dt) \qquad (2.27)$$

which indeed is the coordinate version of the Verlet algorithm. The calculations involved in one step of the algorithm are shown in Fig. 2.4c.
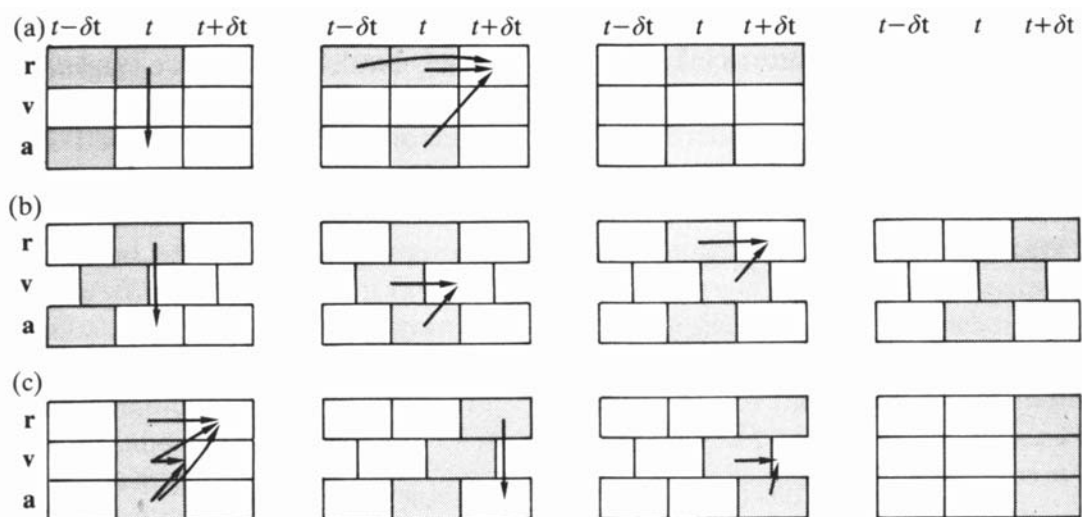
Figure 2.4 Various forms of the Verlet algorithm. (a) Verlet's original method (b) The leap-frog method. (c) The velocity-Verlet form. We show successive steps in the implementation of each algorithm. In each case the stored variables are in grey boxes

To conclude, we must report that the higher-order methods have a much better accuracy for small times. Their biggest drawback is that they are not reversible in time, which results into other problems such as insufficient energy conservation, especially in very long times MD simulations. On the other hand, the Verlet methods are not essentially exact for small times but their inherit time reversibility guarantees that the energy conservation law is satisfied even for very long times. This feature renders the Verlet methods, and usually the velocity-Verlet algorithm, the most appropriate for use in long atomistic MD simulations.

2.2.2 MD in NVT, NPT statistical ensembles

The methods described before consider the solution of Newton's equations of motion in a microcanonical (*NVE*) ensemble. In practice there is usually a need to perform MD simulations under specified conditions of temperature or/and pressure. In the literature there exist a variety of methodologies for performing MD simulations under isochoric of isothermal conditions [4]. Most of these constitute a reformulation of the Lagrangian equations of motion to include the constraints of constant *T* and/or *P*. The two mostly used methods for MD simulations under constant *T* or/and *P* are the Nosé-Hoover and the Berendsen method.

A) The Nosé Hoover Thermostat

To constrain temperature, Nosé [12] introduced an additional degree of freedom, *s*, in the Lagrangian. The parameter *s* plays the role of a heat bath, whose aim is to damp out temperature deviations from the desirable level. This necessitates adding to the total energy an additional potential term of the form

$$V_s = g k_B T \ln s \tag{2.28}$$

and an additional kinetic energy term of the form

$$K_s = \frac{Q}{2}\left(\frac{\dot{s}}{s}\right)^2 = \frac{p_s^2}{2Q}. \tag{2.29}$$

In the above equations, *g* is the total number of degrees of freedom ($g = 3 \, N_{atoms} - N_{bonds} - 3$ with N_{atoms} and N_{bonds} standing for the total numbers of atoms and bonds in the model system, respectively), while Q and p_s represent the ``effective mass'' and momentum, respectively, associated with the new degree of freedom *s*. Equations of motion are

derived from the Lagrangian of the extended ensemble, including the degree of freedom s. Their final form, according to Hoover analysis [13] is

$$\dot{\mathbf{r}}_i = \frac{\mathbf{p}_i}{m_i} \tag{2.30}$$

$$\dot{\mathbf{p}}_i = -\frac{\partial V}{\partial \mathbf{r}_i} - \frac{\dot{s}}{s}\mathbf{p}_i \tag{2.31}$$

$$\dot{p}_s = \left(\sum_{i=1}^{N}\frac{\mathbf{p}^2_i}{m_i} - gk_BT\right)/Q, \qquad p_s = Q\frac{\dot{s}}{s}. \tag{2.32}$$

An important result in Hoover's analysis is that the set of equations of motion is unique, in the sense that no other equations of the same form can lead to a canonical distribution.

The total Hamiltonian of the system, which should be conserved during the MD simulations, now becomes

$$H_{Nose-Hoover} = \sum_{i=1}^{N}\frac{\mathbf{p}^2_i}{m_i} + V(\mathbf{r}^N) + gk_BT\ln s + \frac{p_s^2}{2Q}. \tag{2.33}$$

To construct MD simulations under constant P an analogous reformulation of the Lagrangian was proposed by Andersen [14]. The constant-pressure method of Andersen allows for isotropic changes in the volume of the simulation box. Later Hoover [13] combined this method with the isothermal MD method described before to provide a set of equations that probe MD simulations in the *NPT* ensemble. Parrinello and Rahman [15] have extended the Andersen method to allow the simulation box to respond not only to changes in its size but also in its shape. This is particular important in the simulation of solids (e.g. glassy polymers) since it allows for phase changes in the simulation involving changes in the dimensions and angles of the unit cell.

B) The Berendsen Thermostat - Barostat

Berendsen proposed a simpler way for performing isothermal or/and isobaric MD simulations without the need of using an extended Lagrangian by coupling the system into a temperature or/and pressure bath [16]. To achieve this the system is forced to obey the equations

$$\frac{dT}{dt} = (T - T_{ext})/\tau_T \tag{2.34}$$

$$\frac{dP}{dt} = (P - P_{ext})/\tau_p \tag{2.35}$$

where T_{ext} and P_{ext} are the desired temperature and pressure and τ_T and τ_P are time constants characterizing the frequency of the coupling of the system to the temperature and the pressure baths. The solution of these equations forces velocities and positions to be scaled at every time step by a factor χ_T and x_P, respectively, with

$$x_T = \left(1 + \frac{dt}{\tau_T}\left(\frac{T}{T_{ext}} - 1\right)\right)^{1/2} \tag{2.36}$$

$$x_P = 1 - \beta_T \frac{dt}{\tau_P}\left(P - P_{ext}\right) \tag{2.37}$$

where β_T is the isothermal compressibility of the system.

The method proposed by Berendsen is much simpler and easier to programming than the one proposed by Nosé and Hoover. It suffers, however, from the fact that it is not defined in a certain statistical ensemble. Consequently, there exists no Hamiltonian that is conserved during the MD simulation.

2.2.3 Liouville Formulation of Equations of Motion - Multiple Time Step Algorithms

In section 2.2.1 we presented the most popular algorithms to integrate Newton's equations of motion some of which are not reversible in time. Recently Tuckerman *et al*. [17],[18] have shown how to systematically derive time reversible MD algorithm from the Liouville formulation of classical mechanics.

The Liouville operator L of a system of N degrees of freedom is defined in Cartesian coordinates as

$$iL = \sum_{i=1}^{N}\left[\dot{\mathbf{r}}_i \frac{\partial}{\partial \mathbf{r}_i} + F_i \frac{\partial}{\partial \mathbf{p}_i}\right]. \tag{2.38}$$

If we consider the phase-space of a system $\Gamma = \{\mathbf{r}_i, \mathbf{p}_i\}$ then the evolution of the system from time 0 to time t can be found by applying the evolution operator

$$\Gamma(t) = \exp\left(iLt\right)\Gamma(0). \tag{2.39}$$

The following step is to decompose the evolution operator into two parts such that

$$iL = iL_1 + iL_2 \quad \text{with } iL_1 = \sum_{i=1}^{N}\left[F_i \frac{\partial}{\partial \mathbf{p}_i}\right], \quad iL_2 = \sum_{i=1}^{N}\left[\dot{\mathbf{r}}_i \frac{\partial}{\partial \mathbf{r}_i}\right]. \tag{2.40}$$

For this decomposition a short-time approximation to the evolution operator can be generated via the Trotter theorem [19] as

$$\exp(iLt) = \exp(i(L_1 + L_2)t/P)^P =$$
$$(\exp(iL_1(dt/2))\exp(iL_2 dt)\exp(iL_1(dt/2)))^P + O(t^3/P^2) \qquad (2.41)$$

where $dt = t/P$. Thus the evolution operator becomes

$$\exp(iLdt) = \exp(iL_1\frac{dt}{2})\exp(iL_2\frac{dt}{2})\exp(iL_1\frac{dt}{2}) + O(dt^3) \qquad (2.42)$$

The evolution of the system at time t, Eq. (2.42), using the above factorization, is described through the following scheme [18]

$$\mathbf{r}(dt) = \mathbf{r}(0) + dt\mathbf{v}(0) + \frac{dt^2}{2m}\mathbf{F}[\mathbf{r}(0)] \qquad (2.43)$$

$$\mathbf{v}(dt) = \mathbf{v}(0) + \frac{dt^2}{2m}(\mathbf{F}[\mathbf{r}(0)] + \mathbf{F}[\mathbf{r}(dt)]) \qquad (2.44)$$

which is the well-known velocity-Verlet scheme.

A very efficient algorithm then can be developed, based on the previous factorization, through the use of different time steps for the different parts of the Liouville operator. This is the reversible REference System Propagator Algorithm (rRESPA).

2.2.3.1 rRESPA Algorithm

In the rRESPA algorithm, the above factorization is employed together with an integration of each part of the Liouville operator with a different time step. In addition the forces, $\mathbf{F}$, are also decomposed into fast (short range forces), $\mathbf{F}^f$, and slow (long range forces), $\mathbf{F}^s$, according to $\mathbf{F}(\mathbf{r}) = \mathbf{F}^f(\mathbf{r}) + \mathbf{F}^s(\mathbf{r})$. The total evolution operator is broken up into the following parts $iL = iL_1 + iL_2 + iL_3$ with

$$iL_1 = \sum_{i=1}^{N}\left[\mathbf{F}_i^f(\mathbf{r})\frac{\partial}{\partial \mathbf{p}_i}\right], \qquad iL_2 = \sum_{i=1}^{N}\left[\dot{\mathbf{r}}_i\frac{\partial}{\partial \mathbf{r}_i}\right], \qquad iL_3 = \sum_{i=1}^{N}\left[\mathbf{F}_i^s(\mathbf{r})\frac{\partial}{\partial \mathbf{p}_i}\right]. \qquad (2.45)$$

The heart of the rRESPA algorithm is that the equations of motion are integrated by using two different time steps, i.e. Multiple Time Step (MTS) method. In more details the slow modes (slow forces, iL_3) are integrated with a big time step, Δt, whereas the fast modes (fast forces and velocities iL_1, iL_2) with one smaller time step, δt ($\delta t = \Delta t/n$). The evolution operator becomes

$$\exp(iL\Delta t) = \exp(iL_3\frac{\Delta t}{2})\left[\exp(iL_1\frac{\delta t}{2})\exp(iL_2\delta t)\exp(iL_1\frac{\delta t}{2})\right]^n \exp(iL_3\frac{\Delta t}{2}) + O(\Delta t^3) \qquad (2.46)$$

A very simple flow diagram of the algorithm goes as follows

$$\mathbf{v} = \mathbf{v} + \frac{\Delta t}{2m} * \mathbf{F}^s \left[\mathbf{r}(0) \right]$$

DO $i = 1, n$

$$\mathbf{v} = \mathbf{v} + \frac{\delta t}{2m} * \mathbf{F}^f \left[\mathbf{r}\big((i-1)\delta t \big) \right]$$

$$\mathbf{r} = \mathbf{r} + \delta t * \mathbf{v}$$

CALL short_range_forces

$$\mathbf{v} = \mathbf{v} + \frac{\delta t}{2m} * \mathbf{F}^f \left[\mathbf{r}\big(i\delta t \big) \right]$$

END DO

CALL long_range_forces

$$\mathbf{v} = \mathbf{v} + \frac{\Delta t}{2m} * \mathbf{F}^s \left[\mathbf{r}\big(\Delta t \big) \right]$$

The force calculated n times (fast force) is called the reference force.

2.2.3.2 rRESPA in the NVT Ensemble

A modification of rRESPA algorithm has been proposed for MD simulation in NVT ensemble. The method uses a modification of the Lagrangian of the system based on the Nosé-Hoover approach, described in section 2.2.2.

The difference with the standard rRESPA scheme described before, is that in this case, the total Liouville operator is decomposed as

$$iL = iL_1 + iL_2 + iL_3 + iL_{NH} \tag{2.47}$$

with

$$iL_1 = \sum_{i=1}^{N} \left[\mathbf{F}_i^f(\mathbf{r}) \frac{\partial}{\partial \mathbf{p}_i} \right], \qquad iL_2 = \sum_{i=1}^{N} \left[\dot{\mathbf{r}}_i \frac{\partial}{\partial \mathbf{r}_i} \right], \qquad iL_3 = \sum_{i=1}^{N} \left[\mathbf{F}_i^s(\mathbf{r}) \frac{\partial}{\partial \mathbf{p}_i} \right]. \tag{2.48}$$

Also,

$$iL_{NH} = -\sum_{i=1}^{N} \upsilon_\xi \mathbf{v}_i \bullet \frac{\partial}{\partial \mathbf{v}_i} + \upsilon_\xi \frac{\partial}{\partial \xi} + G \frac{\partial}{\partial \upsilon_\xi} \tag{2.49}$$

where

$$G = \left(\sum_{i=1}^{N} \frac{\mathbf{p}^2_i}{m_i} - g k_B T \right) / Q , \qquad \upsilon_\xi = \dot{\xi} . \tag{2.50}$$

Two modifications of the standard RESPA method can be constructed depended on the application of the extended operator $\exp(iL_{NH}t)$. The first variant of RESPA is useful when the evolution prescribed by the operator $\exp(iL_{NH}t)$ is slow compared with the time scale associated with the reference force. It is formed by writing

$$\exp(iL\Delta t) = \exp(iL_{NH}\frac{\Delta t}{2})\exp(iL_3\frac{\Delta t}{2})\left[\exp(iL_1\frac{\delta t}{2})\exp(iL_2\delta t)\exp(iL_1\frac{\delta t}{2}) \right]^n$$
$$\exp(iL_3\frac{\Delta t}{2})\exp(iL_{NH}\frac{\Delta t}{2}) + O(\Delta t^3) \tag{2.51}$$

and is named XO-RESPA (eXtended system Outside-Reference System Propagator Algorithm). In general, XO-RESPA can be applied in systems that have fast vibrations as the time scale associated with the extended system variable is usually chosen to be slow compared with these motions.

If the motion prescribed by the operator $\exp(iL_{NH}t)$ occurs on the same time scale as that generated by the "fast" forces, then a useful RESPA algorithm must include the application of this operator for the small time step dt. Then the form of the evolution operator is

$$\exp(iL\Delta t) = \exp(iL_{NH}\frac{\delta t}{2})\exp(iL_3\frac{\Delta t}{2})\exp(-iL_{NH}\frac{\delta t}{2})$$
$$\left[\exp(iL_{NH}\frac{\delta t}{2})\exp(iL_1\frac{\delta t}{2})\exp(iL_2\delta t)\exp(iL_1\frac{\delta t}{2})\exp(iL_{NH}\frac{\delta t}{2}) \right]^n \tag{2.52}$$
$$\exp(-iL_{NH}\frac{\delta t}{2})\exp(iL_3\frac{\Delta t}{2})\exp(iL_{NH}\frac{\delta t}{2}) + O(\Delta t^3)$$

The resulting integrator is named XI-RESPA (eXtended system Inside-REference System Propagator Algorithm).

Modifications of the RESPA method, for MD simulations in the NPT statistical ensemble, have been also formulated in an analogous manner. Details can be found in the original papers [17],[18].

2.2.4 Constraint Dynamics in Polymeric systems

One of the most important points for the choice of the best algorithm for the solution of classical equations of motion is, as we show before, the time step of integration. The time step should be chosen such that it is appreciably shorter than the shortest relevant time scale in the simulation. Especially in the simulations of long polymeric systems if we simulate the intramolecular dynamics of polymers explicitly, this implies that our time step should be shorter than the period of the highest-frequency intramolecular motion. This makes the simulation of long polymers very expensive. A technique developed to tackle this problem is to treat the bonds between atoms, which have the highest frequency intramolecular vibrations, as rigid. The MD equations of motion are then solved under the constraint that the bond lengths do not change during the simulation. The motion associated with the remaining degrees of freedom is presumably slower, permitting us of using a longer time step in our simulations.

In the general case the dynamics should satisfy many constraints (e.g. many bond lengths) simultaneously. Let us denote the functions describing the constraints by σ_i with $\sigma_i = \mathbf{r}^2{}_{ij} - d^2{}_{ij}$ where the atoms i and j are at a fixed distance d_{ij}. We now introduce a new Lagrangian in the system that contains all the constraints

$$L^c = L - \sum_i \lambda_i \sigma_i(\mathbf{r}^N) \tag{2.53}$$

where i denotes a set of constraints and λ_i denotes a set of Lagrange multipliers. The new equations of motion corresponding to the new Lagrangian are

$$m_i \ddot{\mathbf{r}}_i = \mathbf{F}_i - \sum_i \lambda_i \frac{\partial \sigma_i}{\partial \mathbf{r}_i} = \mathbf{F}_i - \mathbf{g}_i. \tag{2.54}$$

The second right term denotes the constraint forces. The point now is to find the proper set of Lagrange multipliers λ_i. Two methods that have been used in our MD simulations will be discussed here: The Edberg-Evans-Moriss method and the SHAKE method.

A) Edberg – Evans – Morriss algorithm

This algorithm [20] by using of a linear system of equations in $\{\lambda_{ij}\}$. These linear equations are formulated by considering the second time derivatives of the constraints:

$$\mathbf{r}^2{}_{ij} - d^2{}_{ij} = 0 \Rightarrow 2\mathbf{r}_{ij} \bullet \dot{\mathbf{r}}_{ij} = 0 \Rightarrow \mathbf{r}_{ij} \bullet \ddot{\mathbf{r}}_{ij} + (\dot{\mathbf{r}}_{ij})^2 = 0 \tag{2.55}$$

One then solves the following system of algebraic and differential equations simultaneously:

$$m_i \ddot{\mathbf{r}}_i = \mathbf{F}_i + \mathbf{g}_i \qquad (2.56)$$

$$\mathbf{g}_i = \sum_i \lambda_i \frac{\partial \sigma_i}{\partial \mathbf{r}_i} \qquad (2.57)$$

$$\mathbf{r}_{ij} \bullet \ddot{\mathbf{r}}_{ij} + (\dot{\mathbf{r}}_{ij})^2 = 0 . \qquad (2.58)$$

Note that site velocities enter this formulation explicitly. Upon substitution of the site accelerations from Eq. (2.54) into Eq. (2.58) one obtains a system of linear equations in $\{\lambda_{ij}\}$; thus the determination of the $\{\lambda_{ij}\}$ reduces to the solution of a linear matrix equation in each time step.

B) SHAKE - RATTLE Method

The approach described before has the basic problem that is not computationally cheap because it requires a matrix inversion every time step. The problem is increasing with the number of atoms per polymeric chain and practically becomes inappropriate for long chains with more than about 100 atoms per chain. A simpler scheme, named SHAKE, to satisfy the constraints developed by Ryckaert *et al*. [21].

Considering the classical form of the Verlet algorithm. In the presence of constraints

$$\mathbf{r}^c_i(t + dt) = \mathbf{r}^u_i(t + dt)_i - \frac{dt^2}{m_i} \sum_k \lambda_k \frac{\partial \sigma_k(t)}{\partial \mathbf{r}_i} \qquad (2.59)$$

where $\mathbf{r}^c_i$ are the constrained positions and $\mathbf{r}^u_i$ the positions without the constraints. If we satisfy the constraints at time $t+dt$, then $\sigma^c_k(t+dt) = 0$. But if the system would move along the unconstrained trajectory, the constraints would not be satisfied at $t+dt$. We assume that we can perform a Taylor expansion of the constraints:

$$\sigma^c_k(t + dt) = \sigma^u_k(t + dt) + \sum_{i=1}^{N} \left(\frac{\partial \sigma_k}{\partial \mathbf{r}_i} \right)_{\mathbf{r}^u_i(t+dt)} \bullet \left[\mathbf{r}^c_i(t + dt) - \mathbf{r}^u_i(t + dt) \right] + \mathrm{O}(dt^4) . \qquad (2.60)$$

and by using Eq. (2.59)

$$\sigma^u_k(t + dt) = \sum_{i=1}^{N} \frac{dt^2}{m_i} \sum_{k'} \lambda_{k'} \left(\frac{\partial \sigma_k}{\partial \mathbf{r}_i} \right) \left(\frac{\partial \sigma_{k'}}{\partial \mathbf{r}_i} \right) . \qquad (2.61)$$

The above equation has the structure of a matrix equation

$$\sigma^u_k(t + dt) = dt^2 M \mathbf{\Lambda} \qquad (2.62)$$

By inverting the matrix, we can solve for the vector $\boldsymbol{\Lambda}$. However, as we have truncated the Taylor expansion in Eq. (2.60), we should then compute σ's at the corrected positions, and iterate the preceding equations until convergence is reached.

This procedure is also not computationally cheap as it requires a matrix inversion at every iteration, as in Edberg–Evans–Morriss algorithm. Ryckaert proposed a scheme, the SHAKE method, where the iterative scheme is not applied to all constraints simultaneously but to each constraint in succession. Thus we avoid the need of the inversion of a big matrix. The basic point is that we approximate $\mathbf{r}^c_i - \mathbf{r}^u_i$ as

$$\mathbf{r}^c_i(t+dt) - \mathbf{r}^u_i(t) \approx\sim -\frac{dt^2 \lambda_k}{m_i} \frac{\partial \sigma_k(t)}{\partial \mathbf{r}_i} . \tag{2.63}$$

If then we insert the above equation in Eq.(2.60), we get

$$\sigma^u_k(t+dt) = dt^2 \lambda_k \sum_{i=1}^{N} \frac{1}{m_i} \frac{\partial \sigma_k(t+dt)}{\partial \mathbf{r}_i} \frac{\partial \sigma_k(t)}{\partial \mathbf{r}_i} \tag{2.64}$$

and the Lagrange multiplier λ_k becomes

$$\lambda_k dt^2 = \frac{\sigma^u_k(t+dt)}{\sum_{i=1}^{N} \frac{1}{m_i} \frac{\partial \sigma_k(t+dt)}{\partial \mathbf{r}_i} \frac{\partial \sigma_k(t)}{\partial \mathbf{r}_i}} . \tag{2.65}$$

In a MD simulation we treat all the constraints in succession during one cycle of the iteration and then repeat the process until all constraints have converged to the desired accuracy. An improvement of the SHAKE algorithm known as RATTLE was proposed by Andersen [22]. RATTLE employs the velocity-Verlet algorithm to integrate the dynamical equations.

2.3   The Implementation of the MD Method to Polymeric Systems

For standard problems in physics and chemistry of condensed matter (such as simple fluids containing gas atoms or diatomic molecules) computer simulation considers a small region of matter in full atomistic detail [4]. For simple fluids these methods works because they are homogenous on a scale of about 10 Å already. Reliable model for the effective forces are usually available from quantum chemistry methods.

MD simulations in long flexible polymers encounter a different situation due to the wide spread of length scales characterizing their structure and time scale characterizing their motion as we show in the introduction. As we have already seen in the introduction one solution to the problem of long relaxation times is to follow hierarchical approaches

that are using combination of simulation techniques and theories. A different solution to the above problems is to abandon the chemical detail and concentrate in the dynamics of long wavelengths. This is the case of coarse-graining simulations.

What follows are first a detailed representation of the atomistic molecular model used in the MD simulations and after that a representation of the coarse-grained simulations.

2.3.1 Atomistic Molecular Model

Consider a polyethylene chain in full atomistic representation as the one shown in Fig. 2.5. There are two ways of treating the hydrogen atoms. The one is to treat them explicitly, i.e. explicit atom (EA) models. The second is to introduce spherical segments, as in Fig. 2.5a, representing a CH_2, i.e. united atom (UA) models. There are two types of interactions in this atomistic representation. The first is between atoms that are bonded or next near up to n bonds (bonded interactions). The second one is between atoms that are belonging to different polymeric chains or to the same chain but their distance is above n bonds (non-bonded interactions) [1].
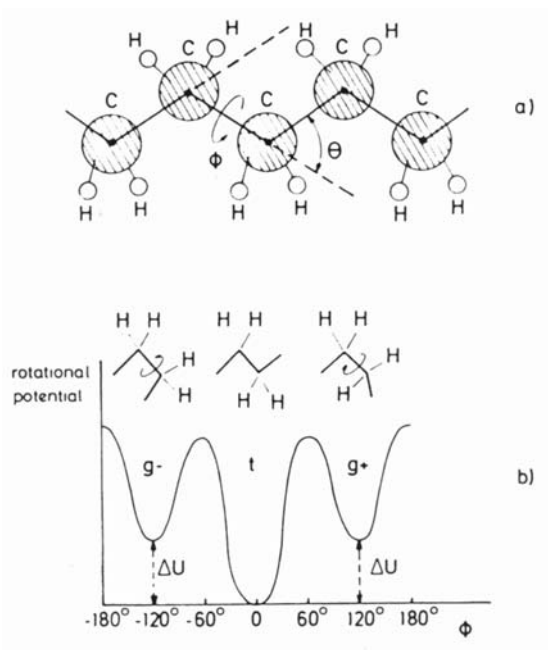
Figure 2.5 (a) Schematic model of a piece of the polyethylene chain in the united atom representation. (b) Qualitative sketch of the torsional potential for alkane chains.

The bonded interactions depend on the type of the polymeric systems. There are, however, three general types of bonded interactions:

a) Interactions between atoms that are connected through a bond. The interaction of the chemical bond can be incorporated through a harmonic potential (bond stretching interaction) of the form

$$V_{stretching}(l) = \frac{1}{2} K_b (l - l_0)^2 \qquad (2.66)$$

where l is the bond length and l_0 is its equilibrium value.

b) For atoms that are belonging to 2 successive bonds a bond-bending potential of the following form is used

$$V_{bending}(\theta) = \frac{1}{2} K_\theta (\theta - \theta_0)^2 \qquad (2.67)$$

where θ is the bond length and θ_0 is its equilibrium value.

c) For atoms that are belonging to 3 successive bonds (see Fig. 2.5b) there is a torsional potential, associated with each dihedral angle ϕ. The type of the torsional potential is usually of the form

$$V_{torsional}(\phi) = \sum_{i=0}^{n} c_i (\cos \phi)^i \qquad (2.68)$$

with n around 3-5 and c_i constants characterizing the potential.

For systems with special types of interactions (double bonds, hydrogen bonds, special dihedral angles, etc.) there are other much more detailed and complicated types of bonded interactions [1].

The non-bonded interactions are usually of two types:

a) The first are *short-range* interactions. These interactions are between atoms belonging to different chains or atoms that are in the same chain but they are separated by more than n (usually 3) bonds apart and have the following Lennard-Jones (LJ) form

$$V_{LJ}(\mathbf{r}) = 4\varepsilon \left[\left(\frac{\sigma}{\mathbf{r}} \right)^{12} - \left(\frac{\sigma}{\mathbf{r}} \right)^6 \right] \qquad (2.69)$$

where ε and σ are parameters characteristic of the type of the atom. The parameters between different type of sites (atoms) are usually determined by the Lorentz-Berthelot rules:

$$\varepsilon_{CH_2-CH_3} = \sqrt{\varepsilon_{CH_2}\varepsilon_{CH_3}} \ , \quad \sigma_{CH_2-CH_3} = \frac{\sigma_{CH_3} + \sigma_{CH_2}}{2} \tag{2.70}$$

b) The second type of non-bonded interactions is the well-known *long-range* Coulomb interactions. Consider a number of atoms N in a cubic box of length L. If periodic boundary conditions are applied and we assume that the system as a whole is electrically neutral, then the Coulomb contribution to the potential energy of this system is

$$V_Q = \frac{1}{2}\sum_{\mathbf{n}}\left(\sum_{i=1}^{N}\sum_{j=1}^{N}\frac{z_i z_j}{\mathbf{r}_{ij} + \mathbf{n}L}\right) \tag{2.71}$$

where z_i and z_j are the charges and the first sum is over all periodic images $\mathbf{n}$. For simulating systems with long-range interactions special simulation techniques needed, such as the Ewald summation, the particle-particle/particle mesh (PPPM) method or the fast multipole method [5].

2.3.2 Coarse - graining Simulations

As we show in the introduction coarse-graining entails replacing a detailed molecular model (e.g. an atomistic model with detailed representation of bonded and non-bonded interactions as the one described in previous section) with a simpler model, cast in terms of fewer variables, without loss of significant information. The coarse-grained model is desirable because it is more manageable computationally in simulations and more amenable to theoretical treatment. The parameters of the coarse-grained model must be determined from those of the detailed through a rigorous mapping procedure.

Many different coarse-grained models have been developed in the literature [1]. These models are both lattice (such as the self avoiding walk model, the bond-fluctuation model etc.) and off-lattice models (like the bead-spring model, the freely jointed chain, the pearl necklace model etc.). The most popular coarse-grained models are that of bead-spring type, where the polymeric chain is represented as a sequence of beads connected with springs. It is often more advantageous not to use a simple harmonic potential, Eq. (2.66), but rather a non-Hookean potential allowing only a finite extensibility of the chains. This is the one so-called FENE potential, which has the following form

$$V_{FENE}(l) = \begin{cases} -0.5 K_{FENE} l^2_{\max} \ln\left[1-\left(l_i/l_{\max}\right)^2\right], & l_i < l_{\max} \\ \infty, & l_i > l_{\max} \end{cases} \tag{2.72}$$

where the constants K_{FENE} and l_{max} are closely related to the parameters ε and σ of the Lennard-Jones potential.

The first pioneering work of coarse-grained MD simulations of the bead-spring model was performed by Kremer and Grest [23]. The have studied the dynamics of various polymer lengths by using the FENE potential. Later many workers used the same model for the study of different systems [24],[25].

The last years many works consider a mapping procedure to go from microscopic description of a polymer chain to the mesoscopic description, which allows a fairly effective simulation procedure on a coarse grained level [26],[27],[28]. A rigorous framework for the mapping to coarse-graining description is offered by the projection operation formalism of the statistical mechanics. For coarse-graining to be successful, the coarse-grained variables must evolve slowly relative to the detailed variables being eliminated from the model description. Interactions at the coarse-grained level are described in terms of the potential of mean force (free energy) derivable by integrating the Boltzmann factor of the detailed model Hamiltonian over all detailed variables being eliminated at each coarse-grained configuration.

The main aim of all the methods that consider the mapping onto a mesoscopic description is to reintroduce atomistic information from quantum-chemical calculations into coarse-grained models. To achieve this usually effective pair potentials of the coarse grained model that will lead uniquely to the atomistic measured pair distribution functions are obtained. In all these approaches a systematic strategy should involve two parts:

- the determination of intramolecular effective potentials (such as bonded or angular potentials) between the mesoscopic variables which are assumed to be bonded and

- the determination of intermolecular effective potentials between nonbonded mesoscopic variables.

However a number of different algorithms have been proposed to obtain effective intramolecular and intermolecular potentials from distribution functions. The simplest approach is to use the potential of mean force as the effective pair potential. This is the effective interaction in the limit of low density, where many-body interactions become quantitatively less significant. At realistic densities, however, this approach leads to overcounting of the many-body interactions, leading to a specious representation of non-

bonded interactions. Despite this deficiency, this approximation has been used to represent the coarse-grained intramolecular interactions in polycarbonates.

In a recent work Briels *et al.* [27] developed a similar simulation procedure to obtain effective interactions between coarse-grained sites in polymer melts. In their approach a microscopic polymer melt is renormalized to a chain of mesoscopic particles, called blobs, representing the center of mass coordinates of parts of the chain. Then the interaction model for the blobs is based on effective pair interactions, which were determined by matching the predetermined structure at the pair-level.

The basic idea of their method is to simulate a coarse-grained system with a pair interaction that is allowed to change in time. The extended system evolve in time such that the final system reproduces a given pair distribution after some time. This is accomplished by minimizing the deviation from the object properties with respect to the force field parameters. The object pair distribution function is obtained from preceding detailed atomistic simulations of the microscopic system.

Recently Briels *et al.* [28] have also performed a rigorous mapping of an atomistic C_{120} melt onto a mesoscopic description of blobs. In more details, they represent the polymer chains as a sequence of n blobs the position of which is the center of mass of λ monomers. In their mapping of C_{120} it was $n = 6$ and $\lambda = 20$. Then they approximated potential of mean force in the mesoscopic, blob, system as a sum of nonbonded, bonded and angular potentials. These potentials were calculated from the corresponding distributions, which were forced to coincide with the distribution functions obtain from the microscopic simulations.

A more mesoscopic approach for the dynamical study of complex systems in longer time and length scales than the atomistic MD simulations is the dissipative particle dynamics (DPD). DPD method introduced by Hoogerbrugge and Koelman, a few years ago [29], for studying the hydrodynamic behavior of solutions. Their technique is based on the simulation of soft spheres, whose motion is governed by certain collision rules. By introducing bead-and-spring type particles, DPD method recently simulated polymer systems [31],[32]. The first applications of DPD methods in polymer systems, consider polymer-surfactant systems and the study of the formation of micelles, networks, mesophases and so forth. Very recently Groot *et al.* [31] have studied the microphase separation of diblock copolymer melt and the effect of hydrodynamic interaction with DPD simulations.

However, the main drawback of the DPD method is the length and time scale interpretation, since the method makes use of arbitrary units. The structural aspects and the energy interaction parameters of the solvents and the polymer chains are given as input to the code. Thus the main goal of the DPD approaches in the near future will be the derivation of a systematic way of determining the input unit, so that will be possible to convert the arbitrary time and length scales of the simulation to real units, readily comparable to experimental data.

All the above works look very encouraging and provide a systematic way of coarse graining many different types of polymers. On the other hand clearly more work is necessary to find proper coarse-grained potentials that reproduce essentially the atomistic information.

CHAPTER 3

POLYMER MELT DYNAMICS AND VISCOELASTICITY:
A LITERATURE SURVEY

3.1. Viscoelastic Behavior of Polymers

At the molecular level there are several important differences between polymeric (or macromolecular) fluids and the simpler "small-like" molecules. The very high molecular weight of common polymeric liquids, the spread molecular weight distribution, the tremendous number of polymer configurations that polymer molecules can assume event at equilibrium, or the very complicate polymer-polymer interactions in polymer concentrated solutions and melts are among them [34],[35]. Because of these differences the flow behavior of polymeric fluids is quite unlike that of the small-molecule fluids, which are satisfactory described by Newtonian fluid dynamics, and is widely to known by the term "viscoelasticity". Viscoelasticity is demonstrated in many applications of these systems. And sometimes it shows up in very simple experiments.

Consider, for example, two identical vertical tubes the bottoms of which are covered by a flat plate, as in Fig. 3.1a. The two tubes are filled with fluids, one Newtonian and the other polymeric, chosen in such a way as to have the same viscosity. When the plate is removed from the bottoms of the tubes the fluids are allowed to flow out by the gravity. The volumetric flow polymeric fluid drains more quickly than the Newtonian fluid (Fig. 3.1b). According to classical hydrodynamics the volumetric flow rate in a tube is inversely proportional to the fluid viscosity. Thus the viscosity of the polymer fluid appears to be lower in the higher shear rate. The decrease in viscosity with increasing shear rate is referred to as *shear thinning*, and the fluid is said to be *pseudoplastic*. Almost all polymer solutions and melts that exhibit a shear-rate dependent viscosity are pseudoplastic. On the other hand, there exist few polymer fluids which

behave oppositely to what we have shown here, that is, they show *shear thickening* and flow out of the tube more slowly than the corresponding Newtonian liquid. A fluid whose viscosity increases with shear rate is called *dilatant*.
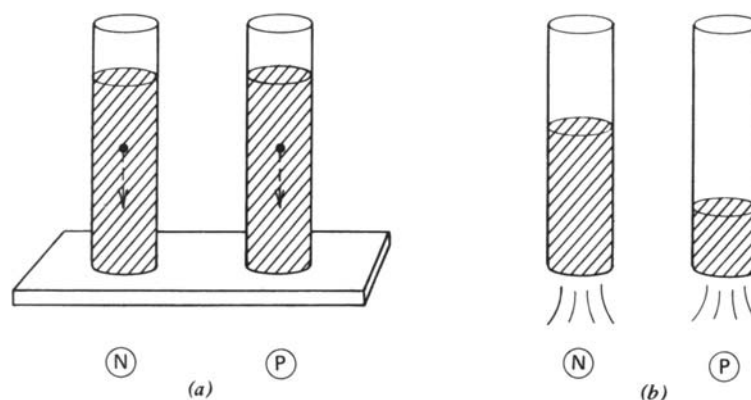
Figure 3.1 Tube flow and shear thinning. In each part the Newtonian behavior is shown in the left; the behavior of a polymer in the right. (a) A tiny sphere falls at the same rate through each; (b) the polymer flows out faster then the Newtonian fluid.

A second phenomenon which the polymeric fluids exhibit in comparison with the Newtonian liquid is demonstrated in the rod-climbing experiment. Consider rotating rods which are inserted into two beakers, one containing a Newtonian fluid and the other a polymer solution. Newtonian liquid behaves exactly as expected. The liquid near the rotating rod is pushed outward by centrifugal force, and the typical dip in the liquid surface near the center of the beaker results. The contrasting behavior of a polymeric fluid is striking. The polymer liquid moves in the opposite direction, toward the center of the beaker and climbs up the rod. This phenomenon is called the *Weissenberg effect*, as Weissenberg was the first to explain such an effect in terms of the normal stresses in polymer fluids undergoing a steady shearing flow.

A particular striking contrast between the viscoelastic behavior of macromolecular fluids and the purely viscous behavior of Newtonian fluids is also provided by the *recoil* experiment. In this experiment a pressure gradient is applied to a polymer solution and the deformation of the polymer solution is recorded. After a short time the pressure gradient is removed and the fluid *recoils*.

Another very interesting experiment involving the siphoning of Newtonian and polymeric fluids (see Fig. 3.2). When the tube is lifted up out of the fluid the flow of the Newtonian liquid through the siphon stops. Not so with the polymer fluid which continuous to flowing up to and through the siphon. This experiment is closely related to

a property of polymeric liquids known as "spinnability", i.e. the stability of a stretching filament of fluid with respect to small perturbations in its cross-sectional area. This spinnability is one of the principal reasons for the commercial importance of many polymers.
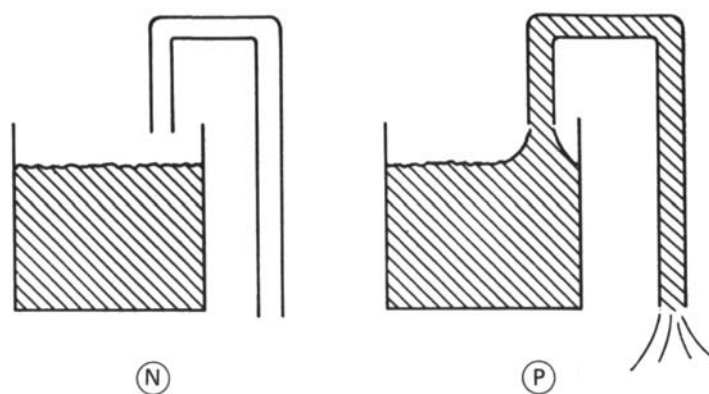
Figure 3.2 The tubeless siphon. When the siphon ifs lifted out of the fluid, the Newtonian liquid (a) stops flowing while the polymer fluid (b) continues to be siphoned.

There are several other phenomena exhibiting the remarkable differences between the behavior of Newtonian and that of polymeric liquids which will not be detailed here. They include the axial annular flow, the extrudate swell, the Uebler effect [34].

All the above phenomena render the theoretical study of polymer dynamics and viscoelasticity quite complicated and this justifies the completely different routes that have been followed, over the years to describe them, ranging from simple mechanical models, to polymer kinetic theory, to molecular models and to nonequilibrium irreversible thermodynamics.

Mechanical Models

Even one polymer molecule is, however, an extremely complex material with an enormous number of degrees of freedom. Thus studying in details its motions and their relations to the nonequilibrium properties would be prohibitively difficult. As a result it has been customary to resort to mechanical models. The rotational isomeric chain state model, the freely jointed chain, the freely rotating chain, the Porod-Kratky wormlike chain and the pearl necklace model are some of the mostly used mechanical models for the description of polymer systems, mainly at equilibrium. Of special interest are the freely jointed bead-spring models where a polymer chain is represented as consists of N

"beads" connected by "springs". When the number of beads N becomes 2 then one recovers the dumbbell model.

Polymer Kinetic Theory

To describe the nonequilibrium dynamics of polymers, with the use of the above mechanical models, a polymer kinetic theory has been developed over the years [35]. Polymer kinetic theory models are formulated around two basic building blocks: an equation for the configurational distribution function and an equation for the stress tensor. In equilibrium systems one can write down a formal expression for the configurational distribution function directly by means of equilibrium thermodynamics. For nonequilibrium systems the situation is much more complicated. The final equation for the configurational distribution function is a second-order differential equation, called the "diffusion equation", since it describes how the system points "diffuse" in the multidimensional configuration space appropriate for the molecular model.

Consider, for example, the elastic dumbbell model and the configurational distribution function $\Psi(\mathbf{Q},t)$, which express the probability that the two beads are found at distance $\mathbf{Q}$ ($\mathbf{Q} = \mathbf{r}_i - \mathbf{r}_{i-1}$) at time t. The starting point for deriving the diffusion equation is a "force-balance" acting on each bead

$$\mathbf{F}^{(h)} + \mathbf{F}^{(b)} + \mathbf{F}^{(u)} + \mathbf{F}^{(e)} = 0 \tag{3.1}$$

where $\mathbf{F}^{(h)}$ is the hydrodynamic drug force, $\mathbf{F}^{(b)}$ is the Brownian force, $\mathbf{F}^{(u)}$ is the intramolecular force acting resulting from the "spring" in the dumbbell and $\mathbf{F}^{(e)}$ is any kind of external force acting on the system. Based on this a diffusion equation for the distribution function $\Psi(\mathbf{Q},t)$ is obtained having the following general form:

$$\frac{\partial \Psi}{\partial t} = -\left(\frac{\partial}{\partial \mathbf{Q}} \bullet \left\{ [\mathbf{k} \bullet \mathbf{Q}] \Psi - \frac{2k_B T}{\zeta} \frac{\partial \Psi}{\partial \mathbf{Q}} - \frac{2}{\zeta} \mathbf{F}^{(u)} \right\} \right) \tag{3.2}$$

where $\mathbf{k}$ is the rate-of-strain tensor describing the form of the applied flow. In the above equation the hydrodynamic force is described through an isotropic $\boldsymbol{\zeta}$ tensor, $\boldsymbol{\zeta} = \zeta \boldsymbol{\delta}$, where ζ is called the friction coefficient.

Once the configurational distribution function has been obtained, an expression for the stress tensor is needed to make the connection with rheological behavior and fluid dynamics. The stress tensor expression accounts for the various mechanisms by which forces are transmitted through the fluid. The total stress in a polymer solution is

presumed to be the sum of contribution from the solvent, π_s, and another, π_p, resulting from the presence of polymer molecules:

$$\pi = \pi_s + \pi_p = -p\delta + \tau \qquad (3.3)$$

where p is the isotopic part of the stress and $\tau = \tau_s + \tau_p$ is the anisotropic part (contribution due to the nonequilibrium conditions). A general form of the τ for the elastic dumbbell is the Kramers relation:

$$\tau = -\eta_s k + \tau^u{}_p \qquad (3.4)$$

with η_s the solvent viscosity and $\tau^u{}_p$ the contribution to the stress due to intramolecular potential

$$\tau^u{}_p = -n\int \mathbf{Q}\mathbf{F}^{(u)}\Psi(\mathbf{Q},t)d\mathbf{Q} = -n\left\langle \mathbf{Q}\mathbf{F}^{(u)}\right\rangle . \qquad (3.5)$$

The elastic dumbbell models are drastic simplifications of the true polymer systems. Their main simplification concerns that they describe the dynamics of polymer systems with only one relaxation time. Despite this, they proved to describe qualitatively the rheological properties of many flexible macromolecules, such as polyethylene, polystyrene or polyisobutylene. For a more quantitatively description of this category of polymeric materials the more realistic bead-spring chain models, which involve a spectrum of relaxation times, should be used. Bead-spring chain models composed of N beads and N-1 springs. If the springs are Hookean, then two popular models arise, the Rouse and the Zimm models, which will be presented in details later in this chapter.

In the case of stiffer polymers that are rodlike, such as proteins in helical forms, poly-n-butylisocyanate or DNA in its helix configuration, rigid models should be used. The rigid dumbbell is such a model, with the multibead rod model being the analog of the bead-spring model. These models account for the orientability of the polymer molecules in flow fields and ignore the less important, for rodlike polymers, molecular stretching and bending motions.

Over the years, a more systematic description of dilute solutions, concentrated solutions and polymer melts through the use of mechanical models, has been offered by the development of the general. In phase-space kinetic theory, the equation of continuity for configuration-space distribution function, the equations of internal motion for the constituents, and the expression for the stress tensor are derived from first principles. In the statistical treatment, it is shown that the actual or "probable" behavior of a physical system is described by the average behavior of a large number, or an "ensemble", of identical systems. If x is a point in the phase space, then the dynamical state of such an

ensemble is described by a distribution of system points in the phase space, $f(\boldsymbol{x}, t)$, and the average behavior is described by the time evolution of such a distribution. The time evolution of f is described through the Liouville equation

$$\frac{\partial f}{\partial t} = -Lf \tag{3.6}$$

where L is the Liouville operator.

The physical properties of the macroscopic system are then ensemble variables of certain dynamical variables or functions in the phase space. If for an arbitrary dynamical variable $B(\boldsymbol{x})$, the average over the ensemble is denoted by the angular brackets

$$\langle B \rangle = \int B(\boldsymbol{x}) f(\boldsymbol{x}, t) d\boldsymbol{x} \tag{3.7}$$

and the *general equation of change* for this is

$$\frac{\partial}{\partial t} \langle B \rangle = \langle LB \rangle \tag{3.8}$$

If we consider, for example, the mass concentration at point $\mathbf{r}$, $\rho(\mathbf{r})$, then by applying the general equation of change for ρ with the operation of the Liouville operator, the well-known equation of continuity is derived

$$\frac{\partial}{\partial t} \rho = -\left(\frac{\partial}{\partial \mathbf{r}} \bullet \rho \mathbf{u} \right) \tag{3.9}$$

where $\mathbf{u}(\mathbf{r}, t)$ is the mass average velocity of molecules.

In an analogy with the classical kinetic theory models and by using the general equation of change one can derive proper expressions for the stress tensor, the equation of continuity for the configuration-space distribution function Ψ, and, consequently, for the diffusion equation.

The molecular description of concentrated polymer solutions and polymer melts, through the phase-space kinetic theory, is a more complicated subject because of the importance in these systems of polymer-polymer interactions. The polymer-polymer interactions are account for primarily by taking into account the constraints imposed on the motion of a polymer molecule resulting from the close proximity of the neighboring molecules. For example, in a concentrated solution or melt the polymer chain finds it very difficult to move sideways and its principle motion is more or less in the direction of the polymer chain backbone. This is accomplished in the theory by requiring that the Brownian motion and the hydrodynamic drug will be highly anisotropic, i.e. by introducing anisotropic an friction tensor ζ.

Network Models

A different approach can be followed for the theoretical study of systems of high molecular weight, where polymer-polymer interactions are very important, through the kinetic theory for network models [35]. In this approach the interactions of the polymer molecules are based on the classical network theories of rubber elasticity. The central approximation in all network theories of macromolecular materials is that polymer-polymer interactions are localized as *junctions*. A junction is a strong local attraction between isolated chains along two different polymer chains at which the interacting points are constrained to coincide. In macromolecular solids, the junction is the point at which there is a permanent *chemical* crosslink. For the macromolecular liquids, junctions are assumed to be temporary *physical* entanglements of various complexities and lifetimes (see Fig. 3.3). This assumption was introduced firstly by Treloar [36]. He studied the behavior of high molecular weight natural rubber and found that its behavior under deformation resembles the behavior of cross-linked rubber. This observation suggested some kind of temporary network structure in which the junctions are not chemical cross-links but points coupled by twisting or looping. These junctions are called entanglements.

(a)   (b)
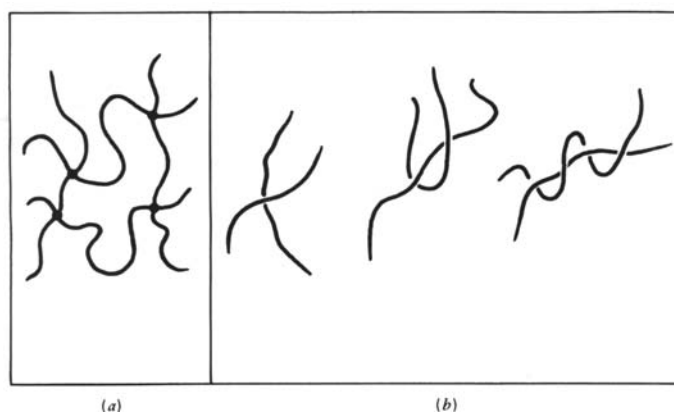
Figure 3.3 Junctions in (a) macromolecular solids and (b) macromolecular network fluids. The junctions in (a) are chemical crosslinks while in (b) are physical entanglements. The variability of junctions in latter case leads to segments of varying complexity.

The entanglements are assumed to be responsible for the dramatic change in the dynamical and rheological behavior of polymeric liquids above a characteristic molecular weight. For example the dependence of zero shear-rate viscosity η_0 with molecular

weight, M, changes from $\eta_0 \sim M^1$ to $\eta_0 \sim M^{3.4}$ for systems with molecular weight $M > M_c$, where M_c is a characteristic molecular weight [2],[37]. At the same time the dependence of the diffusion coefficient on molecular weight scales like $D \sim M^{-1}$ to $D \sim M^{-2}$.

A small element of a macromolecular network is shown in Fig. 3.4, with **Q** denoting the end-to-end vector for a typical segment. In order to properly describe the physical system, creation and destruction terms of the crosslinks are included in the continuity equation. Especially in the case of fluids, it is expected that different kinds of physical entanglements can be formed (see Fig. 3.3b) and that these will exhibit a wide range of degree of permanence. This is the idea of *segment complexity*, used to describe the relative permanence of different segments. The segment distribution function Ψ_{iN} which describes the probability that a segment has complexity i, N random links and end-to-end vector **Q** at time t, changes with time according to

$$\frac{\partial \Psi_{iN}}{\partial t} = -\left(\frac{\partial}{\partial \mathbf{Q}} \bullet [\mathbf{k} \bullet \mathbf{Q}] \Psi_{iN} \right) + L(Q,t) - \frac{\Psi_{iN}}{\lambda(Q,t)} \tag{3.10}$$

where $\mathbf{k}(t)$ is the flow field applied, $L(Q,t)$ denotes the number per unit volume of segments of length Q that are created per unit time at time t and $\lambda^{-1}(Q,t)$ is the probability per unit time that a segment will be destroyed.
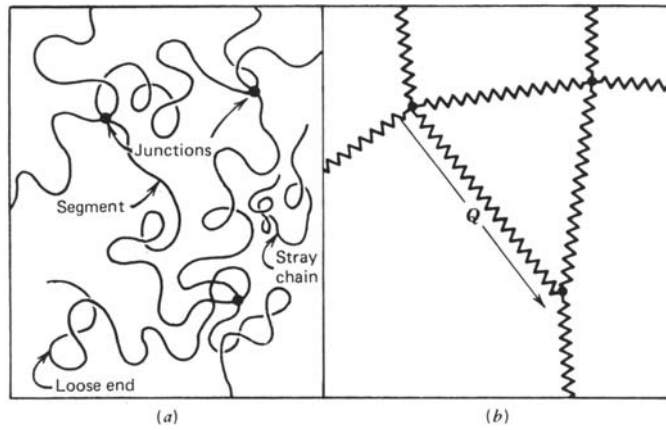
Figure 3.4 Small element of a macromolecular network: (a) actual molecular structure (b) replacement of molecular structure with a spring network structure.

The stress in the network models is produced solely by the network structure, and the total stress at equilibrium, by assuming that each network segment is a Gaussian chain, is given by

$$\boldsymbol{\pi} = \sum_i \sum_N \boldsymbol{\pi}_{iN} = \sum_i \sum_N H_N \langle \mathbf{QQ} \rangle_{iN} \tag{3.11}$$

that is very similar to the intramolecular force contribution to the total stress for bead-spring chain models.

A first description of polymers through network models was given by Lodge. The basic assumptions of the Lodge model are that network junction points move affinely, creation rates are independent of time ($L_{iN} = L_{iN}(Q)$), and that the loss rates λ_{iN} are constants. Then the stress tensor is given by

$$\boldsymbol{\tau} = \int_{-\infty}^{t} M(t - t')\gamma(t, t')dt', \qquad M(t - t') = \sum_{i}\sum_{N}\frac{\eta_{iN}}{\lambda^{2}_{iN}}e^{-(t-t')/\lambda_{iN}} \qquad (3.12)$$

where η_{iN} and λ_{iN} are constants of the model. An exhaustive exploration of the predictions of the Lodge model for a large number of homogeneous deformations has been given by Lodge [35]. In many cases its predictions were found to be in very good agreement with experimental observations. However, its major drawback is that in elongational flow the elongational viscosity becomes infinite, when the elongation rate equals $1/2\lambda_{max}$ (with λ_{max} being the largest of λ_{iN}).

Several modified network models were developed afterwards to improve the rheological predictions of the Lodge model. These models have been modified towards two directions. The first is to consider non-affine motion of the segment junction points. Such a network model was proposed by Phan-Thien and Tanner (PTT network model).

A second group of modifications focused on using more realistic segment kinetics assumptions. In these models creation and loss rates are functions of time. The most popular are the Wagner model, the Acierno-Marita-Marrucci and Titomanlio (AMMT) model and a modification of the PTT model. All of these models show a better prediction of the rheological properties than the Lodge model. The PTT model, for example, shows very good qualitatively agreement with rheological properties of low density polyethylene for both steady-state shear and elongational flows [35].

In, general the theoretical development of the network models is much simpler than that of the phase-space kinetic theory. However, the primary deficiency of these models is their inability to provide the molecular description for the central process of junction (entanglement) formation and destruction. This means that the relaxation spectrum is not given explicitly by the theory in terms of molecular model parameters. This gap is filled by the reptation theory for the study of high molecular weight concentrated solutions and melts, which will be presented in details later.

Non-equilibrium Thermodynamics Based Models

All models presented above are based on the standard polymer kinetic theory. A different approach for the description of complex systems away from equilibrium, which reproduce all the results of the kinetic theory of mechanical models and is thermodynamically consistent, was developed recently by Beris and Edwards [38]. They developed a general framework for modeling transport phenomena of complex systems and for formulating a large number of time-evolution equations in a unified manner. Their methodology is based on a thermodynamically consistent generalization of the Poisson bracket formalism which is able to describe also dissipative processes.

Consider a single particle, one-dimensional system, with $F(x,t)$ an arbitrary function. Then the general form of equation of motion is given through

$$\frac{dF}{dt} = \{F, H\} + [F, H]$$ (3.13)

where H is the Hamiltonian of the system. In the above expression $\{.,.\}$ is the Poisson bracket describing the conservative (convective) effects and $[.,.]$ is the dissipation bracket accounting for non-conservative phenomena. The general form of the Poisson bracket is

$$\{F, G\} = \frac{\partial F}{\partial x} \frac{\partial G}{\partial p} - \frac{\partial G}{\partial x} \frac{\partial F}{\partial p}$$ (3.14)

A general form dissipation bracket is not possible since in involves all non-conservative phenomena. The key idea in Beris and Edwards formalism is the construction of a nonlinear dissipation bracket.

With the development of their general formalism, Beris and Edwards considered many different applications, such as the modeling of viscoelastic transport phenomena, the description of transport and reaction phenomena in multi-fluid systems and the modeling of flow-induced phase transitions. They have also accounted for various basic principles, such as the first and second laws of thermodynamics.

Beris-Edwards formalism for describing the dynamics of nonequilibrium systems was generalized to a General Equation for the Nonequilibrium Reversible-Irreversible Coupling (GENERIC), involving two functionals, the energy and the entropy, by Ottinger and Grmela [39]. The key innovation of the GENERIC formalism is the use of two separate generators, the energy and entropy, for the reversible and irreversible dynamics. Through these two generators, many of the fundamental properties of equilibrium thermodynamics are carried over to nonequilibrium systems. The starting point in the formulation is a projection operation formalism from the atomistic degrees of

freedom to macroscopically monitored ones. The underlying assumption behind a such a projection operation, is that for a given range of time and/or length scales, the macroscopic characteristics of the system can be described by a particular set a variables, called the *dynamic* or *state* variables, with all other statistical variables, called the *relaxed* variables, having reached a quasi-equilibrium state. The next point of the GENERIC formalism is the choice of a proper set of state variables. A proper set of state variables can involve, for example, the vector of structural variables $\mathbf{X}$, the mass density $\rho(\mathbf{r})$, the momentum density $\mathbf{u}(\mathbf{r})$ and the internal energy density state $\varepsilon(\mathbf{r})$ as

$$\mathbf{x} = \left[\mathbf{X(r)}, \ \rho(\mathbf{r}), \ \mathrm{u}(\mathbf{r}), \ \varepsilon(\mathbf{r}) \right] \tag{3.15}$$

The main idea (a postulate) of GENERIC is that the dynamical equation for any system state variable can be expressed through the fundamental equation

$$\frac{d\mathbf{x}}{dt} = \mathbf{L(x)} \bullet \frac{\delta E(\mathbf{x})}{\delta \mathbf{x}} + \mathbf{M(x)} \bullet \frac{\delta S(\mathbf{x})}{\delta \mathbf{x}} \tag{3.16}$$

In this equation the functionals E and S represent the system total energy and total entropy, respectively, expressed in terms of the state variables $\mathbf{x}$, and $\mathbf{L}$ and $\mathbf{M}$ are the Poisson and friction matrices describing reversible and irreversible dynamics, respectively. Unless $\mathbf{x}$ contains all the particle momenta and positions, with such a formalism, we refer to as a coarse-grained description of the system of interest. In the GENERIC framework, Eq. (3.16), is supplemented by two complementary degeneracy requirements

$$\mathbf{L(x)} \bullet \frac{\delta S(\mathbf{x})}{\delta \mathbf{x}} = 0, \quad \mathbf{M(x)} \bullet \frac{\delta E(\mathbf{x})}{\delta \mathbf{x}} = 0 , \tag{3.17}$$

expressing the reversible nature of $\mathbf{L}$ contribution and the conservation of total energy by the $\mathbf{M}$ contribution to the system dynamics, respectively.

The four building blocks E, S, $\mathbf{L}$ and $\mathbf{M}$ convey all the information needed to describe the time evolution of all system state variables away from equilibrium. E and S are needed for the proper description of the (reversible and irreversible contributions to the) system dynamics. Unless all four of them are known, the system description is incomplete. Explicit expressions for E, S, $\mathbf{L}$ and $\mathbf{M}$ have been derived by a projection operator technique from Hamilton's equations of motion.

Recently the framework of GENERIC was re-formulated to allow for conjugated variables, each one defined as the partial derivative of the system entropy density with respect to the corresponding state variable. By extending the canonical ensemble to include the conjugated variables, a thermodynamically founded atomistic MC

methodology (termed GENERIC MC) was developed to obtain the energy E and entropy S of the system away from equilibrium, from first principles [40]. This methodology opened up the way towards the design a new class of algorithms for modeling nonequilibrium systems by employing filed-on MC methods. An application of this methodology will be given in chapter 8, where the rheological properties of polymer systems under steady-state elongational flow are predicted through a hierarchical methodology that involves GENERIC MC and MD simulations.

As said above, the earlier studies of polymer viscoelasticity employed a mechanical analog for polymer chains. In the case of bead-spring models, the corresponding analysis led to the development of the Rouse model for unenetangled systems. For systems where entanglements define their dynamics, the reptation or tube model offered a more clear description. Both of these models will be used often in the next chapters to map atomistic MD data and derive values for the mesoscopic parameters invoked by them. Therefore, a more detailed description of their formulation is given below.
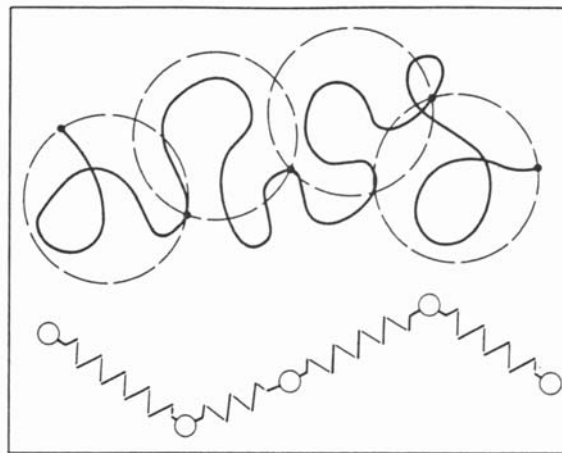
Figure 3.5 Representation of flexible macromolecule by the bead-spring model.

3.2.   The Rouse Model

The Rouse model [6], [41] is special case of the bead-spring chain models discussed in the previous section. According to the Rouse model a polymer chain is represented as a sequence of N Brownian particles (numbered 1,2,..,N) connected by Hookean harmonic springs and moving in a viscous medium representing the background environment formed by all other chains, see Fig. 3.5. Then the dynamics of a polymer

chain is modeled by the Brownian motion of such beads. The basic assumptions of the Rouse model are the following:

- The chain consists of beads connected by springs.

- The excluded volume interaction is neglected.

- Hydrodynamic interaction (HI) between molecules is also neglected.

Let $\{\mathbf{R}_n\}=(\mathbf{R}_1,\mathbf{R}_2,\ldots,\mathbf{R}_n)$ be the positions of the beads (see Fig. 3.5) under equilibrium. The equation of motion of the beads is described by two similar ways. The first is the diffusion equation, (3.2). This equation for a multidimensional system of N particles at equilibrium ($\mathbf{k}=0$) with $\mathbf{R}_i$ the position of i particle becomes

$$\frac{\partial \Psi}{\partial t} = \sum_n \frac{\partial}{\partial \mathbf{R}_n} \bullet \mathbf{H}_{nm} \bullet \left(k_B T \frac{\partial \Psi}{\partial \mathbf{R}_m} + \frac{\partial U}{\partial \mathbf{R}_m} \Psi \right). \tag{3.18}$$

where U is the interaction potential between the Hookean beads and $\mathbf{H}$ is the mobility matrix. This is the so called Smoluchowski equation. The velocities of the particles $\mathbf{V}_n$ are calculated from

$$\mathbf{V}_n = \sum_m \mathbf{H}_{nm} \bullet \mathbf{F}_m, \tag{3.19}$$

which defines the mobility matrix $\mathbf{H}_{nm}$. According to the Rouse model

$$\mathbf{H}_{nm} = \frac{\mathbf{I}}{\zeta} \delta_{nm}. \tag{3.20}$$

An alternative description of Brownian motion is in the form of a Langevin equation:

$$\zeta \frac{dx}{dt} = -\frac{\partial U}{\partial x} + f(t) \tag{3.21}$$

where $f(t)$ is the random force exarted on each particle. In a multidimensional space such as the one described before, the Langevin equation takes the following form

$$\frac{\partial}{\partial t} \mathbf{R}_n(t) = \sum_m \mathbf{H}_{nm} \bullet \left(-\frac{\partial U}{\partial \mathbf{R}_m} + f_m(t) \right). \tag{3.22}$$

The potential for the interaction between adjoining particles has a harmonic form

$$U = \frac{k}{2} \sum_{n=2}^{N} \left(\mathbf{R}_n - \mathbf{R}_{n-1} \right)^2 \tag{3.23}$$

with k the spring constant

$$k = \frac{3k_B T}{b^2}. \tag{3.24}$$

In the above equation b is the statistical segment length (Kuhn length) defining the mean square end-to-end distance by

$$\langle R^2 \rangle = Nb^2 .$$ (3.25)

In this model the Langevin equation, Eq. (3.22), becomes a linear equation for $\mathbf{R}_n$. For internal beads ($n=2,3,…,N$-1) it takes the form:

$$\zeta \frac{d\mathbf{R}_n}{dt} = -k\left(2\mathbf{R}_n - \mathbf{R}_{n+1} - \mathbf{R}_{n-1}\right) + \mathbf{f}_n$$ (3.26)

while for the end beads ($n=1$ and $n=N$) it becomes

$$\zeta \frac{d\mathbf{R}_1}{dt} = -k\left(\mathbf{R}_1 - \mathbf{R}_2\right) + \mathbf{f}_1, \qquad \zeta \frac{d\mathbf{R}_N}{dt} = -k\left(\mathbf{R}_N - \mathbf{R}_{N-1}\right) + \mathbf{f}_N .$$ (3.27)

An important parameter in the Rouse formulation is the friction factor ζ (measured in units of mass per time), i.e., the proportionality constant between the velocity of a bead and the frictional force exerted on the bead as it moves through the "sea" formed by all other particles in the system. Through the fluctuation-dissipation theorem, ζ also defines the mean squared magnitude of the random (Langevin) force on the particle through

$$\langle f_n(t) \rangle = 0, \quad \langle f_{na}(t) f_{mb}(t') \rangle = 2\zeta k_B T \delta_{ab} \delta_{nm} \delta\left(t - t'\right) .$$ (3.28)

Equations (3.26) and (3.27) present a Brownian motion of coupled oscillators. A standard way of treating such a system is through an analysis of normal coordinates or modes $\mathbf{X}_p$, $p = 0,1,2,…,N$-1, each of which is capable of independent motion.

The normal coordinates can be defined in two ways; in terms of the position vectors [41],[42] of the beads, or in terms the connector vectors between beads [35]; the two approaches, of course, lead to consistent results. Without loss of generality, we can use the chemical methylene and methyl segments as beads to define Rouse modes in our atomistic model. The relevant formulations and the equations pertinent to each definition are shown in detail in Appendix C. If we choose to work with the position vectors, then the normal coordinates are given by

$$\mathbf{X}_p = \sum_{j=1}^{N} \Omega_{jp} \mathbf{R}_{j-1}$$ (3.29)

where Ω_{jp} are the elements of the orthogonal matrix $\mathbf{\Omega}$ given by

$$\Omega_{jp} = \sqrt{\frac{2 - \delta_{p0}}{N}} \cos\left(\frac{\left(j - 1/2\right) p\pi}{N}\right)$$ (3.30)

with j=1,2, ..., N and p=0,1, ..., N-1, and $\mathbf{R}_i$ denotes the position vector of bead i.

With the above definition of the normal modes, the exact expression for the time autocorrelation function, $<\mathbf{X}_p(t)\bullet\mathbf{X}_p(0)>$, of the normal mode $\mathbf{X}_p$, is given by Eqs. (C.10) - (C.13) of Appendix C (a general discussion about time correlation functions can be found in appendix A). For $1 \leq p << N\text{-}1$ an approximation to the exact equation can be used by taking the small $p/(N\text{-}1)$ limit in the expression for k_p, Eq. (C.13):

$$\left\langle \mathbf{X}_p(t)\bullet\mathbf{X}_p(0)\right\rangle = \frac{k_B T}{k_p}\exp\left(-\frac{t}{\tau_p}\right) = \frac{Nb^2}{6\pi^2}\frac{1}{p^2}\exp\left(-\frac{t}{\tau_p}\right) \tag{3.31}$$

where τ_p, p=1,2, ...,N-1, denotes the spectrum of relaxation times,

$$\tau_p = \tau_1 / p^2 \tag{3.32}$$

with

$$\tau_1 = \frac{\zeta N^2 b^2}{3\pi^2 k_B T} = \frac{\zeta N \left\langle R^2\right\rangle}{3\pi^2 k_B T} \tag{3.33}$$

being the longest (or Rouse, $\tau_1 = \tau_R$) relaxation time. In the above equations, b^2 denotes the mean-square distance between adjacent beads at equilibrium. In general, $\mathbf{X}_p$ represents the local motion of a chain segment encompassing N / p beads and corresponds to motion on a length scale of the order $(Nb^2/p)^{1/2}$. The zero mode $\mathbf{X}_0$, in particular, represents the center of mass position $\mathbf{R}_{cm}$, the mean-square displacement of which in the Rouse model is given by

$$\left\langle\left(\mathbf{R}_{cm}(t)-\mathbf{R}_{cm}(0)\right)^2\right\rangle = 6\frac{k_B T}{N\zeta}t . \tag{3.34}$$

From this equation and the Einstein relation,

$$D = \lim_{t\to\infty}\frac{\left\langle\left(\mathbf{R}_{cm}(t)-\mathbf{R}_{cm}(0)\right)^2\right\rangle}{6t} \tag{3.35}$$

the self-diffusion coefficient of the center of mass D can be obtained as

$$D = \frac{k_B T}{N\zeta} . \tag{3.36}$$

The normal coordinated $\mathbf{X}_p$ with $p > 0$ represents the internal conformation of the polymer. Consider for example the end-to-end vector $\mathbf{R}(t) = \mathbf{R}_N(t) - \mathbf{R}_0(t)$ which is expressed by $\mathbf{X}_p$ as

$$\mathbf{R}(t) = -4\sum_{p:odd}\mathbf{X}_p(t) . \tag{3.37}$$

Then the time autocorrelation function of the end-to-end vector is calculated as

$$\langle \mathbf{R}(t) \bullet \mathbf{R}(0) \rangle = 16 \sum_{p:1,3,\dots} \langle \mathbf{X}_p(t) \bullet \mathbf{X}_p(0) \rangle$$

$$= \sum_{p:1,3,\dots} \frac{3k_B T}{k_p} \exp\left(-\frac{t}{\tau_p}\right) \tag{3.38}$$

$$= Nb^2 \sum_{p:1,3,\dots} \frac{8}{p^2 \pi^2} \exp\left(-\frac{tp^2}{\tau_1}\right)$$

where $Nb^2 (= <R^2>)$ is the equilibrium (unperturbed) mean square end-to-end distance of chains in the melt. Equation (3.38) indicates that the motion of the end-to-end vector is clearly dominated by the first ($p=1$) mode.

The first mode defines also the zero-shear (i.e., characteristic of the Newtonian plateau) viscosity of the melt through

$$\eta_0 = \int_0^\infty G(t)dt = \frac{\pi^2}{12} \frac{\rho RT}{M} \tau_1 \tag{3.39}$$

where $G(t)$ is the stress relaxation modulus, expressed as

$$G(t) = \frac{\rho RT}{M} \sum_{p=1}^N \exp\left(-\frac{2tp^2}{\tau_1}\right). \tag{3.40}$$

Combining Eqs. (3.33), (3.36), (3.39), η_0 also becomes

$$\eta_0 = \frac{\rho RT \langle R^2 \rangle}{36MD}. \tag{3.41}$$

The above expressions are written in terms of the molecular weight M, the mass density of the melt ρ, and the gas constant R.

A very useful quantity, since it is measured directly in MD simulations, is the mean square displacement of a segment $n, \phi_n(t)$, which is defined as

$$\phi_n(t) = \langle (\mathbf{R}_n(t) - \mathbf{R}_n(0))^2 \rangle. \tag{3.42}$$

and is directly connected with the dynamic structure factor $S(q,t)$. The derivation of $\phi_n(t)$ according to the Rouse model is described in details in Appendix D.

There are two very important remarks concerning the Rouse model. The first is that the Rouse model was first introduced to describe the dynamics of polymer solutions. But the predictions of the model for the molecular weight dependence of the self-diffusion coefficient and the maximum relaxation time, i.e. $D \sim M^1$ and $\tau_1 \sim M^2$, are found to be not consistent with experimental results, which in Θ conditions, are summarized as $D \sim M^{1/2}$ and $\tau_1 \sim M^{3/2}$. This failure of the Rouse model comes mainly from the neglect of the

hydrodynamic interactions, i.e. its "free-draining" assumption. The HI originate from the fact that the velocities of particles depend on the forces acting on their surrounding particles; the force acting on a certain particle causes a fluid motion around it and affects the velocity of other particles. Thus the HI is mediated by the motion of the solvent fluid and is found to be dominant in polymer solutions, especially, in dilute polymer solutions.

Because of this failure, the Rouse model is regarded as inappropriate to model the dynamics of a dilute solution. To account for the above discrepancy, Zimm proposed a modification of the Rouse model that incorporates hydrodynamic interaction [43]. The HI are incorporated through a modification of the mobility matrix $\mathbf{H}_{nm}$ which becomes

$$\mathbf{H}_{nn} = \frac{\mathbf{I}}{\zeta}, \qquad \mathbf{H}_{nm} = \frac{1}{8\pi\eta_s |\mathbf{r}_{nm}|} [\hat{\mathbf{r}}_{nm}\hat{\mathbf{r}}_{nm} + \mathbf{I}] \text{ for } n \neq m \tag{3.43}$$

where $\mathbf{r}_{nm} = \mathbf{R}_n - \mathbf{R}_m$ and $\hat{\mathbf{r}}_{nm}$ is the unit vector in the direction of $\mathbf{r}_{nm}$. $\mathbf{H}_{nm}$ is a nonlinear function of $\mathbf{R}_n - \mathbf{R}_m$ and thus is quite difficult to handle. Zimm [43] introduced the pre-averaging approximation, which replaces $\mathbf{H}_{nm}$ by its average,

$$\mathbf{H}_{nm} \rightarrow \langle \mathbf{H}_{nm} \rangle \equiv \int d\{\mathbf{R}_n\} \mathbf{H}_{nm} \Psi(\{\mathbf{R}_n\}, t) \tag{3.44}$$

In systems near equilibrium one can use the equilibrium distribution function $\Psi_{eq}(\{\mathbf{R}_n\})$ in the average of (3.44). Since the distribution of $\hat{\mathbf{r}}_{nm}$ is independent of $|\mathbf{r}_{nm}|$, $<\mathbf{H}_{nm}>_{eq}$ is written as

$$\langle \mathbf{H}_{nm} \rangle_{eq} = \frac{1}{8\pi\eta_s} \left\langle \frac{1}{|\mathbf{r}_{nm}|} \right\rangle_{eq} \langle \hat{\mathbf{r}}_{nm}\hat{\mathbf{r}}_{nm} + \mathbf{I} \rangle_{eq}. \tag{3.45}$$

Using

$$\langle \hat{\mathbf{r}}_{nm}\hat{\mathbf{r}}_{nm} \rangle_{eq} = \frac{\mathbf{I}}{3} \tag{3.46}$$

we have

$$\langle \mathbf{H}_{nm} \rangle_{eq} = \frac{1}{6\pi\eta_s} \left\langle \frac{1}{|\mathbf{R}_n - \mathbf{R}_m|} \right\rangle_{eq}. \tag{3.47}$$

The analysis of the Zimm model is similar with that of the Rouse model using Eq. (3.47) for the HI instead of Eq. (3.20). The predictions of Zimm's model are found to be in very good agreement with experimental data for dilute polymer solutions. For polymer melts, on the other hand, the "free-draining" limit, is a fairly well assumption. Thus, the Rouse model proved to be a good starting point for the theoretical study of the dynamics of polymer melts.

A second important characteristic of the Rouse model is that it is formulated in terms of three basic parameters. These are the number of beads, N, the length of the statistical segment, b, and the friction coefficient, ζ. It is obvious, through the equations presented above, that if one knows N, b, the density of the system, ρ, and the self-diffusion coefficient, D, of the polymeric system then one can extract all the linear viscoelastic properties of the system, i.e. the spectrum of relaxation times, τ_p, the friction coefficient, ζ, the zero-shear rate viscosity, η_0, etc. This inherit property of the Rouse model gave rise to a number of atomistic MD simulation works, where the self-diffusion coefficient D is calculated directly from the simulation and then the linear viscoelastic properties of the system are calculate with the use of the equations of the Rouse model.

To this direction, Yoon and collaborators [44],[45],[46],[47] have reported results from long MD simulations on three different chain systems (C_{13}, C_{44}, and more recently C_{100}). Their results refer to conformational characteristics, and segmental and terminal relaxation. An important outcome of this work involved comparisons of simulation findings for the dynamics of chains with the predictions of the Rouse model. An analysis of the normal modes of the chains indicated that the Rouse behavior is not followed by the shorter C_{13} and C_{44} chain systems; only the longer C_{100} chain system seemed to conform to Rouse model predictions. Even for this system, however, the behavior was not exactly Rouse: Although the first three modes ($p = 1$ to 3) did follow the exponential decay predicted by the Rouse model, all higher modes showed clear, systematic deviations from that. This is especially interesting in view of neutron spin-echo spectroscopy experiments, which seem to be in very good agreement with the Rouse model [48],[49].

Alternatively, one can obtain viscosity in the linear regime in the course of equilibrium MD simulations, following the Green-Kubo formalism [5]. Mondello and Grest [50] in a series of papers have calculated the zero-shear rate viscosity η_0 both through Green-Kubo relation and by using the expressions of the Rouse model, Eq. (3.39) and (3.41), for small alkanes (C_n, $n < 16$) and found great discrepancies between the results. From their data it was also apparent, however, that these discrepancies decreased with increasing the chain length. Clearly simulations in longer systems need to clear out the situation. In the next chapters a systematic methodology for the prediction of viscoelastic properties of polymer systems is presented, which involves atomistic MD simulations in a wide range of chain lengths, from C_{24} up to C_{250}.
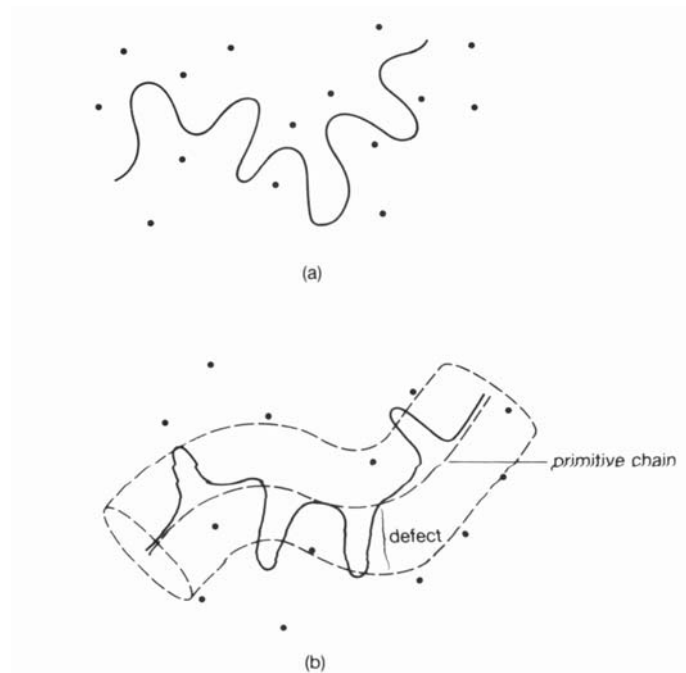
Figure 3.6 (a) A chain in a fixed network. (b) The tube model and the primitive chain.

3.3. The Reptation Theory

The original idea of reptation theory can be found in the study of network (rubber) elasticity. Consider a crosslinked rubber which consists of long strands in polymers (see Fig. 3.6). A strand is schematically shown in Fig. 3.6a. If we consider one chain that moves in a network of fixed chains, then one can see (Fig. 3.6b), that the allowed conformations of the strand is almost confined into a tube-like region shown by the dotted lines. The conformations that go outside of the tube are not allowed because they violate the topological constraints. The group of conformations that are accessible to each other without violating the topological constraints is called the *primitive path* or *primitive chain* [6].

The idea of the primitive tube is intuitively appealing and will be useful also for uncrosslinked systems such as polymer melts. However the basic difference is that, in melts, the tube itself changes with time because all conformations are accessible. de Gennes [51] discussed the Brownian motion of a chain moving through a fixed network. The basic idea is that the motion of the chain is almost confined in a tube-like region

denoted by dotted lines in Fig. 3.6a. As a result of the motion of the chain the tube itself changes with time as shown in Fig. 3.7. For example if the chain moves right, the part B_0B moves in a random direction and creates a new part of the tube which will be constrained for the rest of the chain, while the part of the original tube A_0A is destroyed. This type of motion is called reptation after the Latin reptare, i.e. to creep.

Let us now discuss the motion of a chain in a tube regime such the one described before. The intrinsic properties of the chain are characterized by the number of monomers (or segments) N, the bond length b and the friction coefficient ζ. The topological constraints due to the presence of other chains affect the dynamic properties. However, if we are interested in the large-scale motion of the chain we can disregard the small-scale fluctuations and discuss only the time evolution of the primitive chain.
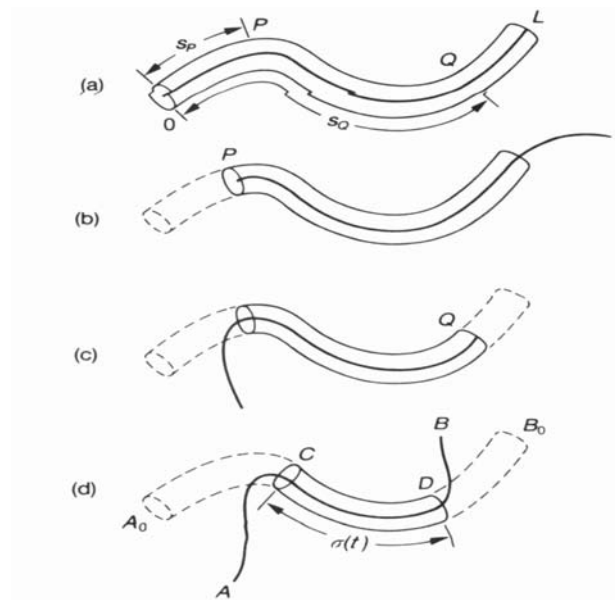
Figure 3.7 Motion of a reptating chain. (a) The original configuration and tube. (b) and (c) As the chain moves right or left some parts of the original tube disappear. (d) The conformation at later time t.

The primitive chain is characterized by three parameters: the contour length L, the diffusion coefficient D_c and the tube diameter a. The parameter D_c can be identified as the diffusion coefficient of the Rouse model

$$D_c = \frac{k_B T}{N\zeta} \tag{3.48}$$

because the motion of the primitive chain corresponds to the overall translation of the Rouse chain along the tube. The tube diameter α is expressed by L since the mean square end-to-end distance of the primitive chain, that is $L\alpha$, must be the same with the one of the Rouse chain, Nb^2. Thus

$$La = Nb^2 = \left\langle R^2 \right\rangle. \tag{3.49}$$

The relaxation of the time autocorrelation function of the end-to-end vector follows a similar expression with the one of the Rouse model as

$$\left\langle \mathbf{R}(t) \bullet \mathbf{R}(0) \right\rangle = Nb^2 \sum_{p:1,3,\dots} \frac{8}{p^2\pi^2} \exp\left(-\frac{tp^2}{\tau_d} \right) \tag{3.50}$$

with τ_d denotes the reptation or disengagement time, since it is the time needed for the primitive chain to disengage from the tube it was confined to at $t = 0$, and given as

$$\tau_d = \frac{\zeta N^3 b^4}{\pi^2 k_B T a^2} \ . \tag{3.51}$$

With the knowledge of $<R^2>$, D and a, the monomer friction coefficient ζ is readily obtained through

$$\zeta = \frac{k_B T a^2}{3N \left\langle R^2 \right\rangle D}, \tag{3.52}$$

and zero-shear rate viscosity η_0 through

$$\eta_0 = \frac{\rho RT}{36MW} \frac{\left\langle R^2 \right\rangle}{D} \frac{\left\langle R^2 \right\rangle}{a^2} \ . \tag{3.53}$$

Due to small-scale fluctuations of the atomistic chain around its primitive path, the actual dynamics of segments is much more complicated that that in the case of the Rouse model. Thus a precise calculation of the mean square displacement of a segment $n, \phi_n(t)$, is difficult but its characteristic features are found to be the following

i) For a very short time the segment does not feel the constraints of the network and $\phi_n(t)$ can be calculated as in the Rouse model. There $\phi_n(t) \sim N^{1/2}$ as in the Rouse model. There is a characteristic time τ_e at which the segmental displacement becomes comparable to α. The time τ_e denotes the onset of the effect of the tube constraints: for $t < \tau_e$ the chain behaves as a Rouse chain in free space, while for $t > \tau_e$ the chain feels the constraints imposed by the tube.

ii) For $t > \tau_e$ the motion of the segment perpendicular to the primitive chain is restricted, but the motion along the primitive path is free. There the mean square displacement found to scale as $\phi_n(t) \sim N^{1/4}$ for $t < \tau_R$ and $\phi_n(t) \sim N^{1/2}$ for $\tau_R < t < \tau_d$.

iii) Finally for the long times $t > \tau_d$ the dynamics is governed by the reptation process and the usual Fickian diffusion is shown: $\phi_n(t) \sim N^1$.

The four regimes with the different scalings of $\phi_n(t)$ are shown schematically in Figure 3.8, taken by Doi and Edwards [6]
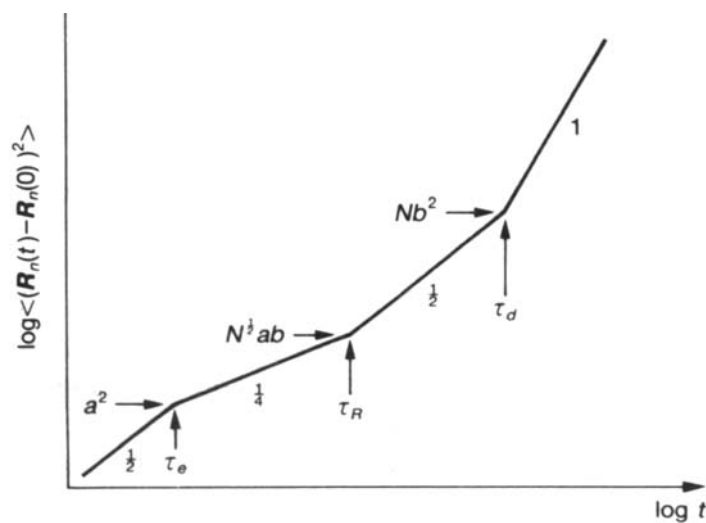
Figure 3.8 Mean square displacement of a chain segment $\phi_n(t)$ against time.

The characteristic behavior of $\phi_n(t)$ served as a useful tool for testing the ideas of the reptation theory through computer simulations. This happen because $\phi_n(t)$ can be calculated directly in MD simulations. To push the simulations to larger systems and longer times, most of these works have been performed with coarse-grained models (described in section 2.3) and next the predicted $\phi_n(t)$ versus time curve is compared to the scalings of $\phi_n(t)$ proposed by the reptation theory to test the validity of the theory [23], [24]. Kremer and Grest performed MD simulations of the bead-spring model for a variety of chain lengths (number of beads from N = 5 up to $N = 400$) [23] and found signals of reptation, as the chain length increases, by observing a clear decrease in the slope of $\phi_n(t)$ at an intermediate regime. For the longer systems they found a decrease in

the slope of $\phi_n(t)$ form 0.5 to about 0.28. Recenlty, Pütz *et al.* extended the simulations, with the same system to longer systems up to $N = 1000$. They reported a slope of about 0.24±0.03 for the intermediate regime in agreement with the scalings of the reptation theory in the $\tau_e < t < \tau_R$ regime [24]. However, even with the longer systems it was not possible to find the scalings for $t > \tau_R$ due to huge increase in τ_d as N increases. At the same time it was not possible to find τ_e and τ_R in real units due to the coarse-graining model.

Experimentally, microscopic signals of reptation dynamics have been evidenced through various measurements. Chu *et al.* reported signals of a tube-like motion of a single DNA chain in an entangled solution using fluorescence microscopy [52]. More recently, neutron spin echo (NSE) experiments in the time range $t = 0.3\text{-}175$ *ns* [53], [54],[55],[56] were consistently analyzed in the context of reptation theory. More precisely the dynamic structure factor *S(q,t)* was calculated and compared with theoretical expressions derived by a variety of models. Reptation theory was found as the only one that provides a consistent description of all the NSE data [57]. At the same time, double-quantum nuclear magnetic resonance (DQ NMR) experiments, probing the translational motion of polybutadiene (PB) chains, gave scaling laws consistent with the reptation theory [58].

Although the pure reptation theory is largely in agreement with experiments there still certain discrepancies remain. The most important one are the observations that the molecular weight dependence of the zero-shear rate viscosity $\eta_0 \sim M^3$ and the maximum (disengagement) relaxation time $\tau_d \sim M^3$ are weaker with those which are measured experimentally; in both cases the measured exponent is higher than 3, around 3.4 [2].

This different molecular weight dependence of the zero-shear rate viscosity was also confirmed in a recent work by Kröger and Hess [25] who reported results from NEMD simulations of flexible FENE chains in a planar Couette flow. By directly calculating η_0 as a function of chain length, a critical chain length was observed at around 100 beads per chain, where a clear change in the power-law dependence of η_0 occurred from 1 to 3.4.

To account for this discrepancy, modifications of the reptation theory have been proposed over the years. First Craessley [59] conducted a series of experiments and pointed out that the observed viscosity and relaxation times are *smaller* than the calculated ones. With empirical formulas he concluded that the discrepancy decreases

with increasing M and diminishes at around $M=800M_c$. Craessley thus conjectured that the pure reptation theory behavior will be observed for very large molecular weight which is preceded by a large cross-over region from Rouse-like to the pure reptation-like behavior. In this regime other relaxation processes occur concurrently with reptation, which decrease the viscosity and hence reduces the discrepancy between the pure reptation theory and experimental obsrvations.

Following the ideas of Craessley [59], two relaxation processes were subsequently suggested to account for the observed discrepancy between theory and experiments: contour length fluctuations (CLF) and constraint release (CR).

According to the pure reptation theory the primitive chain is an inextensible string of contour length L. But, in reality, the contour length of the primitive chain fluctuates with time and this fluctuation plays an important role in the reptation dynamics, mainly for the lower molecular weight species present in the system. Doi [6] performed a detailed examination of the effect of CLF on the reptation and sketched that the disengagement time, with CLF, $\tau_d^{(F)}$ should decrease relative to that of the pure reptation theory, τ_d, as

$$\tau_d^{(F)} \cong \tau_d \left(1 - \frac{X}{\sqrt{L/a}}\right)^2 . \tag{3.54}$$

where X is a numerical constant. A variational calculation [60] found $X \approx 1.5$. The difference in the Brownian motion of a primitive chain with and without CLF is shown in Fig. 3.9.
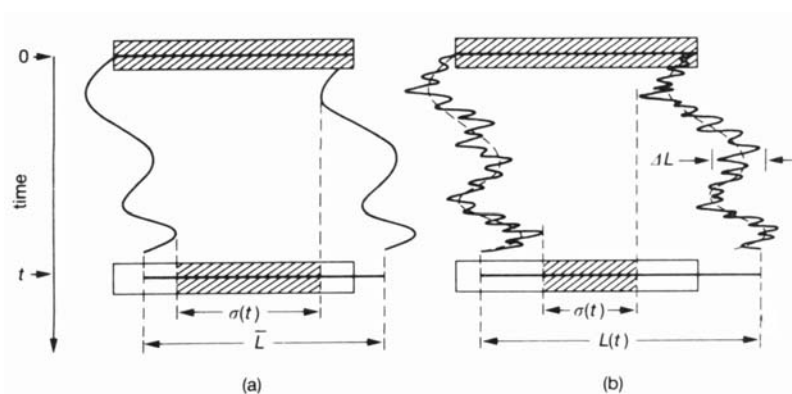

Figure 3. 9 The Brownian motion of a primitive chain with (a) fixed contour length and (b) fluctuating contour length. The oblique lines denote the region that has not been reached by either end of a primitive chain. Obviously the length of the region $\sigma(t)$ decreases faster in (b) than in (a).

A second process that affects reptation dynamics has to do with the reorganization of the tube itself. In the original reptation theory, it is assumed that the tube is fixed in the material and the conformational change occurs only at the ends. It is conceivable that the conformation change of the tube can occur in the middle too. This is the so-called constrain release process, shown in Fig. 3.10. The topological constraints for a polymer can be released (or created) by the reptation of the surrounding polymer chain as shown in Fig. 3.10. This causes the conformational change of the tube in the middle.

Milner and McLeish, in a recent series of papers [61],[62], developed a tube-based theory for the dynamics of entangled *f*-arm star polymers (*f* arms attached by their ends to a single branch point) and linear melts that includes both CLF and CR processes. In star melts, stress is relaxed by arm retraction, in which the free end of a star arm fluctuates down its tube some distance toward the branch point and pops out again, thus "forgetting" the section of tube near the free end. The modification of their theory for linear polymer melts is based on treating them as two-armed stars. They calculated the zero-shear rate viscosity and found it to have an effective exponent around 3.4 for a wide range of molecular weights (up to about 300 M_e) before crossing over to the asymptotic exponent of 3. Corrections to scaling of the diffusion constant have also been reported as $D \sim M^{-2}\left[1 - AM^{-2}\right]$ where A is a constant.
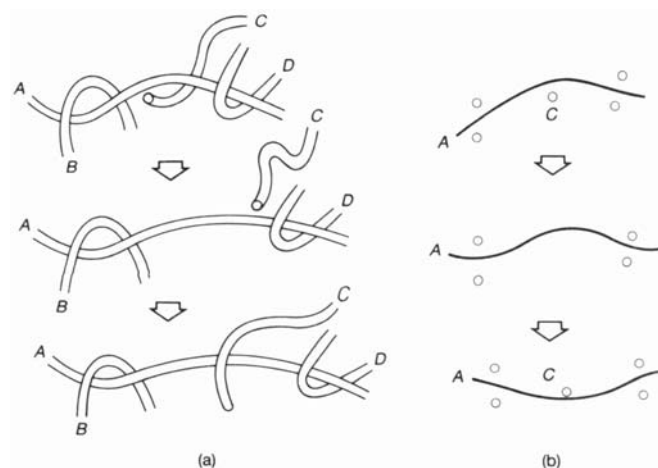

Figure 3.10 The constraint release process. (a) The topological constraints imposed in the chain *A* by *C* are released and recreated by the motion of *C*. (b) Appearance and disappearance of the obstacle *C*. This process causes the deformation of the tube in the middle.

3.4.   Linear Viscoelasticity

In the beginning of this chapter, the basic theoretical approaches for the description of polymer fluids away from equilibrium were presented. The present thesis focuses on the regime of linear viscoelasticity. If we consider a polymer system under an applied deformation then if the deformation is small or applied sufficiently slowly, the molecular arrangements are never far from equilibrium. The mechanical response is then just a reflection of dynamic processes at the molecular level which go on constantly, even for the system at equilibrium. This is the domain of *linear viscoelasticity*. In the regime of linear viscoelasticity the magnitudes of stress and strain are related linearly, and the behavior is completely described by a single function of time.

As we already mentioned before, the response of a viscoelastic polymer material, to an applied deformation changes from solidlike at short times to liquidlike at long times; also the history of loading is crucial. Consider, for example, the stress relaxation experiment where a constant shear (or elongational) strain is imposed instanteounsly or for a certain period and the stress at subsequent times is monitored. For a Hookean solid, the stress is constant because the strain is constant. For a Newtonian liquid the stress is zero because the strain rate is zero. For a polymer (viscoelastic) material the stress decreases with time, starting at some high value and going finally to zero. It is only for small enough strains the ratio of the stress to strain is a function of time alone and then we say that we are in the regime of linear viscoelasticity. This function is a property of the material, called the stress relaxation modulus $G(t)$. The stress at time t, $\sigma(t)$, is then related with the history of deformation in the material and with $G(t)$ through the famous Boltzmann Superposition Principle

$$\sigma(t) = \int\limits_{-\infty}^{t} G(s)\dot{\gamma}(t-s)ds \qquad (3.55)$$

The behavior of $G(t)$ for polymer melts, is sketched in Fig. 3.11 [3]. Four regions are illustrated; the glassy, the transition, the plateau and the terminal regimes. At very short times the response is glassy; the modulus is large but then it falls rapidly as the chains relax locally and over progressively longer distances (transition regime). For short chains (low molecular weight) $G(t)$ proceeds smoothly to zero. For long chains the relaxation rate slows down and the modulus remain relatively flat for a significant period of time before finally resuming its rapid relaxation to zero. This intermediate or plateau regime separates the short time transition regime, where the chain architecture has little

effect, from the long time response, called the terminal region where architectural features as molecular weight have a profound effect [2],[6].
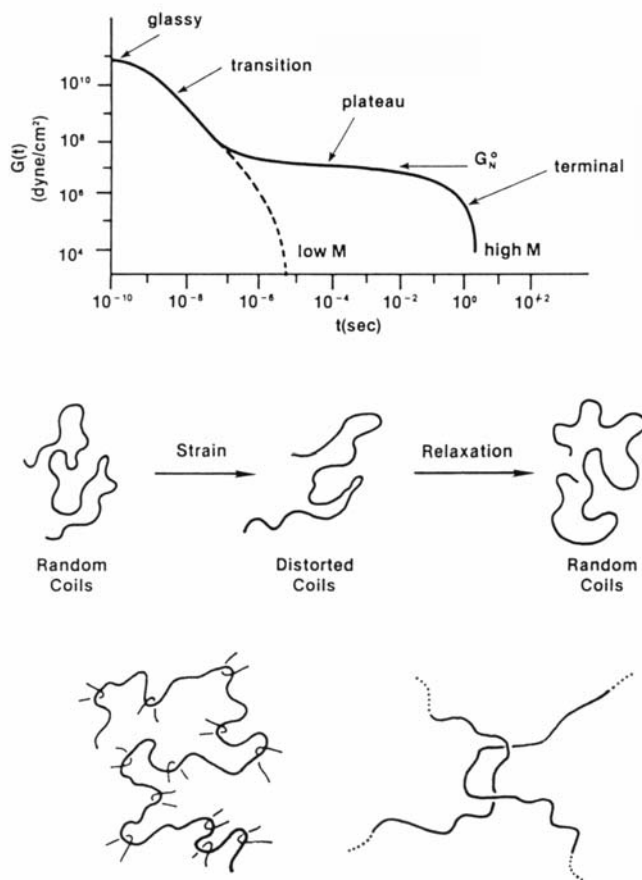
Figure 3.11 Stress relaxation in polymer melts.

In the literature, relatively little simulation work has been conducted to obtain a detailed microscopic understanding of the rheological behavior of polymers under nonequilibrium conditions. However, molecular simulations have been used to probe the response of amorphous polymers to deformation since the mid-1980s. Using molecular mechanics, Theodorou and Suter [63], for example, made a connection between stress-strain curves in the elastic regime and molecular-scale phenomena in a glassy polymer. A similar methodology was followed later by Argon *et al.* [64] to simulate plastic deformation in a polymer glass.

The most popular way for studying polymer elasticity in the rubbery regime with molecular simulations is through the deformation of the simulation box in analogous manner with macroscopic experiments. In a series of papers Gao and Weiner

[65],[66],[67] presented an investigation of the dynamic properties of deformed polymer systems in the rubbery regime, by subjecting the simulation box to a constant-volume elongation at a high, constant rate ($\dot{\varepsilon}$ = 2.77x10^{10} s^{-1}) along the x-direction, by employing a constant-temperature MD algorithm. All simulations were performed with a freely-jointed chain model. This work was followed by a study of the birefringence of the uniaxially stretched system and of the relaxation of the stress developed in response to the imposed continuous deformation of the simulation box at the monomer level.

Brown, Clarke and co-workers were the first to apply the MD method to study the yielding behavior of amorphous, united-atom PE systems constructed from a single "parent" chain [68]. They subjected the PE systems to uniaxial tension by changing the y component of the applied pressure tensor, P_{yy}, at a constant (high) rate (either 5 or 1 *bar* *ps*$^{-1}$).

Recently Yang *et al.* [69],[70] proposed a methodology for studying the dynamics of glassy polymer systems in uniaxial deformation by using MD simulations in a new statistical ensemble, i.e. the $NTL_x\sigma_{yy}\sigma_{zz}$ ensemble. Then they applied a constant strain rate deformation study, on model polyethylene system, by increasing the simulation cell size L_x at a constant rate.

In all of the abocve mentioned works, the simulations have been performed with a brute-force MD method and thus restricted to relatively short chain systems for short time intervals. It is the purpose of this thesis to study of the dynamics of polymer melts through a hierarchical methodology that involves both atomistic MC and MD simulations as well as theoretical models.

The remaining chapters of this thesis are organized as follows: In the first two chapters a detailed investigation of dynamics of unentangled polymer melts and of longer polymer melts in the crossover regime from unentangled to entangled is presented and a direct mapping of the simulation data onto the Rouse and the reptation models is addressed. In chapters 6 and 7, self-diffusion of short n-alkanes and of binary blends of n-alkanes is examined and is directly compared to the predictions of the free volume theory for such systems. Finally in chapter 8, our hierarchical approach is extended to systems that are first brought away from equilibrium (under flowing conditions) and then results from the atomistic modeling of the stress relaxation experiment upon cessation of steady-state elongational flow are presented.

CHAPTER 4

STRUCTURE AND DYNAMICS OF UNENTANGLED POLYMER MELTS

In the previous chapter we presented a review of the theory of polymer melt dynamics and viscoelasticity. We also described in detail, two popular theoretical mesoscopic models of polymer dynamics, the Rouse model for unentangled and the reptation (or tube) model for entangled polymers.

The main objective of this and the next chapters is to present an atomistic MD simulation study of the conformational and dynamic properties of polymer melts of molecular length span the Rouse and crossover to the reptation regime. The atomistic MD simulations are performed on model linear polyethylene melts with molecular length ranging from $N = 24$ up to $N = 250$. Many of the dynamic properties (such as self-diffusion coefficient D) are calculated directly from the MD simulations. Others, however, require that the atomistic MD data are mapped upon a mesoscopic theoretical model. As such we will choose the Rouse model for relatively short PE melts and the reptation for the longer melts.

Most of the simulations will be performed with polyethylene (PE) melts characterized by a uniform distribution of chain lengths with a small polydispersity index around 1.09.

The data in this chapter have been accumulated from simulations on three different systems, covering a range of chain lengths up to the regime of molecular weights just below those corresponding what is believed to be the characteristic molecular weight for the formation of entanglements. The first system is a C_{24}, the second a C_{78} and the third a C_{156} PE melt.

The methodology followed in the work in this and the next chapters is a hierarchical one and combines the power of MC technique to provide equilibrated

configurations and the ability of theoretical models to extract relationships for mesoscopic properties, such as η_0 from a few, well defined molecular parameters, which are accessible through the MD technique. Indeed starting configurations for the MD simulations are obtained by a very efficient *end-bridging* Monte Carlo algorithm [71], [72], [73] which provides vigorous sampling of configuration space, particularly for the longer chains. The fact that the initial configurations have been pr-equilibrated makes possible to track the evolution of the system in the subsequent MD study for a longer time. In details, the methodology is a three-stage hierarchical approach, whereby the dynamic properties of polymer melts are calculated through the following procedure:

a) First exhaustive end-bridging Monte Carlo (EBMC) simulations [73] have been conducted to equilibrate the melts at all length scales. In more details, the EBMC algorithm employs moves that modify the connectivity among polymer segments while preserving a prescribed (narrow) molecular weight distribution. It can thus equilibrate the long-length scale features of a polymer melt orders of magnitude more efficiently than MD or other MC methods, its relative efficiency increasing dramatically with increasing chain length.

b) Relaxed configurations thus obtained are subjected to MD simulation to monitor their evolution in time and extract dynamic properties. During the atomistic MD simulations we have accumulated a large number of dynamical trajectories.

c) Finally a mapping of these trajectories occurred onto a theoretical mesoscopic model. The model used for the unentangled polymer systems simulated in this chapter is the Rouse model discussed in chapter 3.

The end-bridging move, invoked in the first stage, i.e. in the equilibrating MC runs, is a chain connectivity-altering move, which continuously generates chains of different lengths, subject to a prescribed distribution function set by a profile of relative chemical potentials. The equilibrated melts obtained from the end-bridging MC simulations are therefore polydisperse, and, of course, they continue to be so also during the MD. This is a very important feature of the present work because of two reasons: (a) it allows testing the validity of the Rouse model picture that chains in the unentangled polymer regime move as strings of Brownian particles tethered by harmonic springs in a viscous medium whose interaction with the particle is characterized by a single parameter (the friction coefficient ζ); (b) it allows studying the dynamics of many, different-length chains simultaneously, and therefore extracting the dependence of the dynamic properties on chain length without the need for different runs at different chain lengths. Of course, due

to the presence of only a few chains with exactly the same length in the simulation box, the statistics for each chain length is worse than would be obtained from a monodisperse melt simulation; as we shall see, however, in the presentation of results, this does not turn out to be a significant problem. More details and a thoroughly presentation of the EBMC algorithm can be found elsewhere [73].

Particular emphasis is placed here on the prediction of the zero-shear viscosity. As mentioned above, this technologically very important property is very difficult to predict directly for long-chain systems from equilibrium (through the Green-Kubo relation using the time integral of the shear-stress autocorrelation function) or nonequilibrium (through the response to an imposed steady shear field) dynamic simulations. The possibility of predicting the viscosity from the self-diffusion coefficient extracted from MD simulations, through Eq. (3.41), is explored here, and found to be very promising for sufficiently long chains.

This chapter is organized as follows. Section 4.1 presents the molecular model used in the present work and the systems studied here. Results from the MD simulations are presented and compared with experiments and other simulations in section 4.2. Finally, in section 4.3, the major conclusions are summarized.

4.1.   Molecular Model Employed and Systems Studied

The molecular model used in the present MD simulation is presented in Table 4.1. A united-atom description of the PE melt is used where the values of ε and σ are the same for methyl and methylene groups. The values for the parameters of both bonded and non-bonded interactions are taken from the literature[74], [75] and presented in the table.

Table 4.1: Atomistic molecular model used in the MD simulations (model 1).

Type of interaction	Potential Function and Parameters
Nonbonded Interactions	$U_{LJ} = 4\varepsilon \left[\left(\dfrac{\sigma_{ij}}{\mathbf{r}_{ij}} \right)^{12} - \left(\dfrac{\sigma_{ij}}{\mathbf{r}_{ij}} \right)^{6} \right]$ $\sigma_{CH_2} = \sigma_{CH_3} = 3.94 \text{ Å}$ $\varepsilon_{CH_2} = \varepsilon_{CH_3} = 0.098 \text{ kcal/mol}$

Bond Bending	$V_{bending}(\theta) = \frac{1}{2}K_\theta(\theta - \theta_0)^2$
	$K_\theta = 115.2$ kcal/mol rad^{-2}, $\theta_0 = 112^0$
Torsional Potential	$V_{torsional}(\phi) = \sum_{i=0}^{5} c_i (\cos\phi)^i$
	$\phi = 180^0$ for *trans* conformation
	$c_0 = 2.217$, $c_1 = 2.905$, $c_2 = -3.135$, $c_3 = -0.731$,
	$c_4 = 6.271$ and $c_5 = -7.527$ in kcal/mol

Adjacent methyl and methylene groups along each chain backbone are maintained at a fixed distance $l=1.54$ Å from each other using the Edberg-Evans-Morriss algorithm (see section 2.2.4). To make the model sample the configuration-space probability density characteristic of a flexible model in the limit of infinitely stiff bond stretching force constants [77] a Fixman potential [78] is introduced in all MD simulations. The form of the Fixman potential and how it is implemented in our MD simulations are described in Appendix B. Constraint forces associated with the fixed bond length constraints are determined using the method of Edberg, Evans, and Morriss.

In both *NVE* and *NVT* simulations, a 6th-order Gear predictor-corrector scheme is used to integrate the equations of motion in Cartesian coordinates. The code makes use of a Verlet neighbor list to keep the CPU time spent in the calculation of forces at a minimum [4]. For the larger C_{156} chain system, an additional linked-cell list is kept [4]; according to this, the simulation box is divided into 4 sub-cells with the Verlet neighbor list searching for potential neighbors only within the 27 nearest sub-cells. The integration time step is always equal to 1 fs.

The simulations in the *NVT* ensemble further require the use of a Nosé-Hoover thermostat to maintain the temperature fixed at its prescribed value (see section 2.2.2). With the introduction of the Nosé-Hoover thermostat, the total Hamiltonian $H_{Nosé}$, defined as

$$H_{Nose'} = \sum_i \frac{\mathbf{p}_i^2}{2m_i} + V(\mathbf{r}) - \frac{1}{2}\sum_i \lambda_i \left((\mathbf{R}_{i+1} - \mathbf{R}_i)^2 - l^2 \right) + \frac{Q}{2}\left(\frac{\dot{s}}{s}\right)^2 + gk_BT \ln s \qquad (3.56)$$

should be conserved during the run. The first term on the right hand side represents the kinetic energy ($\mathbf{p}_i$ is the momentum vector of site i), the second term is the potential energy (including the Fixman potential), the third term is the contribution to the Hamiltonian due to constraint bond lengths with λ_i being the Lagrange multiplier for the

i-th bond [20], and the last two terms are the contributions due to the thermostat. In our MD runs, $H_{Nosé}$ was found to change by less than 1 % within 1 ns of simulation.

The mean molecular length, N, the number of chains, N_{ch}, the total number of atoms, N_{tot}, and the polydispersity index, I, of each system are presented in Table 4.2.

Table 4.2: Mean molecular length, N, number of chains, N_{ch}, total number of atoms in the system, N_{tot}, and polydispersity index, I, of the systems studied.

System	N	N_{ch}	N_{tot}	I
1	24	32	768	1.09
2	78	40	3120	1.09
3	156	20	3120	1.09

The C_{24} and C_{78} systems were also studied in the *NVE* ensemble and it was confirmed that the resulting dynamics was identical. In all simulations, the volume was kept constant at a value corresponding to a melt density exactly the same as the mean density obtained from the *NPT* EBMC run [73] that yielded the initial configuration for the dynamic simulation. P=1 atm and T=450 K were used in all cases reported here.

The total duration of the MD runs was 8 ns for the C_{24} chain system, 40 ns for the C_{78} system, and about 20 ns for the C_{156} system.

4.2.   Results

A)   Conformational Properties

The equilibrium conformational properties of the polymer melt as obtained from the present MD simulations are compared with those obtained from the EBMC runs. Tables 4.3 and 4.4 present this comparison for the mean-square end-to-end distance $<R^2>$ of the chains and their mean-square radius of gyration $<R_g^2>$, for all three mean chain lengths simulated.

The tables show also the results obtained from MC sampling of isolated continuous unperturbed chains (CUCs) [71]. The agreement between the three sets of data for both $<R^2>$, and $<R_g^2>$ is clear. This agreement with Flory's random coil hypothesis has been noted earlier in well-equilibrated monodisperse PE melts [45],[72]. Here it is shown true for a slightly polydisperse melt as well. One point to notice about the data of Table 4.3 is the large characteristic ratios they correspond to: for the C_{102} chain, for example, C_{102} =

8.35. This value is significantly larger than the value 7.8 obtained by neutron diffraction measurements [79] on molten polyethylene at 413 K. This is because the torsional potential employed in our model enhances *trans* conformational states [72]. Note that a recent simulation work of Yoon and collaborators [46],[47], using a different parameterization than the present work, has yielded results consistent with the measured characteristic ratios.

Additional insight into the structure can be gained by studying the intermolecular mer-mer pair distribution function $g(r)$. Figure 4.1 shows a comparison between the intermolecular mer-mer pair distribution functions $g(r)$ obtained from the MD and the earlier EBMC atomistic simulations. The agreement between the MC and MD simulation predictions is again excellent.

Table 4.3: The mean-square end-to-end distance $<R^2>$ for various chain lengths as obtained from bulk MD runs, from end-bridging MC runs, and from MC sampling of CUCs (P=1 atm, T=450 K).

$<R^2>$ (Å^2)	C_{46}	C_{78}	C_{84}	C_{102}	C_{117}
MD	770 ± 30	1510 ± 20	1640 ± 30	2020 ± 40	2355 ± 50
EBMC	810 ± 30	1490 ± 100	1635 ± 110	2025 ± 120	2330 ± 130
CUCs	810	1500	1624	2020	2340

Table 4.4: The mean-square radius of gyration $<R_g^2>$ for various chain lengths as obtained from bulk MD runs, from end-bridging MC runs, and from MC sampling of CUCs (P=1 atm, T=450 K).

| $<R_g^2>$(Å^2)	C_{46}	C_{78}	C_{84}	C_{102}	C_{117}
MD	107 ± 5	218 ± 10	244 ± 20	292 ± 30	335 ± 40
EBMC	112 ± 7	224 ± 10	247 ± 10	306 ± 30	360 ± 40
CUCs	111 ± 5	227 ± 10	265 ± 10	309 ± 10	333 ± 10
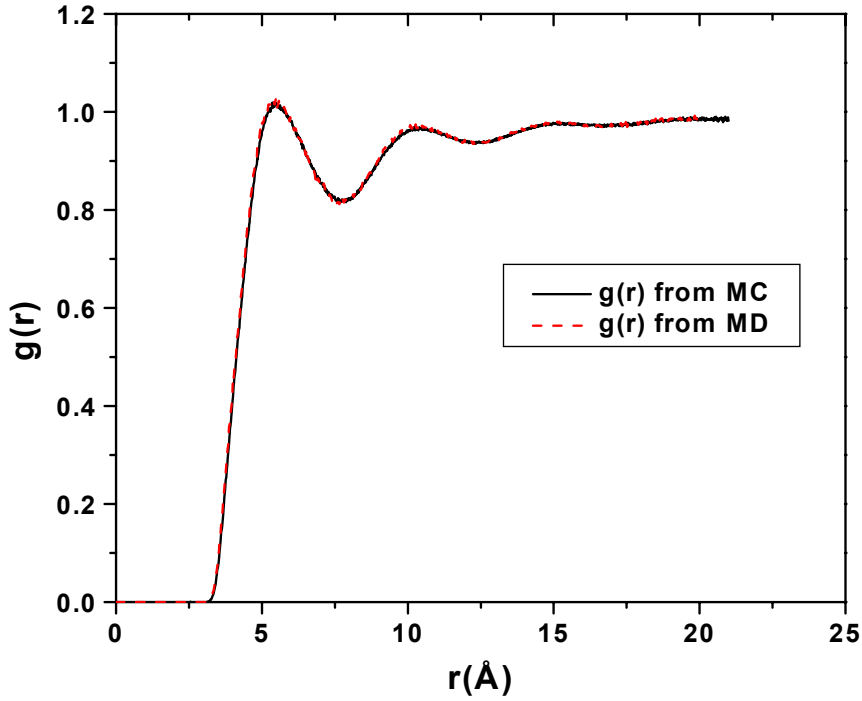
Figure 4.1 Intermolecular mer-mer pair distribution function, g(r), for the C_{78} chain system, as obtained from the end-bridging MC (solid line) and the MD algorithm (dashed line). T=450 K, P=1 atm.

B)   Local - Segmental Dynamics

The local dynamics of the chains, particularly the torsional dynamics, can be quantified in terms of the torsion autocorrelation function, defined as

$$P\left(\phi(t)\right) = \frac{\left\langle \cos\left(\phi(t)\right)\cos\left(\phi(0)\right)\right\rangle - \left\langle \cos\left(\phi(0)\right)\right\rangle^{2}}{\left\langle \cos\left(\phi(0)\right)\cos\left(\phi(0)\right)\right\rangle - \left\langle \cos\left(\phi(0)\right)\right\rangle^{2}} \tag{3.57}$$

The decay of $P\left(\phi(t)\right)$ is shown in Figures 4.2a and 4.2b. Figure 4.2a shows $P\left(\phi(t)\right)$ for three different mean chain length systems, C_{24} (dashed line), C_{78} (solid line) and C_{156} (long-dashed line). The figure shows quite evidently that the local dynamics is faster in the small-molecular weight system, C_{24}, and slower in the large-molecular weight system, C_{156}. The decay of $P\left(\phi(t)\right)$ for the C_{78} system is also shown in Figure 4.2b (solid line); also shown in the same figure (dashed line) is its best fit with a stretched exponential function of the form: $P\left(\phi(t)\right) = \exp\left(-\left(t/t_{c}\right)^{\beta}\right)$. The characteristic relaxation time obtained by the fitting is t_{c} = 4.2 ps and the stretching exponent β = 0.8. The correlation time (integral under curve) is 4.6 ps.

(a)

(b)
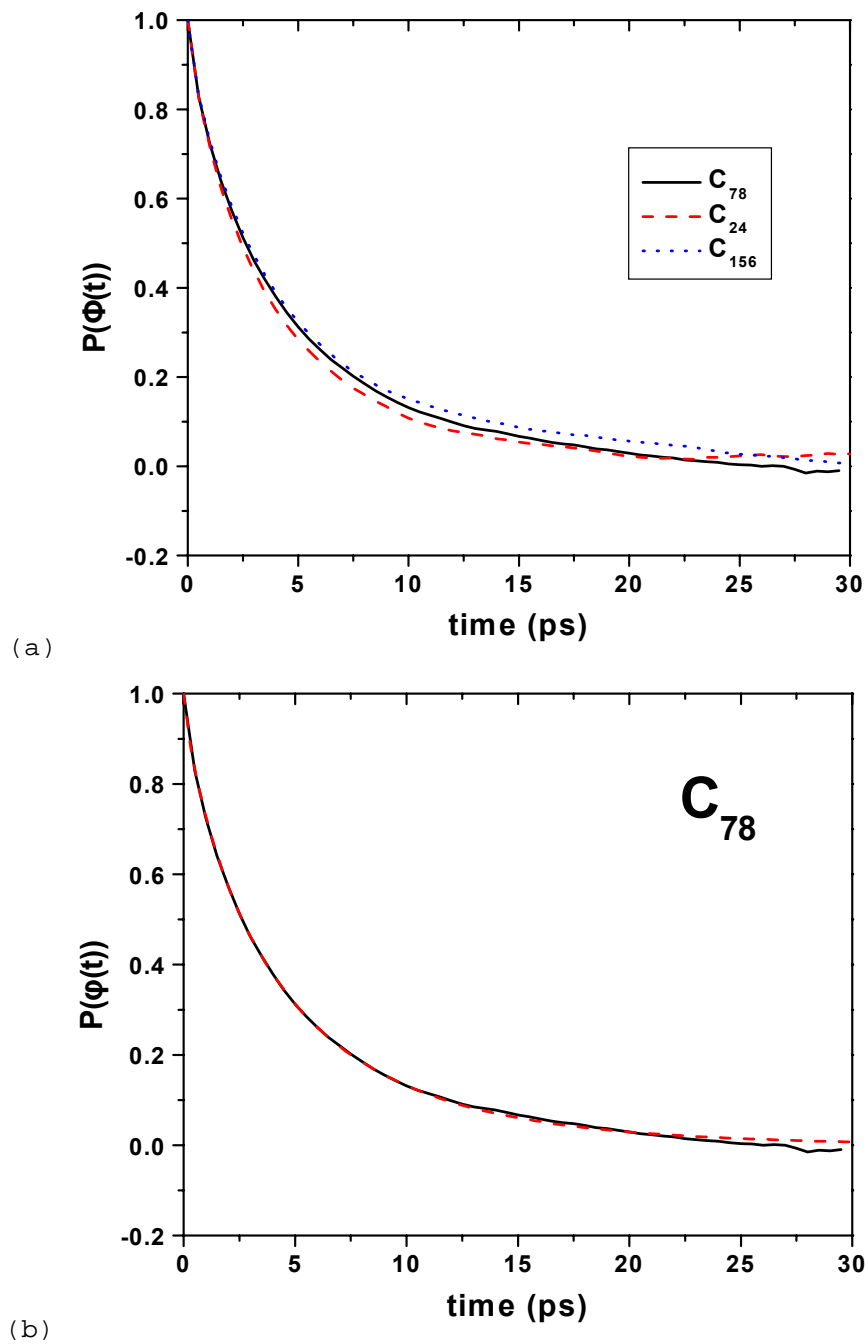
Figure 4.2 Torsional time autocorrelation function (a) for three mean chain length systems, C_{78} (solid line), C_{24} (dashed line) and C_{156} (dotted line) and (b) for the C_{78} chain system (solid line) and its stretched exponential fit (dashed line) (T=450 K and P=1 atm).

C)   Terminal Relaxation Properties

Figure 4.3 presents the decay of the orientational autocorrelation function for the end-to-end vector $\langle \mathbf{R}(t) \bullet \mathbf{R}(0) \rangle / \langle \mathbf{R}^2 \rangle$ as a function of time for three chain lengths (C_{46},

C_{83}, and C_{102}). These chain lengths were tracked in the system with mean molecular weight C_{78}. The rate at which $\langle \mathbf{R}(t) \bullet \mathbf{R}(0) \rangle / \langle \mathbf{R}^2 \rangle$ approaches the zero value is a measure of how fast the chain "forgets" its initial configuration, i.e., of the rate of overall relaxation of the chain.   As we can see in the figure, in order for the quantity $\langle \mathbf{R}(t) \bullet \mathbf{R}(0) \rangle / \langle \mathbf{R}^2 \rangle$ to reach zero (which corresponds to full relaxation of the chains) approximately 1.5 ns are needed for the C_{46} chains. For the C_{83} chains this time increases to about 4.5 ns, and for the C_{102} chains to 9 ns. This fast rise of the relaxation time with chain length shows very convincingly how difficult it is for MD to relax the conformational characteristics of chains with more than about 100 carbon atoms along their backbone.
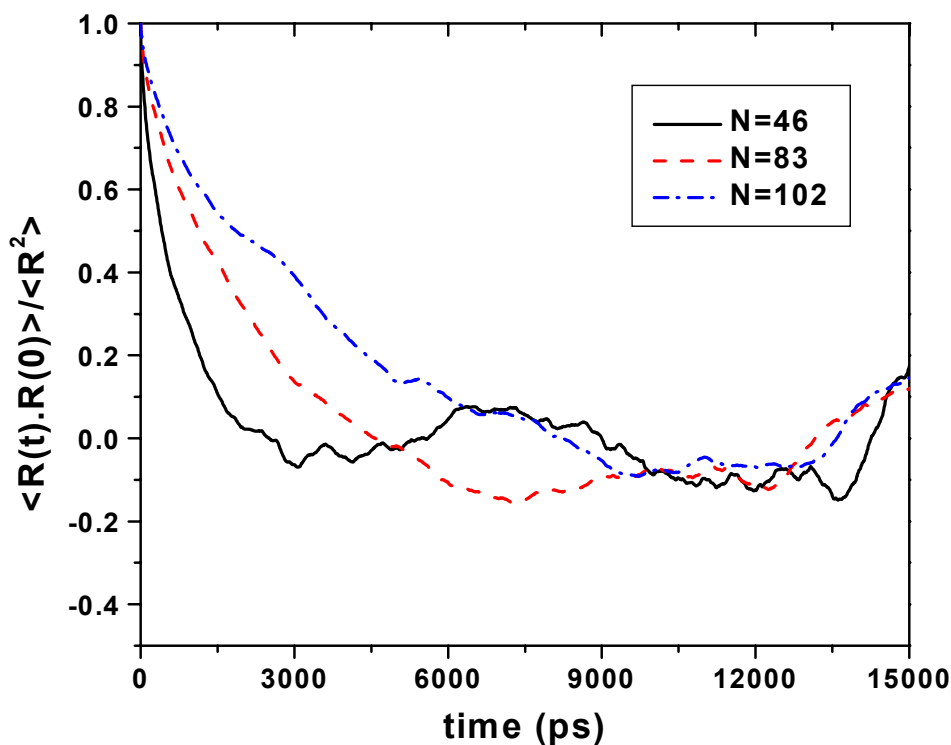
Figure 4.3 Time autocorrelation function for the chain end-to-end vector for various chain lengths N at T=450 K and P=1 atm.

Without loss of generality, we can use the chemical methylene and methyl segments as beads to define Rouse modes in our atomistic model. Here we have used the position vectors for the definition of normal modes (see Appendix C). The results of the normal mode analysis based on the Rouse model are shown in Figures (4.4) – (4.6). Figure (4.4) shows the mean squared amplitudes $<X_p(0)^2>$ as a function of $1/p^2$, for three

different chain lengths, C_{55}, C_{83}, and C_{102}. According to the Rouse model, Eq. (C.14), $<X_p(0)^2>$ should be proportional to $1/p^2$. From the figure it is obvious that this scaling is followed only for the first two normal modes, almost exactly for $N = 10$, and only approximately for $N = 83$ and $N = 55$; the third as well as all higher modes do not follow the Rouse scaling. The deviation from Rouse scaling decreases with increasing chain length. In fact, higher modes for short chains seem to follow a much stronger dependence on p, approximately of the form $1/p^3$, as has also been reported in a recent paper by Paul *et al.* [47].
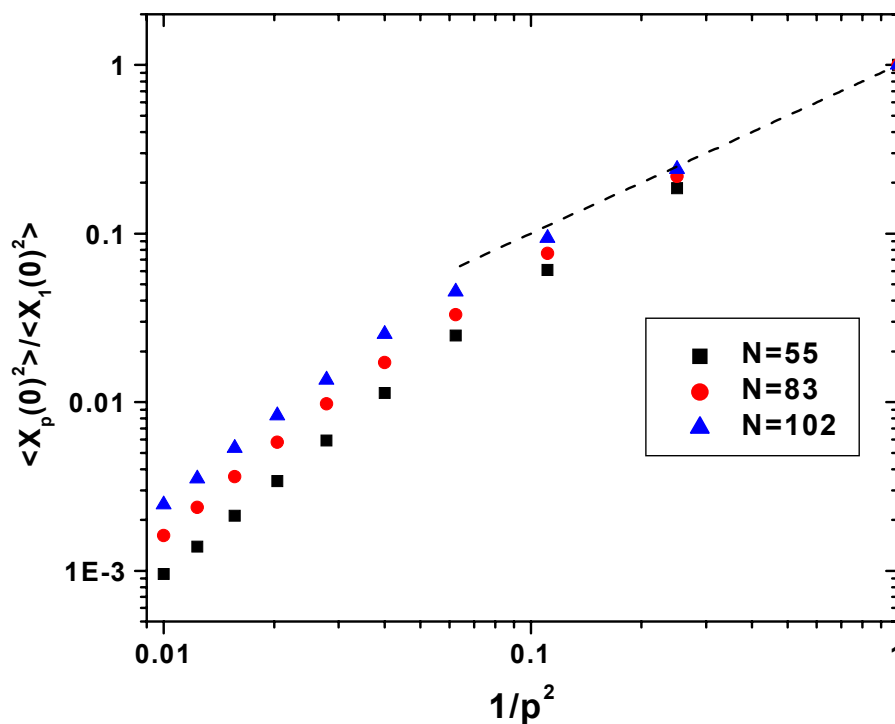
Figure 4.4 Normal mode analysis: The squared amplitudes of the Rouse normal modes $<X_p(0)^2>$ are shown as a function of the inverse squared mode number p in log-log coordinates for C_{55}, C_{83}, and C_{102} chains. The dashed line is drawn with a slope of -1, corresponding to the Rouse model.
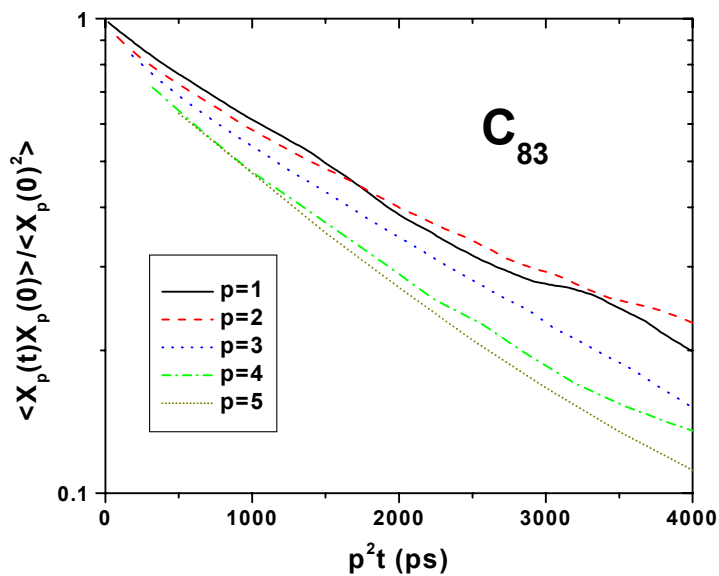
Figure 4.5 Normal mode analysis: Time autocorrelation functions of the first 5 normal modes versus p^2t. Chain length N=83, T=450 K, P=1 atm.
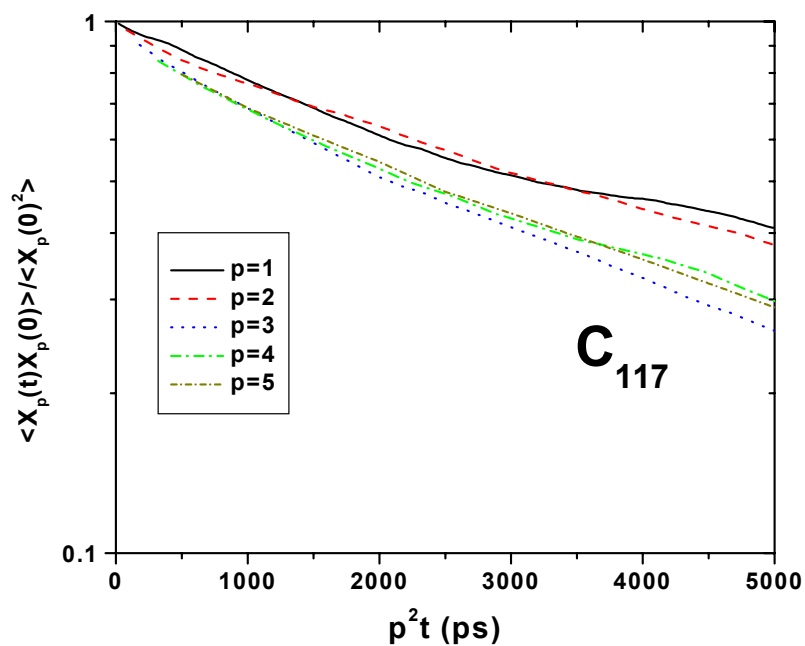
Figure 4.6 Normal mode analysis: Time autocorrelation function of the first 5 normal modes versus p^2t. Chain length N=117, T=450 K, P=1 atm.

Figures 4.5 and 4.6 show the logarithm of the normalized time autocorrelation function $\langle \mathbf{X}_p(t) \bullet \mathbf{X}_p(0) \rangle / \langle \mathbf{X}_p(0)^2 \rangle$ as a function of $p^2 t$ for the modes p = 1 to 5, and for two different chain lengths, C_{83} and C_{117}. If chains behaved identically as Rouse chains at all length scales, then all lines on each graph should have collapsed onto a single straight line. This is not seen in Figures 4.5 and 4.6. Only the first two modes (p=1 and 2) fall on the same line, which is straight to a good approximation; all higher modes, including the p = 3 mode, show clear deviations from Rouse scaling. The deviations are, in fact, more pronounced for the shorter C_{83} chains than for the C_{117} chains. The origin of these deviations should be sought in the length scale of the motion that higher modes correspond to: As p increases, the subchain whose relaxation is described by the p_{th} mode gets smaller and smaller and the Gaussian assumption provides only a poor representation of the conformational statistics of such subchains. This also justifies the smaller deviations seen in the case of C_{117} chains.

By fitting the simulation results for each mode between p = 1 and p = 5 to an exponential function, estimates of the relaxation times τ_p were obtained. Of greatest importance, of course, is the value of the longest time τ_1, since this (a) governs the long length scale relaxation of the chain, and (b) defines, through Eq. (3.39), the viscosity of the melt. According to Eq. (3.33), τ_1 should increase quadratically with chain length N. The data reported in Table 4.5 show an increase of τ_1 with chain length N, which is almost quadratic, mainly for the longer chains. According to Eq. (3.32), τ_p should be proportional to the inverse squared order of the normal mode p. This means that the ratios τ_1/τ_2 and τ_1/τ_3 should assume values of 4 and 9, respectively. From Table 4.5 one can see that the ratio τ_1/τ_2 is roughly 4 for almost the entire range of chain lengths present in our system, within the error bars of the simulation. This ratio clearly exhibits an increasing tendency with increasing chain length, suggesting a slight departure of the second mode from the Rouse prediction. The ratio τ_1/τ_3, on the other hand, is significantly larger than 9 for most chain lengths, suggesting that chains are too short for their third mode to behave in a Rouse-like fashion.

Although the normal mode analysis results reported here have all been based on the definition of normal modes through the position vectors, exploratory calculations with the normal modes defined through the connector vectors were found to conform perfectly to the scalings reported in Appendix C.

Table 4.5: The three first relaxation times τ_p and their ratios for various chain lengths as obtained from bulk MD runs (P=1 atm, T=450 K).

	C_{46}	C_{83}	C_{90}	C_{102}	C_{117}
τ_1 (ps)	800 ± 100	2800 ± 100	3600 ± 200	4200 ± 200	4800 ± 400
τ_2 (ps)	230 ± 30	860 ± 70	890 ± 60	920 ± 70	1040 ± 100
τ_3 (ps)	90 ± 10	285 ± 20	350 ± 20	380 ± 30	450 ± 80
τ_1/τ_2	3.5 ± 0.63	3.3 ± 0.29	4.05 ± 0.35	4.5 ± 0.41	4.6 ± 0.65
τ_1/τ_3	8.9 ± 1.49	9.8 ± 0.9	10.3 ± 0.82	11.0 ± 1.02	10.7 ± 2.2

One way to check the validity of the picture of exponentially decaying modes is to reconstruct the time autocorrelation function for the chain end-to-end vector, Eq. (3.38), and compare it with that obtained directly from the MD simulation. For the case of C_{83} chains, this is shown in Figure 4.7: the solid line represents the curve obtained from the simulation while the dashed line shows the reconstructed curve based on the first 5 normal modes, using the τ_1 values reported in Table 4.5 and Eq. (3.38) . The figure shows that the Rouse model reproduces quite faithfully the simulation curve, and this indicates that the model can reliably capture the long- (if not the short-) time dynamics of chains.
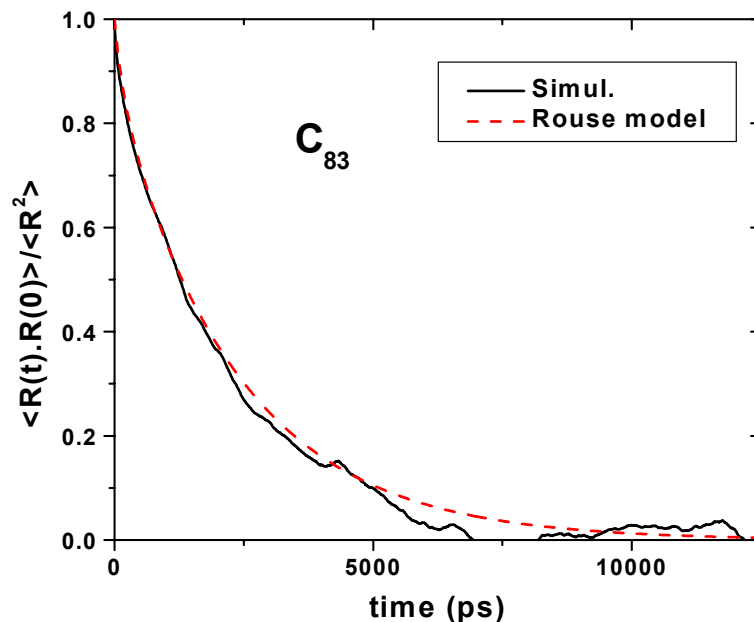
Figure 4.7 Time autocorrelation function for the chain end-to-end vector as extracted directly from the simulation (solid line) and as calculated from the Rouse model using the τ_1 value derived from the normal mode analysis. Chain length N=83, T=450 K, P=1 atm.

D)   Self-diffusivity

The self-diffusion behavior of the chains is examined in Figure 4.8, which shows a typical plot of the mean-square displacement of the chain center of mass $\left\langle \left(\mathbf{R}_{cm}(t) - \mathbf{R}_{cm}(0) \right)^2 \right\rangle$ for three different chain lengths (C_{46}, C_{83}, and C_{117}) as a function of time t. In the small-time regime (times shorter than the longest relaxation time), a non-Fickian, sub-diffusive behavior is observed, where $\left\langle \left(\mathbf{R}_{cm}(t) - \mathbf{R}_{cm}(0) \right)^2 \right\rangle \propto t^{0.8}$, as has already been observed in other simulations, both with atomistic [47] and with coarse-grained models [1]. In the long-time ($t > \tau_1$) regime, however, a linear dependence of on t is indeed seen, and this permits the calculation of the self-diffusion coefficient D through the Einstein relation, Eq. (3.18). By repeating the procedure for various chain lengths, D can be tabulated as a function of N; the results are shown in Table 4.6.
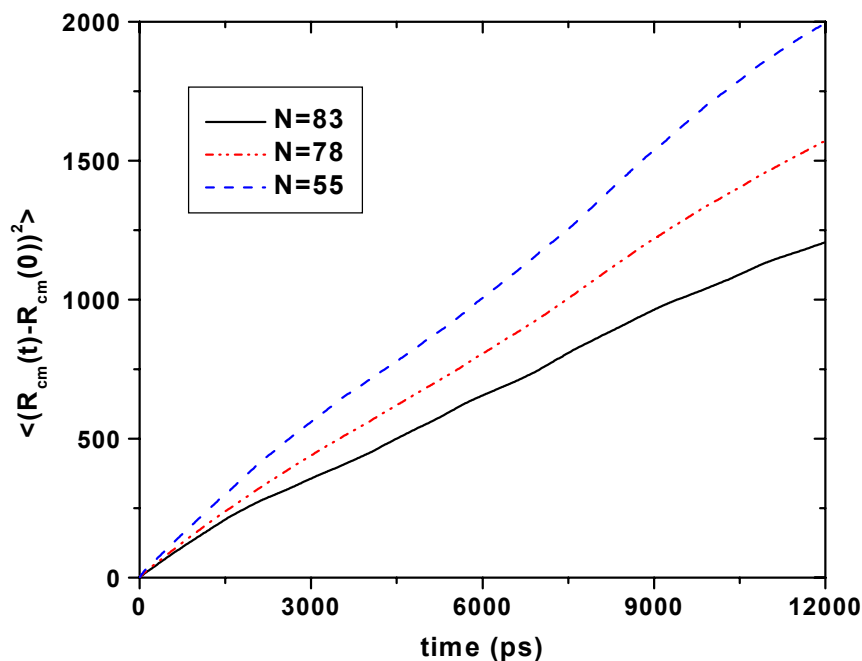
Figure 4.8 The chain center-of-mass mean-square displacement as a function of time for three chain lengths: C_{83} (solid line), C_{78} (dashed line), and C_{55} (dotted line).

E)   Segmental Friction Coefficient

Values of the segmental friction coefficient ζ_D extracted from D through Eq. (3.36) are shown in the sixth row of Table 4.6. Estimates of the same quantity ζ_τ, extracted from the Rouse times listed in the second row of Table 4.6 through Eq. (3.33) are shown in the fifth row of the same table. Estimates of the zero-shear rate viscosity obtained from ζ_D using Eq. (3.41) of the Rouse model are listed in the seventh row of Table 4.6. In the fourth and eighth row of Table 4.6 experimental data [80] for D and η_0 are shown for almost monodisperse molecular weight polyethylene melts found in the literature. The first point to notice about the data presented in Table 4.6 is the very good agreement between simulation and experimental values for the self-diffusion coefficient D: both for the C_{46} and C_{90} chains considered, the experimentally measured values are very close to the simulation results. An interesting point to remark concerns the friction coefficient ζ: Although the two values, ζ_τ and ζ_D, obtained from τ_1 and D, respectively, show some deviations for the shorter chains, for the longer chains they fall within the error bars of each other. This can be seen better in Figure 4.9, where ζ is plotted as a function of N: The friction coefficient ζ_D and ζ_τ values are low and different from each other in the short-chain regime ($N < 40$), but exhibit common values for longer chains. We regard the values of ζ_D as more representative of the melts studied; they can be obtained with less statistical error from the simulation trajectories, rely merely on the Einstein equation for the diffusivity and are therefore less dependent on the validity of the Rouse model. As N increases and the Rouse model gets more and more representative of the actual system, the two values ζ_D and ζ_τ should come closer; the figures do support this. On the other hand, according to the Rouse model, ζ should be a constant, independent of chain length. The results of our MD simulations show that this is not true: according to Figure 4.9, ζ_D becomes independent of chain length N only for chains longer than C_{70}. More specifically, Figure 4.9 shows that ζ increases from a small value (close to 0.15×10^{-9} *dyn s/cm*) representative of a short-chain alkane-like behavior, to a plateau value (around 0.45×10^{-9} *dyn s/cm*) characteristic of the long-chain Rouse behavior. This is an important result of the present work, since it defines the threshold in chain length, above which the Rouse model should be expected to provide a realistic description of the dynamics of unentangled polymer melts. One should note that the points displayed in Figure 4.9 were obtained from systems of various sizes and mean chain lengths. The points with $N \leq 46$

were obtained from the system with mean length C_{24}, the points with $46 \leq N \leq 117$ were obtained from the system with mean length C_{78}, and finally the last two points were obtained from the system with mean chain length C_{156}. For some points (for example C_{90} and C_{102}) ζ were extracted from both the C_{78} and C_{156} mean chain length systems; these values were found practically identical. This proves that the friction factors are not significantly affected by mean molecular weight and system size at these chain lengths. Additional evidence for the system size-independence of our results comes from the following observation: Running the C_{78} simulation with the same molecular weight distribution in a box four times larger than the one for which results are reported here yielded identical dynamics for all chain lengths.
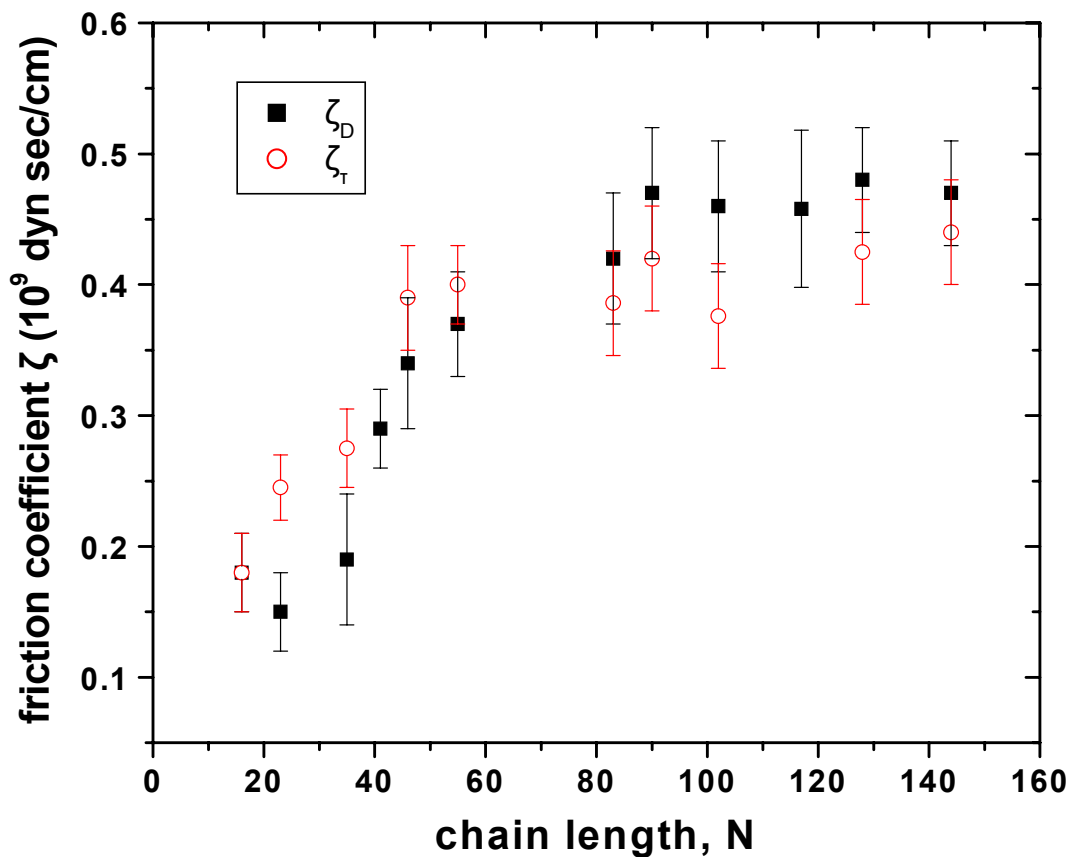

Figure 4.9: The friction coefficient ζ versus chain length N, as obtained from the Rouse relation between ζ and diffusion coefficient D (ζ_D, squares) and from the Rouse relation between ζ and the longest relaxation time τ_1 (ζ_τ, circles).

F)   Zero-Shear Rate Viscosity

Of great importance is the calculation of the zero-shear rate viscosity η_0 from the simulations, and its comparison with experimental data. In contrast to D, which is a primary property obtained directly from the simulation, η_0, like ζ, is evaluated by invoking the Rouse model, Eq. (3.41).

Therefore, η_0 should be expected to be predicted reliably only for those chain lengths for which the Rouse model also provides a valid description of the system, i.e., for $N > 60$ to 70. This explains the large difference observed between the calculated and the experimentally-measured η_0 values for the C_{46} chains, but it also justifies the very good agreement seen for the longer C_{90} system. Unfortunately, no experimental values of η_0 were found in the literature for chains longer than C_{90} and shorter than C_{150} with which to compare our simulation results.

Table 4.6: Maximum relaxation time τ_1, friction coefficient ζ, self-diffusivity D and zero shear-rate viscosity η_0 versus chain length.

	C_{46}	C_{83}	C_{90}	C_{117}	C_{128}
τ_1 (ps)	800 ± 100	2800 ± 100	3600 ± 200	4800 ± 500	7500 ± 400
D (10^{-6} cm^2/s)	4.0 ± 0.2	1.98 ± 0.1	1.46 ± 0.1	1.16 ± 0.2	1.0 ± 0.1
D_{exp} (10^{-6} cm^2/s)	4.6		1.4		
ζ_τ (10^{-9} dyn s/cm)	0.39 ± 0.04	0.386 ± 0.04	0.42 ± 0.04	0.32 ± 0.06	0.425 ± 0.04
ζ_D (10^{-9} dyn s/cm)	0.34 ± 0.05	0.38 ± 0.04	0.47 ± 0.05	0.46 ± 0.06	0.48 ± 0.04
η_0 (cp)	1.46 ± 0.07	5.8 ± 0.03	8.6 ± 0.5	12.9 ± 1.5	
$\eta_{0,exp}$ (cp)	2.5		9.2		

4.3. Conclusions

In this chapter we presented results about the conformational and dynamical properties of linear PE melts with molecular length up to C_{156}, that is below of the experimentally believed critical molecular weight for the formation of entanglements M_e. A hierarchical methodology was followed: First well-equilibrated polymer configurations were obtained through a powerful Monte Carlo algorithm, the EBMC. Then long atomistic MD simulations were conducted. The simulation results finally, were mapped

onto the Rouse model. Two different formulations of the normal modes were analyzed: one based on the position vectors and another one based on the connector vectors.

Results were presented for the conformation and the dynamic properties of linear PE melts of uniform chain length distribution and polydispersity index 1.09 for a variety of mean chain lengths from detailed atomistic MD simulations. Before subjecting the systems to the MD simulation, exhaustive equilibration at all length scales was achieved by use of the end-bridging MC algorithm. A wide range of chain lengths, ranging from C_{20} to about C_{150}, have been analyzed for times longer than about 12 ns to calculate reliably their dynamic properties.

The most significant result of this work is the evaluation of the friction coefficient ζ, an important mesoscopic parameter invoked by the Rouse model to describe the interactions of the chain backbone with the viscous medium. The simulation results demonstrated the presence of a minimum chain length value around C_{60}, above which ζ is a constant, chain length-independent parameter of the system. In the regime of chain lengths corresponding to this constant, asymptotic value of ζ, the zero-shear viscosity η_0 was calculated from the Rouse model and found to be in excellent agreement with measured values. Results were also presented for the self-diffusivity D as a function of chain length; these were found to be within a few percent of the experimentally measured values.

In the next chapter we will extend the hierarchical methodology followed here to polymeric systems of chain lengths greater than C_{150}, corresponding to what experimentally is referred as the onset of the entangled regime. A mapping of the atomistic MD data onto the reptation theory and a comparison with available experimental   data   will   also   be   presented.

CHAPTER 5

DYNAMICS OF POLYMER MELTS IN THE CROSSOVER REGIME BETWEEN UNENTANGLED AND ENTANGLED

In the previous chapter we presented atomistic MD simulation results with model systems with model systems of molecular length less than or equal to C_{156}, i.e. just below of the characteristic value of molecular weight which experimentally is known that forms entanglements. The simulation allowed us to calculate the spectrum of relaxation times of the melts, their diffusion coefficients and their zero-shear rate viscosity. To get many of these properties, the atomistic MD simulation data had to be mapped onto the Rouse model of polymer dynamics. Here the study is extended to polymer melts with molecular weight higher than C_{156} up to C_{250}, that is to systems on the crossover regime from unentangled to entangled.

As described in chapter 4, in order to get the rheological properties, the atomistic MD data need to be mapped onto a mesoscopic model. For the systems studied in this chapter, the reptation model will be invoked. In contrast, however, to the Rouse model where the mapping is direct, for the reptation model, the mapping is indirect and is realized through the *notion of the primitive path*. Thus a significant part of this chapter is dedicated to the development of a consistent methodology for defining the primitive path. The model used and the systems studied are described in section 5.1. Section 5.2 presents the methodology for mapping the atomistic MD simulation data onto the reptation model. Results for the diffusivity, dynamic structure factor, friction factor and zero-shear rate viscosity of the model PE simulated here are presented in section 5.3 and compared directly against recently obtained experimental data. Major conclusions and current efforts are summarized in section 5.4.

5.1.   Molecular Model – Systems Studied

The molecular model used in the atomistic MD simulations of the model systems investigated here is the same as the one used in our MD simulations of unentangled PE, which was described in details in section 4.2 (see Table 4.1). Regarding the MD methodology the only difference is that adjacent methyl and methylene groups along each chain backbone are maintained at a fixed distance $l = 1.54$ Å from each other using the SHAKE and RATTLE method as compared to the use of Edberg, Evans, and Morriss. Also the equations of motion are integrated with a velocity Verlet method (see section 2.2.1 and 2.2.4).

The systems studied here are of relatively long molecular weight and are shown in Table 5.1. In more details in Table 5.1 are shown the mean molecular length, N, the number of chains, N_{ch}, the total number of atoms, N_{tot}, and the polydispersity index, I, of each system. As we can see for the two longer systems the total number of atoms in the system is 5000 much larger than what is found in the literature. Initial configurations were obtained, as in the study of unentangled polymer melts, from EBMC simulations [73] of the same model systems at the same T and P. The overall simulation time was 200 ns for the C_{156} chain system, 250 ns for the C_{200} system, and 300 ns for the C_{250} system.

In order to track the dynamics of these systems for as long as needed to extract the desired properties (like the self-diffusion coefficient D) a multiple time step (MTS) algorithm is used. The method chosen is the reversible REference System Propagator Algorithm (rRESPA), described in details in section 2.2.4. Using rRESPA, we have been able to speed up the calculations involved in a typical NVT MD method by 2-5 times over the conventional algorithm. In all simulations reported in this chapter, the smaller time step dt was taken equal to 2 fs and the larger time step Dt equal to $5dt$, $i.e.$ 10 fs.

All simulations were conducted in the NVT statistical ensemble, at $T = 450$ K and $P = 1$atm,

Table 5.1: Mean molecular length, N, number of chains, N_{ch}, total number of atoms in the system, N_{tot}, and polydispersity index, I, of the systems studied.

System	N	N_{ch}	N_{tot}	I
1	156	20	3120	1.05
2	180	20	3600	1.05

| 3 | 200 | 25 | 5000 | 1.04 |
| 4 | 250 | 20 | 5000 | 1.04 |

5.2. Mapping onto Reptation Theory

A. Mapping of atomistic trajectories onto the primitive path

Mapping atomistic MD data onto the reptation model is a subtle task. The usual approach followed in the literature, as also stated in chapter 3, is to conduct coarse-graining simulations and then compare the mean square displacement of the chain segment $\phi_n(t)$, obtained directly from the simulations, with the predictions of the pure reptation theory.

In the present work a different procedure is followed in which the atomistic MD data are mapped onto the reptation model through a coarse-graining of the atomistic chain configurations onto their primitive paths. This has been a very challenging problem and was addressed only very recently by Kröger *et al.* [83] based on definition of the primitive path (PP). According to the reptation hypothesis, the primitive path is the shortest path connecting the two ends of the chain with same topology as the chain itself relative with the topological constraint (see section 3.3). From its definition, it is understood that the path must be a curve following the contour of the chain but in a softer way, avoiding many of the kinks of the chain. This idea is used to define a projection of the polymer chain with a set of $i = 0,1,..,N$ atomistic coordinates $\mathbf{x}_i^0$ onto a set of $i = 0,1,..,N$ coarse-grained coordinates $\mathbf{x}_i$. The projection is shown schematically in Fig. 5.1. To carry out the projection a mechanical system is assumed with two types of Hookean springs. The first type connects adjacent beads within the projected primitive path, the second type connects the projected beads of primitive path with the atomistic beads (atoms). The energy of this mechanical system is

$$E \quad \propto \quad \frac{k_1}{2}\sum_{i=0}^{N}\left(\mathbf{x}_i - \mathbf{x}_i^0\right)^2 + \frac{k_2}{2}\sum_{i=0}^{N}\left(\mathbf{x}_{i+1} - \mathbf{x}_i\right)^2 = \frac{1}{2}\sum_{i=0}^{N}\left(\mathbf{x}_i - \mathbf{x}_i^0\right)^2 + \frac{\xi^2}{2}\sum_{i=0}^{N}\left(\mathbf{x}_{i+1} - \mathbf{x}_i\right)^2 \quad (5.1)$$

where k_1 and k_2 are the spring constants:

$$k_1 = \frac{3k_B T}{a^2}, \qquad k_2 = \frac{3k_B T}{b^2} \quad \text{and} \quad \xi = b/a \qquad (5.2)$$

The coordinates of the primitive path are obtained by solving the force equations (minimizing the energy) $\partial E / \partial \mathbf{x}_i = 0$. This results into a $(N+1)$ x $(N+1)$ block diagonal system of linear equations of the form

$$\frac{\partial E}{\partial \mathbf{x}_i} = 0 \Rightarrow \left(\mathbf{x}_i - \mathbf{x}_i{}^0\right) - \xi^2 \left(\mathbf{l}_{i+1} - \mathbf{l}_i\right) = 0, \quad \text{for } i = 0,1,\ldots,N \qquad (5.3)$$

where connectors between neighbors along the chains contours $\mathbf{l}_i \equiv \mathbf{x}_i - \mathbf{x}_{i-1}$ for i = 1,2,...,N and $\mathbf{l}_0 = \mathbf{l}_{N+1} \equiv 0$ have been introduced in order to keep the notation short.
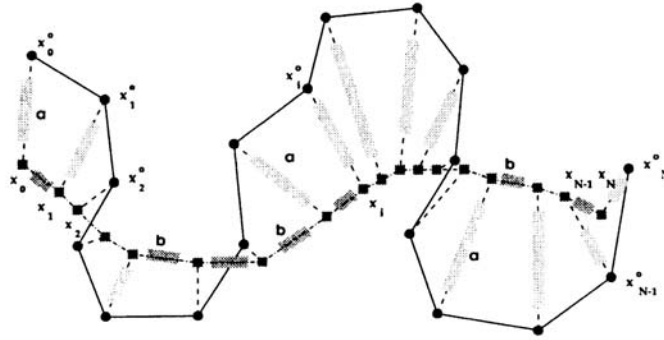

Figure 5.1 Mechanical model used for the projection of an atomistic chain onto one of its primitive paths. Black dots: atomistic chain, squares: beads of the primitive path.

Summation over i in Eq. (5.2) yields one of the desired properties of the projection, the conservation of the center of mass, i.e. $\sum_{i=0}^{N} \mathbf{x}_i = \sum_{i=0}^{N} \mathbf{x}_i{}^0$. The contour length of the primitive path L can be calculated as $L = \sum_i |\mathbf{x}_i - \mathbf{x}_{i-1}| = \sum_i |\mathbf{l}_i|$.

The projection involves a single parameter ξ, governing the stiffness of the chain in the coarse-grained (primitive path) representation. Different values of ξ lead to different parameterizations, i.e., to different primitive paths and, consequently, to different values of the contour length L. Then the tube diameter a can also be obtained from Eq. (3.--) of the reptation theory, Eq. (3.--). As the parameter ξ is increased, chain "coarse-graining" is achieved and information about atomistic details is virtually lost. A typical projection of an atomistic chain (from the C_{200} system) onto its PP is shown in Fig. 5.2.
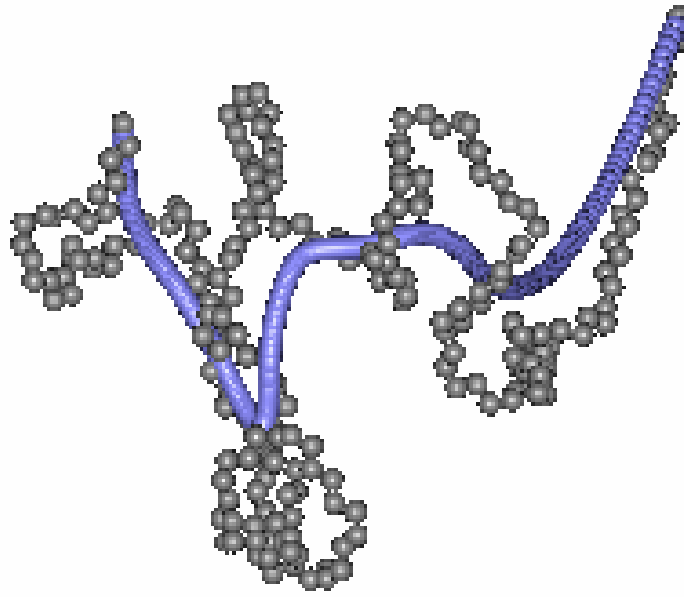
Figure 5.2 View of an atomistic chain of a C_{200} system (gray beads) and its corresponding primitive path (blue beads).

A critical point of the mapping procedure concerns the two ends of the primitive path $\mathbf{x}_0$ and $\mathbf{x}_N$. Two different cases have been explored:

a) The *fixed-ends* case. This means that the coordinates of the ends of the PP are the same with the ends of the atomistic chain, i.e. $\mathbf{x}_0 = \mathbf{x}_0^0$ and $\mathbf{x}_N = \mathbf{x}_N^0$ (see the projection shown in Fig. 5.2). The contour length of the PP in the C_{200} system in the fixed-ends case is shown in Figure. 5.3 and the tube diameter, obtained through Eq. (3.49), in Figure. 5.4 (stars). As ξ increases the atomistic detail is lost and the contour length decreases (tube diameter increasing).

b) The *free-ends* case. There also the coordinates $\mathbf{x}_0$ and $\mathbf{x}_N$ are calculated by using Eq. (5.2). The contour length of the PP for the C_{200} system for the free ends projection is shown in Figure. 5.3 and the tube diameter in Figure. 5.4 (circles). It is obvious from Figure. 5.3 that as ξ increases the contour length always decreases reaching very small, unrealistic, values. If the "coarse graining" approach is correct then the distribution of bond lengths of the PP, I(s), should be uniform. For both cases the average distribution of lengths for the contour position s is presented in Figure 5.5 for a C_{200} system. As we can see, I(s), with fixed ends is almost uniform whereas for free ends, a shrinking of the coarse grained PP chain bonds at the ends is observed. This unrealistic situation can be solved through the incorporation of a force at the ends of the chain (*Maxwellian daemon*).
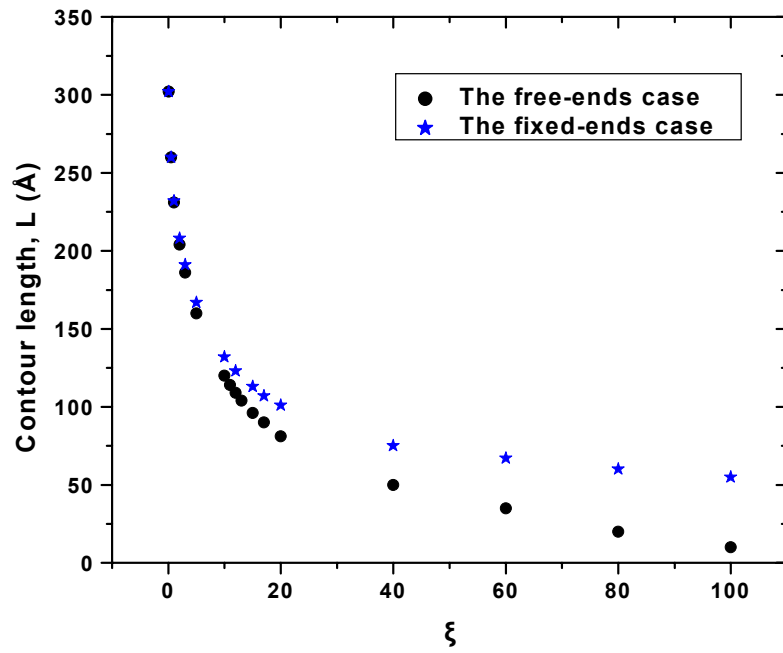
**Figure. 5.3**   The contour length L of the primitive path for the C_{200} system for various values of the parameter ξ.
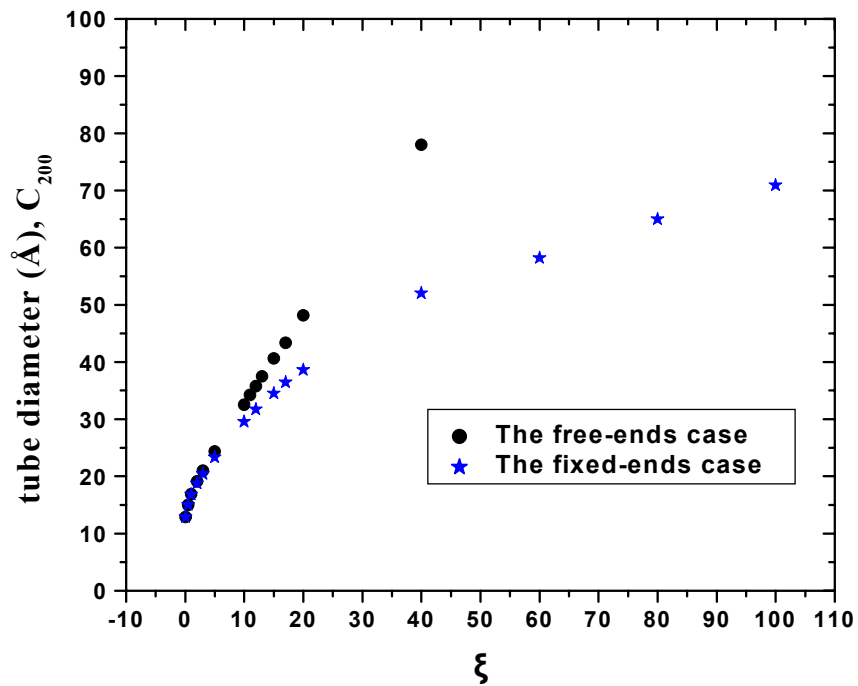

Figure. 5.4 The tube diameter α for the C_{200} system for various values of the parameter ξ.

The physical origin of the force is explained in Fig. 5.6 and it is related with the number of possible choices that a chain end has to move outside of the tube (entropic origin). One can intuitively understand it by considering the dynamical process at the chain end. Suppose in a time dt the chain end moves one step in a random direction (see Fig. 5.6b). If it moves to positions A_1, A_2, A_3, the contour length increases, whilst if it moves to A_0, the contour length decreases. Thus there is an imbalance in the change, which tends to increase the contour length and causes the force.

The Maxwellian daemon consists of a force of constant strength and direction of the last bond of the chain pointing to the end. The force depends on the mesh of the network, i.e on the tube diameter α. At the one end, $i = 0$, is

$$F_0 = A \frac{\mathbf{x}_0 - \mathbf{x}_1}{\left| \mathbf{x}_0 - \mathbf{x}_1 \right|} \tag{5.4}$$

and at the other end, $i = N$, is

$$F_N = A \frac{\mathbf{x}_N - \mathbf{x}_{N-1}}{\left| \mathbf{x}_N - \mathbf{x}_{N-1} \right|} \tag{5.5}$$

where $A = \dfrac{k_B T}{a}$ [6]. The coordinates now of the two ends $\mathbf{x}_0$ and $\mathbf{x}_N$ are given through

$$\mathbf{x}_0 = \frac{1}{1 + \xi^2} \left(\mathbf{x}_0{}^0 + \xi^2 \mathbf{x}_1 + F_0 \right) \quad \text{and} \quad \mathbf{x}_N = \frac{1}{1 + \xi^2} \left(\mathbf{x}_N{}^0 + \xi^2 \mathbf{x}_{N-1} + F_N \right) \tag{5.6}$$

whereas those of the internal beads are given through Eq. (5.2). The Eqs. (5.2) - (5.5) are become now a nonlinear coupled system of equations for the unknown variables $\mathbf{x}_i$ in terms of the variables $\mathbf{x}_i{}^0$. In this case not only are the variables $\mathbf{x}_i$ coupled, but also the components x, y and z, through the modulus $\left| \mathbf{x}_0 - \mathbf{x}_1 \right|$ and $\left| \mathbf{x}_N - \mathbf{x}_{N-1} \right|$. To solve this system of equations a Newton-Raphson scheme was implemented. The distribution of bond lengths for various values of the force is presented in Figure 5.7. Obviously, as the force F_{eq} is increasing the shrinking of the PP bonds at the ends is decreasing and for a proper value of F_{eq} the distribution becomes uniform. The distribution of the inner bonds of the PP is not affected at all. When the distribution becomes uniform the contour length L and the tube diameter α become almost the same with those of the fixed-ends case.
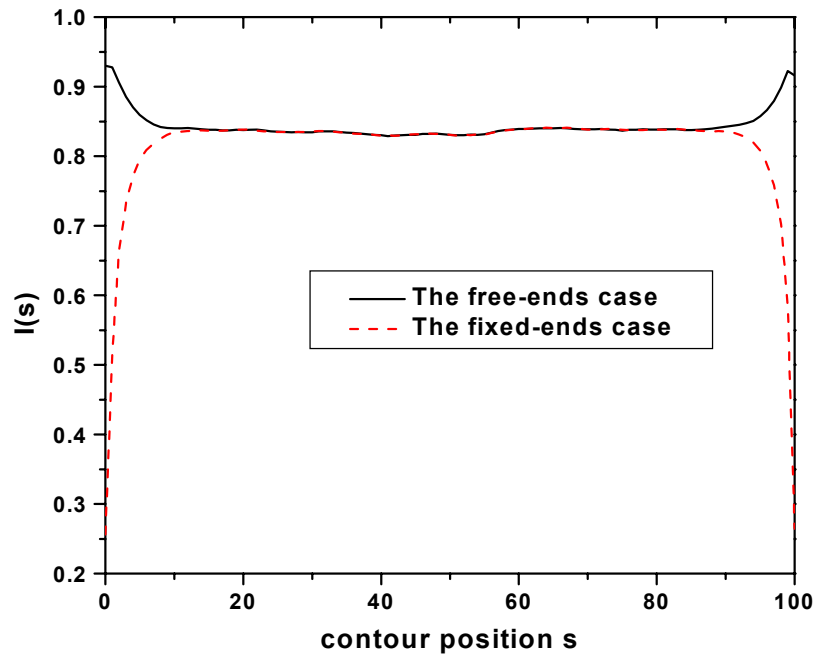
**Figure 5.5** Distribution of bond lengths of the primitive path using free or fixed ends case.
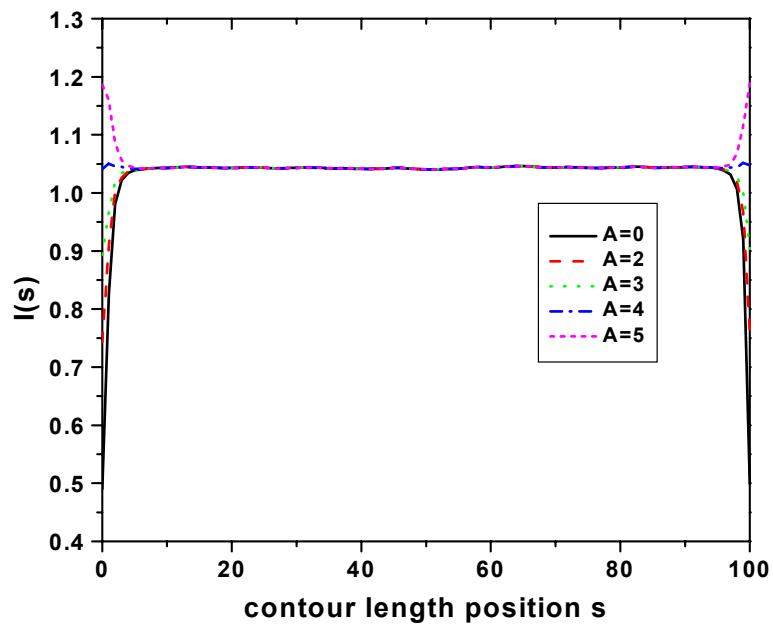
Figure 5.7 Distribution of bond lengths of the primitive path using free with Maxwellian daemon for different values of the force.
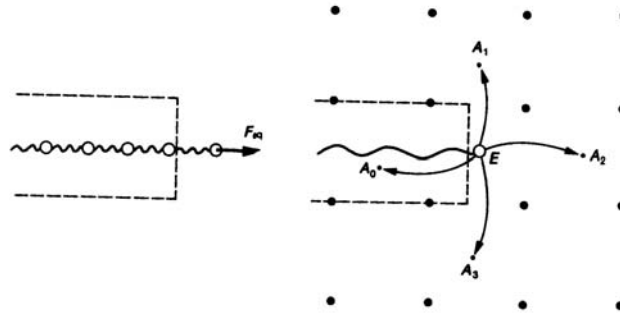
Figure 5.6 Equilibrium tension acting on the end of the primitive chain F_{eq} (Maxwellian daemon) and the physical origin of the force F_{eq}.

B. Mapping of atomistic dynamics onto the reptation dynamics

Once the projection from the atomistic to the primitive path representation is made, the problem reduces to the consistent determination of the parameter ξ. The procedure followed here is based on monitoring of the mean-square displacement of the primitive path points, $\phi(s,s;t)$, and not of the atomistic segments. The former is defined as:

$$\phi(s,s;t) \equiv \left\langle \left(\mathbf{R}(s,t) - \mathbf{R}(s,0) \right)^2 \right\rangle, \tag{5.7}$$

where $\mathbf{R}(s,t)$ is the position vector of the primitive segment at contour length s at time t. According to reptation theory [6]:

$$\phi(s,s;t) = 6Dt + \sum_{p=1}^{\infty} \frac{4\langle R^2 \rangle}{p^2 \pi^2} \cos\left(\frac{p\pi s}{L} \right)^2 \left[1 - \exp\left(-tp^2 / \tau_d \right) \right], \tag{5.8}$$

where the sum is over all normal modes p and τ_d is the disengagement time. For small times ($t < \tau_d$), Eq. (5.8) simplifies to:

$$\phi(s,s;t) = 6Dt + 2 \left(\frac{3}{\pi} \langle R^2 \rangle D \right)^{1/2} t^{1/2}. \tag{5.9}$$

In the present work, the following procedure is adopted in order to map the dynamics from the atomistic MD trajectories uniquely onto the reptation model. First, a value of the parameter ξ is chosen and a mapping onto the primitive path is made, and then Eq. (5.7) is used to calculate $\phi(s,s;t)$, averaged over all s values. For times $t < \tau_d$, the resulting curve is compared to the one obtained from Eq. (5.9), using the values of $<R^2>$ and D calculated directly from the atomistic MD simulations. The procedure is repeated until an optimum ξ value is found for which the two curves coincide. This mapping is performed self-consistently, without any additional adjustable parameters or any

experimental input. It also allows extracting reliably the tube diameter a, while utilizing atomistically obtained MD data only for times shorter than τ_d. Thus, the total duration of the MD simulations required is governed solely by the time needed to calculate the diffusion coefficient D reliably.

With the knowledge of $<R^2>$, D and a, the friction coefficient ζ and the zero-shear rate viscosity η_0 are readily obtained through, Eqs. (3.52) and (3.53).

5.3. Results

A)   Structural Properties

First a validation of the MD simulation data is presented through a comparison of the equilibrium conformational properties of polymer melts obtained with those from MC simulations. Tables 5.2 and 5.3 present this comparison for the mean square end-to-end distance $<R^2>$ of the chains and their mean square radius of gyration $<R_g^2>$ for all four systems studied. In the tables also shown are the results from MC sampling of isolated continuous unperturbed chains (CUCs) [73].

Table 5.2: Observed values for the chain mean square end-to-end distance $<R^2>$ for C_{156}, C_{180}, C_{200}, C_{250}.

$<R^2>$ (Å^2)	C_{156}	C_{180}	C_{200}	C_{250}
MD	3000 ± 100	3500 ± 100	4000 ± 100	4800 ± 100
EBMC	3000 ± 100	3450 ± 100	4100 ± 100	4700 ± 100
CUC	3000	3500	4050	4700

Table 5.3: Observed values for the radius of gyration, $<R_g^2>$ of C_{156}, C_{180}, C_{200}, C_{250}.

$<R_g^2>$ (Å^2)	C_{156}	C_{180}	C_{200}	C_{250}

MD	510 ± 25	590 ± 30	650 ± 20	810 ± 20
EBMC	510 ± 20	580 ± 20	640 ± 20	805 ± 20
CUC	510	580	650	800

B)   Self-Diffusion

Figure 5.8 shows the mean-square displacement of the chain centers of mass, $\left\langle \left(R_{cm}(t) - R_{cm}(0) \right)^2 \right\rangle$, for the C_{156}, C_{200} and C_{250} systems. From the linear part of these curves the self-diffusion coefficient D can be obtained through the Einstein's relation, Eq. (3.35).
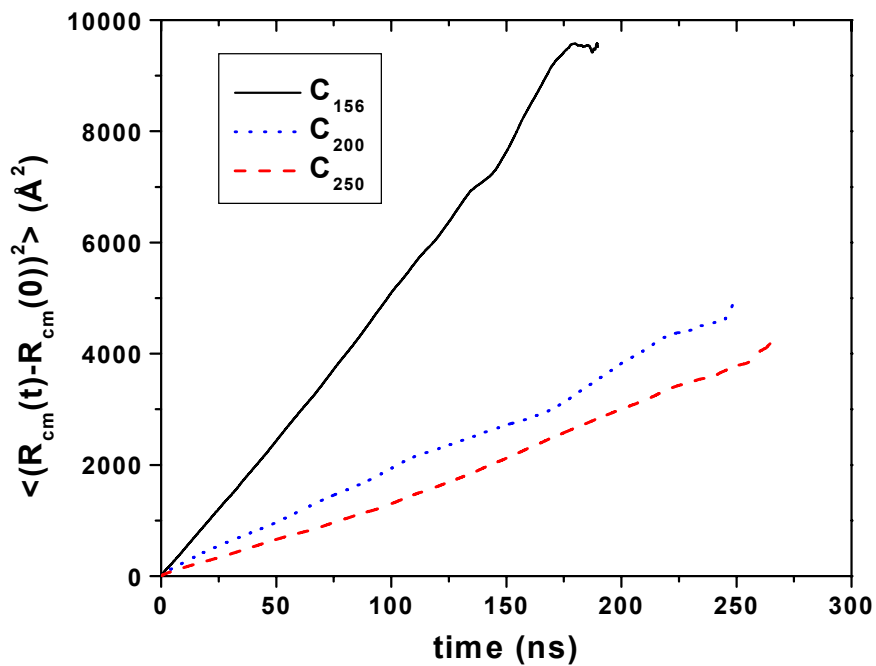

Figure 5.8   Mean square displacement of the center of mass for the C_{156} (solid), C_{200} (dot) and C_{250} (dashed) systems.
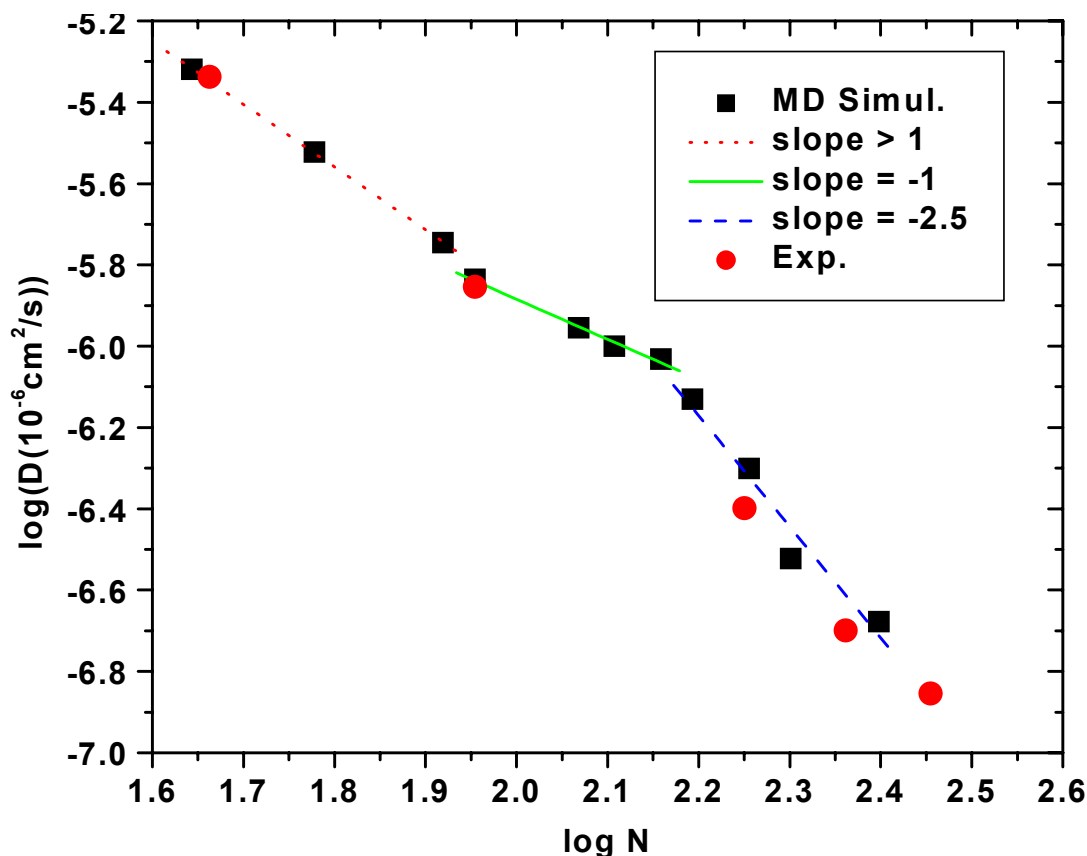
Figure 5.9   Predicted and experimental self-diffusion coefficients D vs chain length N in a log-log plot (T=450K, P=1atm).

Figure 5.9 presents predictions for the self-diffusion coefficient D as a function of mean chain length N, obtained from the slope of the mean-square displacement of chain centers-of-mass as a function of time, in the linear regime, through the Einstein relation. For comparison, also shown in the figure are values of D obtained from the NVT MD simulations presented in the previous chapter of systems with molecular length C_{24}-C_{117} [81]. Three distinct regions appear in the figure:

a) A small-MW, alkane-like behavior (N<60), where D follows a power-law dependence $D{\sim}MW^{-b}$, with b>1. In this regime, chain end effects, which can be described through a free volume theory, dominate the system dynamics [75]. In the next chapter a detailed discussion of the dynamics of systems in this regime will be given.

b) An intermediate, Rouse-like regime (from N=60-70 up to N=156) where $b \approx 1$. The dynamics of systems in this regime described in details in the previous chapter.

c) A long chain-length, reptation-like regime (N>156), where chain diffusivity exhibits a dramatic slow down, $b \approx 2.5$. According to the original formulation of

reptation theory, the latter exponent should be 2. Phenomena such as contour length fluctuations (CLF) and constraint release (CR) typically accelerate the escape of the chain from the tube, causing an increase in D and a decrease in η_0. A recently proposed theory that incorporates CLF and CR phenomena predicts a stronger exponent, between –2.2 and –2.3 [62]. These values agree with recent experimental results for concentrated polymer solutions and melts, which suggest an exponent between –2.2 and –2.4 for a variety of polymer systems [84], [85].

C) Dynamic Structure Factor S(q,t)

A quantity which is accessible experimentally and gives us valuable information about the Brownian motion of polymers is the dynamic structure factor, $S(q,t)$ [6]. By measuring the intensity of the scattered light, one can extract $S(q,t)$ as

$$S(q,t) \equiv \sum_{nm} \exp\left[i\mathbf{q} \bullet \phi(n,m;t)\right] \tag{5.10}$$

where $\mathbf{q}$ is the scattering vector and n, m denote atom labels. If n and m belong to the same chain then the single-chain dynamic structure factor is calculated. In Eq. (5.10), $\phi(n,m;t)$ is the time correlation function of chain segments n and m defined as:

$$\phi(n,m;t) \equiv \left\langle \left(\mathbf{R}(n,t) - \mathbf{R}(m,0)\right)^2 \right\rangle, \tag{5.11}$$

with $\mathbf{R}(n,t)$ denoting the position vector of the chain segment n at time t and $\mathbf{R}(m,0)$ the position vector of the chain segment m at time 0. For an isotropic sample, Eq. (5.10) reduces to

$$S(q,t) = \sum_{nm} \sin\left[q\phi(n,m;t)\right] / q\phi(n,m;t). \tag{5.12}$$

Of interest is the normalized single-chain dynamic structure factor, which is measured directly by the neutron spin echo (NSE) experiments. This is defined as:

$$S'(q,t) = \frac{S(q,t)}{S(q,0)} = \frac{\displaystyle\sum_{nm} \sin\left[q\phi(n,m;t)\right] / q\phi(n,m;t)}{\displaystyle\sum_{nm} \sin\left[q\phi(n,m;0)\right] / q\phi(n,m;0)}. \tag{5.13}$$

Eq. (5.13) can also be used to extract $S'(q,t)$ directly from the MD simulations by recording the time correlation function of chain segments n and m.

The Rouse model gives an analytic expression also for the single-chain intermediate dynamic structure factor. The calculation of the time correlation function

$\phi(n,m;t)$ for the finite Rouse model is described in details in appendix D. By using Eqs. (D.4) and (D.13), the dynamic structure factor $S(q,t)$ has the form,

$$S(q,t) = \frac{1}{N} \exp\left[-q^2 Dt\right]$$

$$\sum_{n,m}^{N} \exp\left\{ \begin{array}{l} -\dfrac{q^2 b^2}{12N} \sum_{p=1}^{N-1} \dfrac{1}{\sin^2\left(\dfrac{p\pi}{2N}\right)} \left[\cos\left(\dfrac{p\pi(m-1/2)}{N}\right) - \cos\left(\dfrac{p\pi(n-1/2)}{N}\right)\right]^2 \\ \\ -\dfrac{q^2 b^2}{6N} \sum_{p=1}^{N} \dfrac{1}{\sin^2\left(\dfrac{p\pi}{2N}\right)} \cos\left(\dfrac{p\pi(n-1/2)}{N}\right) \cos\left(\dfrac{p\pi(m-1/2)}{N}\right) \left[1-\exp\left(-\dfrac{t}{\tau_p}\right)\right] \end{array} \right\}$$

(5.14)

where N denotes the number of statistical segments in the chain, b the statistical segment length and D the center-of-mass diffusion coefficient.

In the high N limit, the following approximations apply: $i-1/2 \cong i$ and $\sin^2\left(\dfrac{p\pi}{2N}\right) \cong \left(\dfrac{p\pi}{2N}\right)^2$ (for $p<<N$). With the help of these, the following well-known expression for the dynamic structure factor $S(q,t)$ is derived (through Eqs. (D.5) and (D.11))

$$S(q,t) = \frac{1}{N} \exp\left[-q^2 Dt\right]$$

$$\sum_{n,m}^{N} \exp\left\{ -\frac{q^2 b^2}{6}|n-m| - \frac{2q^2 Nb^2}{3\pi^2} \sum_{p=1}^{N} \frac{1}{p^2} \cos\left(\frac{p\pi n}{N}\right) \cos\left(\frac{p\pi m}{N}\right) \left[1-\exp\left(-\frac{t}{\tau_p}\right)\right] \right\} \cdot$$

(5.15)

For $q<R^2> << 1$, only the overall diffusion of the chains is monitored and, then, $S(q,t) = \exp(-q^2 Dt)$.

Recently a modification of the Rouse model, the semiflexible chain model (SFCM), was proposed by Harnau *et al* [86],[87] that incorporates local chain stiffness effects. According to the SCFM, the Rouse mode relaxation times are given by:

$$\tau^b{}_p = \frac{\tau_R}{p^2 + \alpha_b p^4} = \frac{\tau_R}{p^2 + \dfrac{\pi^2 C^2{}_\infty}{4N^2 \sin(\theta/2)^4} p^4} \qquad (5.16)$$

where the term proportional to p^4 is the correction to the Rouse model due to rigidity effects. For the smaller normal modes, the $\tau^b{}_p$'s are almost equal to τ_p's but for the higher mode numbers, the $\tau^b{}_p$'s decrease faster than the corresponding τ_p's. The single-chain dynamic structure factor is again calculated using Eq. (5.14) but the relaxation times τ_p are now taken by Eq. (5.16).

Figures 5.10a-d present results for the intermediate dynamic structure factor for various values of the scattering vector q (0.04 Å^{-1}, 0.12 Å^{-1}, 0.20 Å^{-1}, 0.28 Å^{-1} and 0.36 Å^{-1}) as obtained directly from the MD simulation by using Eq. (5.13) (symbols) for the four systems studied in this work: C_{78}, C_{156}, C_{200} and C_{250}, respectively. The data for the C_{78} system have been obtained from previous MD simulations. Also presented in the figures are the predictions of Eq. (5.14) using either the finite Rouse model (solid lines) or the semiflexible chain model that incorporates chain stiffness (dashed lines) for these systems. The numbers of statistically independent segments N_k entering into these expressions and the statistical segment length b were calculated from the MD simulation data using $N_k b^2 = <R^2>$ and $N_k b = L_c$ where L_c is the contour length of the chai.

Based on our earlier investigations of the zero-shear rate viscosity, diffusion coefficient, normal-mode analysis and friction coefficient, the C_{78} PE melt follows quite faithfully Rouse dynamics [81], at least at the length scale of the chain end-to-end distance. Fig. 5.10a confirms this also for the single-chain dynamic structure factor, for wave vectors whose length q is below about 0.20 Å^{-1}. For higher q values, our atomistic MD data show $S'(q,t)$ to decay significantly more slowly than what is required by the Rouse model, almost for all times. In this case, by accounting for rigidity effects, the semiflexible chain model of Harnau $et\ al.$, the agreement with the simulation data improves somewhat, particularly at shorter times. For much longer times the predictions from the semiflexible chain model and the Rouse model are indistinguishable. In general, it is confirmed that stiffness corrections to the chain motion are not enough to fully account for the slowing down of the relaxation at intermediate and longer times observed in our MD simulations. Similar conclusions have been drawn recently experimentally based on $S'(q,t)$ data collected in polybutadiene [90] and polyisobutylene [91] melts.

For the three other PE melts studied, the situation is different. For the C_{156}, C_{200} and C_{250} systems systematic deviations are clearly observed in the entire regime of wavevector lengths q studied, particularly at higher q values. For example, for the C_{156} PE melt, there is no q value in the interval [0.04 Å^{-1} - 0.4 Å^{-1}] for which agreement with the Rouse model is seen.

(a)

(b)

(c)

(d)
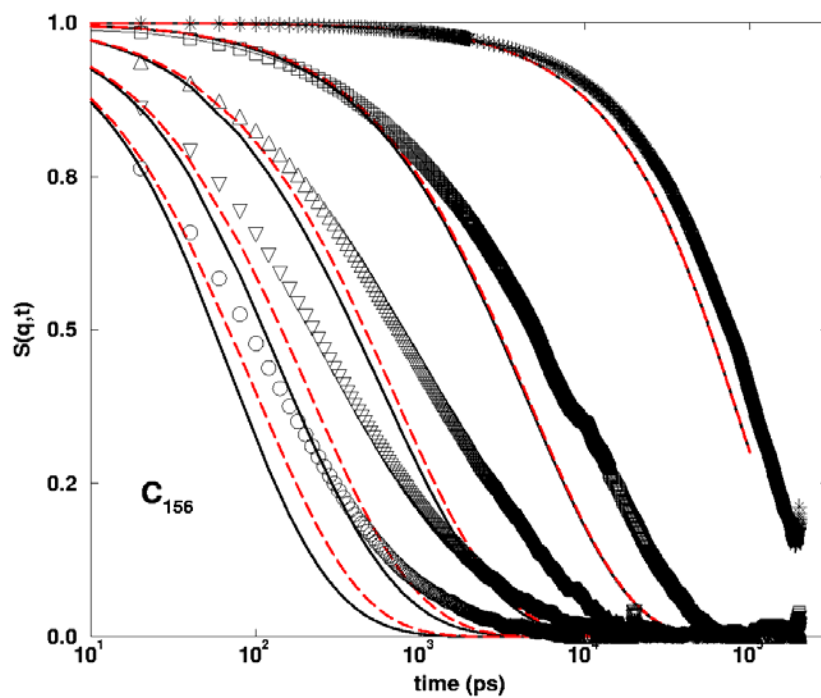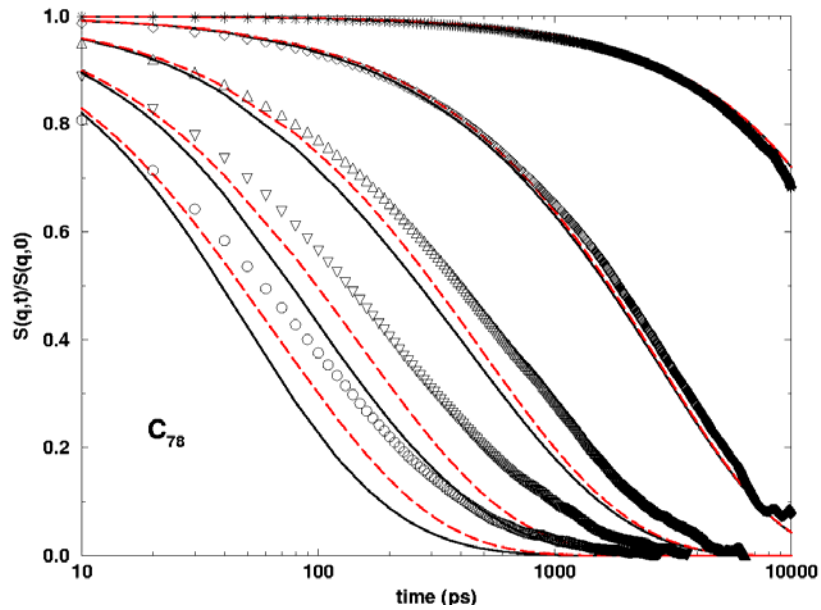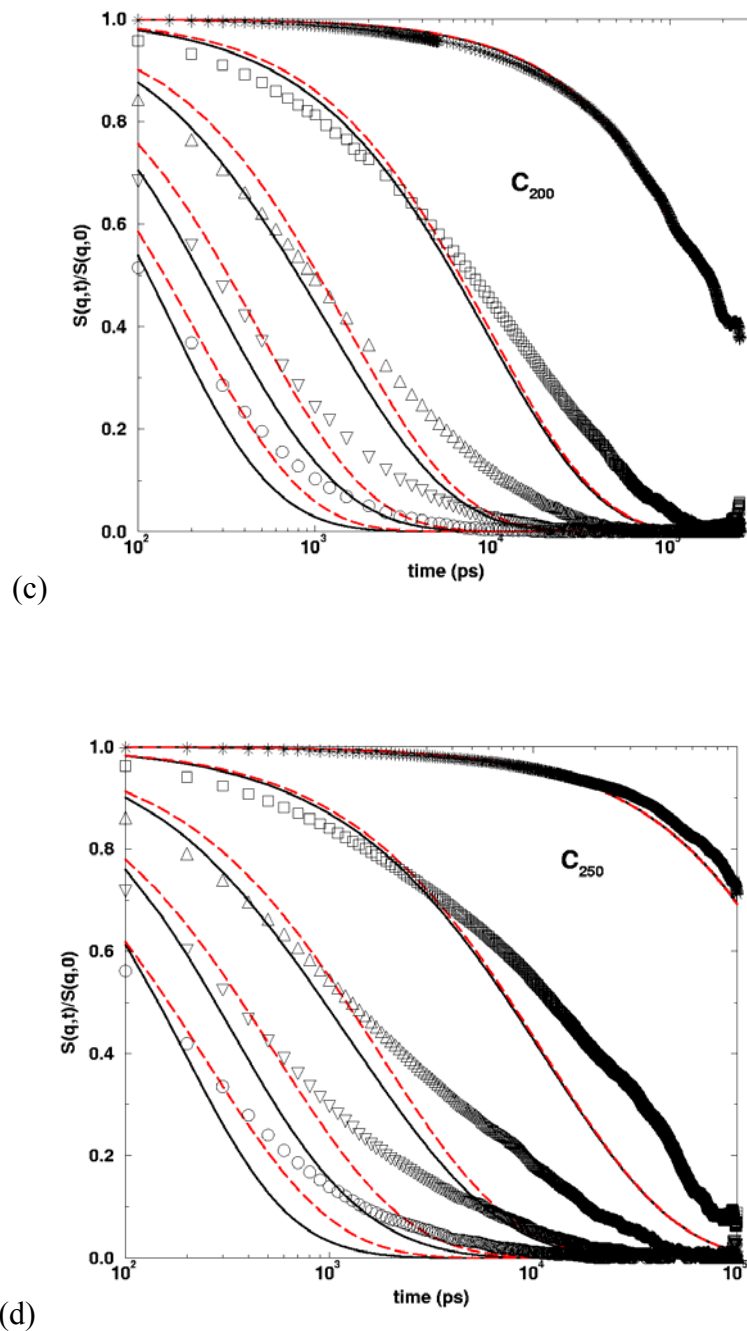
Figure 5.10   Normalized single-chain dynamic structure factor $S(q,t) / S(q,0)$ obtained from the MD simulations (symbols) for various values of the q vector (from top to bottom q= 0.04 Å^{-1}, 0.12 Å^{-1}, 0.20 Å^{-1}, 0.28 Å^{-1} and 0.36 Å^{-1}) for different molecular weights, (a) C$_{78}$, (b) C$_{156}$, (c) C$_{200}$ and (d) C$_{250}$. With the solid lines are the predictions from the Rouse model and with the dashed those from the Harnau *et al.* model.

Comparatively, the dependence of the decay of the single-chain dynamic structure factor $S(q,t)$ with time on chain length is shown in Figure 5.11. This Figure presents

$S(q,t)$- versus-t curves at two q values (0.12 Å^{-1} and 0.28 Å^{-1}) for all chain lengths studied here (symbols), together with the corresponding Rouse model predictions (continuous lines). The deviations from the standard Rouse behavior built up for the longer chain length systems C_{156}, C_{200} and C_{250} at all times (particularly for the $q = 0.28$ Å^{-1} case) are evident.

De Gennes proposed an expression for the decay of $S(q,t)$ with time based on the reptation model for q values in the interval, $1/<R^2> << q/2\pi << 1/a$ [92]. Unfortunately, for the melts studied here, the two limits $1/<R^2>$ and $1/a$ are of the same order of magnitude which renders the use of the formula inapplicable. To overcome this limitation, new atomistic MD simulations should be executed on significantly longer (and larger) model PE melts such as C_{1000} for times on the order of a few hundreds of nanoseconds. Results from these very promising simulations are under production and will be presented in a forthcoming publication.
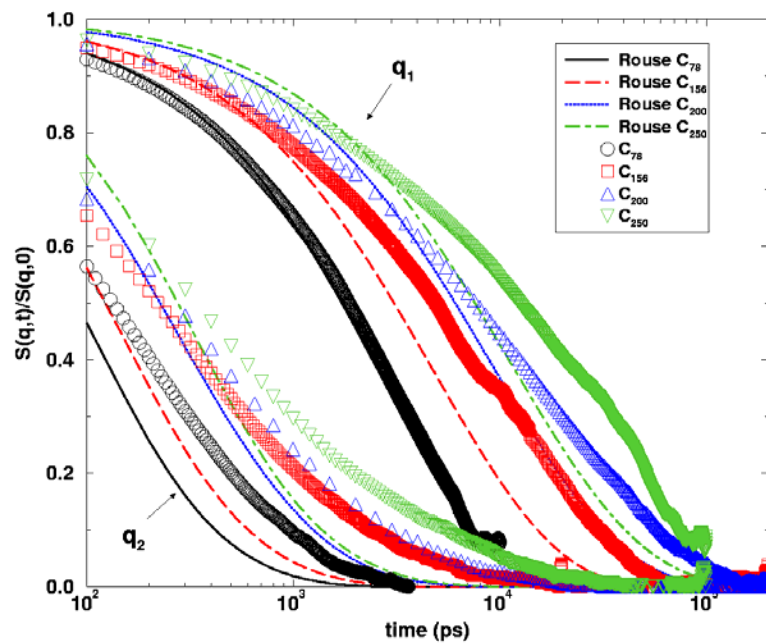

Figure 5.11 $S(q,t) / S(q,0)$ for the four systems shown in Figs. (5.10a) – (5.10d) for two values of q vector: $q_1 = 0.12$ Å^{-1} and $q_2 = 0.28$ Å^{-1} (symbols: MD simulations, lines: Rouse predictions).
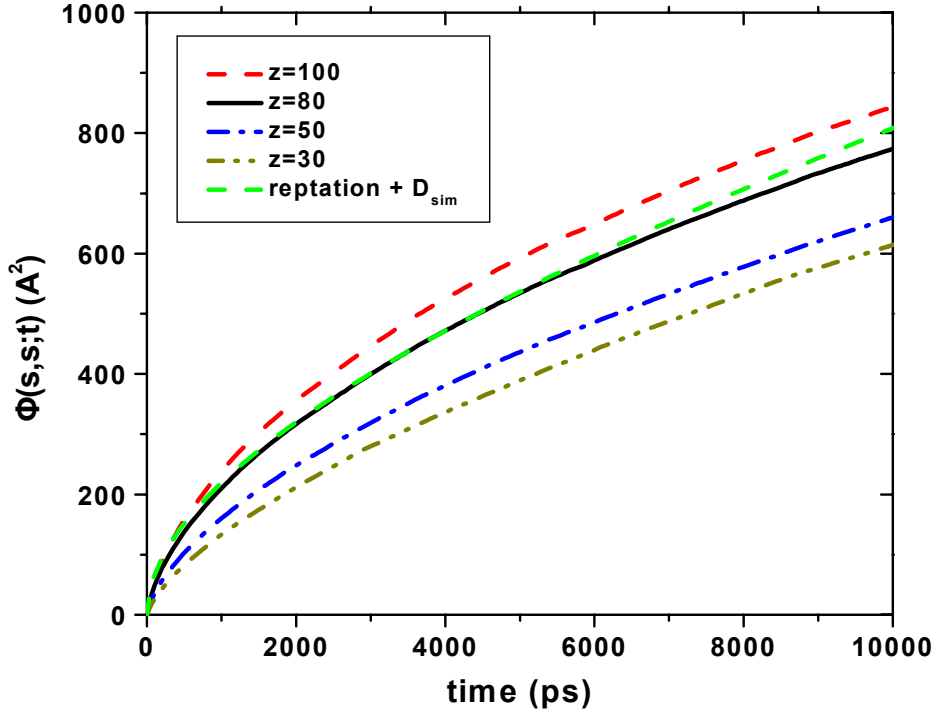
Figure 5.12   Mean-square displacement of the primitive path segments $\phi(s,s;t)$ vs time, averaged over all s, as predicted from mapping the atomistic MD data onto the reptation theory for various values of the parameter ξ determining the entanglement spacing. The solid curve corresponds to the pure reptation theory prediction, Eq. (5.9), using the values of D and $<R^2>$ obtained directly from the MD simulations.

D)   Friction Factor – Zero-shear Rate Viscosity

The friction factor ζ and the zero-shear rate viscosity η_0 can be calculated according to the Rouse model directly from the D, with the same way describing to the previous chapter, and by using the Eqs. (3.36) and (3.41). On the other hand, to calculate ζ and η_0 from the reptation theory, Eqs. (3.52) and (3.53) we need the tube diameter α.

To calculate the tube diameter α we follow the procedure described in section III b. Typical curves of the mean-square displacement of the primitive path points $\phi(s,s;t)$ for the C_{200} PE melt as a function of time t are shown in Figure 5.12. It is seen that the value of ξ which provides a consistent mapping of the atomistic MD data onto the reptation theory is $\xi=80\pm5$. For this value, the tube diameter a is calculated to be $a \sim 60$ Å. The same a value is obtained from mapping the C_{250} system, too. This value is larger than the one extracted from rheological experiments with high MW PE melts, which is around 34-40 Å [6]. The main reason for this, is that the value of a is actually different for the

relatively short PE systems investigated in this work (C_{200} and C_{250}) than for long-chain polyethylene, as pointed out by Richter *et al.* [54]. In contrast, for the shorter C_{180}, C_{156} and C_{78} systems, no physical value of a could be identified for which a consistent mapping of the atomistic MD data onto the reptation model is achieved.
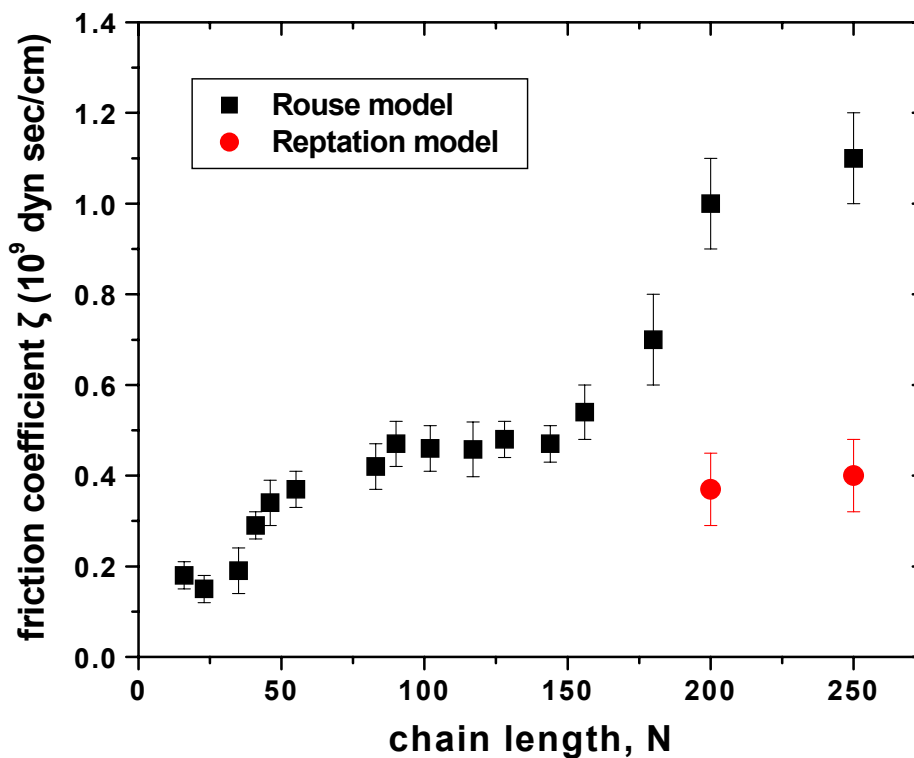
Figure 5.13   Monomer friction coefficient ζ vs chain length N, obtained from mapping the atomistic MD data onto the Rouse model (filled circles) or the reptation model (open circles).

Figure 5.13 shows results for the monomeric friction factor ζ as a function of the mean chain length N, over the entire range of molecular lengths studied. Filled circles depict results obtained from mapping the atomistic MD data onto the Rouse model, whereas open circles depict results obtained from mapping the atomistic MD data onto the reptation model. According to its definition, ζ should be independent of chain length, its value determined solely by the chemical constitution of the chain. The figure shows clearly that, at around C_{156}, a change in the mechanism of the dynamics takes place, which cannot be accommodated by the Rouse model, unless a chain-length dependent ζ is assumed. In contrast, in this regime ($N>156$), the reptation model provides a consistent description of the system dynamics characterized by a constant (0.4×10^{-9} *dyn s/cm*),

chain-length independent ζ value per methylene or methyl segment. It is clear that, in the reptation regime, the experimentally obtained ζ values bracket those extracted from the detailed atomistic MD simulations.

Figure 5.14 presents the zero-shear rate viscosity η_0 as a function of the molecular weight for all the systems studied here. For the systems smaller than C_{156} the Rouse model, Eq. (3.41) was used, whereas for the longer systems the reptation formula, Eq. (3.53) was used. Also reported in the figure are experimental η_0 values that we carried out in a series of linear monodisperse PE melts [81]. The η_0 values obtained from the reptation model using a value for the entanglement spacing α equal to 60 Å. The agreement of the simulation results with the experimental ones are remarkable in all systems studied here.
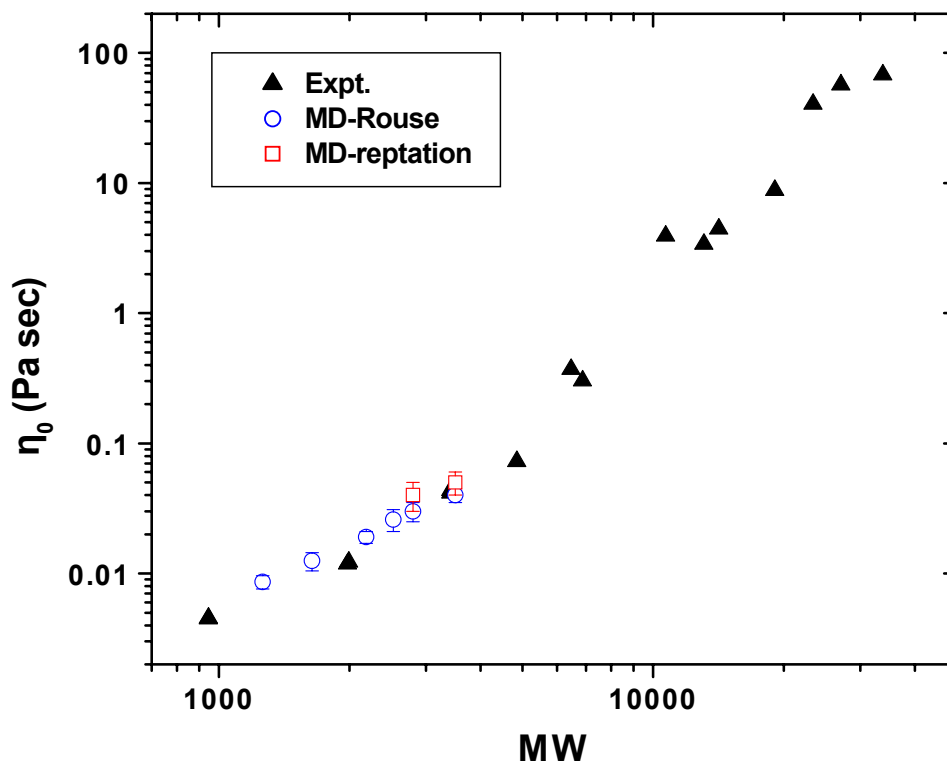
**Figure 5.14**   Zero-shear rate viscosity η_0 vs chain length N, obtained from the MD simulation and the Rouse model for the small N (circles) or the reptation model for the higher N (squares). Also shown in the figure are experimentally obtained η_0 values (triangles).

5.4.   CONCLUSIONS

In this chapter, results were presented from very long (up to 300ns), equilibrium atomistic MD simulations with model PE melt systems of molecular length C_{78} up to C_{250} to study the crossover from Rouse to entangled polymer melt regime. A dramatic slowdown of the self-diffusion coefficient D was observed when the molecular length of the polymer crossed over the C_{156} length. For $N>156$, the power-law exponent, quantifying the dependence of D on N, was found to be stronger than the one predicted from the Rouse model, and in very good agreement with a recently proposed reptation theory, which incorporates contour length fluctuations and constrained release mechanisms [62]. It also agrees very well with recent experimental data [84].

The single chain dynamic structure factor $S(q,t)$ was also calculated for various q values for four systems. Deviations from the Rouse model were found as q increases (big values of q correspond to smaller lengths that do not exhibit Rouse-like behavior as shown in chapter 4) and as the molecular weight increases (influences of the entanglements).

A consistent way of mapping the atomistic MD data onto the reptation theory was also presented. The mapping involved an intermediate projection step of the atomistically detailed chains onto primitive paths [83]. For chain lengths $N>156$, the reptation model was capable of producing consistent results for ζ. The tube diameter a was estimated to be about 60 Å. The zero-shear rate viscosity η_0 was also calculated, using Rouse model for the shorter systems and the reptation theory for the longer ones. The values of η_0 extracted from the simulations were seen to agree remarkably well with recently obtained experimental η_0 measurements on model linear PE's.

CHAPTER 6

DYNAMICS OF SHORT *N*-ALKANES – THE FREE VOLUME THEORY

In chapters 4 and 5 an investigation of the dynamics of polymer systems consisting of molecular lengths in the range between C_{24} and C_{250} was presented through an atomistic MD simulation study. It was observed that:

- Systems of molecular length less than about C_{60} are characterized by a segmental friction coefficient ζ, which is less than the value extracted from longer systems.

- Systems of molecular length greater than C_{60} and up to about C_{150} are characterized by a segmental friction coefficient which is constant, independent of chain length, as required by the chemical similarity of these systems. These systems were also seen to obey remarkably well Rouse dynamics.

- Systems of molecular length greater than C_{150} were seen to present significant deviations from Rouse dynamics, conforming better to the reptation theory. A mapping of the dynamics of these systems to the reptation model through the notion of the primitive path gave ζ values consistent with those extracted through the Rouse model from the smaller systems.

Clearly the dynamics of the shorter systems (with molecular length $N < C_{60}$) is not Rouse and is most probably dictated by chain end effects which are more pronounced in this regime. Additional evidence that the dynamics of these systems is not Rouse-like came from the study of the self-diffusion of these *n*-alkane systems which was seen to follow a scaling law of the form

$$D(M,T) = AM^b \qquad (6.1)$$

with the value of *b* significantly lower than −1 (see Fig. 5.9). It is the purpose of this chapter to explore the details of this dynamics through the help of a recently proposed free volume theory that combines elements of Rouse dynamics with chain-end free volume effects. Particular emphasis will be given to understanding the mechanism governing the diffusive properties of these systems and how they are affected by the temperature. Results will be reported for: (a) the density ρ and (b) the self-diffusion coefficient *D*, of *n*-alkane liquids as a function of the molecular weight *M* of the melt and the temperature *T*, through atomistic MD simulations with model *n*-alkane melts in the regime between C_{16} and C_{60}. The simulation results will be compared against a recent experimental study of von Meerwall *et al*. [93] and the predictions of a combined Rouse-free volume theory [93],[94],[96].

To elucidate the role of the excess chain-end free volume, we will explicitly calculate the free volume of chain ends relative to that of atoms deeper along the chain, following the methodology proposed by Greenfield and Theodorou [97]. Thus, results will also be presented for the excess free volume of chain ends over middle chain atoms and its dependence on temperature. This will allow us to test the hypothesis of the chain-end free volume theory that the steeper exponent observed in the relationship between self-diffusion coefficient *D* and molecular weight *M* for short *n*-alkane melts is attributable to the additional host effect. According to this, the relationship between *D* and *M* is dictated by the excess free volume of chain ends relative to that of interior segments along the chain (chain-end free volume). In the theory, the fraction of free volume provided by chain ends is assumed to be inversely proportional to *M* so that its effects increasingly enhance *D* at low *M*. The resulting expression for the diffusion coefficient is then a combination of Rouse diffusion and chain-end free volume host effects.

This hypothesis has been tested, very recently, in a series of papers by von Meerwall *et al*. [95],[93],[96] who documented the diffusion of strictly monodisperse *n*-alkanes (and *cis*-1,4 PI) melts in a range of temperatures *T*. The self-diffusion coefficient was measured with pulsed-gradient spin-echo methods [93],[98],[100]. They confirmed the power-law form of *D* and found very good agreement for the diffusion both in *cis*-1,4 PI and in *n*-alkane melts with the combined theory. von Meerwall *et al*. [93] also derived the apparent thermal activation energies of the self-diffusion coefficient as a function of *M*.

The chapter is organized as follows. First, the basic elements of the free volume theory based on the concept of the chain-end free volume host effect, as reported by Bueche [94] and von Meerwall *et al*. [93] are reviewed. Then section 6.2 presents the molecular model and the simulation strategy followed to study the density and the self-diffusion of monodisperse *n*-alkane oligomers in atomistic detail. Results from the atomistic MC and MD simulations for the density, free volume and self-diffusion coefficient of the *n*-alkane liquids and their dependence on molecular weight and temperature are presented in sections 6.3-6.5 and compared directly against the experimentally measured data. The major conclusions of the work are summarized in section 6.6.

6.1 Chain-End Free Volume Theory

According to the free volume theory, the diffusive properties of short molecules in the sub-Rouse regime are controlled by the availability of free volume in the system. More specifically, the total volume in the liquid is divided into two components: the occupied volume and the free volume. Molecular transport is presumed to rely onto the continuous redistribution of free-volume elements within the liquid. The free-volume theory was originally proposed by Cohen and Turnbull [101] and was further developed by many others [102],[103]. Later Vrentas *et al*. [104] developed the free volume theory to describe the diffusion of penetrant into a penetrant-polymer system. Detailed representation of their theoretical approach is given in the next chapter in the study of binary blends of *n*-alkanes liquids.

Bueche proposed that the higher mobility of chains in short-chain melts is mainly due to the significant effect of the extra free volume around chain ends. His basic idea was that a polymer chain end would contribute a certain amount of free volume to the system merely because it is not chemically bound within the certain portion of the chain.

More recently, the theory was revised by von Meerwall *et al*. to take into account the simultaneous Rouse and free volume effects [93]. According to this approach, the self-diffusion is predominantly Rouse in character, but corrections need to be made to account for the significant effect of the excess free volume in these systems due to chain ends. The following general expression for the self-diffusion coefficient in short-chain, monodisperse polymer melts is given

$$D(M,T) = A \exp\left(-E_a / RT\right) M^{-1} \exp\left[-B_d / f(T,M)\right] \qquad (6.2)$$

where the prefactor *A* is a constant characterizing the particular polymer but otherwise independent of chain length and/or temperature. One can distinguish three terms in Eq. (6.2). The first exponential term describes thermal activation effects, with E_α being the thermodynamic activation energy required for the chain end to perform jumps between accessible neighboring sites. This, in fact, is a measure of the energy required for the chain to break free from its neighbors before moving into a contiguous free volume void. The second term (M^{-1}) recognizes the Rouse dependence of the diffusivity on the diffusant molecular length or mass. And the last term represents the contribution to the self-diffusion coefficient due to the excess free volume of chain ends. B_d is a volume overlap parameter, while *f* plays the role of a fractional free volume, which is highly dependent on *T* and on *M* at low molecular weights.

The fractional free volume is described by the following equation:

$$f(T,M) = f(T,\infty) + 2V_e(T)\rho(T,M)/M \tag{6.3}$$

that is, by the sum of two terms: The first represents the segmental hole free volume and depends only on temperature. The second is a chain-end contribution to free volume: V_e is the chain-end free volume existing in addition to the regular contribution of the last monomer in units of cm^3 per (mol of chain ends). Expression (6.3) for the fractional free volume can be solved to give the mass density of the melt through

$$\rho(T,M) = [1/\rho(T,\infty) + 2V_e(T)/M]^{-1} \tag{6.4}$$

That is, the inverse mass density (specific volume) has the form of a hyperbolic function of molecular weight. Clearly,

$$f(T,M) - f(T,\infty) = 1 - \frac{\rho(T,M)}{\rho(T,\infty)} \tag{6.5}$$

6.2 Molecular Model, Methodology and Systems Studied

In the two previous chapters in the study of long PE melts we have used a united atom model (UA), where methylenes are treated as single units. For the study of diffusion of short *n*-alkanes, however, explicit atom models (EA), where carbons and hydrogens are treated as separated units, are more found in the literature to be accurate than the UA models. In a recent study Mondello and Grest [106] performed a series of MD simulations on short *n*-alkanes with different UA and EA models and compared with self-diffusion experimental data. They proposed a new UA model, which exhibits very good agreement for the self-diffusion coefficient with both EA model and experimental

data. The model used by Mondello and Grest is described in Table 6.1. A potential cutoff distance of 9.062 Å is used.

Table 6.1: Atomistic molecular model used in the MD simulations of short *n*-alkanes (model 2).

Type of interaction	Potential Function and Parameters
Nonbonded Interactions	$U_{LJ} = 4\varepsilon \left[\left(\dfrac{\sigma_{ij}}{\mathbf{r}_{ij}} \right)^{12} - \left(\dfrac{\sigma_{ij}}{\mathbf{r}_{ij}} \right)^{6} \right]$ $\sigma_{CH_2} = \sigma_{CH_3} = 4.01\ \text{Å}$ $\varepsilon_{CH_2} = 0.093\ \text{kcal/mol}$ $\varepsilon_{CH_3} = 0.227\ \text{kcal/mol}$
Bond Bending	$V_{bending}(\theta) = \dfrac{1}{2} K_\theta (\theta - \theta_0)^2$ $K_\theta = 124.18\ \text{kcal/mol rad}^{-2},\ \theta_0 = 114^0$
Torsional Potential	$V_{torsional}(\phi) = \displaystyle\sum_{i=0}^{3} c_i (\cos\phi)^i$ $\phi = 180^0$ for *trans* conformation $c_0 = 1.736,\ c_1 = 4.500,\ c_2 = 0.764,$ $c_3 = -7.000$ in kcal/mol

Furthermore, adjacent methyl and methylene groups are maintained at a fixed distance *l*=1.54Å using the SHAKE and RATTLE method.

With the above model we have studied the temperature and molecular weight dependence of the density and the diffusion *n*-alkanes. The *n*-alkane liquids that have been simulated are shown in Table 6.2. All the systems are fully monodisperse, i.e. *I* = 1.0.

Table 6.2: Molecular length, N, number of chains, N_{ch}, total number of atoms in the system, N_{tot} and temperatures, T, at which the systems have been studied.

System	N	N_{ch}	N_{tot}	T (K)
1	16	50	800	323, 343, 383, 403 and 443
2	26	35	910	323, 343, 383, 403 and 443
3	36	35	1260	343, 383, 403 and 443
4	44	30	1320	343, 383, 403 and 443

| 5 | 60 | 16 | 960 | 383, 403 and 443 |

In all simulations conducted a Multiple Time Step integrator, the rRESPA algorithm, has also been used. The smaller time step *dt* was taken equal to 1 fs and the larger time step *Dt* equal to 5*dt*, i.e., 5 fs, the overall simulation time ranging from 10 ns to 60 ns, depending on the length of the *n*-alkane and the temperature.

Results will be presented about the density and self-diffusion coefficient of linear monodisperse alkanes of length ranging from C_{16} to C_{60} as a function of temperature and molecular weight. The results will be analyzed in terms of the concept of the Bueche-von Meerwall free volume theory that combines Rouse diffusion with chain end free volume effects, described in the previous section. In all cases, the results are directly compared to the experimental data for these molecular systems published by von Meerwall *et al*. [93].
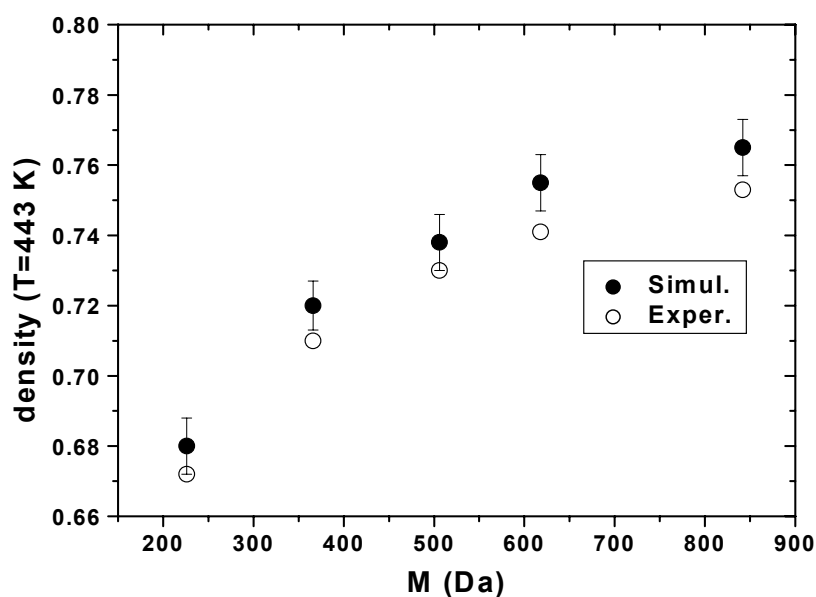
**Figure 6. 1**   Simulation predictions for the density ρ of liquid *n*-alkanes (filled circles) and experimentally measured values (open circles), as a function of their molecular weight *M*, at *T*=443K.

6.3 Density of liquid n-alkanes

Fig 6.1 shows results for the density ρ of the liquid *n*-alkanes as a function of molecular weight, at *T*=443K (filled circles). Also shown in the Figure (open circles) are

the experimentally measured density values [93]. It is seen that the density ρ increases fast with *M*, particularly at low *M*'s. The rate with which ρ increases with *T* is constantly decreasing, but above C_{60} ρ seems to approach a constant value, which for the *n*-alkanes studied here is a unique function of the temperature *T*. The Figure also shows that, overall, the agreement with the experimentally measured densities is satisfactory. For all *n*-alkanes studied, the maximum deviation between the predicted and the measured values is less than about 2%, which agrees with the results of our previous study with significantly longer PE melts. The same level of agreement holds true also for the other temperatures studied.

Fig. 6.2 shows in detail the model predictions for ρ as a function of the length of the *n*-alkane, for all temperatures investigated. Each ρ-versus-*M* curve can be separately fitted to Eq. (6.4) by adjusting the two parameters $\rho(T,\infty)$ and $V_e(T)$. The first denotes the value of the density at infinite *M*, and the second the excess free volume of chain ends; both parameters are functions of temperature only. All fits (solid lines in Fig. 6.2) are seen to be particularly satisfactory, which allowed us to extract the temperature dependence of $\rho(T,\infty)$ and $V_e(T)$; this is demonstrated in Fig. 6.3. Both $\rho(T,\infty)$ and $V_e(T)$ are seen to vary exactly linear in *T*, in agreement with the Cohen-Turnbull proposition:

$$1/\rho(T,\infty) = a + bT = 1.1 + 0.00095T(^0C)$$
$$V_e(T) = c + dT = 15.85 + 0.063T\left(^0C\right)$$

$$(6.6)$$

The corresponding experimental values are [93]:

$$1/\rho(T,\infty) = a + bT = 1.142 + 0.00076T(^0C)$$
$$V_e(T) = c + dT = 13.93 + 0.06T\left(^0C\right)$$

$$(6.7)$$

with the temperature expressed in ^0C. The good qualitative and quantitative agreement with the experimental data is expected given the consistency of the simulation predictions for the density of these systems with the corresponding measured values.
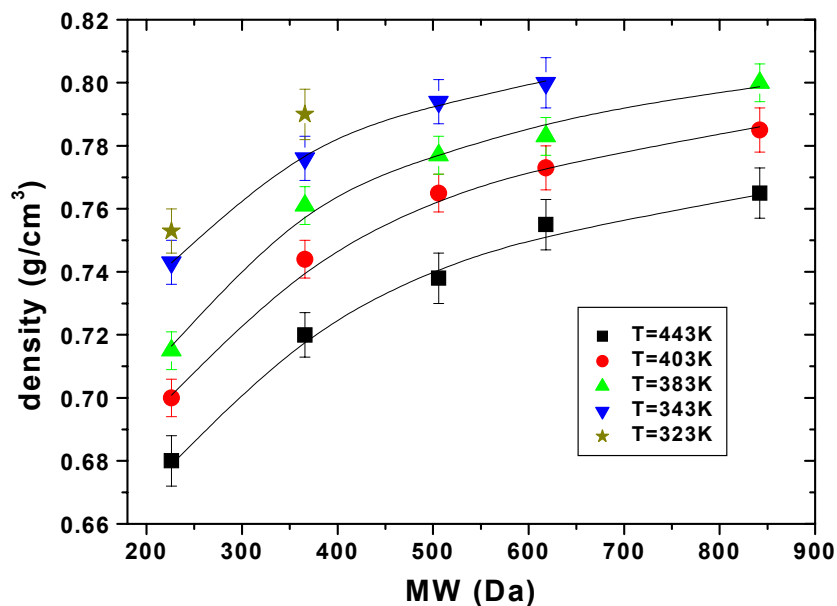
Figure 6. 2   Simulation predictions for the density ρ of the liquid *n*-alkanes as a function of their molecular weight *M*, at different temperatures.
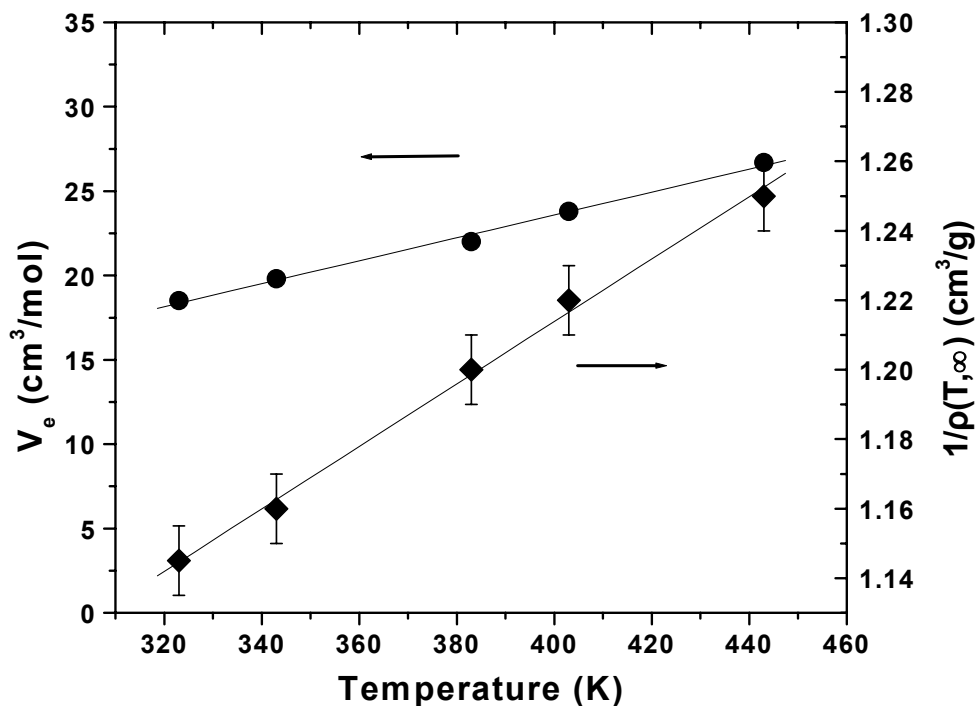
Figure 6. 3 Temperature dependence of the parameters V_e and $1/\rho(T,M)$ for the *n*-alkane melts. The results have been obtained by fitting the simulation predictions for the density ρ to Eq. (6.4).

6.4 Geometrical Analysis of Free Volume

The parameter V_e, the free volume of chain ends, plays a particular role in the theory of Bueche. According to his definition, "free volumes as discussed here refer only to packets of free volume that are too large to reach nearly instantaneous equilibrium at temperatures which are below T_g" [94]. Thus, to get more insight into V_e, we carried out a direct calculation of the free volume in the systems investigated here, following the geometric analysis proposed by Greenfield and Theodorou [97]. The method conducts first a tessellation of space into Delaunay tetrahedra, considering the center of every LJ unit as a point in space. A Delaunay tetrahedron corresponds to four neighboring atoms surrounding a small "hole" in the bulk polymer. The size of the atoms is then increased to their corresponding van der Waals radii and a calculation of the empty space inside each Delaunay tetrahedron is carried out. The unoccupied volume corresponding to each atom is calculated by summing the unoccupied volumes of all tetrahedra in which the reference atom participates.
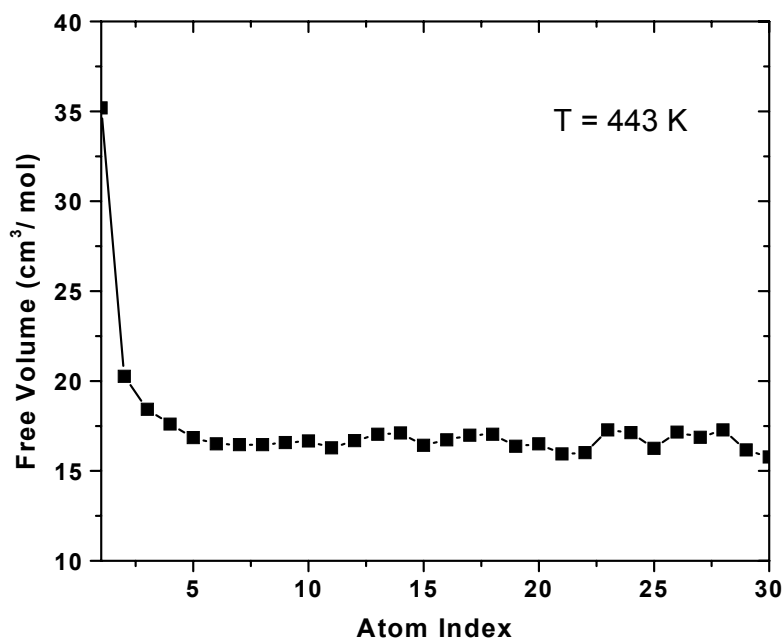
Figure 6. 4   Values of the geometrically calculated free volume V^g_{ends} around a chain atom as a function of the position number of the atom along the chain backbone. The results have been obtained by the method proposed by Greenfield and Theodorou, involving tessellation of the model systems in Delaunay tetrahedra.

The free volume around each atom in the *n*-alkane systems studied in the present work, as a function of its position along the chain, as calculated by applying the Greenfield-Theodorou approach for the C_{60} melt at $T = 443K$, is shown in Fig. 6.4. Clearly, the distribution of free volume along the chain is symmetric around the chain midpoint. It is also seen that the free volume around chain ends is significantly higher than the free volume around inner atoms along the chain; this is a result of the non-connectivity of chain ends. Fig. 6.4 shows that, typically, nonuniformities in the distribution of free volume along the chain persist over only a region of 4 to 5 atoms from the two chain ends. Beyond this region, the distribution becomes uniform.

The unoccupied volume around chain ends, V^g_{ends} (the superscript *g* being used to denote free volumes calculated by the geometric analysis of Greenfield and Theodorou), varies significantly with temperature. This variation is shown in Fig. 6.5. The values reported in the Figure have been obtained after a thorough calculation over hundreds of different configurations accumulated during both the *NPT* MC and the *NVT* MD simulations and averaged over all *n*-alkane melts simulated. Also shown in the figure are the values of V_e derived from the experimental densities. It is seen that the two values follow the same behavior with *T*. However, the calculated values are systematically higher than the ones extracted experimentally. This should have been expected given that V_e refers not to the entire unoccupied volume around chain ends but to packets of free volume greater than a "critical" value. If it is assumed that this "critical" value is the unoccupied free volume around the interior atoms in the chain V^g_{inner}, then one can define a geometric chain-end free volume, V^g_e, through the relation

$$V^g_e = \sum_{i=1}^{k} \left(V^g_i - V^g_{inner} \right) \tag{6.8}$$

where *k* is the number of atoms for which V^g is higher than V^g_{inner} (typically k=4-5 as shown in Fig. 6.4). How this changes with *T* and how it compares to the values of free volume extracted indirectly from the experimental densities is shown in Fig 6.5. by the triangles. Remarkably, the values of chain-end free volume V^g_e calculated geometrically through Eq. (6.8) are practically the same as those obtained from the fittings to the predicted densities and are also very close to those extracted experimentally.
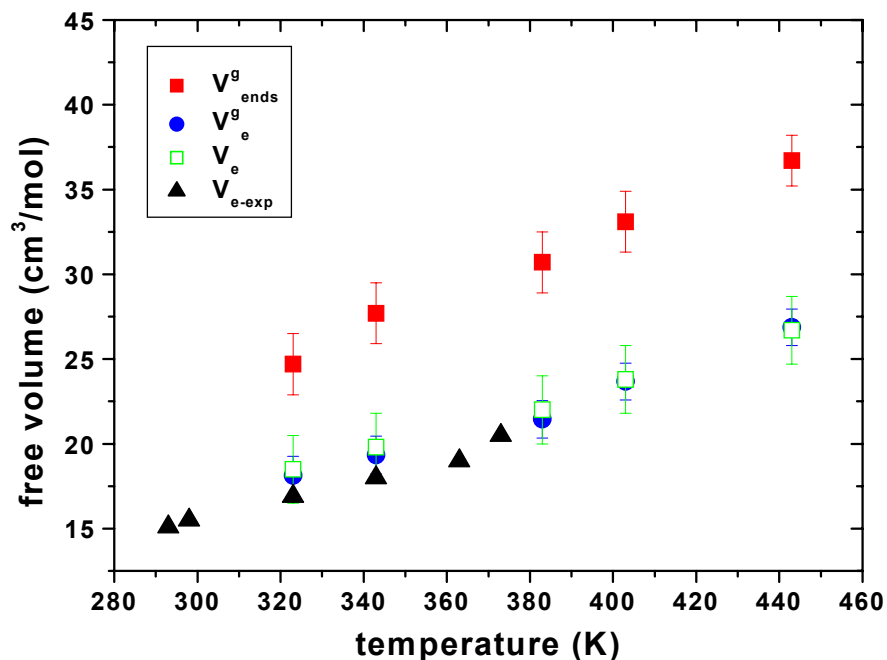
Figure 6. 5   Values of the free volume V^g_{ends} calculated geometrically by the method of Greenfield and Theodorou around chain ends (filled squares). Also shown in the figure are the results for the geometrically chain-end free volume V^g_e over that of inner atoms along the chain (open squares), data for V_e (circles) and experimentally available data for V_e (filled triangles); the two last data have been obtained by fitting the experimental densities to the theoretical expression.

The definition of the chain-end free volume through Eq. (6.8) is consistent with the usual interpretation of V_e (see Eq. (6.4)) as the free volume around chain ends in excess of that generated near any segment in the chain. In general, in studies of the diffusion of a small penetrant molecule through a polymer matrix, one distinguishes between two types of free volume: the unoccupied free volume and the accessible free volume. The unoccupied free volume is the total free volume in the polymer. The accessible free volume is that part of the total (or unoccupied) free volume through which the penetrant molecule can diffuse, and is calculated based on the probe radius of the molecule. In the present study, the accessible free volume is calculated based on a probe radius equal to the size of adjacent molecular segments, which also controls intermolecular distance. Thus, Eq. (6.8) gives in essence the accessible free volume for the diffusion of a chain segment around the ends of the chain, in addition to that generated near any other segment along the chain.
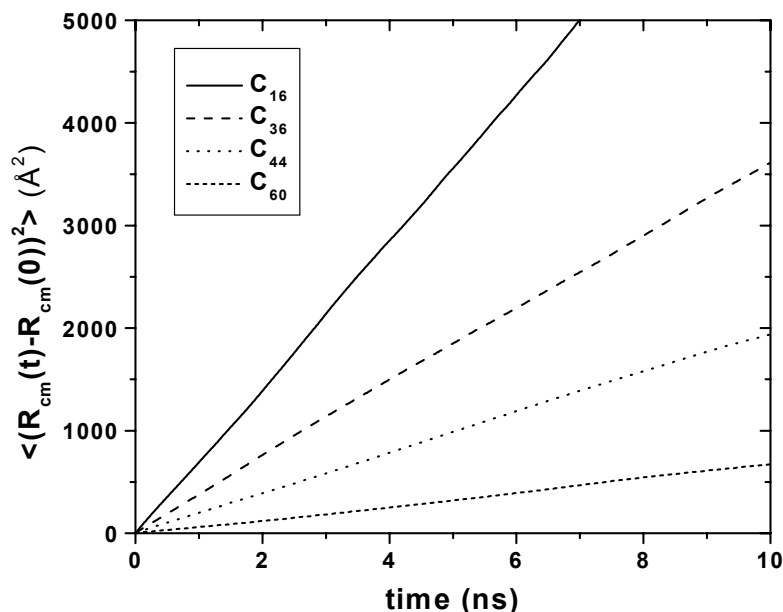
Figure 6. 6   Typical plots of the mean square displacement of the chain centers of mass as a function of time for the C_{16}, C_{36}, C_{44}, and C_{60} *n*-alkane systems, obtained from the present *NVT* MD simulations with the rRESPA multiple time step algorithm (T=443K).

6.5 Diffusion of liquid *n*-alkanes

As we have already seen in previous chapters the self-diffusion coefficients D of the melts simulated with the MD method are determined with the help of the Einstein relation. Typical plots of the mean-square displacement of the chain centers of mass as a function of time t, for most of the *n*-alkanes studied (C_{16}, C_{36}, C_{44} and C_{60}), are shown in Fig. 6.6. It is seen that, in the long-time regime, all curves reach an asymptotic, linear behavior, characteristic of Fickian diffusion, the slope of which can be used to determine D. Results for D for all melts simulated as a function of the molecular length N and of the system temperature T are shown in Fig. 6.7. Also shown in Fig. 6.7 are the experimentally measured D values from the NMR experiments [93] at T=403K. The agreement is extremely good for the majority of the alkanes studied.
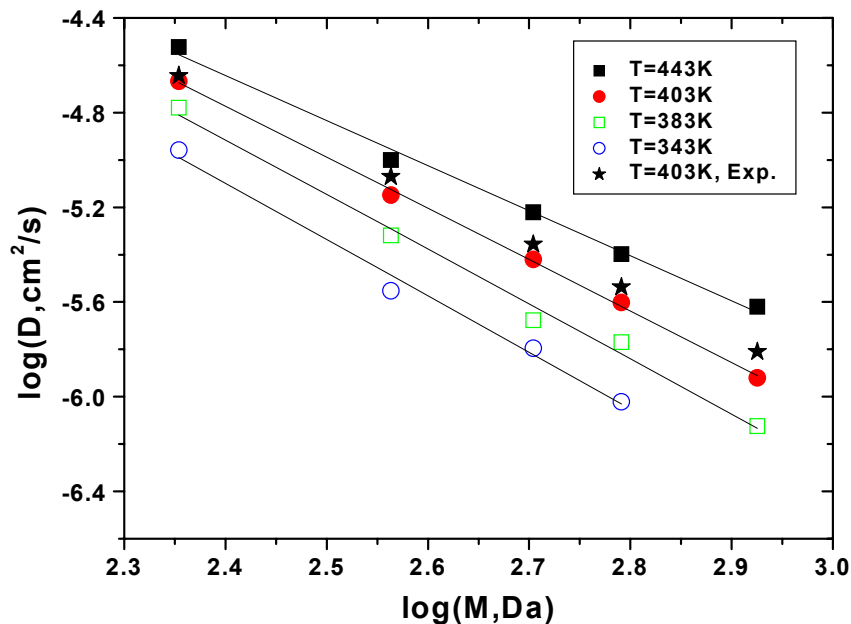
Figure 6. 7   Simulation predictions for the self-diffusion coefficient *D* of the *n*-alkane liquids, as a function of their molecular weight at different temperatures. A detailed comparison of the scaling exponent b with the experimental data of von Meerwall *et al*. [93] is given in Table 6.3.

Also interesting is that the best fits of the diffusivities to the power-law expression of Eq. (6.1) are almost perfect (solid lines in Fig. 6.7), with the exponent *b* quantifying the dependence of *D* on the molecular weight *M* of the alkanes varying smoothly in the temperature range studied ($b = -2.4$ at 343 K, while $b = -1.9$ at 443 K), as shown in Table 6.3.

Table 6.3: Simulation results for the value of the exponent *b* quantifying the dependence of the self-diffusion coefficient *D* on molecular weight *M*, obtained by fitting the MD simulation predictions to the power law of Eq. 1 for the *n*-alkane melts. Experimentally measured *b* values are also shown.

T (K)	b(T)	
	Simulation predictions	**Experimental values**
343	-2.4	-2.35
383	-2.26	-2.18
403	-2.1	-2.04

443	-1.9	-1.88

From Arrhenius plots of $\log D$ vs $1/T$ we can extract the thermal activation energy of the melts studied and compare them directly to the values measured experimentally. Such plots are shown in Fig. 6.8. From the slope of the plots we can calculate the apparent activation energies E_a^{app} for self-diffusion in the n-alkane melts through the equation:

$$E_a{}^{app} = -\frac{R}{0.434}\frac{\partial(\log D)}{\partial(1/T)} \tag{6.9}$$
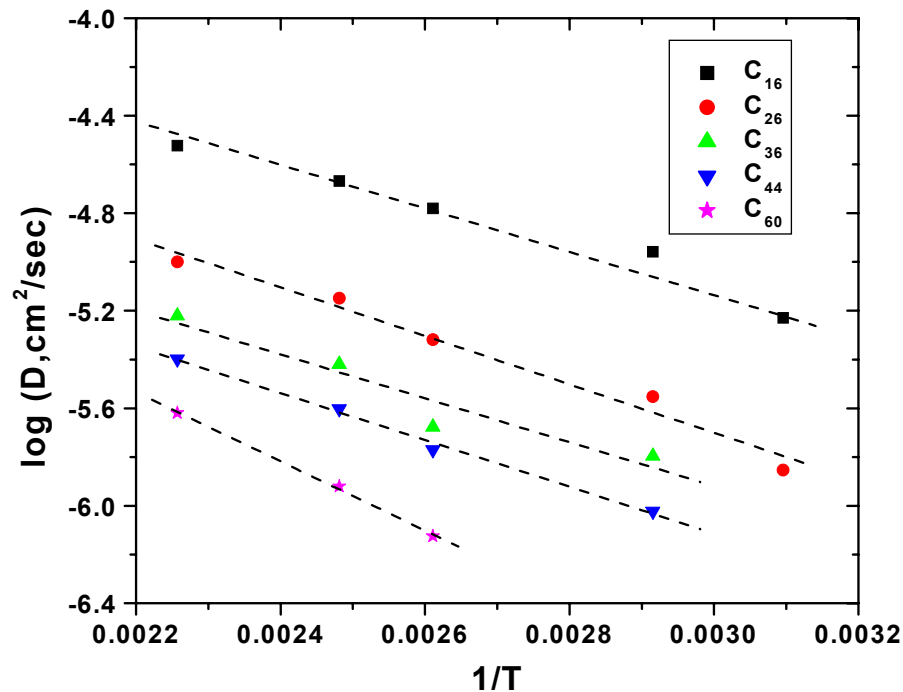
**Figure 6. 8** Simulation predictions for the self-diffusion coefficient $\log D$ of the *n*-alkane liquids, as a function of the temperature for various molecular weights.

Results for the *M* dependence of E_a^{app} are shown in Fig. 6.9, together with the experimental data. It is seen that E_a^{app} rises from 4.3 kcal/mol for the C_{16} alkane to 6.0 kcal/mol for the C_{60} alkane; this agrees remarkably well with the measured values. Furthermore, by using the results for the density-based free volume of chain ends $V_e(T)$ and the density simulation data, it is possible to fit Eq. (6.2) by substituting $f(T,M)$ and

$\rho(T,M)$ from Eqs. (6.3, 6.4) to the diffusivity simulation data. The fits involve two adjustable parameters: the fractional free volume $f(T,\infty)$ and the quantity $A'\left(= A\exp\left(-E_a / RT\right)\right)$, both of which depend on temperature. It was found that

$$f\left(T,\infty\right) = (0.085 + 0.00065T(^0C)) \pm 0.01 \tag{6.10}$$

while, experimentally, $f\left(T,\infty\right) = 0.1 + 0.0007T(^0C)$ [93]. By analyzing the results for the parameter A', using an Arrhenius interpretation similar to the one described above for the apparent activation energy E_a^{app}, a thermodynamic activation energy E_α for segmental jumps can be obtained averaged over all molecular weights. It was found that:

$$\left\langle E_\alpha \right\rangle_M = 0.55 \pm 0.30 \text{ kcal/mol}$$

in reasonable agreement with the experimental value $\left\langle E_\alpha \right\rangle_M = 0.80 \pm 0.25\,\text{kcal/mol}$.
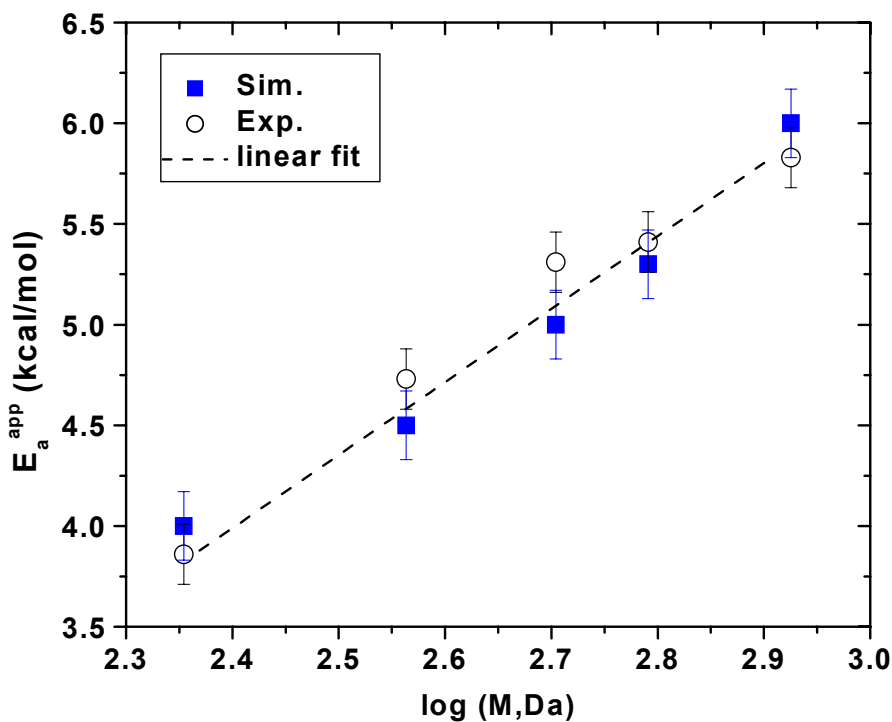
Figure 6. 9   Results for the apparent thermal activation energy E_a^{app} of self-diffusion of the *n*-alkane liquids as a function of their molecular weight obtained from an Arrhenius plot through the diffusivity data at various temperatures (squares). Also shown in the figure are the experimental data of von Meerwall *et al.* [93] (circles).

6.6 Conclusions

Results have been presented from detailed atomistic simulations for the density and self-diffusion of monodisperse *n*-alkane liquids. Initially, long MC simulations were performed in the *NPT* statistical ensemble in order to equilibrate the melts and calculate their density. The relaxed configurations at the end of the MC stage were used as input to the MD algorithm in order to calculate the transport properties of these melts through equilibrium MD simulations in the *NVT* statistical ensemble. The atomistic configurations accumulated during the *NPT* MC and the *NVT* MD simulations were also analyzed geometrically; this allowed us to calculate the accessible volume (free volume) around each atom in the system, particularly around chain ends. The geometric analysis was carried out by employing the method of Greenfield-Theodorou [97], through the construction of Delaunay tetrahedra. Linear, monodisperse *n*-alkane systems of length ranging from C_{16} to C_{60} were thus investigated at temperatures ranging from 323 to 443 K.

Results about the density of the *n*-alkane melts were found to differ at most by less than 2% from the measured values. By fitting the density-versus-molecular weight *M* data to a hyperbolic function, we were able to estimate the contribution V_e of chain free ends to the free volume of the system, as a function of the temperature *T*. This was compared to independent data obtained from the tessellation of space in Delaunay tetrahedra. The two sets of data were seen to be consistent with each other and with available experimental data only when the free volume V^g around each chain end obtained directly from the geometric analysis was reduced by the corresponding free volume value around an inner atom along the chain, to define a geometrically calculated chain-end free volume, V^g_e.

The values of V_e obtained from the simulated *M*-dependence of the density and from the geometric free volume analysis for the *n*-alkanes were found to be in excellent agreement with recently obtained experimental results [93].

By applying the Einstein relation, the self-diffusion coefficient of the *n*-alkane melts was further calculated as a function of chain length and temperature. Predicted values for *D* were found to be in excellent agreement with the recent experimental data of von Meerwall *et al.* [93], for all systems simulated. *D* was seen to obey a power law of the form $D \sim M^b$, the exponent *b* varying smoothly with temperature from −2.4 at 323 K to −1.9 at 443 K for *n*-alkanes. By further mapping the simulation results onto the

combined Bueche-von Meerwall theory for the self-diffusion of short alkanes, expressions were obtained for the fractional free volume $f(T,\infty)$ and the apparent activation energy E_α^{app} as a function of temperature and molecular weight, respectively.

The work presented in this chapter focused on the study of density and of the self-diffusion of short *n*-alkane liquids and its connection with the free volume available to chain ends or the free volume available to chain ends relative to chain inner atoms. In the following chapter a detailed investigation of the structure and the dynamics of binary blends of *n*-alkane liquids is presented. The results will be directly compared with two variations of free volume theory: the free volume theory of Vrentas and Duda developed to describe the diffusion of a penetrant into a penetrant-polymer system and a variation of the chain-end free volume theory, described in this chapter, for the study of diffusion of binary blends. The results will also be compared against available experimental data.

CHAPTER 7

DIFFUSION OF BINARY LIQUID
N-ALKANE MIXTURES

In chapter 6 results were presented for the self-diffusion properties of short *n*-alkane liquids from atomistic MD simulations with model systems of molecular length up to C_{60}. These systems were found not to obey Rouse dynamics; in contrast they were found to conform better with the principles of a free volume theory where chain-end effects are explicitly considered in the analysis. In addition to the self-diffusion properties, the mutual diffusion properties of binary mixtures of such n-alkane melts are also of importance. The mobility of small molecules in macromolecular materials, for example, dictates the effectiveness of polymerization reactors operating under conditions of partial or full diffusion control, as well as the physical and chemical characteristics of the polymer produced. Molecular weight distribution and average molecular weight, on the other hand, are among the physical properties that are influenced by the diffusion-controlled termination step of free radical polymerization reactions. In addition, molecular transport affects the mixing of plasticizers with polymers, the removal of residual monomer or solvent from polymers through devolatilization processes and the formation of films, coatings and foams from polymer-solvent mixtures **Error! Reference source not found.**.

From the point of view of theoretical developments, the most successful theory for describing the molecular diffusion of penetrants in polymer-penetrant systems is the free volume theory proposed by Vrentas and Duda [103]. This theory is based in the assumption of Cohen and Turnbull [101] that molecular transport relies on the continuous redistribution of free volume elements within the liquid. The availability of free volume within the system controls the molecular transport. This model describes mass transfer in solutions consisting of long polymer chains mixed with small solvent molecules both above and below T_g. Through a careful estimation of the adjustable

parameters, the theory can be applied to a wide variety of systems of different concentrations, temperatures and molecular weights.

The basic principles of the free volume theory have been used extensively by many researchers in order to study the diffusion of oligomer probes or solvents in polymer matrixes, melts or solutions. Using nuclear magnetic resonance (NMR), Waggoner *et al*. [109], recently measured the self-diffusion coefficients of several solvents in different polymers, at polymer concentrations ranging from 0 to 50 wt % at 25^0C and reported very good agreement with the free-volume approach, mainly at higher polymer concentrations.

Building on the idea of free volume theory, Meerwall *et al*. [110],[111] extended the chain-end free volume theory described in section 6.1, to predict the diffusion of binary blends of *n*-alkane and PE melts. To test their theory, they employed the pulsed-gradient spin-echo (PGSE) NMR method to measure the self-diffusion coefficient D in a series of binary alkane-polymer blends, over the full concentration range of the *n*-alkanes, at various temperatures. The parameters needed in the theory to predict the diffusion coefficients have been obtained from their previous study of the monodisperse *n*-alkanes [95]. The combined theory was seen to reproduce the experimental data for the diffusion coefficients of both components in the binary blends at least semiquantitatively, for the whole range of concentrations of the solvent component.

Motivated by the above works, in this chapter, the simulation study presented in chapter 6 for pure *n*-alkane melts, is extended to binary liquid *n*-alkane blends. The main objective of this work is to calculate the self-diffusion properties of a smaller alkane (solute) dissolved in a longer molecular weight polymeric matrix and how these are affected by the concentration of the solute. A comparison with the predictions of the free volume theory proposed by Vrentas and Duda [103] and the combined chain end free volume theory proposed by Bueche [94] and von Meerwall [95] will also be presented.

This chapter is organized as follows: Section 7.2 presents the molecular model used in the present work, outlines the basic characteristics of the methodology and gives a complete account of the mixtures studied. The following two sections, 7.3 and 7.4, review the basic assumptions and the most important equations of the free volume theory proposed by Vrentas and Duda and the combined Rouse and chain-end free volume theory presented by Bueche and von Meerwall. Results from the MD simulations and a detailed comparison with the two theories and available experimental data are presented in sections 7.5 and 7.6. Finally, section 7.7 summarizes the major results of this work.

7.1. Molecular Model, Systems studied and Methodology

The molecular model used in the MD simulations of the binary blend of *n*-alkane liquids is the NERD model. This model found in the literature to reproduce very well the phase equilibria and the volumetric (density) properties of binary blends [112]. The parameters of the model is described Table 7.1.

Table 7.1: Atomistic molecular model used in the MD simulations of short *n*-alkanes (NERD model).

Type of interaction	Potential Function and Parameters
Nonbonded Interactions	$U_{LJ} = 4\varepsilon\left[\left(\dfrac{\sigma_{ij}}{\mathbf{r}_{ij}}\right)^{12} - \left(\dfrac{\sigma_{ij}}{\mathbf{r}_{ij}}\right)^{6}\right]$ $\sigma_{CH_2} = 3.93$ Å $\sigma_{CH_3} = 3.91$ Å $\varepsilon_{CH_2} = 0.091$ kcal/mol $\varepsilon_{CH_3} = 0.207$ kcal/mol
Bond Bending	$V_{bending}(\theta) = \dfrac{1}{2}K_\theta\left(\theta - \theta_0\right)^2$ $K_\theta = 124.1875$ kcal/mol rad^{-2}, $\theta_0 = 114^0$
Torsional Potential	$V_{torsional}(\phi) = c_0(1 + \cos\phi) + c_1(1 - \cos 2\varphi) + c_2(1 + \cos 3\phi)$ $\phi = 180^0$ for *trans* conformation $c_1 = 0.7054$, $c_2 = -0.1355$, $c_3 = 1.5724$ in kcal/mol

The equations of motion were integrated with a velocity Verlet method where the XI-RESPA algorithm has been incorporated.

In the following discussion, we will denote as 1 (2) the lighter (heavier) component of an alkane mixture. Four different liquid *n*-alkane mixtures were simulated at various values of the weight fraction w_1 of the lighter component. The systems are presented in Table 7.2

Table 7.2: Molecular length of the two components, N_1 and N_2, temperature, T, and weight fraction of lighter component w_1.

System	N_1	N_2	$T(K)$	w_1
1	5	78	474	0.025, 0.07, 0.163 and 0.32
2	10	78	458	0.025, 0.21, 0.25 and 0.44
3	12	60	403.5	0.0, 0.024, 0.14, 0.2, 0.3, 0.4, 0.5, 0.6, 0.7, 0.8 and 1.0
4	12	60	473.5	0.0, 0.024, 0.14, 0.2, 0.3, 0.4, 0.5, 0.6, 0.7, 0.8 and 1.0

For the two C_{78} systems (system 1 and 2) the polydispersity index of C_{78} component was $I = 1.08$. On the other hand for the two C_{12}-C_{60} systems the polydispersity index of C_{78} component was $I = 1.0$. The overall simulation time ranged from 5 to 20 ns, depending on the composition and size of the system studied.

The construction of initial configurations for the above systems is not trivial at all, and this may explain why MD studies of such systems have never appeared in the literature. The traditional simulation techniques for mixture simulations, initially developed for small molecules, fail when implemented for polymer mixtures because they invoke insertions or deletions of molecules; the efficiency of the success rate of these moves is very low when at least one of the components is hard to rearrange, as happens with dense polymers, and/or the the molecules inserted are long and complicated, as in the case of long oligomers.

Here we take advantage of a recently proposed novel MC simulation study [113] for the prediction of sorption equilibria of oligomers in polymer melts, which allows collecting well-equilibrated configurations of binary mixtures of an arbitrary composition. The method is based in the implementation of two novel, connectivity-altering moves, i.e. *scission* and *fusion*. Scission involves creation of an oligomer from the end of a polymer molecule; fusion, on the other hand, leads to formation of a new by joining a polymer and an oligomer end-to-end. The main advantage of the two moves lies in that they create oligomer molecules from the already existing polymer chains, thus, avoiding the conventional insertion and deletion moves.

The two new moves achieve extremely fast equilibration of the oligomer weight fraction for any length of the oligomer in the bulk of high-molecular weight polymers and allow predicting the solubility of long oligomers in a polymer matrix over a wide range of fugacities of the oligomers. In the present MD simulations, the volume was always kept constant at a value corresponding to the mean density obtained from the MC runs.

7.2. Free Volume Theory of Vrentas and Duda

The free-volume theory of transport [107],[109],[115],[116],[117],[118] provides a convenient and useful method for predicting and correlating solvent self-diffusion coefficients for polymer-solvent systems. The idea that molecular transport is regulated by free volume was first introduced by Cohen and Turnbull [101]. The diffusion process depends on the probabilities that a molecule will obtain sufficient energy to overcome attractive forces and that a fluctuation in the local density will produce a hole of sufficient size so that the diffusing molecule can jump. According to this, the solvent diffusion coefficient, D_1, in a binary mixture may be written as

$$D_1 = D_0 \exp(-\gamma \overline{V}_1^* / \overline{V}_{FH})$$ (7.1)

where D_0 is a constant pre-exponential factor, $\overline{V}_1^*$ is the critical molar free volume required for a jumping unit of component 1 (solvent), $\overline{V}_{FH}$ is the free volume per mole of all individual jumping units in the solution and γ is an overlap factor, which is introduced because the same free volume is available to more than one jumping units.

In the original Cohen and Turnbull representation, a jumping unit was envisioned as a single hard-sphere molecule undergoing diffusion. Vrentas and Duda generalized the theory of Cohen and Turnbull to describe motion in binary liquids by using the relationship

$$\overline{V}_{FH} = \frac{\hat{V}_{FH}}{w_1 M_{1j} + w_2 M_{2j}}$$ (7.2)

where $\hat{V}_{FH}$ is the specific hole free volume of a liquid with weight fraction w_i of species i and with jumping unit molecular weights M_{ij} ($i = 1$ or 2). Combining Eqs. (7.--) and (7.--) and introducing an activation energy, associated with the fact that a jumping unit must overcome the attractive forces with adjoining molecules prior to a diffusive step, the

solvent self-diffusion coefficient D_1 in a rubbery polymer-penetrant mixture can be determined using the following expressions [107]:

$$D_1 = D_0 \exp\left(-\frac{E}{RT}\right)\exp\left(-\frac{\gamma(w_1\hat{V}_1^* + w_2\xi\hat{V}_2^*)}{\hat{V}_{FH}}\right) \tag{7.3}$$

$$\frac{\hat{V}_{FH}}{\gamma} = w_1 \frac{K_{11}}{\gamma}(K_{21} - T_{g1} + T) + w_2 \frac{K_{12}}{\gamma}(K_{22} - T_{g2} + T) \tag{7.4}$$

In these equations, $\hat{V}_i^*$ is the specific hole free volume of component i required for a jump, T_{gi} is the glass transition temperature of component i, and ξ is the ratio of the critical molar volume of the solvent to that of the polymer jumping unit. In addition, E is the energy per mole that a molecule needs to overcome attractive forces which hold it to its neighbors, whereas K_{11} and K_{21} are free volume parameters for the solvent (lighter component) and K_{12} and K_{22} are free volume parameters for the polymer (heavier component).

The concentration dependence of E can be described approximately by considering two energies E_p and E_s, one for the polymer and another for the solvent. For solvent mass fractions roughly in the range of 0-0.9, E is essentially constant and equal to E_p. As the pure solvent limit is approached, the surroundings of a solvent molecule change and E approaches the value of E_s. In order to avoid unacceptable parameter interaction effects present in applying nonlinear regression analysis, it is necessary to replace the terms containing D_0 and E_s by an average value over the temperature interval:

$$\overline{D}_0 \approx D_0 \exp\left(-\frac{E_s}{RT}\right) \tag{7.5}$$

In this case Eq. (7.3) becomes:

$$D_1 = \overline{D}_0 \exp\left(-\frac{E^*}{RT}\right)\exp\left(-\frac{\gamma(\omega_1\hat{V}_1^* + \omega_2\xi\hat{V}_2^*)}{\hat{V}_{FH}}\right) \tag{7.6}$$

where

$$E^* = E_p - E_s \tag{7.7}$$

To evaluate the solvent self-diffusion coefficient D_1, we should first calculate all the parameters appearing Eqs. (7.4)-(7.8). To this end we follow a semipredictive method proposed by Vrentas and Vrentas [115],which consists of the following steps:

a. The specific hole free volumes $\hat{V}_1^*$ and $\hat{V}_2^*$ are equated to equilibrium liquid volumes at 0 K, which can be determined using methods summarized by Haward [119].

b. The parameters K_{12}/γ and K_{22}-T_{g2} can be determined using data for WLF constants and the glass transition temperature T_g through the following expressions:

$$\frac{K_{12}}{\gamma} = \frac{\hat{V}_2^*}{2.303(C_1^g)_2(C_2^g)_2} \tag{7.8}$$

$$K_{22} - T_{g2} = (C_2^g)_2 - T_{g2} \tag{7.9}$$

where $(C_1^g)_2$ and $(C_2^g)_2$ are the WLF constants for the polymer.

c. The quantities $\bar{D}_0$, K_{11}/γ, K_{21}-T_{g2} can be determined from viscosity-temperature and density-temperature data for the solvent, by performing a nonlinear regression analysis on the expression for the temperature dependence of the viscosity η_1 of the pure solvent:

$$\ln \eta_1 = \ln \left(\frac{0.124 \times 10^{-16} \tilde{V}_c^{2/3} RT}{M_1 \hat{V}_1^0} \right) - \ln \bar{D}_0 + \frac{\hat{V}_1^*}{\left(K_{11}/\gamma\right)\left(K_{21} + T - T_{g1}\right)} \tag{7.10}$$

In this equation, M_1 is the molecular weight of the solvent, $\tilde{V}_c$ is the molar volume of the solvent at its critical temperature, and $\hat{V}_1^0$ is the specific volume of the pure solvent at T.

d. Finally E^* and ξ are calculated through solvent diffusion data at w_1=0, where Eq. (7.7) becomes:

$$\ln D_1\left(\omega_1 = 0\right) = \ln \bar{D}_0 - \frac{E^*}{RT} - \frac{\gamma\xi\hat{V}_2^*}{K_{12}\left(K_{22} + T - T_{g2}\right)}, \tag{7.11}$$

which can be rearranged to yield the following expression:

$$Y = E^* + \xi X, \quad Y = -RT\left(\ln D_1 - \ln \bar{D}_0\right), \quad X = \frac{RT\left(\dfrac{\gamma\hat{V}_2^*}{K_{12}}\right)}{T + K_{22} - T_{g2}}. \tag{7.12}$$

With as few as two diffusivity data points, it is possible to construct Y versus X plots using Eqs. (7.11) and (7.12). The slope and the intercept of this straight line yield

E^* and ξ respectively. In our work these two diffusivity data points needed are obtained directly from the simulation for a weight fraction of the solvent component $w_1 \cong 0$.

7.3. Chain-end free volume theory proposed by Bueche and von Meerwall.

The chain end free volume theory, first proposed by Bueche [94], describes how the free-volume effects due to molecular chain ends modify the classical Rouse behavior by enhancing D at low M. A combined theory of Rouse diffusant and chain-end free-volume host effects (BM theory) for monodisperse polymer liquids was described in details in the previous chapter. Here we present the extension of the BM theory proposed recently by von Meerwall *et al.* [110] to describe the self-diffusion in binary liquid polymer blends. According to this the two self-diffusion coefficients D_i ($i = 1$ or 2) in binary blends of monodisperse polymer liquids are a function of the temperature T, of the molecular weights M_1 and M_2 of the two components, of the volume fraction of the lighter component, υ_1, and of its fractional free volume, f, as follows:

$$D_i(T, M_1, M_2, \upsilon_1) = A \exp(-E_\alpha / RT) M_i^{-1} \exp[-B_d / f(T, M_1, M_2, \upsilon_1)] \qquad (7.13)$$

There are obvious the similarities between this expression and the corresponding one used for the prediction of the self-diffusion coefficient of the monodisperse polymer liquids, Eq. (6.2). The prefactor A is a constant characterizing the particular polymer, but which otherwise independent of chain length and/or temperature. As analyzed in the previous chapter, according to this equation, the diffusion coefficient is the product of three terms. The first exponential term describes thermal activation effects with E_α being the thermodynamic activation energy required for the chain end to perform jumps between accessible neighboring sites. The second term (M^1) recognizes the Rouse dependence of the diffusivity on the diffusant molecular length or mass. And the third term represents the contribution to the self-diffusion coefficient due to the excess free volume of chain ends. B_d is the volume overlap term; it is a measure of the open volume required for motion of a penetrant molecule or segment thereof relative to the volume of a polymer segment involved in a unit jump process. It is considered to be not far from unity but may depend on the size, shape, and flexibility of the penetrant. Finally f (T, M_1, M_2, υ_1) plays the role of a fractional free volume, which is highly dependent on T, M_1, M_2 and υ_1, the latter being the volume fraction of the lighter component. The value of

υ_1 is easily related to the measured weight fraction w_1, given the known component densities ρ_i which are available in literature, through the equation:

$$\upsilon_1 = \frac{w_1}{w_1 + (1 - w_1)\dfrac{\rho_1}{\rho_2}} \qquad (7.14)$$

In the absence of entanglements, the familiar Rouse M^1 scaling should apply to each component separately, and thus the two diffusion coefficients in binary *n*-alkane blends should differ across the whole concentration range by a constant factor, the inverse ratio of their molecular weights. The reason for this expected "ideal" solution behavior is the universally postulated equal availability of all accessible (hole) free volume to both diffusing components or their motional segments, combined with the absence of any significant volume change of mixing. With these assumptions and including the dependence of the free volume fraction *f* on υ_1, as proposed by Bueche, we obtain:

$$f(T, M_1, M_2, \upsilon_1) = f_\infty(T) + 2V_E(T)\rho[T, M^*(\upsilon_1)] / M^*(\upsilon_1) \qquad (7.15)$$

This equation describes that the dependence of the free volume fraction *f* should be entirely confined to the chain-end term driven by V_E, the free volume of one mole of chain ends. $f_\infty(T)$ denotes the fractional free volume of the melt at infinite molecular weight, and $1/M^*$ represents a volume-weighted average of the inverse molecular weights of the two components:

$$1/M^*(\upsilon_1) = \upsilon_1 / M_1 + (1 - \upsilon_1) / M_2 \qquad (7.16)$$

The density ρ can be calculated directly from the specific volume through the relation:

$$\rho[T, M_1, M_2, \upsilon_1] = [1/\rho_\infty(T) + 2V_E(T)/M^*(\upsilon_1)] \qquad (7.17)$$

where $\rho_\infty(T)$ is the melt density at infinite molecular weight.

Eqs. (7.14)-(7.18) are expected to apply in binary unentangled *n*-alkane mixtures. All the parameters needed, i.e. $1/\rho_\infty(T)$, $V_E(T)$, $f_\infty(T)$, A and E_α exhibit linear temperature-dependencies to a good approximation. As it was also seen in the previous chapter von Meerwall *et al.* extracted the above parameters from fittings to density and self-diffusion of a series of liquid *n*-alkanes, from C_8 to C_{60}, and found [93]:

$$1/\rho_\infty(T) = [1.142 + 0.00076T(^0C) \pm 0.005] \quad cm^3/g \qquad (7.18)$$

$$V_E(T) = [13.93 + 0.060T(^0C) \pm 0.3] \quad cm^3/mol \qquad (7.19)$$

$$f_\infty(T) = [0.100 + 0.0007T(^0C) \pm 0.002] \qquad (7.20)$$

$$< E_\alpha >= [0.81 \pm 0.25] \quad kcal\,/\,mol \tag{7.21}$$

$$A = [0.306 \pm 0.009] \quad cm^2\,mol\,/\,g\,sec \tag{7.22}$$

With these values of the parameters one can predict the diffusion coefficient D_i of component *i* for a binary blend of *n*-alkane mixtures over the entire range of concentrations w_i.

7.4. Structure of Binary Blends

Results will be presented concerning the structure and self-diffusion coefficient of liquid binary blends for the four systems simulated as a function of the concentration (weight fraction) of the lighter (solvent) component. The results will be analyzed and compared with the two free volume theories described in the previous section: the detailed molecular free volume theory proposed by Vrentas and Duda [107] and the theory proposed by Bueche and von Meerwall [110] that combines Rouse diffusion and chain-end free volume effects. For the C_{12}-C_{60} systems, the results are also directly compared to the recently published experimental data of von Meerwall *et al.* [110].

At first we check the structural properties of the simulated blends and their dependence of these properties on the concentration of the solvent component, w_1.

Table 7.1 shows the mean square end-to-end distance $<R^2>$ and the mean square radius of gyration $<R^2_g>$ of the C_{60} and C_{12} alkanes respectively, in the C_{12}-C_{60} system at T=403.5K for various values of the weight fraction of C_{12}, w_1. It is clear that any effect of w_1 on the dimensions of both C_{12} and C_{60} is below the detection threshold of the simulation. Similarly, no effect of the concentration w_1 can be found in the dihedral angle distribution of both C_{12} and C_{60} when C_{12} is dissolved in C_{60}. The same behavior was sheen in the other systems simulated and is in agreement with the detailed MC studies of these binary systems [113].

Table 7.1. Predicted values of the chain mean square end-to-end distance $<R^2>$ and of the radius of gyration $<R^2_g>$ for the two components of the C_{12}-C_{60} blend at T=403K, for various weight fractions of C_{12}.

	C_{12}		C_{60}	
w_1	$<R^2>$ (Å^2)	$<R^2_g>$(Å^2)	$<R^2>$(Å^2)	$<R^2_g>$(Å^2)

0.2	135 ± 20	16 ± 1	1480 ± 100	200 ± 50
0.4	136 ± 15	15.5 ± 1	1450 ± 100	190 ± 40
0.7	136 ± 10	15.5 ± 0.5	1460 ± 100	190 ± 35

Direct information about some structural features of the simulated systems can be obtained by inspecting the intermolecular mer-mer pair distribution functions $g(r)$. Figures 7.1(a)-7.1(c) show the intermolecular pair distribution functions for the pairs C_{60}-C_{60}, C_{60}-C_{12} and C_{12}-C_{12} in C_{12}-C_{60} mixtures of various compositions at T=403K. The intermolecular $g(r)$ for C_{60}-C_{12} seems to exhibit higher values compared to the C_{60}-C_{60} distribution function, especially as regards the first peak. This phenomenon, also seen in the MC study of a C_5-C_{78} system [113] leads to the conclusion that polymer atoms (or atoms of the heavier component) prefer to be surrounded by atoms of the higher component rather than by atoms of other polymer chains, proving that C_{12} is a good solvent for C_{60}. As the weight fraction of C_{12} increases, the intermolecular pair distribution function for C_{60}-C_{60} pairs falls, indicating that polymer atoms on different chains are more separated from one another, as they are surrounded by more and more oligomer molecules.

(a)

(b)

(c)
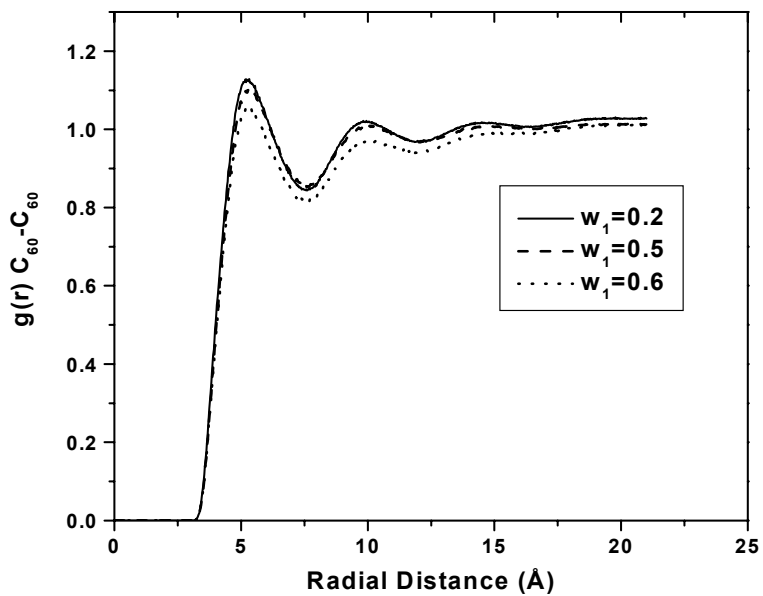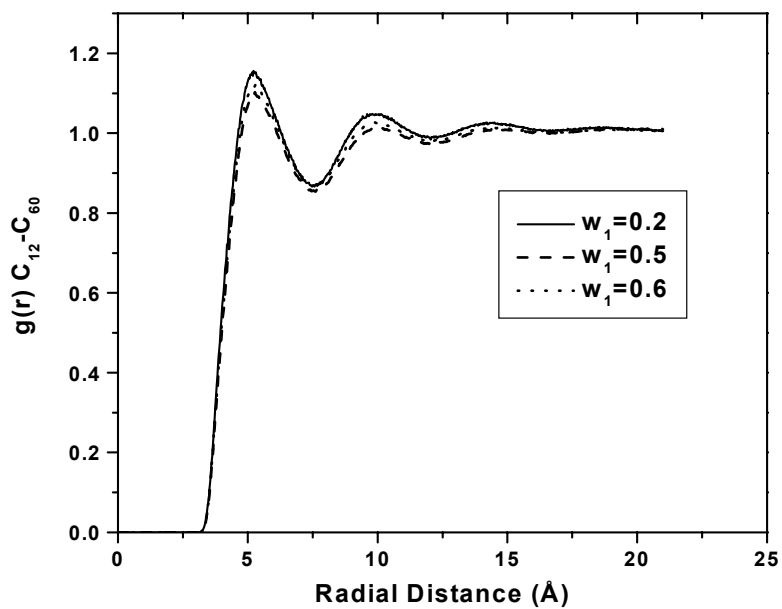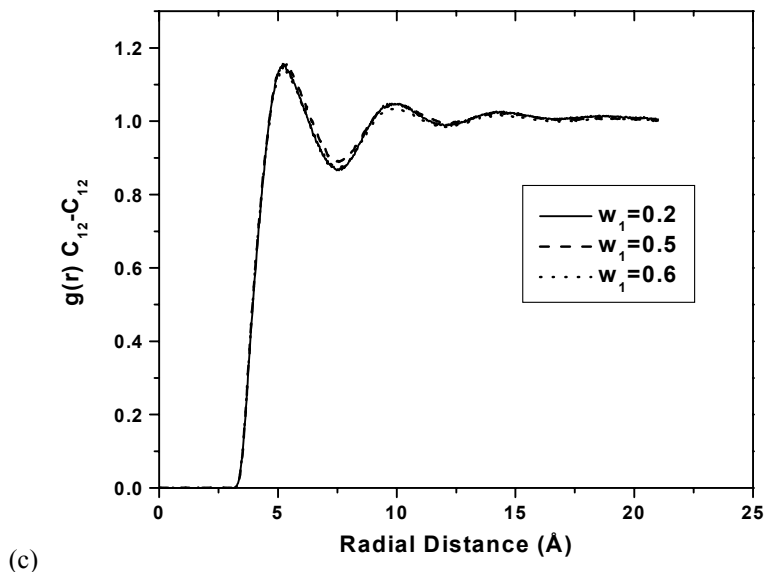
Figure 7.1   Intermolecular mer-mer pair distribution function at different C_{12} weight fractions for (a) C_{60}-C_{60}, (b) C_{60}-C_{12} and (c) C_{12}-C_{12} pairs, in a C_{12}-C_{60} blend, at *T*=403.5K.

Also of interest are the higher values of *g*(*r*) for C_{12}-C_{12} pairs compared to C_{60}-C_{12} pairs, which betray a tendency of C_{12} to cluster together, mainly at lower concentrations of C_{12}. This is expected from the form of the Lennard-Jones potential used in our MD simulations, i.e., the NERD model. In this model, the interaction parameter ε is higher for the CH_3 atoms (end segments) than for the CH_2 atoms (middle segments); this end effect is stronger for C_{12} than for C_{60} where end segments are scarce.

The intermolecular pair distribution functions for the other binary systems, C_5-C_{78} at *T*=474K, C_{10}-C_{78} at *T*=458K and C_{12}-C_{60} at *T*=473.5K, display the same behavior as described above. In particular, the end effect phenomenon is stronger in the C_{10}-C_{10} pairs and even stronger in the C_5-C_5 pairs, where chain ends play a more prominent role.

An even more detailed report on the structural and conformational properties of the binary *n*-alkane - polymer systems can be found in a MC study of the solubility of long alkanes in linear polyethylene [113]

7.5. **Terminal Relaxation – Diffusion of Binary Blends**

Fig. 7.2 shows the orientational autocorrelation function of the end-to-end vector $\langle \mathbf{R}(t) \bullet \mathbf{R}(0) \rangle / \langle R^2 \rangle$ for the C_{12} chains in the C_{12}-C_{60} binary system at T=403.5K as a

function of the weight fraction w_1 of C_{12}. The rate at which $\langle \mathbf{R}(t) \bullet \mathbf{R}(0) \rangle / \langle R^2 \rangle$ approaches the zero value is a measure of how fast the chain "forgets" its initial configuration. Obviously, as w_1 increases, the autocorrelation function of the end-to-end vector $\langle \mathbf{R}(t) \bullet \mathbf{R}(0) \rangle / \langle R^2 \rangle$ of C_{12} decays faster, i.e. the overall relaxation time of C_{12} decreases. This is expected because as C_{12} is dissolved in the heavier C_{60} component, the total free volume within the system increases due to additional free volume that the solvent (lighter component) contributes to the mixture. Consequently, the relaxation time of each component in the binary system decreases.
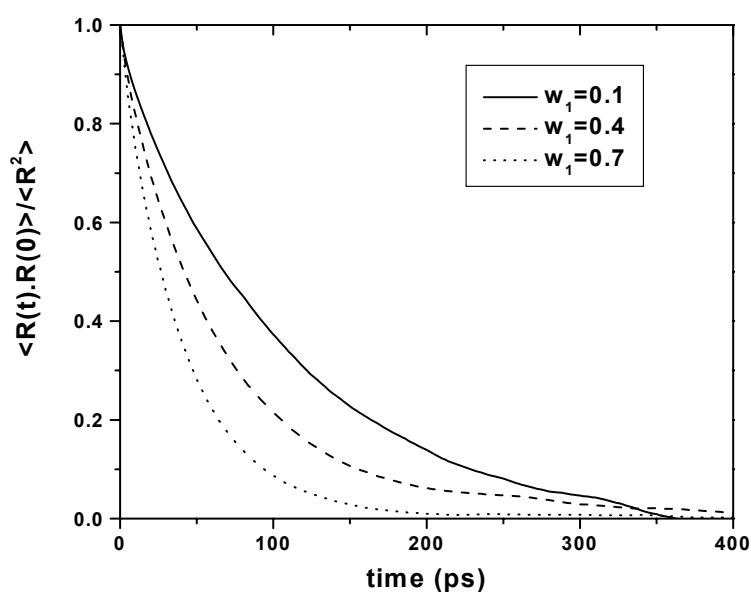
Figure 7.2   Autocorrelation function of the end-to-end distance of C_{12} in the binary C_{12}-C_{60} blend at T=403.5K as a function of the weight fraction of C_{12}.

Fig. 7.3 shows a typical plot of the mean square displacement of the center of mass for the C_{12} and C_{60} components in the C_{12}-C_{60} binary system at T=403.5K. From the long-time, linear part of the two curves one can calculate the diffusion coefficients for C_{12} and C_{60} liquids.
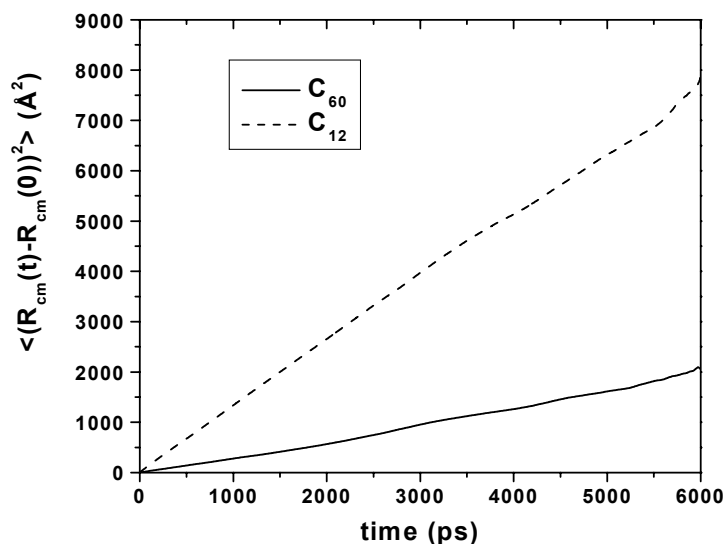
Figure 7.3   Mean square displacement of the center of mass of C_{12} and C_{60} molecules in a C_{12}-C_{60} blend at T=473.5

Results for the diffusion coefficient of the lighter component (solvent) D_1, for all binary *n*-alkane blends simulated, as a function of the alkane weight fraction w_1, are shown in Figures 7.4-7.7. Also presented in the same figures are the predictions from the free volume theory of Vrentas and Duda and from the combined theory of Bueche and von Meerwall.

To calculate D_1 according to the molecular free volume theory of Vrentas and Duda, we followed the scheme described in steps (a)-(d) of section 7.3. The viscosity data of the solvent for every system were obtained from the literature [120],[121]. For C_{12}, viscosity data as a function of temperature are shown in Fig. 7.8 together with the fits of Eq. (7.11). The two diffusivity data points for the solvent at $w_1 \cong 0$, needed in step (d), were calculated directly from MD simulations with model binary systems containing just a few (up to 3) solvent molecules ($w_1 \cong 0.01$) at two different temperatures for every system, and are shown in Table 7.2. Table 7.3 shows in detail the values of all the parameters needed for the evaluation of D_1 for every system simulated.

Table 7.2. MD estimates of alkane self-diffusivities at $w_1 \rightarrow 0$ used for the evaluation of the E^* and ξ parameters in the Vrentas-Duda theory.

	C_5-C_{78}	C_{10}-C_{78}	C_{12}-C_{60}
T_1 (K)	450	420	403.5
D_1 (T_1) (10^{-5} cm^2/mol)	2.1	0.9	1.517

	C$_5$-C$_{78}$	C$_{10}$-C$_{78}$	C$_{12}$-C$_{60}$
T$_2$ (K)	474	458	473.5
D$_1$ (T$_2$) (10^{-5} cm^2/mol)	2.8	2.2	2.28

With the values of the parameters listed in Table 7.3 and using Eqs. (7.5)-(7/8), one can predict the solvent diffusion coefficient D_1 for every system studied, as a function of concentration w_1. Predicted values are shown in Figures 7.4-7.7 as dashed lines. The corresponding D_1 predicted values from the chain end free volume theory of Bueche and von Meerwall are shown in the same Figures 4-7 as solid lines. The values are calculated from Eqs. (7.14)-(7.18), with the parameters obtained from fitting the density and diffusion in *n*-alkane melts, Eqs. (7.19)-(7.23).

For all binary systems the self-diffusion coefficient D_i of component *i* increases as the concentration w_1 of the solvent molecules increases. This can be explained in the same way as the decrease in the relaxation time of each component discussion in conjunction with Fig. 7.2, i.e. the total free volume within the system increases due to the additional free volume contributed by the solvent component to the mixture in which it is dissolved.

Table 7.3. Values of the parameters used in the calculation of the self-diffusion coefficient of the solvent in binary *n*-alkane mixtures according to the free volume theory of Vrentas and Duda.

	C$_5$-C$_{78}$ 474 K	C$_{10}$-C$_{78}$ 458 K	C$_{12}$-C$_{60}$ 403.5 K	C$_{12}$-C$_{60}$ 473.5 K
$\hat{V}_1^*$,(cm^3/gr)	1.143	1.041	1.078	1.078
$\hat{V}_2^*$ (cm^3/gr)	0.956	0.956	0.959	0.959
K_{11}/γ ,(10^{-3}cm^3/gr K)	3.0	2.0	1.02	1.02
K_{21}-T_{g1} , (K)	-80	-180	-80	-80
K_{12}/γ , 10^{-4}cm^3/gr K	4.61	4.61	4.61	4.61
K_{22}-T_{g2} , (K)	-140.9	-140.9	-140.9	-140.9
$\overline{D}_0$, (10^{-4}cm^2/sec)	1.9	2.0	9.45	8.85
$\overline{D}_0$, (10^{-4}cm^2/sec) (fit)	1.5	1.85	9.86	8.27
E^* , (kJ/mol)	-4.	-3.	0.8	0.1

ξ	0.45	0.53	0.55	0.5

Figure 7.4 shows how the diffusion coefficient D_1 of C_5 compares with the predictions of the two theories described above for the binary system C_5-C_{78} at T=474K over a range of weight fractions w_1 of C_5. The free volume theory predicts a good qualitative description of the simulation results for D_1. Also shown in the figure are results from fitting the free volume theory, Eq. (7.7), to the simulation results, using only one parameter, the preexponential factor $\bar{D}_0$. The value of $\bar{D}_0$ that gives the best fit is also shown in Table 7.3. It is obvious that, with a small correction of $\bar{D}_0$ (from $1.9x10^{-4}$ to $1.5x10^{-4}$ cm^2/sec), excellent quantitative agreement can be established with the simulation results, for the whole range of concentrations studied here. On the other hand, the predictions of the Bueche-von Meerwall theory seem to deviate from the MD simulation results, particularly at the higher C_5 concentrations. One reason for this is that both components of this system, C_5 and C_{78}, are outside the range of lengths of the *n*-alkanes (between C_{10} and C_{60}) from which the values of the parameters of the theory, Eqs. (7.19)-(7.23), were obtained.

Figure 7.5 shows results for the diffusion coefficient of C_{10}, in the binary system C_{10}-C_{78} at T=458K and various values of the weight fraction w_1 of C_{10}. Here again, the free volume theory describes the MD results very well. The agreement is exceptionally good, especially for the smaller weight fractions. As w_1 increases, the predictions of the free volume theory diverge slightly from the results of the MD simulations. Again, with a very small adjustment of $\bar{D}_0$ in the expression for D_1, Eq. 10 (from $2.0x10^{-4}$ to $1.85x10^{-4}$ cm^2/sec) the agreement between the two sets of data becomes excellent. For this system, the values predicted from the Bueche-von Meerwall theory (solid line) also seem to be in a better agreement with the simulation predictions than for the C_5-C_{78} system, especially at smaller solvent weight fractions w_1.
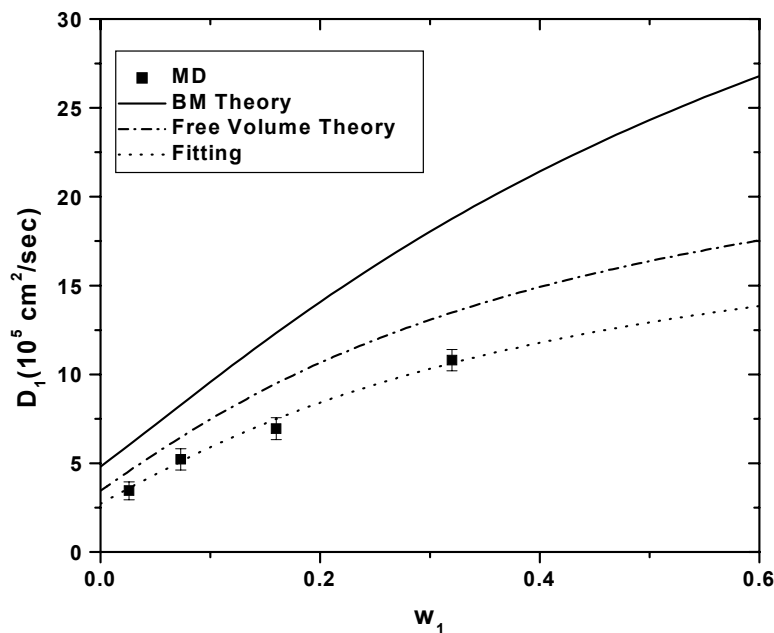
Figure 7.4   Self-diffusion coefficient of the C_5 alkane in a C_5-C_{78} system at T=474K and comparison with the predictions of: (a) the Bueche- von Meerwall theory (solid line) and (b) the free volume theory of Vrentas - Duda (dashed line). The dotted line presents a fit of the free volume theory to the simulation data where only the pre-exponential factor has been used as an adjustable parameter.
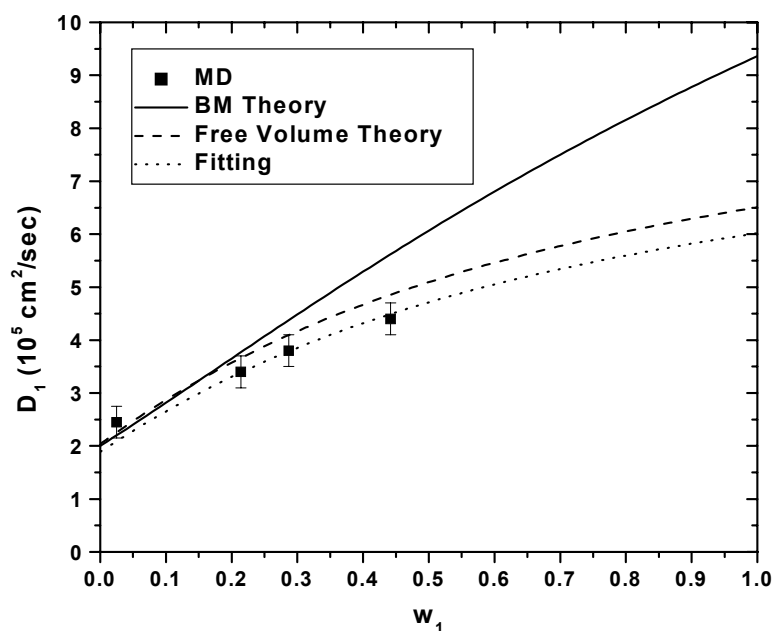
Figure 7.5   Same as in Fig. 7.4 but for the C_{10} alkane in a C_{10}-C_{78} blend at *T*=458K.
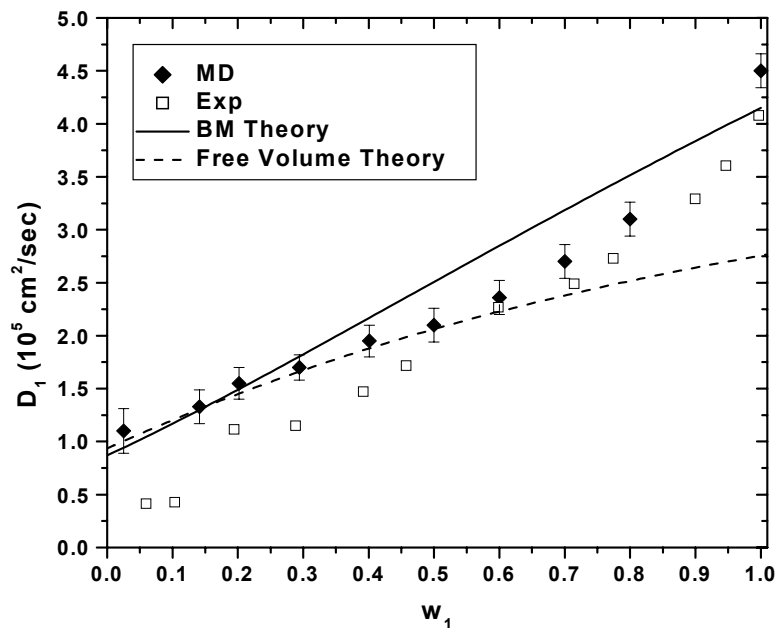
Figure 7.6   Self-diffusion coefficient of the C_{12} alkane in a C_{12}-C_{60} system at *T*=403.5K (circles) and comparison with the predictions of: (a) the Bueche - von Meerwall theory (solid line) and (b) of the free volume theory of Vrentas - Duda (dashed line). Experimental data [110] are shown as squares.
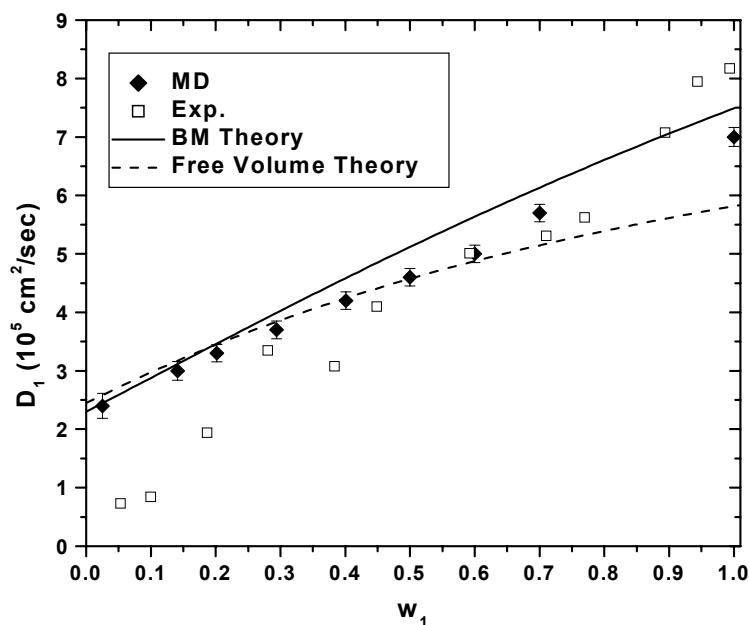
Figure 7.7   Same as in Fig. 7.6 but for a C_{12}-C_{60} system at *T*=473.5K.
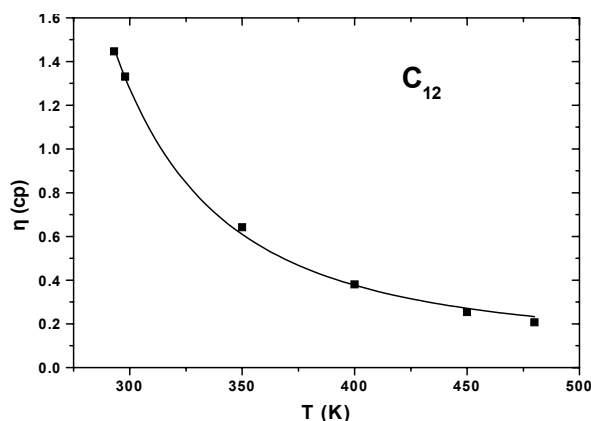
Figure 7.8   Viscosity - temperature data for the pure C_{12} used in the calculation of the self-diffusion coefficient of solvent in binary *n*-alkane blends, according to the free volume theory of Vrentas and Duda.

Figures 7.6 and 7.7 show the self-diffusion coefficient of C_{12} in C_{12}-C_{60} mixtures, at *T*=403.5K and at *T*=473.5K, which have been simulated here in the entire range of concentrations of the C_{12} component. In the same figures, experimental results from PGSE NMR measurements, obtained recently by von Meerwall *et al.* [110] for the same binary system are also presented. For both systems, the simulation results are seen to be close to the experimental data for the medium and larger values of w_1. On the contrary, significant deviations are observed in the regime of small weight fractions of C_{12} (w_1 < 0.2-0.3), which is not entirely unexpected, since the experimental values are reported to be unreliable in this range [110]. Predictions from the free volume theory are in excellent agreement with the MD data and in good agreement with the experimental values for concentrations w_1 < 0.7, without any fitting of the preexponential factor $\bar{D}_0$. In the high w_1 regime (w_1 > 0.7), the free volume theory seems to underestimate the solvent diffusion coefficient. This is explained by the fact that free volume theory has been developed to describe solvent diffusion in concentrated and semi-dilute solutions, and is inappropriate for solutions which are very rich in the solvent component (dilute solutions). On the other hand, the Bueche-von Meerwall theory seems to predict quite reliably the solvent diffusion coefficient D_1 over the entire concentration range, at least semiquantitatively.

Values of the self-diffusion coefficient of the polymer component, C_{60}, for the C_{12}-C_{60} systems at the two temperatures studied are shown in Figure 7.9. Also presented in the same figure, are the results of experimental PGSE measurements and the predictions of the Bueche-von Meerwall theory. As stated before, the free volume theory does not

predict the diffusion of the polymer component. The agreement between the MD results and the experimental data is excellent over the entire range of concentration w_1. The Bueche-von Meerwall theory seems to describe the diffusion coefficient of polymer compound very well, especially in the regime of intermediate values of w_1.
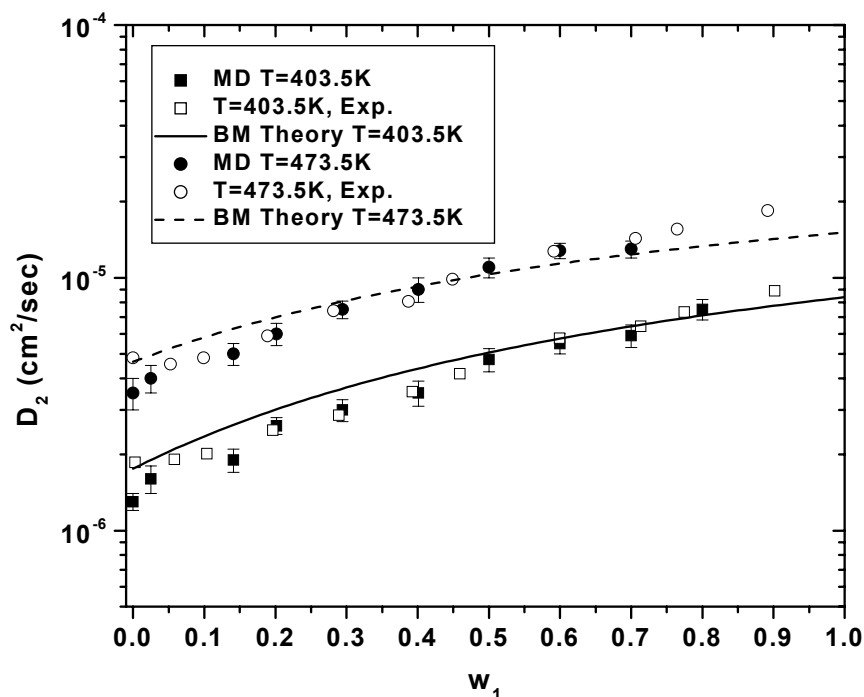
Figure 7.9   Diffusion coefficient of the C_{60} molecules in C_{12}-C_{60} blends of various compositions, at *T*=403.5K (open circles) and *T*=473.5K (open squares), and comparison with experimental data (solid symbols). The solid lines represent the predictions of the Bueche - von Meerwall theory.

The diffusion coefficients of both C_{12} and C_{60} components in the C_{12}-C_{60} system at *T*=403.5K are shown in Fig. 7.10. The figure also shows the corresponding experimental values as well as the predictions of the Bueche-von Meerwall theory. The ratio D_1/D_2 is observed to remain constant over the whole concentration range, exhibiting the 'ideal' solution behavior which is predicted by the theory.

From all systems simulated, Figs. 7.5-7.10, it is obvious that the two theories examined here, i.e. the free volume theory and the Bueche-von Meerwall theory, approach each other very much in the limit of low concentrations of the solvent molecule, w_1. For small and intermediate values of w_1 the free volume theory is seen to

be in much better agreement with MD estimates of D_1 than the combined theory. At higher w_1 values, however, i.e., in dilute solutions, the free volume theory becomes unreliable, which should be expected, since presupposes a sufficient amount of polymer-polymer contact. On the other hand, the combined theory of Bueche-von Meerwall can cover the entire concentration range, at least semiquantitatively, as it combines concepts from both free volume and dilute solution theories.
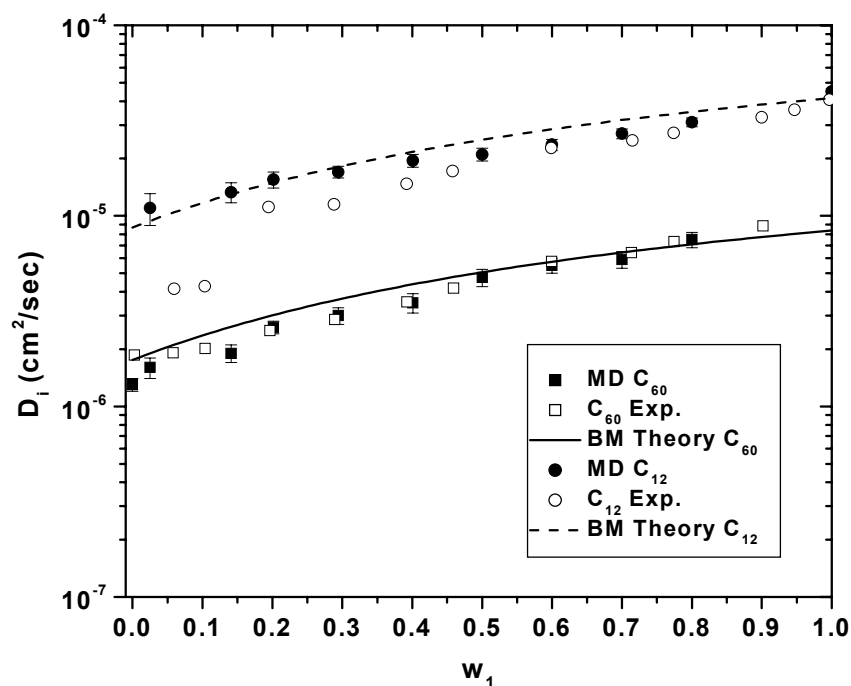
Figure 7.10   Diffusion coefficients of the C_{12} and C_{60} molecules in a C_{12}-C_{60} blend at T=403.5K as function of composition w_1, displaying the "ideal" solution behavior.

7.6. CONCLUSIONS

In this chapter we study the self- diffusion of binary liquid blends of *n*-alkanes and polymers. First we have given a thorough overview of the two most popular free volume theories: (a) the free volume theory proposed by Vrentas and Duda for the prediction of diffusivity of small penetrants into a polymer matrix and (b) the combined Rouse diffusion and chain-end free volume theory of Bueche and von Meerwall, designed to describe the diffusion coefficient of both components in a binary liquid system.

Then results have been presented from detailed atomistic MD simulations for four systems that have been simulated at various values of the weight fraction of the alkane

(solvent) component w_1. For all systems studied, it was observed that both diffusion coefficients increase when the concentration w_1 of solvent increases. This can be attributed to the increase in total free volume due to the additional free volume contributed by the solvent component when it is dissolved in the polymer.

The simulation results have been compared to the predictions of two theories described above. The parameters of the free volume theory of Vrentas and Duda were estimated following a semipredictive scheme proposed by Vrentas and Vrentas. This scheme requires experimental viscosity-temperature data for the solvent component, available in the literature, and at least two solvent self-diffusivity data points at different temperatures; the latter were obtained from MD simulations in the limit $w_1 \cong 0$. Predictions of the free volume theory were found to be in very good agreement with the MD simulation results for small and intermediate w_1 values ($w_1 < 0.7$-0.8). In the dilute regime ($w_1 > 0.7$-0.8), however, the free volume theory significantly underestimates the solvent diffusion coefficient. This should be expected, given that one of the major assumptions of the free volume theory is the presence of a significant amount of polymer molecules in the mixture.

The parameters needed in applying the combined Rouse diffusion and chain-end free volume theory of Bueche and von Meerwall theory were taken from regressions of density and diffusion data of a series of monodisperse liquid *n*-alkane systems performed by von Meerwall *et al*. [96]. The theory was found to describe MD results for the diffusion of both components over the entire range of concentrations semiquantitatively, particularly for the two C_{12}-C_{60} blends.

The MD simulation results for the diffusion coefficient of components C_{12} and C_{60} in the C_{12}-C_{60} blends at the two different temperatures were further compared with recently obtained experimental data by von Meerwall and collaborators [110]. The agreement was very satisfactory, especially for the range of intermediate concentrations where the experimental measurements were most reliable.

CHAPTER 8

ATOMISTIC MODELING OF THE STRESS RELAXATION EXPERIMENT UPON CESSATION OF STEADY-STATE UNIAXIAL ELONGATIONAL FLOW

8.1. Introduction

In the chapters, 4 to 7, results from atomistic MD simulations were presented concerning the dynamic and viscoelastic properties of polymer melts, and the diffusion properties of short n-alkane liquids and of binary blends of n-alkane. In all cases, the simulations were performed on model systems under *equilibrium* conditions. We also introduced and described a hierarchical simulation approach for getting at the linear viscoelastic properties of long-chain polymer melts. Overall, this approach relied upon conducting equilibrium atomistic MD simulations, accumulating dynamical properties and time autocorrelation functions, and mapping these properties and autocorrelation functions onto the corresponding expressions given by an appropriate coarse-grained (mesoscopic) theoretical model of polymer dynamics. In this way, key parameters of the coarse-grained model such as the friction factor ζ and the tube diameter α were estimated from the atomistic simulations.

In this chapter, a new methodology is involved for extracting the dynamic and rheological properties of polymer melts by probing directly the dynamics of melts away from equilibrium. In the literature the simulations of dynamics of liquids away from equilibrium is usually studied by means of the nonequilibrium Molecular Dynamics (NEMD) method [122]. With NEMD simulations liquids under special types of flows, such as shear flow have been studied. NEMD simulations of steady-state shear flow can lead directly to the shear viscosity. With polymers, simulating low shear rates, comparable to those encountered in most processing operations, is also possible algorithmically; it is not very useful in practice, however, as the huge fluctuations in

instantaneous stress (on the order of 1 MPa for typical model system sizes) make it impossible to resolve the average stress with which the system responds to flow. Subtraction techniques [122], [123], [124] designed to resolve the nonequilibrium stress response from the fluctuations through comparison with equilibrium trajectories initiated at the same configurations, run into problems of trajectory divergence. A promising alternative approach for resolving the response of nonequilibrium systems at small driving forces is the transient time correlation function approach of Morris and Evans [123]; This approach has been applied successfully to shear and elongational flow [125] simulations of simple fluids and is only now being extended to polymers.

In practice, the problem of resolving signal from noise in low-strain-rate NEMD simulations has forced most existing NEMD investigations of flow into the regime of very high strain rates (in excess of 10^9 s^{-1}). There the average stress is high enough to be resolved from the fluctuations. For liquids with long relaxation times, such as polymer melts, however, two new severe problems arise. First, the Deborah number (ratio of dominant material relaxation time to the characteristic time of the flow) is much higher than one, which means that the simulated flow is in a strongly nonlinear regime. Extremely important linear viscoelastic properties, such as the stress relaxation modulus and the zero-shear-rate viscosity, characteristic of the ``Newtonian plateau'' regime, are inaccessible by the NEMD simulation. Secondly, the mere attainment of steady-state conditions within the duration of a NEMD simulation initiated at an equilibrium configuration becomes problematic, as the relaxation time of the molecules may well exceed the duration of the simulation. It is thus understandable that NEMD simulations of flow of alkane fluids longer than C_{100} have never been performed [128].

The simulation of elongational flows, in particular, presents special difficulties for traditional NEMD techniques, due to the finite time requirement imposed by the contraction of the simulation cell normal to the direction of elongation. To overcome this problem, in a series of papers, Todd and Daivis [125],[130],[131] calculated the elongational viscosity by applying an oscillating elongational strain rate; more recently, the same researchers proposed a new method for simulating elongational flow in a two-dimensional atomic fluid, involving spatially and temporally periodic boundary conditions [131].

Here a different approach for the study of viscoelastic properties of polymer liquids under processing conditions is presented. Our approach based on the principles of non-equilibrium thermodynamics and atomistic MC and MD simulations and its aim is to

study polymeric systems which are initially away from equilibrium. To achieve this molecular dynamics simulations are conducted starting from a large ensemble of configurations *oriented* along the *x*- direction, and representing a melt under steady-state uniaxial elongational flow. This is the first basic ingredient of this work.

A second, equally important feature is the execution of the atomistic MD simulations onto a new statistical ensemble, i.e. the $NTL_x\sigma_{yy}\sigma_{zz}$ ensemble introduced recently by Yang *et al*. [68], [70]. In more details Yang *et al.* proposed a MD technique for the simulation of uniaxial tension and compression of model amorphous polymer systems based again in the deformation of the simulation box in one direction. The MD simulations conducted in the $NTL_x\sigma_{yy}\sigma_{zz}$ statistical ensemble. Model linear PE systems were simulated with the new technique near and below the glass transition temperature T_g, and good qualitative agreement with experimental data was reported. More details about the $NTL_x\sigma_{yy}\sigma_{zz}$ statistical ensemble can be found in Appendix E.

The work presented here involves 3 stages. First configurations are obtained from a MC method where the chains are oriented through a thermodynamic field. We then observe the isothermal relaxation of these configurations to thermodynamic equilibrium, keeping their dimension along the *x*- direction constant and the average normal pressure in the *y*- and *z*- directions equal to the atmospheric pressure. That is, we simulate an experiment of stress relaxation upon cessation of a steady-state uniaxial elongational flow. In the course of the MD simulations we track the temporal evolution of the ensemble-averaged stress and of the overall conformational characteristics of the chains. We develop analytical expressions for these quantities as functions of time by solving the Rouse model under the initial and boundary conditions corresponding to our atomistic computer experiment. By mapping our simulation results onto the Rouse analytical expressions, we determine the friction factor or, equivalently, the Rouse time τ_R. Finally, we compare this estimate against the estimate previously obtained from equilibrium MD.

This chapter is organized as follows. Section 8.2 outlines the computational strategy employed in somewhat greater detail than described above. Section 8.3 present the Rouse model equations describing the evolution in time of the quantities, which are monitored during the transient MD simulations. In section 8.4 the calculation of stress in our MD simulations is described in details. Results from detailed atomistic simulations on two systems studied, a C_{24} and a C_{78} PE melt, are presented in section 8.5. In this section we also discuss how the simulation results compare against the predictions of the Rouse model and against previous results obtained from MD simulations on the same

systems under equilibrium conditions. Finally section 8.6 summarizes the main conclusions of the present work.

8.2.   A Hierarchical Methodology

Our computational strategy for simulating *stress relaxation upon cessation of steady-state uniaxial elongational flow* involves the following three stages:

Stage I: Generation of oriented configurations.

In the first stage, termed stage *I*, a coarse-grained description of the polymer melt is invoked through the definition of the conformation tensor, **c**, which is an overall, global descriptor of the long length-scale conformation of polymer chains. The conformation tensor, **c**, is defined as the second moment tensor of the end-to-end distance vector of a polymer chain reduced by one third the unperturbed end-to-end distance and averaged over all chains in the system:

$$\mathbf{c}(t) = 3 \left\langle \frac{\mathbf{R}(t)\mathbf{R}(t)}{\left\langle R^2 \right\rangle_0} \right\rangle \tag{7.23}$$

In above equation **R** stands for the end-to-end vector of a macromolecule and $<R^2>_0$ is the mean-squared magnitude of that vector in the equilibrium, quiescent state, where chains are unperturbed to an excellent approximation [73].

The Helmholtz free energy per chain A/N_{ch} is assumed to be a function not only of the mass density ρ and temperature T of the melt but also of the conformation tensor **c** through the following equation.

$$\frac{A}{N} - \frac{A_0}{N} \equiv \frac{A}{N}(T,\rho,\mathbf{c}) - \frac{A_0}{N}(T,\rho,\mathbf{I}) = \frac{\tilde{G}}{N} - \frac{\tilde{G}_0}{N} - b\frac{M}{N_A}\left(\frac{1}{\rho} - \frac{1}{\rho_0}\right) + k_B T \boldsymbol{\alpha} : \mathbf{c} \tag{7.24}$$

The partial derivatives of the Helmholtz free energy A/N_{ch} with respect to ρ and **c** define two thermodynamic fields: a scalar pressure-like quantity *b* and a tensorial thermodynamic field **α**. The tensorial field **α** plays the role of a steady-state flow field, whose application can orient and/or deform the chains, depending on its form and the strength of its matrix elements. The case that has interested us mostly in our studies is one wherein the field **α** has only one non-zero element, the component α_{xx}. The physical meaning of such a form for the field **α** has been explained in detail in the relevant publications [72] and [132]: It corresponds to the case of a steady-state uniaxial elongational flow, with α_{xx} being indicative of the Deborah number of the flow. As such,

the quantity α_{xx} can be considered as a product of the longest relaxation time of the polymer melt times the elongational strain rate of the applied steady-state flow field. The higher the value of α_{xx} relative to unity, the more nonlinear the character of the applied elongational flow.

With the above definitions, a series of detailed atomistic EBMC simulations can be initiated on model melt systems at various values of the orienting thermodynamic field α_{xx}, starting from the zero value ($\alpha_{xx}=0$, equilibrium, quiescent, field-free state). Large ensembles of uniaxially stretched, anisotropic melt configurations can thus be accumulated at prescribed conditions of temperature T, field b, set of relative chemical potentials $\boldsymbol{\mu}^*$ defining the distribution of chain lengths, and field strength α_{xx}. The use of the EBMC algorithm ensures full equilibration of the strained configurations at all length scales in all simulations, subject to the imposed α_{xx}. The method has already been applied [72],[132] with considerable success to generate oriented and/or deformed PE melt configurations for many different systems from C_{24}, up to C_{1000} (subscript indicates mean chain length), all characterized by uniform chain length distributions with polydispersity index less than 1.09 (chain length ranging from half the mean to 1.5 the mean chain length); thousands of uncorrelated, strained configurations representative of these melts under conditions of steady-state, uniaxial elongational flow at a variety of α_{xx} values ranging from 0 to 0.75 have been sampled.

Stage II: From field-on EBMC simulations to field-off MD simulations.

In the second stage of the calculations reported in this paper, termed stage II, the field α_{xx}, which causes orientation and/or deformation of the model polymer systems, is removed. The system is thus left to return back to the field-free, equilibrium state, which should be characterized by the absence of any spatial anisotropy. However, the way the system is allowed to return to equilibrium is not unique; the path to be followed depends on the macroscopic boundary conditions imposed on the sample. These define a corresponding statistical ensemble in which the MD simulations tracking the relaxation process must be conducted.

In this work, the MD simulation takes place in the $NTL_x\sigma_{yy}\sigma_{zz}$ statistical ensemble, similar to the ensemble introduced by Ryckaert and Klein [133] for MD simulations of crystalline phases consisting of infinitely long PE chains. The present paper follows the extended $NTL_x\sigma_{yy}\sigma_{zz}$ ensemble formalism by Yang *et al.* [68][70] for studying the dynamics of glassy polymer systems in uniaxial deformation. In this ensemble, the

variables kept constant are: the total number of chains N_{ch} and the length of each chain, therefore the total number of interacting mers N; the temperature T; the length L_x of the simulation box in the direction of elongation x; and the average normal stress $(\sigma_{yy} + \sigma_{zz})/2$ in the lateral directions y and z, set equal to minus the ambient atmospheric pressure P_{ext} (i.e., $[\sigma_{yy} + \sigma_{zz}] / 2 = - P_{ext}$, t>0). These are the macroscopic constraints encountered following the process of fiber spinning at the end of the spinning operation, when the fibers are kept at constant extension and the stress σ_{xx} in the direction of pulling is allowed to relax from its initial value to the equilibrium, field-free value, equal to $-P_{ext}$ (i.e., $\sigma_{xx}(t \rightarrow \infty) = -P_{ext}$). On the other hand, the length of the simulation box in the directions y and z is free to change, so that the instantaneous volume of the system is consistent with the instantaneous value of the stress component σ_{xx}. (Of course, at the end of the simulation, when the system has fully returned to equilibrium, the volume ought to be equal to the one corresponding to the density of the equilibrium system.)

In addition to monitoring the temporal evolution of the stress component $\sigma_{xx}(=\sigma_{xx}(t))$ during the $NTL_x\sigma_{yy}\sigma_{zz}$ MD simulations, we also observe and record as a function of time t the evolution of certain ensemble-averaged descriptors of the chain long length-scale configuration. These descriptors include the diagonal components of the chain conformation tensor (c_{xx}, c_{yy} and c_{zz}) and the chain mean-square end-to-end distance $<R^2>$. The time evolution of all these quantities contains important information about the system, since it can ultimately be related to the spectrum of relaxation times characterizing the dynamics of the normal modes of the system [6]. The simulation results for the evolution of these quantities are fit to closed-form equations arising from analyzing the dynamics of the system through a coarse-grained molecular model. This is undertaken in the third stage of the methodology.

Stage III: Mapping to a Coarse-Grained Model of Dynamics.

In the third stage, termed stage III, the Rouse model of polymer dynamics is chosen and then equations are derived based on this, which express the evolution of the system structure and of the stress tensor in the rheological experiment considered. The ensemble averaged results from the MD simulations are mapped onto these equations to extract the coarse-grained model parameters, therefore the material functions of interest, from chemical constitution. In chapter 4 we have already seen a mapping of the atomistic equilibrium MD simulation data onto the equilibrium Rouse model. Here we derive

additional equations based on the Rouse model, which express the evolution of the system structure and of the stress tensor in the rheological experiment considered.

Our computational strategy is overall based upon the following testable assumptions:

(i) The starting configurations, obtained through EBMC in the presence of an orienting field, are representative of those expected for the actual polymer system having obtained steady state at constant applied elongational strain rate. Strong support for this assumption is provided by comparisons of properties of the oriented configurations sampled by EBMC against experiment. For example, the index of refraction and stress tensors calculated from the oriented configurations conform to the stress optical law, with a stress optical coefficient in excellent agreement with that measured in polyethylene melts [132].

(ii) The degree of pre-alignment introduced in the initial configurations corresponds to an effective strain rate that is low enough for the subsequent relaxation experiment to lie entirely within the linear response regime. This is ensured by the use of α_{xx} values which are always lower than 0.75 in sampling the initial configurations. The physical interpretation of α_{xx} as a strain rate multiplied by the longest relaxation time, i.e. as a Deborah number, is supported by our previous studies of the free energy and stress in such oriented melts [132]. Furthermore, the practical coincidence of the relaxation time spectrum extracted from the current nonequilibrium simulations to that extracted earlier from equilibrium MD simulations of the same systems [81] demonstrates a posteriori that our computer experiments have been conducted in the linear regime. (iii) At any point along the relaxation experiment, the stress tensor can be computed from the conformation tensor **c** and the fields b and **α** through a free-energy based expression, which will be discussed later. This expression has been tested under steady-state flow conditions in [132]. It is further tested under transient conditions in this work, by direct comparison against stress values calculated by the molecular virial theorem and found to be fully consistent with the latter. Use of this thermodynamic expression affords calculating the stress with much less statistical noise than would otherwise be possible.

8.3.   Calculations by the Rouse model

As already stated in section 8.2, stage III of our methodology involves mapping atomistic simulation results for the temporal evolution of certain averaged quantities onto a coarse-grained theoretical model, the aim being to extract the spectrum of relaxation times of the system. For the two unentangled polymer melts studied here, the C_{24} and C_{78} systems, the Rouse model is a suitable coarse-grained molecular model. In chapter 3 we presented the basic assumptions of the Rouse model and reviewed its formulation in terms of the normal modes. Particular emphasis was placed on the equations describing the relaxation of the normal modes and the mean-square displacement of the chain center of mass under equilibrium conditions. In addition in chapter 4 we showed that, by suitably mapping the simulation results onto the Rouse model equations, one can extract (a) the spectrum of relaxation times, τ_p, $p=1,2,...,N$ and (b) the friction factor ζ quantifying the frictional force felt by a monomer in the melt as it moves through the environment formed by all other mers.

In the present work we will extend the analysis to a system which, initially, is away from equilibrium, and which, subsequently, is allowed to return to equilibrium by releasing the macroscopic field that keeps it in a steady-state non-equilibrium state. More specifically, we will be concerned with a melt of linear chains that have been oriented by means of a steady state elongational flow field, represented in our simulations by the imposed tensorial thermodynamic field α_{xx}. Initially the melt is in a steady state away from equilibrium, with all microscopic elements of its structure fully adjusted to the imposed α_{xx} [132]. At time $t=0$ the field α_{xx} is switched off and the system is allowed to return to equilibrium, keeping the length L_x constant and the average lateral normal stress $(\sigma_{yy}+\sigma_{zz})/2$ equal to $-P_{ext}$.

The purpose of the present section is to use the Rouse model in order to derive the equations describing the time evolution of the stress tensor component σ_{xx} and of the conformation tensor component c_{xx} for this stress relaxation experiment.

8.3.1. Relaxation of the stress component σ_{xx}

The Rouse model predicts an equation for the calculation of the stress tensor component σ_{xx} through the autocorrelation function of the normal modes $\mathbf{X}_p$ as [6]:

$$\sigma_{xx}(t) = \frac{N_{ch}}{V} \sum_{p=1}^{N} k_p \left\langle X_{px}(t) X_{px}(t) \right\rangle \qquad (7.25)$$

with $\mathbf{X}_p$ being the mode of order p and k_p the spring constant corresponding to the pth mode. According to Eq. (7.25), to calculate σ_{xx} we need to calculate the average quantity $<X_{px}(t)X_{px}(t)>$ over all stochastic trajectories consistent with the correct initial and boundary conditions. To do this, we use the Smoluchowski equation. During the process of relaxation ($t>0$), no external field is exerted on the chains; therefore, for times $t>0$, the form of the Smoluchowski equation, that should be considered is the one corresponding to a velocity gradient field $\kappa_{\alpha\beta} = 0$ α, β [6]:

$$\frac{\partial}{\partial t}\left\langle X_{px}(t)X_{px(t)}\right\rangle = -\frac{2p^2}{\tau_R}\left(\left\langle X_{px}(t)X_{px}(t)\right\rangle - \frac{k_BT}{k_p}\right) \tag{7.26}$$

where τ_R ($= \tau_1$) represents the Rouse or longest relaxation time of the chain. The relaxation time τ_p of the higher modes are expressed in terms of τ_R, $\tau_p = \tau_R / p^2$. The friction constants ζ_p for modes $p \geq 1$ satisfy $\zeta_p = k_p / \tau_p$.

To solve Eq. (7.26), we need to provide an initial condition for the unknown quantity $<X_{px}(t)\ X_{px}(t)>$ for $t = 0$. The time $t = 0$ coincides with the moment the field is just turned off, that is, the value $<X_{px}(t=0)\ X_{px}(t=0)>$ is representative of the steady-state elongational flow period that precedes the relaxation under investigation. The value of this quantity is of course a function of the elongational flow field α_{xx}, applied previously in the course of the field-on EBMC simulations.

To calculate $<X_{px}(t)\ X_{px}(t)>$ at the end of the steady-state elongational flow we will invoke again the Smoluchowski equation. Since the field α_{xx} is exerted on the melt during the entire duration of the steady-state elongational flow, the form of the Smoluchowski equation that should be considered in this case is that corresponding to a velocity gradient field with all other components zero except for the xx-component, which equals α_{xx}. The form for the time evolution equation of $<X_{px}(t)\ X_{px}(t)>$ now becomes [6]:

$$\frac{\partial}{\partial t}\left\langle X_{px}(t)X_{px(t)}\right\rangle = 2\frac{k_BT}{\zeta_p} - 2\left(\frac{k_p}{\zeta_p} - \frac{\alpha_{xx}}{\tau_R}\right)\left\langle X_{px}(t)X_{px}(t)\right\rangle \tag{7.27}$$

with initial condition corresponding to an equilibrium undeformed melt:

$$\text{at } t = 0, \qquad \left\langle X_{px}(0)X_{px}(0)\right\rangle = \frac{k_BT}{k_p} \tag{7.28}$$

The solution to the initial value problem of Eqs. (7.27) and (7.28) is given by

$$\left\langle X_{px}(t)X_{px}(t)\right\rangle = \frac{k_BT}{k_p}\left(\frac{p^2}{p^2-\alpha_{xx}}\right) - \frac{k_BT}{k_p}\left(\frac{p^2}{p^2-\alpha_{xx}}\right)\exp\left(-2\left(p^2-\alpha_{xx}\right)\frac{t}{\tau_R}\right) \tag{7.29}$$

From Eq. (7.29) it is seen that the steady-state value of the quantity $\langle X_{px}(t) X_{px}(t) \rangle$ under the applied field value α_{xx} is

$$\lim_{t \to \infty} \langle X_{px}(t) X_{px}(t) \rangle = \frac{1}{1 - \dfrac{\alpha_{xx}}{p^2}} \frac{k_B T}{k_p} = B_{xx,p} \frac{k_B T}{k_p} \tag{7.30}$$

where

$$B_{xx,p} \equiv \frac{1}{1 - \dfrac{\alpha_{xx}}{p^2}} \tag{7.31}$$

denotes the factor by which the variance of the pth mode $\langle X_{px}(t) X_{px}(t) \rangle$ increases at steady-state under the applied field value α_{xx} relative to equilibrium. Clearly, $B_{xx,p} > 1$. In addition, Eq. (7.30) shows that the higher the value of p the smaller the relative increase of the corresponding averaged quantity $\langle X_{px}(t) X_{px}(t) \rangle$.

The value of the averaged quantity $\langle X_{px}(t) X_{px}(t) \rangle$ at $t = \infty$ for the steady-state elongational flow is the initial condition that should be used in conjunction with Eq. (7.26)in order to calculate the temporal evolution of the quantity $\langle X_{px}(t) X_{px}(t) \rangle$ during the field-off relaxation process. The result is

$$\langle X_{px}(t) X_{px}(t) \rangle = \frac{k_B T}{k_p} \left(1 + \left(B_{xx,p} - 1 \right) \exp\left(-\frac{2t}{\tau_p} \right) \right) \tag{7.32}$$

By substituting Eq. (7.32) into Eq. (7.25) and rearranging terms, we end up with the following equation describing the stress relaxation during the $NTL_x\sigma_{yy}\sigma_{zz}$ experiment:

$$\frac{\sigma_{xx}(t) - \sigma_{xx}(\infty)}{\sigma_{xx}(0) - \sigma_{xx}(\infty)} = \frac{\sum_{p:all} \left(B_{xx,p} - 1 \right) \exp\left(-\dfrac{2t}{\tau_p} \right)}{\sum_{p:all} \left(B_{xx,p} - 1 \right)} \tag{7.33}$$

Here $\sum_{p:all} \left(\equiv \sum_{p=1}^{all} \right)$ denotes summation over all positive integer numbers p. $\sigma_{xx}(0)$ is the value of $\sigma_{xx}(t)$ at time $t=0$; in our atomistic simulations this corresponds to the end of the EBMC simulations or equivalently to the beginning of the $NTL_x\sigma_{yy}\sigma_{zz}$ MD simulations. Similarly, $\sigma_{xx}(\infty)$ is the value of $\sigma_{xx}(t)$ at time $t = \infty$; clearly, $\sigma_{xx}(\infty) = -P_{\text{ext}}$.

Eq. (7.33) is the equation describing the relaxation of the stress component $\sigma_{xx} = \sigma_{xx}(t)$ in the computational experiments carried out in the present work, according to the

Rouse model. It is this equation against which the $NTL_x\sigma_{yy}\sigma_{zz}$ MD simulations results ought to be compared in order to extract the spectrum of relaxation times $\tau_p, p = 1,2,...$, of the system.

8.3.2. The relaxation of the conformation tensor component c_{xx}

In terms of the normal coordinates, c_{xx}, defined through Eq. (7.23), is given by the following equation [6]:

$$c_{xx} = \frac{3}{\langle R^2 \rangle_0} 16 \sum_{p:odd} \langle X_{px}(t) X_{px}(t) \rangle \tag{7.34}$$

Thus, by directly substituting Eq. (7.32) for $<X_{px}(t)X_{px}(t)>$ into Eq. (7.34), and after rearranging terms, we obtain

$$\frac{c_{xx}(t) - c_{xx}(\infty)}{c_{xx}(0) - c_{xx}(\infty)} = \frac{\sum_{p:all} \left(\frac{B_{xx,p} - 1}{k_p} \right) \exp\left(-\frac{2t}{\tau_p} \right)}{\sum_{p:all} \left(\frac{B_{xx,p} - 1}{k_p} \right)} \tag{7.35}$$

As with the relaxation of the stress component σ_{xx}, $c_{xx}(0)$ is the value of $c_{xx}(t)$ at time $t=0$, i.e., at the end of the EBMC simulations or equivalently at the beginning of the $NTL_x\sigma_{yy}\sigma_{zz}$ MD simulations. Similarly, $c_{xx}(\infty)$ is the value of $c_{xx}(t)$ at time $t=\infty$ of the stress relaxation experiment; clearly, $c_{xx}(\infty)=1$.

Eq. (7.35) is the pertinent equation describing the relaxation of the conformation tensor component $c_{xx} = c_{xx}(t)$ in the computational experiments of the present work, according to the Rouse model. As with Eq. (7.33) for the stress tensor component σ_{xx}, Eq. (7.35) offers an additional way for extracting the spectrum of relaxation times $\tau_p, p = 1,2,...$, by fitting the simulation results for the relaxation of the quantity c_{xx}.

An important point to notice about Eqs. (7.33) and (7.35) is that the longest time governing the relaxation of the stress and conformation tensor components, $\sigma_{xx}(t)$ and $c_{xx}(t)$, is $\tau_R / 2$. This is half the time characterizing the decay of the time autocorrelation function of the first normal mode ($p = 1$) in the equilibrium state:

$$\langle \mathbf{X}_p(t) \bullet \mathbf{X}_p(0) \rangle = \frac{k_B T}{k_p} \exp\left(-\frac{t}{\tau_p}\right) = \frac{Nb^2}{6\pi^2} \frac{1}{p^2} \exp\left(-\frac{t}{\tau_p}\right) \tag{7.36}$$

and half the longest relaxation time governing the decay of the autocorrelation function of the end-to-end vector at equilibrium, Eq. (3.20):

$$\frac{\langle \mathbf{R}(t) \bullet \mathbf{R}(0) \rangle}{\langle R^2 \rangle_0} = \sum_{p:odd} \frac{8}{p^2 \pi^2} \exp\left(-\frac{tp^2}{\tau_1}\right) \tag{7.37}$$

In the case of the oriented configurations the autocorrelation function of the end-to-end vector $\langle \mathbf{R}(t) \bullet \mathbf{R}(0) \rangle$ can also be calculated. This function can be obtained, as:

$$\langle \mathbf{R}(t) \bullet \mathbf{R}(0) \rangle = 16 \sum_{p:odd} \langle \mathbf{X}_p(t) \bullet \mathbf{X}_p(0) \rangle \tag{7.38}$$

In order to calculate the quantities $\langle \mathbf{X}_p(t) \bullet \mathbf{X}_p(0) \rangle$ we follow the same procedure as we did for $\langle \mathbf{X}_p(t) \bullet \mathbf{X}_p(t) \rangle$ in the case of conformation and stress tensors. During the process of relaxation the quantity $\langle \mathbf{X}_p(t) \bullet \mathbf{X}_p(0) \rangle$ follows the Smoluchowski equation:

$$\frac{\partial}{\partial t} \langle X_{p\gamma}(t) X_{p\varepsilon(t)} \rangle = -\frac{p^2}{\tau_R} \langle X_{p\gamma}(t) X_{p\varepsilon}(t) \rangle, \quad \forall, \quad \gamma, \varepsilon \tag{7.39}$$

with the same boundary condition, Eq. (7.30), introduced above:

$$\langle X_{p\gamma}(t) X_{p\varepsilon(t)} \rangle = B_{\gamma\varepsilon,p} \frac{k_B T}{k_p} \tag{7.40}$$

and

$$B_{\gamma\varepsilon,p} = \begin{cases} \dfrac{1}{1 - \dfrac{\alpha_{xx}}{p^2}}, & \text{if } \gamma = \varepsilon = x \\ 1, & \text{otherwise} \end{cases} \tag{7.41}$$

By solving the above equation we can obtain $\langle X_{p\gamma}(t) X_{p\varepsilon}(0) \rangle$:

$$\langle X_{p\gamma}(t) X_{p\varepsilon}(0) \rangle = B_{\gamma\varepsilon,p} \frac{k_B T}{k_p} \exp\left(-\frac{t}{\tau_p}\right) \tag{7.42}$$

Finally, by substituting in Eq. (7.38) the autocorrelation function of the end-to-end distance, we get:

$$\frac{\langle \mathbf{R}(t) \bullet \mathbf{R}(0) \rangle}{\langle R^2 \rangle_0} = \sum_{p:odd} \left[\frac{8}{3\rho^2 \pi^2} \left(2 + \frac{1}{1 - \dfrac{\alpha_{xx}}{p^2}} \right) \exp\left(-\frac{tp^2}{\tau_1}\right) \right] \tag{7.43}$$

As we can see, the dominant characteristic time for the decay of the end-to-end distance under the nonequilibrium relaxation conditions considered is again τ_R, exactly as under equilibrium conditions, Eq. (7.37).

The quantities c_{xx} and σ_{xx} decay with characteristic time $\tau_R / 2$ and not τ_R because they are related to the *second moment* of **R**. This means that, by observing the relaxation of the stress or conformation tensor of the pre-strained system back to equilibrium, one can extract the spectrum of relaxation times τ_p, $p = 1,2,...$, in half the CPU time that would be required for monitoring the decay of the time autocorrelation function of the normal modes of the same system at equilibrium, or the decay of the autocorrelation function of the end-to-end vector under equilibrium or nonequilibrium conditions. This is a significant observation, since it reduces by a factor of 2 the problem of long relaxation times, which plagues dynamic simulation of long-chain systems. This advantage, however, occurs at price, namely larger statistical error in the dynamical information that can be accumulated within a single MD run.

During the transient relaxation of the pre-strained system, the system state evolves continuously, thus rendering impossible the application of the usual equilibrium MD trick of multiple time origins for reducing the statistical uncertainty of computed time correlation functions. The advantage of time translation invariance of equilibrium simulations is lost. In the relaxation experiments considered here, the only way to reduce the large fluctuations present in $\sigma_{xx}(t)$ and $c_{xx}(t)$ is to average over many MD runs initiated at different strained configurations, all runs conforming to the same macroscopic $NTL_x\sigma_{yy}\sigma_{zz}$ conditions. This means that *a large number* of initially pre-strained configurations need to be subjected to $NTL_x\sigma_{yy}\sigma_{zz}$ MD simulations; the ensemble-averaged results at every time instant t will be those corresponding to averages at time t over all nonequilibrium trajectories generated in this way. As will be seen immediately below, such averaging over many dynamical trajectories quickly reduces the statistical uncertainty of structural results and leads to rather smooth curves. Usually, averaging over about 100 trajectories is found to be sufficient for the results at every time instant to be calculated with an error less than about only a few percent. Ideally, for the particular system studied and the particular α_{xx} value with which the system has been brought to the oriented state, *all* strained configurations sampled during the EBMC run could be used in the averaging process. One should note that each set of MD simulations starting from

different configurations corresponding to the same α_{xx} can be conducted in parallel, thus greatly reducing the time required for obtaining the rheological properties.

8.4. Calculation of the stress

In the simulations, the stress tensor is calculated in two ways: the first is by applying the molecular virial theorem [134]. The use of the molecular stress tensor relies on scaling molecular center-of-mass positions with the boundaries of the simulation box, while holding all intramolecular distances constant. For model systems consisting of macromolecules of overall dimensions comparable to the simulation box size, this scaling of space is quite inhomogeneous. This has not been observed to cause problems in simulation practice. Trial calculations based on the atomic stress tensor, with due consideration of the constraint forces on the interaction sites, have led to results indistinguishable from those obtained by the molecular virial theorem. It is noted that localizing the momentum on center of mass positions or on atomic positions for the purpose of calculating the stress are just two of an infinite number of possibilities [135], all of which give the same average stress tensor under equilibrium or steady-state conditions. The time autocorrelation function of the instantaneous stress at short times may depend on which definition is used for the stress. However, the integral underneath it is invariant and is related to the viscosity (see below).

The second way implemented in this work to calculate the stress is to use the Helmholtz energy function and affine deformation assumption extensively discussed in refs. [72] and [132]. According to the latter approach, the stress tensor at every time t can be calculated from the ensemble-averaged values of mass density ρ, conformation tensor c_{xx} c_{xx} and partial derivative of the Helmholtz energy function with respect to c_{xx} at time t, through

$$\sigma_{xx}(t) = -P_{ext} + 2\frac{R}{M}T\rho(t)c_{xx}\left[\left.\frac{\partial\left(A/N_{ch}\right)}{\partial c_{xx}}\right|_{T,\rho,c_{[xx]}}\right]_{c_{xx}=c_{xx}(t)} \tag{7.44}$$

where P_{ext} denotes the equilibrium (atmospheric) pressure and M the number average molecular weight of the system. In writing down Eq. (7.44), the assumption has been made that, due to the elongational character of the stress relaxation process, the ensemble-averaged values of all off-diagonal components of the conformation tensor are identically zero; this assumption is confirmed by our MD simulations. In Eq. (7.44), the

symbolism $\left[\partial\left(A/N_{ch}\right)/\partial c_{xx}\big|_{T,\rho,,c_{[xx]}}\right]_{c_{xx}=c_{xx}(t)}$ denotes the partial derivative of the

Helmholtz energy per chain with respect to c_{xx} at a value of c_{xx} equal to that

characterizing the melt at time t. The latter value of c_{xx} is calculated as an ensemble

average at time t over all MD trajectories initiated at configurations corresponding to the

same steady-state elongational flow state. The function $\partial\left(A/N_{ch}\right)/\partial c_{xx}\big|_{T,\rho,c_{[xx]}}$ $(=\alpha_{xx})$ has

been accumulated and plotted against c_{xx} in the elasticity calculations of the systems

simulated here, which are presented in details elsewhere [72]. Here it is obtained by

looking up the value of α_{xx} corresponding to c_{xx} in the $c_{xx}(\alpha_{xx})$ plots of Figure 7 of ref.

[72].

8.5.   Results

The molecular model used in the present study is exactly the same as the one used

in the equilibrium MD simulations of the same systems C_{24} and C_{78} (model 1). All the

parameters of the model are presented in details in Table 4.1. As already explained in the

previous section, all results reported in this work have been obtained from MD

simulations carried out in the statistical ensemble $NTL_x\sigma_{yy}\sigma_{zz}$. Details of the formulation

of the $NTL_x\sigma_{yy}\sigma_{zz}$ statistical ensemble are presented in Appendix D. The total Hamiltonian

of the system, derived from the Lagrangian,

$$H_{NTL_x\sigma_{yy}\sigma_{zz}} = \sum_i \frac{p_i^2}{2m_i} + V(\mathbf{r}) - \frac{1}{2}\sum_\kappa\sum_i \lambda_i^\kappa\left(\left(\mathbf{r}_{i+1,\alpha}-\mathbf{r}_{i,\alpha}\right)^2 - l^2\right) +$$
$$\frac{Q}{2}\left(\frac{\dot{s}}{s}\right)^2 + (g+1)\frac{\ln s}{\beta} + \frac{W}{2}\left(\frac{\dot{A}}{s}\right)^2 + P_{ext}L_xA \tag{7.45}$$

should be conserved during the run. The first term on the right hand side represents the

kinetic energy, the second term is the potential energy (including the Fixman potential),

the third term is the contribution to the Hamiltonian due to constraint bond lengths with

λ_I^κ being the Lagrange multiplier for the i-th bond of chain κ, and the last four terms are

the contributions due to the thermostat and the fluctuating box cross-sectional area in the

plane yz. In our MD runs, $H_{NTL_x\sigma_{yy}\sigma_{zz}}$ was found to change by less than 1% within 1 ns of

simulation.

Results will be presented from averaging over about 100 $NTL_x\sigma_{yy}\sigma_{zz}$ MD trajectories for each stress relaxation experiment, initiated at ensembles of strained configurations of two PE melt systems: a 32-chain C_{24} and a 40-chain C_{78} PE melt. The reader is reminded that each melt is labeled by its number average chain length $\overline{X}$; both melts are characterized by uniform chain length distributions, ranging from $\overline{X}/2$ to $3\overline{X}/2$. Averages of conformational properties reported here are taken over all chains present in each melt.

Extensive end-bridging Monte Carlo (EBMC) simulations have been performed on both model systems at various field values α_{xx}. 0, which have resulted from such EBMC simulations, show the evolution of the conformation tensor components, c_{xx}, c_{yy} and c_{zz} with CPU time for the two PE melt systems, the C_{24} and C_{78}, at field values $\alpha_{xx} = 0.75$ and $\alpha_{xx} = 0.3$, respectively. In Figure 8.1b one can see the transition from the field-free, equilibrium isotropic structure to a structure significantly oriented along the x- direction due to the imposed field α_{xx}. In principle, all configurations in the plateau regime of the EBMC simulations (between the filled triangles in Figures 8.1a,b) are excellent starting points for performing the $NTL_x\sigma_{yy}\sigma_{zz}$ MD simulations. Due to CPU time limitations, however, only about 100 of these configurations were chosen for each system to be subjected to a $NTL_x\sigma_{yy}\sigma_{zz}$ MD simulation. The results shown in the next of this section have been obtained after averaging over runs initiated at this relatively small number of configurations.
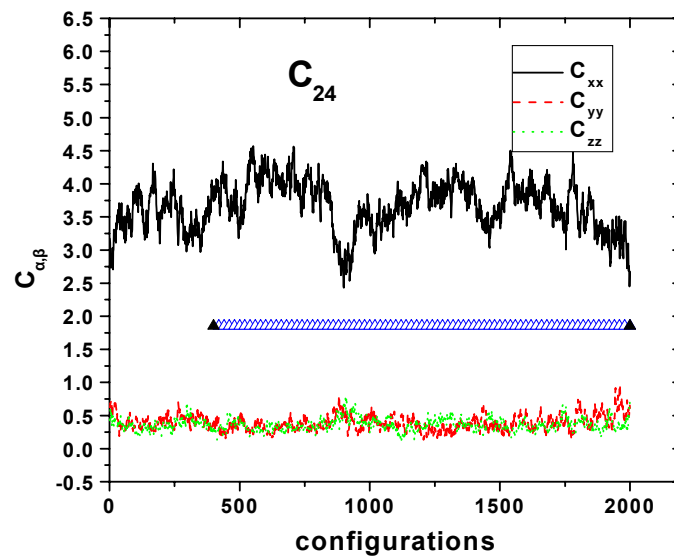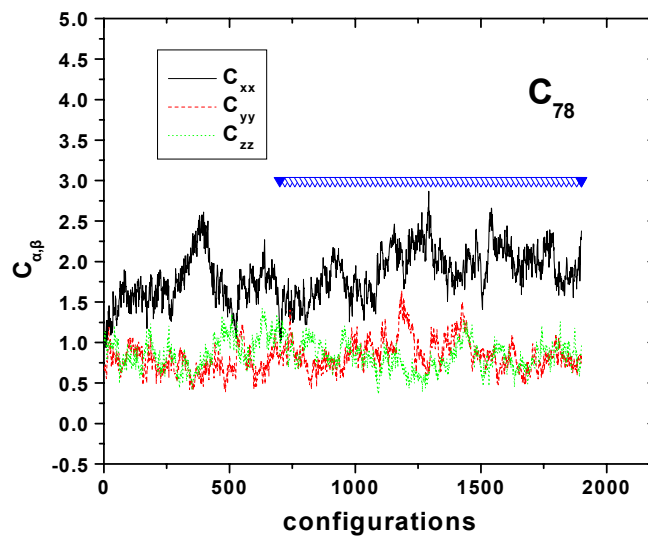
(b)

Figure 8.1 Schematic showing the plateau region from which pre-strained configurations, obtained by using the EBMC algorithm in the presence of the orienting field α_{xx}, were chosen to be subjected to $NTL_x\sigma_{yy}\sigma_{zz}$ MD simulations, for (a) the C_{24} and (b) the C_{78} PE melt systems. Due to CPU time limitations, only a small representative sample of these configurations was chosen for the $NTL_x\sigma_{yy}\sigma_{zz}$ MD simulations. The actual configurations used are indicated by the open triangles and the two filled triangles on each end.

## A) Equilibrium conformational properties

In order to ensure that, in the limit of very long times, where the stress tensor should have attained its equilibrium value, the $NTL_x\sigma_{yy}\sigma_{zz}$ algorithm behaves as the usual NVT algorithm, we first compared the equilibrium characteristics of melts obtained after long $NTL_x\sigma_{yy}\sigma_{zz}$ simulations against the equilibrium characteristics obtained from end-bridging Monte Carlo simulations at a zero field (i.e., for $\alpha_{xx} = 0$) or from equilibrium MD simulations.

Fig. 8.2a and 8.2.b show the evolution in time of the mean square end-to-end distance $<R^2>$ for the C_{24} and C_{78} PE melts studied, averaged over all simulated trajectories. For both systems, the initial values of $<R^2>$ are much higher than the equilibrium ones, indicative of significant elongation of the chains along the x-direction due to the imposed field α_{xx}. As time goes on, however, $<R^2>$ in both systems is seen to decrease continuously, approaching an asymptotic value characteristic of the system under field-free, equilibrium conditions. For the C_{24} melt this value is seen to be 350 ± 20 Å, whereas for the C_{78} melt it is about 1530 ± 50 Å. The dashed straight lines in the

same figures show the corresponding equilibrium $<R^2>$ values for the C_{24} and C_{78} systems respectively as obtained from EBMC or *NVT* MD simulations on the same systems under field-free, equilibrium conditions presented in chapter 4. These results, together with the corresponding results for the mean-square radius of gyration $<R^2_g>$ and the specific volume *v* of the two melts, are summarized in Tables 8.1 and 8.2. Clearly, the agreement between EBMC, *NVT* MD and $NTL_x\sigma_{yy}\sigma_{zz}$ MD-based results for the equilibrium properties of the two melts is excellent. This shows that, in the limit of infinite time ($t \rightarrow \infty$), the correct equilibrium properties are recovered by the $NTL_x\sigma_{yy}\sigma_{zz}$ MD method.

Table 8.1: Equilibrium results for the mean-square chain end-to-end distance $<R^2>$, the mean-square chain radius of gyration $<R^2_g>$, and the specific volume *v* for the C_{24} melt system as obtained by using (a) the present $NTL_x\sigma_{yy}\sigma_{zz}$ MD algorithm in the limit of long times; (b) equilibrium *NVT* MD (chapter 4) and (c) the EBMC algorithm in the absence of any field ($\alpha_{xx}=0$) (T=450 K and P_{ext}=1 atm).

	$NTL_x\sigma_{yy}\sigma_{zz}$	NVT	EBMC
$<R^2>$ (Å^2)	350 ± 20	350 ± 20	350 ± 20
$<R_g^2>$ (Å^2)	50 ± 10	50 ± 10	50 ± 10
V (cm^3/g)	1.419±0.08	1.385	1.409±0.05
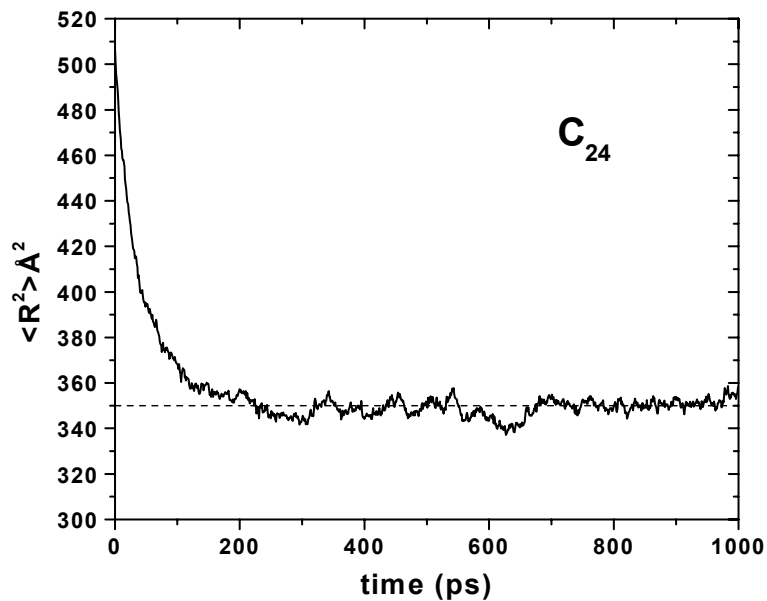
(a)
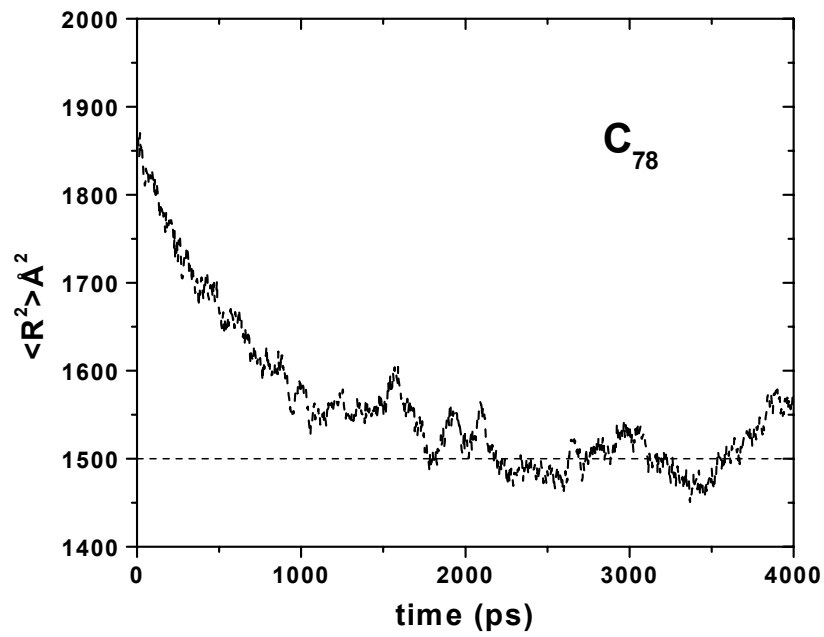
(b)

Figure 8.2 Time evolution of the mean-square chain end-to-end distance $<R^2>$ for (a) the C_{24} and (b) the C_{78} PE melt systems, averaged over all $NTL_x\sigma_{yy}\sigma_{zz}$ trajectories (T=450 K, P_{ext}=1 atm). The dashed lines in the figures show the equilibrium values of the mean square chain end-to-end distance $<R^2>_0$ for the two systems, obtained by EBMC or NVT MD equilibrium simulations

Table 8.2: Same as in Table 8.1 for the C_{78} system.

	NTL$_x\sigma_{yy}\sigma_{zz}$	NVT	EBMC
$<R^2>$ (Å^2)	1530 ± 50	1510 ± 40	1490 ± 100
$<R_g^2>$ (Å^2)	220 ± 10	225 ± 20	224 ± 10
v (cm^3/g)	1.23 ± 0.05	1.26	1.283± 0.003

Figures 8.3.a and 8.3.b show the time evolution of the lengths L_x and L_y (=L_z) of the model box in the x, y and z dimensions, averaged over all $NTL_x\sigma_{yy}\sigma_{zz}$ runs on the C_{24} and C_{78} PE melts. As required from the macroscopic restrictions imposed in the $NTL_x\sigma_{yy}\sigma_{zz}$ statistical ensemble, the box length L_x along the strain direction remains constant during the simulation. On the contrary, the lengths L_y and L_z in the other two directions fluctuate. The reader is reminded that the results shown in Figure 8.3 are actually averages over ca. 100 transient MD trajectories; each individual trajectory shows much higher fluctuations in L_y (= L_z). Despite the averaging, an oscillatory "ringing" pattern is seen in the evolution of L_y (= L_z). This ringing behavior is caused by the fact that the instantaneous box lengths L_y and L_z do not evolve independently but they are constrained to be equal to each other, as only one dynamic variable, the cross-sectional area A, is integrated in time. Recent simulations in the $NT\sigma_{xx}\sigma_{yy}\sigma_{zz}$ statistical ensemble [136], where all 3 box lengths L_x, L_y and L_z are allowed to evolve independently in time by employing the Berendsen method [16], are seen not to exhibit this ``ringing" behavior. For the C_{24} PE melt the density in the strained state is significantly higher than in the field-free state [72]. Thus L_y and L_z are seen to be always above the value of L_x, displaying the tendency of the system to return to the density of the equilibrium state. As mentioned above, the ensemble-average values of L_y and L_z at $t\rightarrow\infty$ are such that the density of the system is exactly the one corresponding to the same melt under equilibrium conditions.
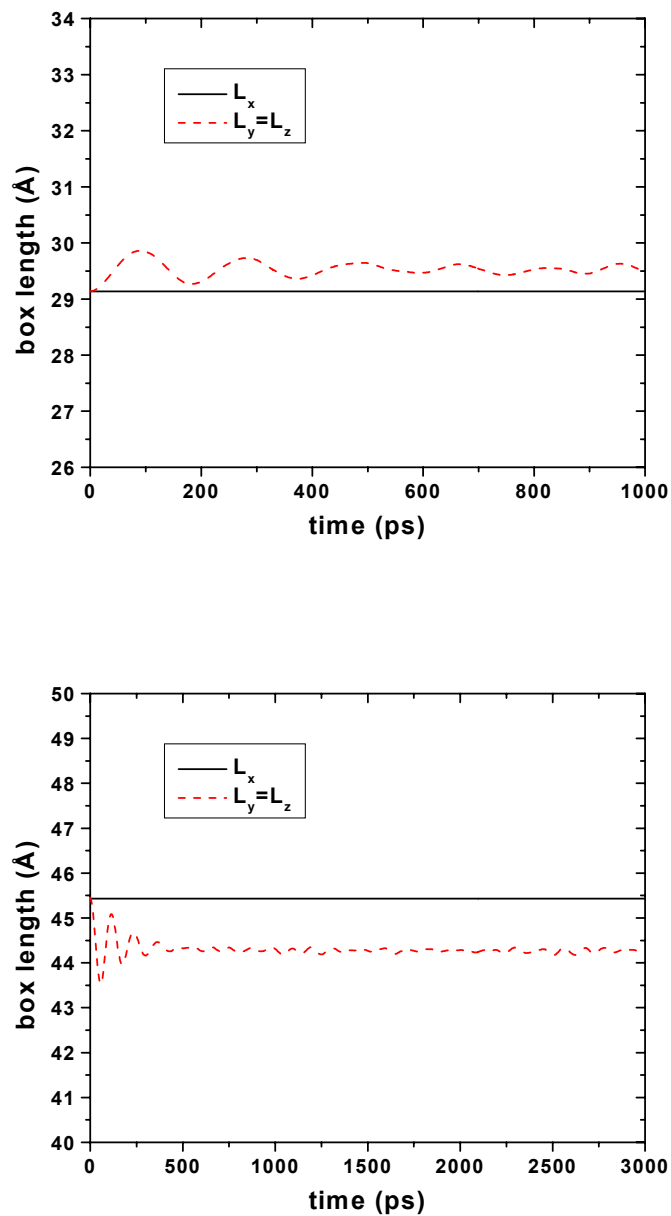
Figure 8.3 Time evolution of the lengths L_x and $L_y = L_z$ of the simulation box, as obtained from averaging over all simulated trajectories for (a) the C_{24} and (b) the C_{78} PE melt systems (T=450 K, P_{ext}=1 atm).
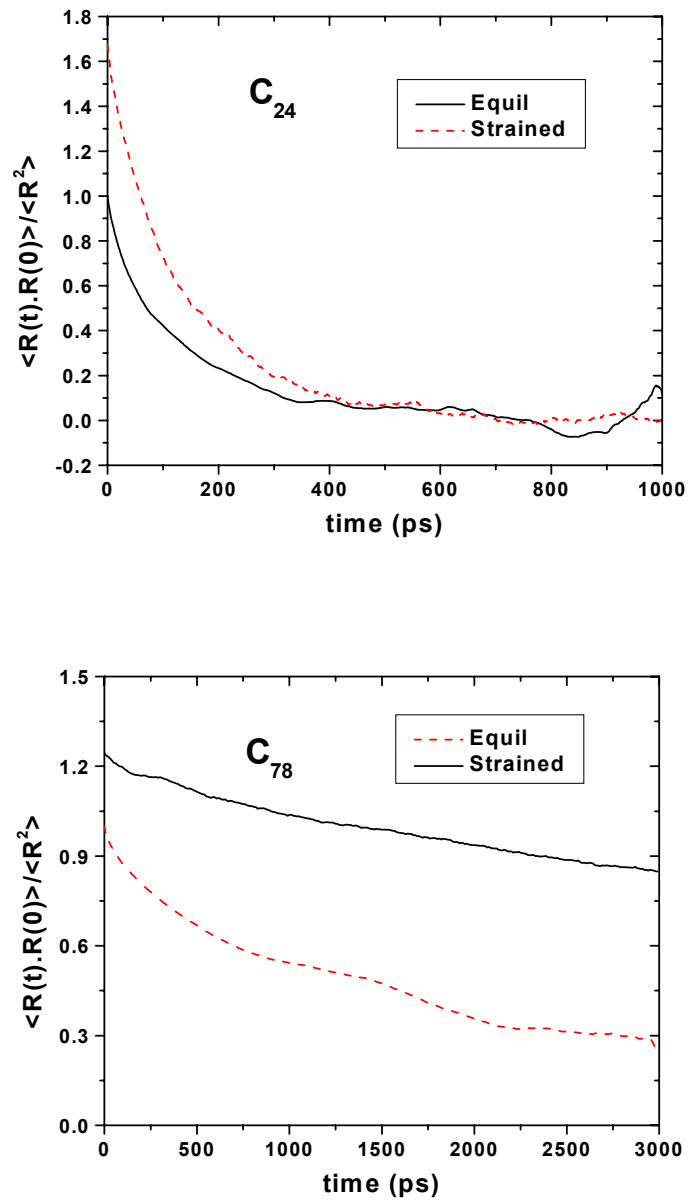
Figure 8.4 Decay of the scaled chain end-to-end vector orientational autocorrelation function $\langle \mathbf{R}(t)\cdot\mathbf{R}(0)\rangle / \langle R^2 \rangle_0$ in real time t for (a) the C_{24} and (b) the C_{78} PE melt systems. Solid lines correspond to results obtained from the preoriented configurations with the present $NTL_x\sigma_{yy}\sigma_{zz}$ MD algorithm and dashed lines correspond to results obtained from isotropic configurations with the equilibrium NVT MD algorithm (T=450 K, P_{ext}=1 atm).

B)   Relaxation of the chain end-to-end vector.

Figures 8.4a and 8.4b present the time autocorrelation function of the scaled end-to-end vector reduced by the equilibrium mean-square end-to-end distance, $\langle \mathbf{R}(t) \cdot \mathbf{R}(0) \rangle / \langle R^2 \rangle_0$, for the C_{24} and C_{78} PE melt systems, respectively. The rate at which this function approaches zero is a measure of the global relaxation of the chain, because it describes how fast the chain *forgets* its initial configuration. Also shown in the figures (dashed lines) are the corresponding curves obtained from the equilibrium *NVT* simulations on the same systems presented in chapter 4. The value obtained from the initially strained configurations at time $t = 0$ is larger than 1 because of the orientation in the x direction. The figures show clearly that, for each system, the time scale over which $\langle \mathbf{R}(t) \bullet \mathbf{R}(0) \rangle / \langle R^2 \rangle_0$ drops to zero is the same in both equilibrium and nonequilibrium simulations; it is governed by the Rouse time τ_R. Overall, about 300 ps are needed in the C_{24} melt system and certainly more than 3 ns in the C_{78} melt system, for $\langle \mathbf{R}(t) \bullet \mathbf{R}(0) \rangle / \langle R^2 \rangle_0$ to drop to zero. The fact that the maximal relaxation time is practically identical under equilibrium and nonequilibrium conditions confirms that the nonequilibrium experiments have been conducted in the linear regime.

C)   Relaxation of the conformation tensor components.

Figures 8.5.a and 8.5b show the time evolution of the diagonal components, c_{xx}, c_{yy} and c_{zz} of the conformation tensor for the C_{24} and C_{78} melt systems, respectively. For both systems the initial value of c_{xx} is significantly higher than 1, whereas those of c_{yy} and c_{zz} are a little smaller than 1, indicative of the oriented conformations induced by the imposed steady-state elongational flow field α_{xx}. As time evolves, c_{xx} drops, whereas c_{yy} and c_{zz} increase continuously, approaching the steady-state, field-free value of 1, indicative of fully equilibrated, isotropic structures in the absence of any deforming or orienting field. As already explained previously, all these results have been obtained through averaging over about 100 trajectories, all started at configurations oriented by the same value of the steady-state elongational flow field α_{xx}.

An interesting observation about the curves in Figures 8.5a and 8.5b is the following: Due to the cylindrical symmetry of the oriented structures, c_{yy} and c_{zz} should be equal at any time t and their time evolutions should be identical. Figure 8.5a shows this to be indeed true for the C_{24} system. For the C_{78} chain system, however, there appear

to be some deviations between c_{yy} and c_{zz}. This is statistical effect resulting from incomplete averaging. This can be understood if we take a look at Figure 8.1b, which shows the values of the three diagonal components of the conformation tensor in the plateau region of the steady-state elongational flow EBMC simulations. The initial configurations subjected to the $NTL_x\sigma_{yy}\sigma_{zz}$ MD simulations have been taken in their majority from the right-most part of the plateau region, where c_{yy} is higher than c_{zz}.
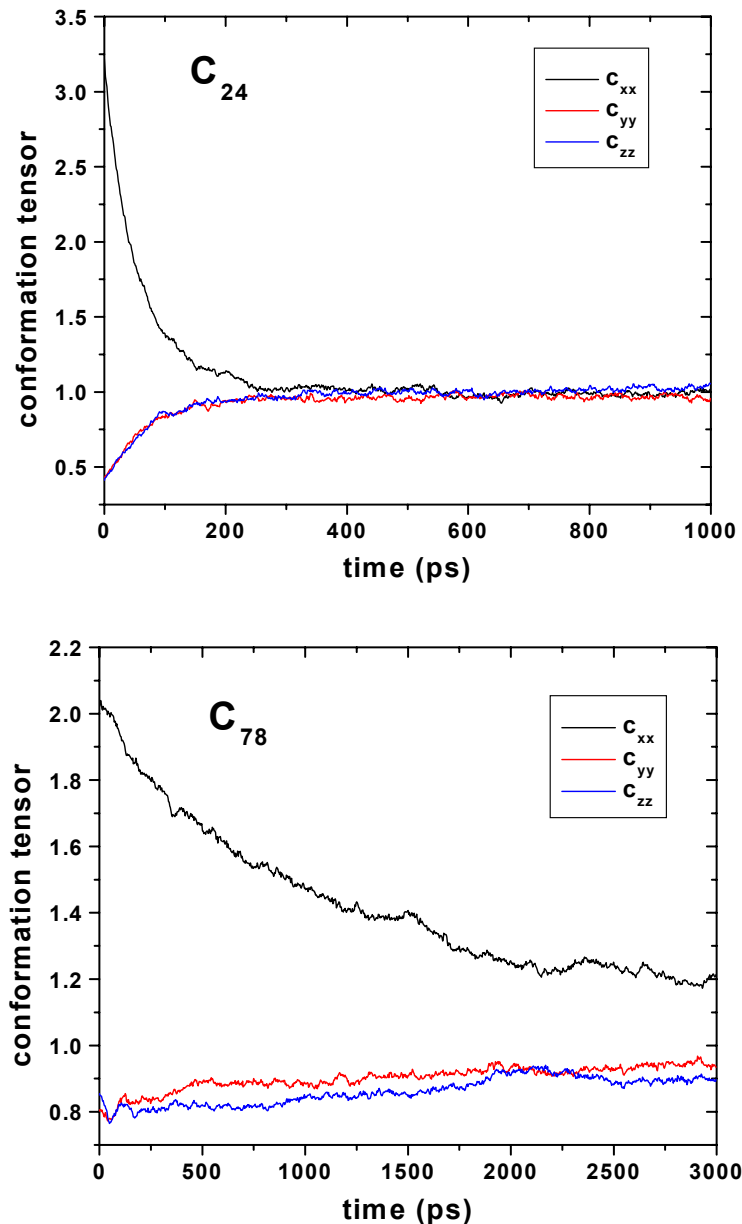

Figure 8.5 Evolution of the diagonal components c_{xx}, c_{yy} and c_{zz} of the conformation tensor **c** with time t for (a) the C_{24} and (b) the C_{78} PE melt systems. Results are averaged over all $NTL_x\sigma_{yy}\sigma_{zz}$ trajectories ($T = 450$ K, $P_{ext} = 1$ atm).

This manifests itself in the deviations seen in the MD relaxation curves. Clearly, a larger number of strained configurations from the plateau region of Figure 8.1b should be subjected to $NTL_x\sigma_{yy}\sigma_{zz}$ MD simulation in order for the two curves is c_{yy} and c_{zz} to fall on top of each other, as happens with the C_{24} system.

D)   Relaxation of the stress tensor components.

Figure 8.6 shows the time evolution of the stress tensor component σ_{xx}, for the C_{24} PE melt systems studied. Two curves are shown in each figure. The thin solid line tracks the evolution of σ_{xx} as obtained from applying the molecular virial theorem on the relaxing configurations and averaging over all dynamical trajectories. The thick dashed line tracks the evolution of σ_{xx} as obtained from applying the thermodynamic stress equation, Eq. (7.44), based on the current values of c_{xx} and $\partial A / \partial c_{xx}$, the latter taken from the melt elasticity simulations of ref. [72]. As expected, in both figures the estimates based on the virial theorem are subject to much higher statistical uncertainty, owing to the fluctuations in the instantaneous configurations. Clearly, averaging over many configurations is needed in order to improve the statistical quality of the virial theorem results. Apart from high-frequency noise, the virial theorem results display an oscillatory character similar to that of $L_y = L_z$, discussed in conjunction with Figure 8.3. When the noise and oscillations are smoothed out, the ensemble averaged stress $\sigma_{xx}(t)$ from the virial theorem is in very good agreement with the thermodynamic estimate obtained from c_{xx} and $\partial \left(A / N_{ch} \right) / \partial c_{xx}$. This is an important result, as it opens up the possibility of calculating stress with high precision directly from ensemble average conformational properties, based on a free energy function accumulated via efficient MC runs. The utility of Eq. (7.44) under transient conditions is demonstrated here for the first time. The transverse components σ_{yy} and σ_{zz} are displayed in Figure 8.7. Both σ_{yy} and σ_{zz} fluctuate continuously around the constant value $-P_{\text{atm}}$, as required by the macroscopic restrictions placed on the $NTL_x\sigma_{yy}\sigma_{zz}$ ensemble. Similar are the plots for the C_{78} system.
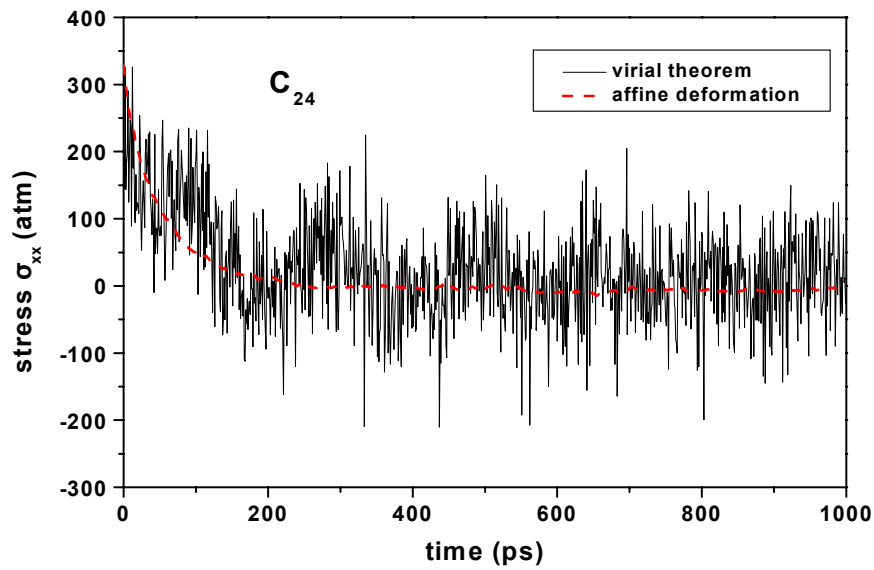
Figure 8.6 Evolution of the component σ_{xx} of the stress tensor with time t for the C_{24} system. The results at every time t have been obtained by applying either the virial theorem and averaging over all dynamical trajectories (thin solid line) or by using the thermodynamic expression, as explained in the text (thick broken line). Simulation conditions: T=450 K, P_{ext}=1 atm.
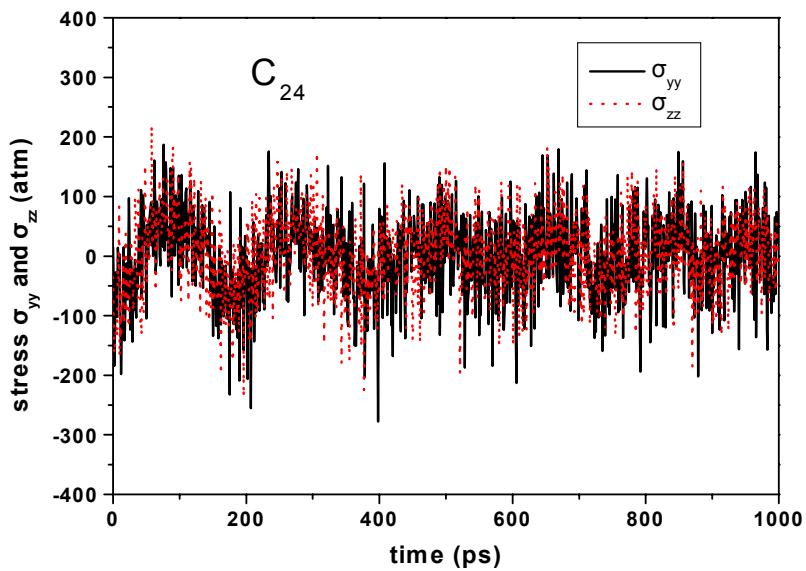

Figure 8.7 Evolution of the components σ_{yy} and σ_{zz} of the stress tensor with time t for the C_{24} system.

E)   Comparison to the Rouse model predictions.

For the two systems studied, the curves showing the relaxation of the quantities c_{xx} and σ_{xx} in the course of the $NTL_x\sigma_{yy}\sigma_{zz}$ runs, the latter quantity calculated from the thermodynamic expression, Eq. (7.44), are plotted collectively in Figures 8.8a and 8.8b for C_{24} and C_{78}, respectively. Also plotted in the same figures are best fits to $\sigma_{xx}(t)$ for the two model systems based on the Rouse model expression, Eq. (7.33). Two observations are important in Figures 8.7a and 8.7b: First, the time scale for the relaxation of the quantities c_{xx} and σ_{xx} is significantly smaller than the time scale characterizing the decay of the end-to-end vector autocorrelation function, $\langle \mathbf{R}(t) \bullet \mathbf{R}(0) \rangle / \langle R^2 \rangle_0$, shown in Figures 8.4a and 8.4b. According to the Rouse model predictions, Eqs. (7.33),(7.35) and (7.36), the dominant time governing the relaxation of c_{xx} and σ_{xx} should be shorter than that governing the relaxation of $\langle \mathbf{R}(t) \bullet \mathbf{R}(0) \rangle / \langle R^2 \rangle_0$ by a factor of 2. The simulation conforms closely to this prediction. Second, the fits to the stress relaxation function based on the Rouse model are indeed quite close. The same excellent comparison holds for the component c_{xx} of the conformation tensor. Results from fitting the Rouse model expression to the quantity $\langle \mathbf{R}(t) \bullet \mathbf{R}(0) \rangle / \langle R^2 \rangle_0$ under equilibrium conditions have been reported in chapter 4. Quantitative results from all three fittings are shown in Table 8.3. Table 8.3 presents the longest relaxation time τ_1 or Rouse time τ_R that best fits each one of the two curves in Figures 8.8a and 8.8b and the equilibrium curves in Figures 8.4a and 8.4b for the two PE melts simulated. To an excellent approximation, all estimates of τ_R are equal. This is a very significant result of the present work, because it shows that one can get the relaxation time spectra of an unentangled PE melt by performing $NTL_x\sigma_{yy}\sigma_{zz}$ MD simulations of stress relaxation on pre-oriented structures. Owing to the close relationship of c_{xx} and $\boldsymbol{\alpha}$ with the $\mathbf{RR}$ tensor, observing their decay in the course of a transient nonequilibrium simulation leads to the relaxation spectrum in half the simulation time that is required to observe the decay of $\langle \mathbf{R}(t) \bullet \mathbf{R}(0) \rangle / \langle R^2 \rangle_0$ under equilibrium or nonequilibrium conditions. The coincidence of relaxation time spectra between the current stress relaxation simulation and our earlier equilibrium MD runs on the same melts shows that the present stress relaxation MD simulations allow accessing the linear viscoelastic response of long-chain melts, which is practically impossible with previously applied nonequilibrium molecular dynamics methods.
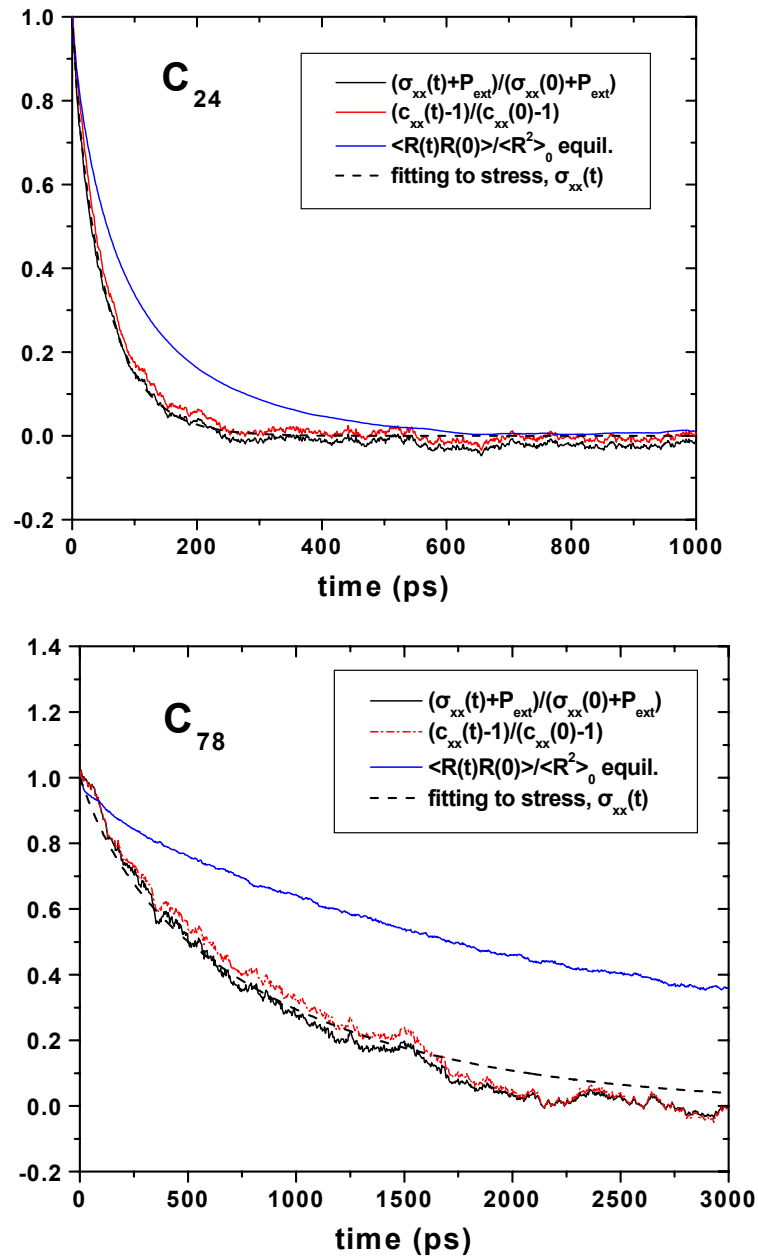
Figure 8.8 Collected results for the evolution with time t of (i) the conformation tensor component $c_{xx}(t)$, as an average over all $NTL_x\sigma_{yy}\sigma_{zz}$ trajectories, and (ii) the stress tensor component σ_{xx}, calculated from c_{xx} and $\partial(A/N_{ch})/\partial c_{xx}$ for (a) the C_{24} and (b) the C_{78} PE melt systems. Also shown in the figures are the best fits to the stress $\sigma_{xx}(t)$ according to the Rouse model.

The efficiency of our $NTL_x\sigma_{yy}\sigma_{zz}$ method is expected to increase for longer-chain, entangled PE melt systems, because the presence of entanglements should facilitate the return of the strained structures back to equilibrium. Consequently, the proposed methodology has the potential of alleviating the problem of long relaxation times

characterizing PE melts of high MW, by significantly cutting down the CPU times relative to those required to track the evolution of the corresponding equilibrium systems. Of course, simulation of a large number of dynamical trajectories initiated at preoriented configurations is needed, but this is not a problem given the availability of multiprocessor parallel machines and of the EBMC algorithm.

Table 8.3: Maximum relaxation time τ_R (ps), as obtained from fitting Eqs. (7.33) and (7.35) to $NTL_x\sigma_{yy}\sigma_{zz}$ MD results, and Eq. (7.36) to equilibrium NVT MD results (T=450K and P_{ext}=1 atm).

MD method	Quantity observed	C_{24}	C_{78}
$NTL_x\sigma_{yy}\sigma_{zz}$	$\dfrac{c_{xx}(t)-c_{xx}(\infty)}{c_{xx}(0)-c_{xx}(\infty)}$	115 ± 5	1950 ± 100
$NTL_x\sigma_{yy}\sigma_{zz}$	$\dfrac{\sigma_{xx}(t)-\sigma_{xx}(\infty)}{\sigma_{xx}(0)-\sigma_{xx}(\infty)}$	115 ± 5	2000 ± 10
equilib. NVT	$\langle \mathbf{R}(t)\bullet\mathbf{R}(0)\rangle$	115 ± 10	2030 ± 100

F)   The shear stress relaxation modulus $G(t)$.

The shear stress relaxation modulus, $G(t)$, can be reconstructed from the values of τ_R obtained by mapping the simulation results to the Rouse model, using the equation [..]:

$$G(t)=\frac{\rho RT}{M}\sum_{p:all}\exp\left(-\frac{2p^2t}{\tau_1}\right) \tag{7.46}$$

The results for the C_{24} and C_{78} chain systems simulated in this work are shown in Figure 8.9. The Rouse model describes mainly the terminal region and is not valid for very short times. In Figure 8.9 the curves based on Eq. (7.46) are shown for times longer than the relaxation time of a polymer segment of size equal to the Kuhn segment of a PE chain. A rough calculation shows that such a Kuhn segment consists of about 10 bonds, which suggests a relaxation time on the order of 20 ps [137]. This time is also consistent with the time needed for the full decorrelation of the torsional degrees of freedom of a PE

chain at the same temperature. The figure shows clearly that for times $t \geq 20$ ps the predicted $G(t)$ functions exhibit the usual Rouse behavior, characteristic of an unentangled system.

The shear stress relaxation modulus can also be calculated by using the relevant Green-Kubo equation. According to the latter, the zero-shear rate viscosity η_0 is given by the time integral of the time autocorrelation function of the off-diagonal components of the instantaneous stress-tensor [138]:

$$\eta_0 = \frac{V}{k_B T} \int_0^\infty \left\langle \sigma_{\alpha\beta}(0)\sigma_{\alpha\beta}(t) \right\rangle \tag{7.47}$$

By combining this with equation

$$\eta_0 = \int_0^\infty G(t)dt \tag{7.48}$$

valid for an unentangled melt in the limit of linear viscoelasticity, we conclude that G(t) can be estimated as

$$G(t) = \frac{V}{k_B T} \left\langle \sigma_{\alpha\beta}(0)\sigma_{\alpha\beta}(t) \right\rangle \tag{7.49}$$

The instantaneous stress tensor in the above equations should be calculated by MD simulations from equilibrium (i.e., quiescent) conditions, by using the virial theorem. Due to the strong fluctuations in the values of the off-diagonal components of the instantaneous stress tensor, extremely long configurational averaging is required in order to calculate $G(t)$ accurately [81]. We have conducted a large number of equilibrium NVT MD runs for the C_{24} system, each for a time period of about 1ns, and the result for $G(t)$ obtained through Eq. (7.49), by applying also the technique of averaging over multiple time origins, is shown in Figure 8.9 by the dashed line. It is evident in the figure that the short time scale, Green-Kubo prediction for the evolution of $G(t)$ with t is above the curve obtained by the Rouse equation, corresponding to the regime of intermediate and long time scales. It is also evident that, within the statistical noise, the part of the curve following the typical Rouse behavior constitutes a smooth continuation of the part of curve obtained with the Green-Kubo relation. A further point to notice in Figure 8.9 is the value of $G(t)$ at time $t = 0$. This value is about $9.0 \ 10^9$ Pa, which is somewhat higher than the value of $G(t)$ (about 10^9 Pa) for a polymer in the glassy regime; it drops quickly to the value of $2 \ 10^8$ Pa over the time interval 0.1 to 1 ps, beyond which it exhibits a weaker time dependence, quite similar to the one seen in our Rouse model-based

predictions. The statistical noise of results for $G(t)$ obtained through the Green-Kubo relation makes it impossible to address reliably the regime $t > 10$ ps, which is most interesting from the point of view of rheological properties in the terminal region.
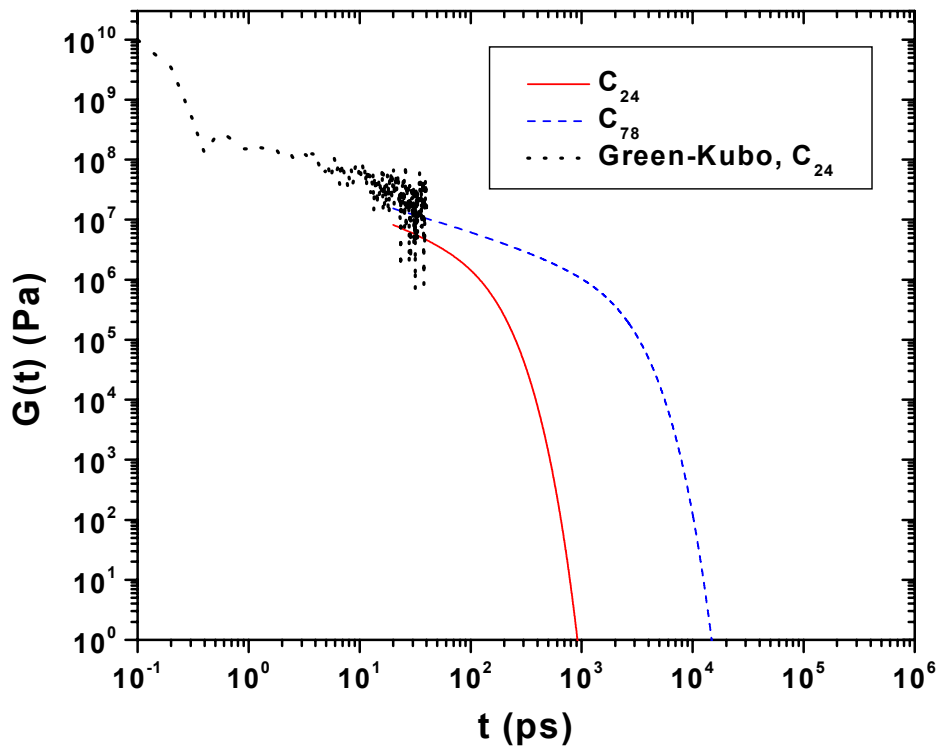
Figure 8.9 The relaxation modulus $G(t)$ for the C_{24} and the C_{78} PE chain systems. The curves have been reconstructed with the values of τ_R obtained by mapping the simulation results onto the Rouse model. $G(t)$ for C_{24}, as calculated directly from the Green-Kubo expression, is shown as a broken line on the left-hand side, short time region of the figure.

8.6.   Conclusions

Pre-strained PE melt configurations have been subjected to detailed atomistic MD simulations in the $NTL_x\sigma_{yy}\sigma_{zz}$ statistical ensemble. The pre-oriented configurations have been sampled with the end-bridging MC algorithm in the presence of an orienting field α_{xx}, representative of steady-state elongational flow at Deborah numbers smaller than 1. In the $NTL_x\sigma_{yy}\sigma_{zz}$ MD simulations, the field α_{xx}, which caused the polymer melt orientation during the EBMC calculations, is removed and the return of the system back to equilibrium is monitored. Constraining the box length L_x in the x-direction causes a gradual decrease of the stress component σ_{xx} down to its field-free equilibrium value (-

P_{ext}). The physical experiment being simulated, therefore, is stress relaxation upon cessation of steady-state, uniaxial elongational flow.

Results have been presented for the temporal evolution of the stress component σ_{xx}, the diagonal components c_{xx}, c_{yy} and c_{zz} of the conformation tensor $\mathbf{c}$, and the scaled end-to-end vector orientational autocorrelation function $\langle \mathbf{R}(t) \bullet \mathbf{R}(0) \rangle / \langle R^2 \rangle_0$. All these results have been accumulated as configurational averages over many $NTL_x\sigma_{yy}\sigma_{zz}$ trajectories initiated at different pre-strained configurations corresponding to the same value of α_{xx} for two model PE melt systems with uniform molecular weight distributions and polydispersity index 1.09: a 32-chain C_{24} and a 40-chain C_{78} melt.

The average stress σ_{xx} of the ensemble of relaxing configurations has been calculated as a function of time in two ways: via the molecular virial theorem, and via a thermodynamic expression involving the functional dependence of the Helmholtz energy upon the conformation tensor; the latter functional dependence has been determined previously through EBMC simulations of oriented melts. The two ways of calculating the stress yield consistent results, with the free energy-based expression being subject to much less statistical noise than the molecular virial expression. The utility of the thermodynamic expression is thus confirmed under (linear) nonequilibrium conditions.

By solving the appropriate Smoluchowski equation for the evolution of the time autocorrelation functions $\langle \mathbf{X}_p(t) \bullet \mathbf{X}_p(0) \rangle$ of the Rouse normal modes $\mathbf{X}_p$, $p = 0,1,2,...$, subject to the initial conditions of the simulated relaxation experiment, analytical expressions have been derived for the time evolution of all three quantities σ_{xx}, c_{xx} and $\langle \mathbf{R}(t) \bullet \mathbf{R}(0) \rangle / \langle R^2 \rangle_0$. These analytical expressions provide an excellent description of the simulation results. By fitting the simulation results to the analytical expressions, the longest or Rouse relaxation time τ_R has been extracted for the two PE melts studied, the C_{24} and C_{78}. Identical values for the time τ_R are obtained from the relaxation of σ_{xx}, c_{xx} and $\langle \mathbf{R}(t) \bullet \mathbf{R}(0) \rangle / \langle R^2 \rangle_0$, which proves the internal consistency of the simulation results and the ability of the Rouse model to describe the viscoelastic properties of these two PE melts. Furthermore, the values of τ_R and the associated relaxation time spectra extracted from the relaxation simulations are identical to those determined in the past through equilibrium simulations of the same melts. This confirms that the present simulations have been carried within the linear regime.

The shear stress relaxation modulus $G(t)$ has been calculated from the equilibrium autocorrelation function of the instantaneous shear stress at short times and from the spectrum of relaxation times extracted by mapping the simulation results onto the Rouse model at long times. The two approaches yield consistent results and a shape of the $G(t)$ function typical of unentangled melts.

The simulation results and the Rouse analysis show that the relaxation of σ_{xx} and c_{xx} takes place in a time scale shorter by a factor of 2 than the time characterizing the decay of the end-to-end vector orientational autocorrelation function $\langle \mathbf{R}(t) \bullet \mathbf{R}(0) \rangle / \langle R^2 \rangle_0$ under equilibrium or nonequilibrium conditions. By reducing the CPU time required to capture the spectrum of relaxation times of long linear PE melts by a factor of two, the present methodology helps alleviate the problem of long relaxation times, from which all equilibrium and non-equilibrium MD simulations of long-chain melts have suffered. By relying on the EBMC algorithm for generating large numbers of uncorrelated, oriented initial configurations and employing a precise thermodynamic expression of the stress cast in terms of the dependence of the free energy on coarse-grained structural variables, such as the conformation tensor, this method opens up the way towards the dynamic simulation of truly polymeric, entangled systems.

CHAPTER 9

CONCLUSIONS AND RECOMMENDATIONS

3.5. Conclusions

The design of efficient and reliable molecular modeling techniques for predicting the physical properties of polymers from chain chemical constitution is a challenging but worthwhile objective. In particular, modeling dynamic properties in the molten state is of great significance in all polymer processing industries, since these properties govern the processability of the melts. This explains the recent increased interest in dynamic simulations of chain liquids, particularly of systems that composed of longer chain molecules or molecules with a more complex than linear architecture.

The main object of the work presented here was to offer a clear understanding of the dynamics of polymer melts from the molecular point of view through atomistic molecular dynamics simulations. To overcome the inherit limitations of atomistic MD simulations a hierarchical methodology was followed that combines both MC and MD simulations and a direct mapping of the MD simulation data onto proper theoretical mesoscopic models. The hierarchical methodology is a three-stage approach, whereby the dynamic properties of polymer melts are calculated through the following procedure:

d) First the simulated systems are equilibrated through a very powerful MC algorithm, the end-bridging Monte Carlo (EBMC) method. With this algorithm very long polymer melts have been fully equilibrated at all length scales. This method can equilibrate the long-length scale features of a polymer melt orders of magnitude more efficiently than MD or other MC methods, its relative efficiency increasing dramatically with increasing chain length.

e) After the relaxed configurations obtained are subjected to detailed atomistic MD simulations to study their dynamic and rheological properties. The MD simulations involving a MTS algorithm and track the evolution of the modeled systems for time up to a few hundreds of ns.

f) Finally a mapping of the MD simulation data onto an appropriate theoretical mesoscopic model was performed. The model used for unentangled polymer systems was the Rouse model whereas for the longer systems was the reptation theory.

With the above hierarchical scheme results were presented for the dynamic and viscoelastic properties of several systems. Model PE systems have been simulated with various molecular length s, ranging from C_{16} up to C_{250}. By applying the Einstein relation, the self-diffusion coefficient was calculated exhibits three distinct regions:

d) A small-MW, alkane-like behavior ($N<60$), where D follows a power-law dependence $D\sim MW^{-b}$, with $b>1$. Detailed MD simulations in this range of molecular lengths show an exponent b varying smoothly with temperature from 2.4 at 323 K to 1.9 at 443 K. In this regime, chain end effects, which can be described through a free volume theory, dominate the system dynamics. The contribution V_e of chain free ends to the free volume of the system was calculated by fitting the density-versus-molecular weight M data to a hyperbolic function,, as a function of the temperature T. This was compared and found in excellent agreement with independent data obtained from the tessellation of space in Delaunay tetrahedra and with experimental data. By further mapping the simulation results onto the combined Bueche-von Meerwall theory for the self-diffusion of short alkanes, expressions were obtained for the fractional free volume $f(T,\infty)$ and the apparent activation energy E_α^{app} as a function of temperature and molecular weight, respectively.

e) An intermediate regime (from $N=60-70$ up to $N=156$) where $b \approx 1$. The dynamics of systems in this regime is quite well described with the Rouse theory.

f) A long chain-length, reptation-like regime ($N>156$), where chain diffusivity exhibits a dramatic slow down, $b \approx 2.5$. According to the original formulation of reptation theory, the latter exponent should be 2. Phenomena such as contour length fluctuations (CLF) and constraint release (CR) typically accelerate the escape of the chain from the tube, causing an increase in D and a decrease in η_0. A recently proposed theory that incorporates CLF and CR phenomena predicts a stronger exponent, between –2.2 and –2.3. These values agree with recent experimental results for concentrated polymer solutions and melts, which suggest an exponent between –2.2 and –2.4 for a variety of polymer systems [..].

We have also presented a consistent way of mapping the atomistic MD data onto the Rouse and the reptation molecular models. The mapping onto the reptation theory involved an intermediate projection step of the atomistically detailed chains onto primitive paths [..]. The Rouse model was seen to produce consistent (chain-length independent) results for the monomer friction factor ζ only in the interval of chain lengths $70<N<156$. For chain lengths $N>156$, only the reptation model was capable of producing consistent results for ζ. The tube diameter a was estimated to be about 60 Å. The zero-shear rate viscosity η_0 was also calculated, using Rouse model for the shorter systems and the reptation theory for the longer ones. The values of η_0 extracted from the simulations were seen to agree remarkably well with recently obtained experimental η_0 measurements on model linear PE's.

The single chain dynamic structure factor $S(q,t)$ was also calculated directly from the atomistic MD simulations for various q values. Deviations from the Rouse model were found as q increases (big values of q correspond to smaller lengths that do not exhibit Rouse-like behavior) and as the molecular weight increases (influences of the entanglements).

The diffusion of binary blends of n-alkane liquids was also studied with the methodology presented above. The simulation results have been compared to the predictions of two free volume theories; (a) the free volume theory proposed by Vrentas and Duda for the prediction of diffusivity of small penetrants into a polymer matrix and (b) the combined Rouse diffusion and chain-end free volume theory of Bueche and von Meerwall, designed to describe the diffusion coefficient of both components in a binary liquid system.

The predictions of the free volume theory were found to be in very good agreement with the MD simulation results for small and intermediate w_1 values ($w_1 < 0.7$-0.8). In the dilute regime ($w_1 > 0.7$-0.8), however, the free volume theory significantly underestimates the solvent diffusion coefficient. This should be expected, given that one of the major assumptions of the free volume theory is the presence of a significant amount of polymer molecules in the mixture.

The parameters needed in applying the combined Rouse diffusion and chain-end free volume theory of Bueche and von Meerwall theory were taken from regressions of density and diffusion data of a series of monodisperse liquid *n*-alkane systems performed

by non Meerwall *et al*. [..]. The theory was found to describe MD results for the diffusion of both components over the entire range of concentrations semiquantitatively.

To study the flow properties of the polymeric systems the above methodology has been extended to systems under non-equilibrium (flowing) conditions. A new MC method has been developed for the application of a thermodynamic field, MD simulations conducted in a new statistical ensemble and the simulation data were mapped onto the proper expressions the mesoscopic model predicts for systems under the corresponding flowing conditions.

For the generation of the initial oriented configurations a modification of the EBMC was developed to generate configurations under nonequilibrium conditions. Sampling oriented melts under conditions of steady-state elongational flow with this algorithm relies upon postulating that the free energy of such a melt is a function of density, temperature, and of a coarse-grained descriptor of the overall conformation of chains, which we call the conformation tensor, **c**. The partial derivatives of the free energy with respect to the elements of **c** define a thermodynamic field **α**, whose elements are physically analogous to Deborah numbers. Oriented configurations corresponding to steady-state uniaxial elongational flow, such as that encountered in fiber spinning, are sampled with EBMC under a prescribed value of α_{xx}, all other elements of **α** being zero. In the present work this value of α_{xx} is everywhere smaller than 1, to keep the computer experiments within the linear viscoelastic regime.

Then the oriented melt configurations have been subjected to detailed atomistic MD simulations in the $NTL_x\sigma_{yy}\sigma_{zz}$ statistical ensemble. In the $NTL_x\sigma_{yy}\sigma_{zz}$ MD simulations, the field α_{xx}, which caused the polymer melt orientation during the EBMC calculations, is removed and the return of the system back to equilibrium is monitored. Constraining the box length L_x in the x-direction causes a gradual decrease of the stress component σ_{xx} down to its field-free equilibrium value ($-P_{ext}$). The physical experiment being simulated, therefore, is stress relaxation upon cessation of steady-state, uniaxial elongational flow.

The hierarchical approach for the study of non-equilibrium systems described here, overcomes several limitations of conventional NEMD simulations, as they have been applied in the past to polymer melts: (a) There is no strain rate imposed externally in the course of the dynamic simulation; the melt is allowed to relax *at its own pace*, and not forced into flow situations that are far removed from experimental and processing practice. (b) Initial oriented configurations are prepared with EBMC, not MD, under

conditions corresponding to small-strain rate, steady-state elongational flow. EBMC is much more efficient than MD in equilibrating properties, which depend on structure at the length scale of entire chains. It thus yields a well-defined ensemble of preoriented configurations, no matter how long the chains or how weak the orienting fields are. The use of weak orienting fields ensures that the whole relaxation experiment is conducted within the linear viscoelastic regime. (c) Stress is calculated from the overall chain conformation via a free energy-based expression, which affords excellent signal-to-noise ratio. Stresses based on this expression are found to be fully consistent with average stresses from the molecular virial theorem, to the extent that fluctuations in the latter allow such a comparison.

Results have been presented for the temporal evolution of the stress component σ_{xx}, the diagonal components c_{xx}, c_{yy} and c_{zz} of the conformation tensor $\mathbf{c}$, and the scaled end-to-end vector orientational autocorrelation function $\langle \mathbf{R}(t) \bullet \mathbf{R}(0) \rangle / \langle R^2 \rangle_0$. All these results have been accumulated as configurational averages over many $NTL_x\sigma_{yy}\sigma_{zz}$ trajectories initiated at different pre-strained configurations corresponding to the same value of α_{xx} for two model PE melt a C_{24} and a C_{78} melt.

The simulation results and the Rouse analysis show that the relaxation of σ_{xx} and c_{xx} takes place in a time scale shorter by a factor of 2 than the time characterizing the decay of the end-to-end vector orientational autocorrelation function $\langle \mathbf{R}(t) \bullet \mathbf{R}(0) \rangle / \langle R^2 \rangle_0$ under equilibrium or nonequilibrium conditions. By reducing the CPU time required to capture the spectrum of relaxation times of long linear PE melts by a factor of two, the present methodology helps alleviate the problem of long relaxation times, from which all equilibrium and non-equilibrium MD simulations of long-chain melts have suffered. By relying on the EBMC algorithm for generating large numbers of uncorrelated, oriented initial configurations and employing a precise thermodynamic expression of the stress cast in terms of the dependence of the free energy on coarse-grained structural variables, such as the conformation tensor, this method opens up the way towards the non-equilibrium simulation of truly polymeric, entangled systems.

3.6.   Recommendations for Future Work

The recommendations of this work for future plans consider the study of two different regimes: dynamics of polymer systems at equilibrium and dynamics of polymer systems under non-equilibrium.

a.   The present study focused on the estimation of the diffusion and rheological properties of long, entangled PE up to C_{250}, for the first time from atomistic MD simulations. The systems studied here are in the crossover regime from Rouse to reptation dynamics. To get a more clear picture of the polymer dynamics of well entangled systems and of the validity of the reptation theory, MD simulations of longer systems are needed. Thus, future plans concerns the extension of the hierarchical methodology presented here to even longer PE melts, from C_{400} up to C_{1000}. These systems are expected to be well in the entangled regime and a direct comparison with NSE and double-quantum nuclear magnetic resonance (DQ NMR) experiments can be performed.

b.   The second part of our hierarchical approach concerns the study of polymer systems under flowing conditions. The atomistic modeling of the stress relaxation experiment upon cessation of steady-state elongational flow has been presented. The future plans concern the extension of the methodology to other types of steady-state flows, such as the simple shear and the biaxial elongational flow. This will be possible with the use of the proper values of the thermodynamic field **α**.

APPENDIX A

TIME CORRELATION FUNCTIONS

An important quantity characterizing the degree to which two dynamical quantities are correlated in time is the time correlation function, which is operationally defined in the following way. Consider a physical quantity A and suppose we measure it for many samples in the equilibrium state. The time autocorrelation function of $A(t)$ is defined [6], in a discretized form, as

$$C_{AA}(t) = \langle A(t)A(0)\rangle = \frac{1}{T}\sum_{\tau=1}^{T} A(\tau)A(t+\tau) \tag{A.1}$$

Typical behavior of $<A(t)A(0)>$ is as follows. At time $t = 0$, $C_{AA}(0)$ is positive and equal to the mean square of A in the equilibrium state, $\langle A^2\rangle$. As time passes the value of $A(t)$ becomes uncorrelated with $A(t+\tau)$ and consequently the value of $C_{AA}(t)$ decreases. After a sufficiently long time the $A(t)$ and $A(t+dt)$ becomes totally uncorrelated and $\lim_{t\to\infty}\langle A(t)A(0)\rangle = \langle A(0)\rangle\langle A(t)\rangle = \langle A\rangle^2$. Thus the correlation function of A decays with time from $\langle A^2\rangle$ to $\langle A\rangle^2$.

In practice what we are doing is first to have measures of the physical quantity A at equal intervals of time dt. Then we average over T time origins the product of A at time τdt and A at time tdt later (multiple time origin technique). For each value of t, the value of $t+\tau$ must not exceed the total number of times we have calculated A. Thus the short-time correlations are determined with slightly better statistical precision as the number of terms in the average, T, is larger. Time correlation functions of different properties are discussed in many chapters.

APPENDIX B

THE FIXMAN POTENTIAL

Consider a macromolecular, polymer, chain of N atoms with constraint bond lengths of the form

$$l_i = \left| \mathbf{R}_i - \mathbf{R}_{i-1} \right|, \quad i = 1,2,\ldots,N\text{-}1 \tag{B.1}$$

There are two models to incorporate properly in the simulation the fixed bonds [..]. The first is the *rigid model* where the momenta conjugated to constrained coordinates are ignorable. Ignoring them gives arise to an additional coupling between the unconstrained coordinates, a coupling that is not present in potential energy. The second one is the *flexible model in the limit of infinite stiffness*, where the conjugated momenta are thermally activated. Then, at equilibrium, the coupling between unconstrained coordinates arises solely from the potential energy. Thus when we are treating a rigid model an additional potential should be used to make the model sample the configuration-space probability characteristic of a flexible model in the limit of infinitely stiff bond stretching force constants. This is the so-called Fixman potential [..].

The Fixman potential for a chain of N sites numbered from 0 to N-1, (N-1) bonds numbered from 1 to N-1 and (N-2) bond angles numbered from 1 to N-2, has the form [78]

$$V_{Fixman} = \frac{k_B T}{2} \ln \left[\det \mathbf{H}_N \right] + k_B T \ln \left(l_1^2 l_2^2 \ldots l_{N-1}^2 \right) \tag{B.2}$$

where $l_1 = l_2 = \ldots = l_{N-1} = l$ are the constant bond lengths and $\mathbf{H}_N$ is the matrix

$$\mathbf{H}_N = \begin{pmatrix} \mu_1 & \gamma_1 & & & 0 \\ \gamma_1 & \mu_2 & & & 0 \\ & & 0 & 0 & \\ 0 & & \mu_{N-2} & \gamma_{N-2} \\ 0 & & \gamma_{N-2} & \mu_{N-1} \end{pmatrix} \tag{B.3}$$

with

$$\mu_i = \frac{1}{m_{i-1}} + \frac{1}{m_1}, \qquad \gamma_i = \frac{\cos\theta_i}{m_i} \tag{B.4}$$

In this equation m_i is the mass of the i-th skeletal site and θ_i the i-th bond angle. The determinant $h_N = \det \mathbf{H}_N$ can be calculated recursively, through the equation

$$h_i = \mu_{i-1}h_{i-1} - (\gamma_{i-2})^2 h_{i-2} \qquad\qquad 3 \leq i \leq N \tag{B.5}$$

with $h_1 = 1$ and $h_2 = (1/m_0)+(1/m_1)$. The total Fixman potential, V_{Fixman}, is a sum of contributions of the form of Eq. (B.2) from all "parent" chains in the system.

The force on any particle i in the model system due to the Fixman potential is calculated as

$$\mathbf{F}_i^{Fixman} = -\frac{\partial V_{Fixman}}{\partial \mathbf{R}_i} \tag{B.6}$$

with $\mathbf{R}_i$ the position vector of the particle, by making use of the recursive relations, Eq. (B.5).

APPENDIX C

DISCRETE ROUSE MODEL

The Rouse model can be defined for a continuous model chain and for a discrete polymer chain. The solution for a continuous model chain is described in details elsewhere [6]. For mapping the molecular simulation results onto the Rouse model, however, the continuous form of it is not valid since the physical system consisting of discrete atoms. Thus it is more appropriate for someone to use the discrete solution of the Rouse model. This is described in this appendix.

The basic key in the Rouse model, as it was stated in section 3.2, is the notion of normal modes. Consider a physical system consisting of N atoms (beads). The normal modes, or coordinates, in the Rouse model can be defined using either the position vectors $\mathbf{R}_i$ ($i=0,1,...,N$-1) or the connector vectors $\mathbf{Q}_i \equiv \mathbf{R}_i - \mathbf{R}_{i-1}$ ($i=1,..,N$-1) of the beads. Although both definitions should lead to consistent results, as they involve a linear transformation between the two sets of vectors, the final equations for the time autocorrelation functions of the normal modes present some differences, which will be reported in this Appendix.

The first way to define the normal coordinates is through the position vectors [..] through the

$$\mathbf{X}_p = \sum_{j=1}^{N} \Omega_{jp} \mathbf{R}_{j-1} \tag{C.1}$$

where Ω_{jp} are the elements of the orthogonal matrix $\mathbf{\Omega}$ given by

$$\Omega_{jp} = \sqrt{\frac{2 - \delta_{p0}}{N}} \cos\left(\frac{(j-1/2)p\pi}{N}\right) \tag{C.2}$$

The eigenvalues of $\mathbf{\Omega}$ are given by

$$\lambda_p = 4\sin^2\left(\frac{p\pi}{2N}\right), \qquad p = 0,1,...N \tag{C.3}$$

The second way is to define the normal coordinates through the connector vectors, $\mathbf{Q}_j$ [35]

$$\mathbf{X}_p = \sum_{i=1}^{N-1} \Omega'_{jp} \mathbf{Q}_j \tag{C.4}$$

where $\mathbf{Q}_j = \mathbf{R}_{j+1} - \mathbf{R}_j$ and Ω'_{jp} are the elements of the orthogonal matrix $\mathbf{\Omega'}$, given by

$$\Omega'_{jp} = \sqrt{\frac{2}{N}} \sin\left(\frac{jp\pi}{N}\right) \tag{C.5}$$

with j=1,...,N-1 and p=1,...,N-1. The eigenvalues of $\mathbf{\Omega'}$ are given by

$$\lambda'_p = 4\sin^2\left(\frac{p\pi}{2N}\right), \qquad p = 1,2,...N \tag{C.6}$$

Note that $\mathbf{\Omega'}$ is a (N-1) x (N-1) matrix, whereas $\mathbf{\Omega}$ is a N x N matrix. On the other hand, the matrix $\mathbf{\Omega}$ is singular, its first eigenvalue being zero and all its nonzero eigenvalues coinciding with those of $\mathbf{\Omega'}$.

The analysis to find the time autocorrelation function of the normal modes proceeds by transforming the Langevin equation for the position vectors to a corresponding equation for the normal coordinates, using the orthogonality property of the matrices $\mathbf{\Omega}$ or $\mathbf{\Omega'}$. An important step in the transformation procedure is the way in which the random forces on the beads are transformed from the original to the eigenvector space. If, for example, $\mathbf{f}_n$ is the random force on bead n in the original Cartesian space, then the existence of a friction factor ζ for the interaction of beads with the viscous medium implies that

$$\left\langle f_{n\alpha}(t) f_{m\beta}(t') \right\rangle = 2\zeta k_B T \delta_{nm} \delta_{\alpha\beta}(t - t') \tag{C.7}$$

To be able to derive the time autocorrelation function for the normal modes, a similar expression should be written for the transformed force $\mathbf{f}_p$ on mode p, that is, we assert that there exists a friction constant ζ_p such that

$$\left\langle f_{p\alpha}(t) f_{q\beta}(t') \right\rangle = 2\zeta_p k_B T \delta_{pq} \delta_{\alpha\beta}(t - t') \tag{C.8}$$

The task therefore is to find the relation between ζ_p and ζ for the two definitions of the normal modes.

In the case where the normal modes are defined based on the position vectors of the beads we have

$$\left\langle f_p(t) f_p(0) \right\rangle = \frac{\zeta_p^2}{\zeta^2} \sum_{j=1}^{N-1} \Omega^{-1}_{pj} \Omega^{-1}_{pj} \left\langle f_j(t) f_j(0) \right\rangle =$$
$$= \frac{\zeta_p^2}{\zeta^2} \left(\frac{2 - \delta_{p0}}{N}\right) 2\zeta k_B T \delta(t) \sum_{j=1}^{N-1} \cos^2\left(\frac{(j - 1/2)p\pi}{N}\right) \tag{C.9}$$

and from Eq. (C.8) we have

$$\zeta_p = \frac{N\zeta}{(2-\delta_{p0})\sum_{j=1}^{N-1}\cos^2\left(\frac{(j-1/2)p\pi}{N}\right)} = \begin{cases} \dfrac{N\zeta}{1(N-1)} \cong \zeta, & p=0 \\[4mm] \dfrac{N\zeta}{2N/2} = \zeta, & p>0 \end{cases} \qquad (\text{C.10})$$

In the case where the normal modes are defined based on the connector vectors of the beads, following a similar approach, it is found that:

$$\zeta_p = \frac{N\zeta}{4\left(1-\cos\left(\dfrac{p\pi}{N}\right)\right)\sum_{j=1}^{N-1}\sin^2\left(\dfrac{pj\pi}{N}\right)} = \begin{cases} \dfrac{N\zeta}{4\left(1-\cos\left(\dfrac{p\pi}{N}\right)\right)}, & p=0 \\[6mm] \dfrac{\zeta}{2\left(1-\cos\left(\dfrac{p\pi}{N}\right)\right)}, & p>0 \end{cases} \qquad (\text{C.11})$$

After having defined the relation between ζ_p and ζ, the time autocorrelation function for the normal modes is written as

$$\left\langle X_{p\alpha}(t)X_{q\beta}(0)\right\rangle = \delta_{pq}\delta_{\alpha\beta}\frac{k_BT}{k_p}\exp\left(-\frac{t}{\tau_p}\right) \qquad (\text{C.12})$$

where k_p ($p = 1,2,...,N\text{-}1$) is found from the spring constant $k = (3k_BT)/b^2$ of the Rouse chain as

$$k_p \equiv k\frac{\zeta_p}{\zeta}\sin^2\left(\frac{p\pi}{N}\right) \qquad (\text{C.13})$$

Since two different expressions are found for ζ_p, depending on the definition of the normal modes, k_p is also different.

Since k_p defines the magnitude of the normal modes and not their time evolution, the two alternative definitions differ only in the dependence of the intensity of the normal modes on the mode number. According to the first definition of the normal modes using the position vectors we have

$$\left\langle \mathbf{X}_p(0)^2 \right\rangle = 3\left\langle X_{pa}(0)^2 \right\rangle = 3\frac{k_B T}{k_p} = 3\frac{k_B T}{k\dfrac{\varsigma_p}{\varsigma}\lambda_p} =$$

$$= 3\frac{k_B T}{3\dfrac{k_B T}{b^2}\dfrac{\varsigma}{\varsigma}4\sin^2\left(\dfrac{p\pi}{2N}\right)} = 3\frac{b^2}{12\sin^2\left(\dfrac{p\pi}{2N}\right)} \overset{p \ll N}{=} \frac{N^2 b^2}{\pi^2}\frac{1}{p^2} \qquad (C.14)$$

On the other hand according to the definition of the normal modes using the connector vectors

$$\left\langle \mathbf{X}_p(0)^2 \right\rangle = 3\left\langle X_{pa}(0)^2 \right\rangle = 3\frac{k_B T}{k_p} = 3\frac{k_B T}{k\dfrac{\varsigma_p}{\varsigma}\lambda_p} = 3\frac{b^2\left[1-\cos\left(\dfrac{p\pi}{2N}\right)\right]}{6\sin^2\left(\dfrac{p\pi}{2N}\right)} =$$

$$= 3\frac{b^2}{6}\frac{1-\cos^2\left(\dfrac{p\pi}{2N}\right)+\sin^2\left(\dfrac{p\pi}{2N}\right)}{\sin^2\left(\dfrac{p\pi}{2N}\right)} = 3\frac{b^2}{3} = b^2 \qquad (C.15)$$

As regards the definition of the spectrum of relaxation times and the exponential decay of the normal modes, the two definitions produce identical results, because these depend on the ratio ς_p / k_p, which is the same in the two cases. The corresponding equations were given in section 3.2 of Chapter 3.

APPENDIX D

DYNAMIC STRUCTURE FACTOR S(q,t) FOR THE ROUSE MODEL

The dynamic structure factor $S(q,t)$ is a very important property because it is easily accessible experimentally and gives useful information about the time evolution of a system. $S(q,t)$ is defined as

$$S(q,t) \equiv \sum_{nm} \exp\left[i\mathbf{q} \bullet \phi(n,m;t)\right] \tag{C.16}$$

where $\mathbf{q}$ is the scattering vector and n, m denote atoms belonging to the same chain. $\phi(n,m;t)$ is the time correlation function of chain segments n, m defined as:

$$\phi(n,m;t) \equiv \left\langle \left(\mathbf{R}(n,t) - \mathbf{R}(m,0)\right)^2 \right\rangle, \tag{C.17}$$

with $\mathbf{R}(n,t)$ denoting the position vector of the chain segment n at time t and $\mathbf{R}(m,0)$ the position vector of the chain segment m at time 0.

A basic assumption of the Rouse model is that the distribution of the random force acting on atom n, $f_n(t)$ is Gaussian. The distribution of position vectors $(\mathbf{R}_m(t) - \mathbf{R}_n(0))$ is a linear function of $f_n(t)$, thus is also Gaussian. Then

$$\left\langle \exp\left[i\mathbf{q}\bullet\left(\mathbf{R}_m(t) - \mathbf{R}_n(0)\right)\right]\right\rangle = \exp\left[\frac{1}{2}\sum_{a=x,y,z}\left(-q_a^2\left\langle\left(\mathbf{R}_m(t) - \mathbf{R}_n(0)\right)^2\right\rangle\right)\right]. \tag{C.18}$$

But $q_x^2 = q_y^2 = q_z^2 = \dfrac{\mathbf{q}^2}{3}$ we finally obtain

$$S(q,t) = \frac{1}{N}\sum_{n,m}\exp\left[-\frac{\mathbf{q}^2}{6}\left\langle\left(\mathbf{R}_m(t) - \mathbf{R}_n(0)\right)^2\right\rangle\right] \tag{C.19}$$

or from the definition of the correlation function $\phi_{nm}(t)$, Eq. (C.17)(..))

$$S(q,t) = \frac{1}{N}\sum_{n,m}\exp\left[-\frac{\mathbf{q}^2}{6}\phi_{nm}(t)\right] \tag{C.20}$$

Then the main objective is to calculate the time correlation function $\phi_{nm}(t)$. The result is slightly different if we are using the continuous than the discrete Rouse model.

D.1: Continuous Rouse model

The whole procedure for the calculation of the time correlation function $\phi_{nm}(t)$ is presented in details in Appendix 4.III of Ref. [6].

According to the continuous Rouse model model [..]

$$\mathbf{X}_p(t) \equiv \frac{1}{N} \int_0^N dn \cos\left(\frac{p\pi}{N}\right) \mathbf{R}_n(t) \tag{C.21}$$

and through a back transformation

$$\mathbf{R}_j(t) = \mathbf{X}_0(t) + 2\sum_{p=1}^{\infty} \mathbf{X}_p(t) \cos\left(\frac{p\pi j}{N}\right) \tag{C.22}$$

The time correlation function $\phi_{nm}(t)$ now becomes

$$\phi(n,m,t) = \left\langle \left[\left(\mathbf{X}_o(t) - \mathbf{X}_o(0)\right) + 2\sum_{p=1}^{\infty}\left(\cos\left(\frac{p\pi n}{N}\right)\mathbf{X}_p(t) - \cos\left(\frac{p\pi m}{N}\right)\mathbf{X}_p(0)\right)\right]^2 \right\rangle \tag{C.23}$$

and by using the expressions for the correlation of the normal modes

$$\phi(n,m,t) = \left\langle \left(\mathbf{X}_o(t) - \mathbf{X}_o(0)\right)^2 \right\rangle +$$

$$4\frac{Nb^2}{2\pi^2}\sum_{p=1}^{\infty}\frac{1}{p^2}\left[\left(\cos\left(\frac{p\pi m}{N}\right) - \cos\left(\frac{p\pi n}{N}\right)\right)^2 - 2\cos\left(\frac{p\pi m}{N}\right)\cos\left(\frac{p\pi n}{N}\right)\left[1 - \exp\left(-\frac{tp^2}{\tau_R}\right)\right]\right] \tag{C.24}$$

Finally from Eq. C.12 and from the fact that

$$\sum_{p=1}^{\infty}\frac{1}{p^2}\left(\cos\left(\frac{p\pi m}{N}\right) - \cos\left(\frac{p\pi n}{N}\right)\right)^2 = \frac{\pi^2}{2N}|n - m| \tag{C.25}$$

we get

$$\phi_{nm}(t) = 6Dt + b^2|n - m| + \frac{4Nb^2}{\pi^2}\sum_{p=1}^{\infty}\frac{1}{p^2}\cos\left(\frac{p\pi m}{N}\right)\cos\left(\frac{p\pi n}{N}\right)\left[1 - \exp\left(-\frac{tp^2}{\tau_R}\right)\right] \tag{C.26}$$

D.2: Discrete (finite) Rouse model

According to the discrete Rouse model, and by using the position vectors, the normal modes are given by equations (C.1) - (C.3). Through a back transformation, the position vectors are calculated from the normal coordinates through the relation

$$\mathbf{R}_j(t) = \mathbf{X}_0(t) + 2\sum_{p=1}^{\infty} \sqrt{\frac{2-\delta_{p0}}{N}} \cos\left(\frac{p\pi(j-1/2)}{N}\right)\mathbf{X}_p(t). \tag{C.27}$$

Then we follow the same procedure described in the previous section. Now the time correlation function of the normal modes are given from equations (C.11) - (C.13). Thus $\phi_{nm}(t)$ becomes

$$\begin{aligned}
\phi(n,m,t) = &\left\langle \frac{1}{N}\left(\mathbf{X}_o(t) - \mathbf{X}_o(0)\right)^2 \right\rangle + \\
&\frac{b^2}{2N}\sum_{p=1}^{N-1}\frac{1}{\sin^2\left(\frac{p\pi}{2N}\right)}\left[\left(\cos\left(\frac{p\pi(m-1/2)}{N}\right) - \cos\left(\frac{p\pi(n-1/2)}{N}\right)\right)^2\right] + \\
&\frac{b^2}{N}\sum_{p=1}^{N-1}\frac{1}{\sin^2\left(\frac{p\pi}{2N}\right)}\left[\cos\left(\frac{p\pi(m-1/2)}{N}\right)\cos\left(\frac{p\pi(n-1/2)}{N}\right)\left[1-\exp\left(-\frac{tp^2}{\tau_R}\right)\right]\right]
\end{aligned} \tag{C.28}$$

APPENDIX E

MD SIMULATIONS IN THE NTL$_x$σ$_{yy}$σ$_{zz}$ STATISTICAL ENSEMBLE

An ensemble proper for the modeling of uniaxial tension experiments is the $NTL_x\sigma_{yy}\sigma_{zz}$ statistical ensemble [69]. The ensemble is illustrated in Fig. E.1. The quantities that are kept constant during molecular simulations in this statistical ensemble are the following:

- the total number of atoms in the system N,

- the temperature T,

- the box length in the direction of elongation L_x and

- the two normal stresses σ_{yy} and σ_{zz}.
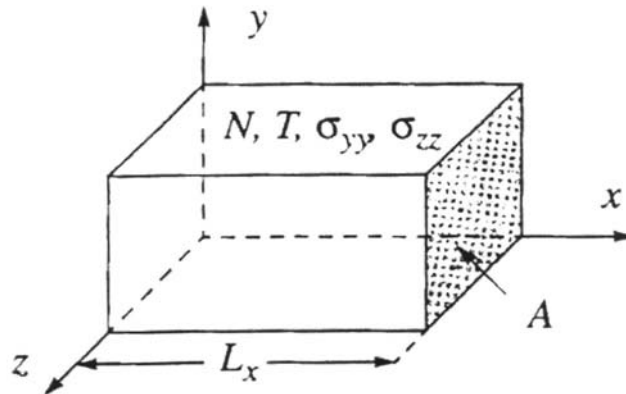
Figure E.1 The $NTL_x\sigma_{yy}\sigma_{zz}$ statistical ensemble

The $NTL_x\sigma_{yy}\sigma_{zz}$ ensemble can be viewed as a hybrid between the well-known NVT ensemble in the x direction and the isothermal-isobaric (NPT) ensemble in the y and z directions. The temperature T is kept fixed at a prescribed value, by employing the Nose-Hoover thermostat; the latter introduces an additional dynamical variable in the system, the parameter s, for which an evolution equation is derived. Also kept constant during the simulation is the box length L_x in the x direction; on the contrary, the box lengths in

the other two directions, L_y and L_z, respectively, although always kept equal, are allowed to fluctuate. This is achieved by making use in the simulation of an additional dynamical variable, the cross-sectional area $A(=L_yL_z)$ of the simulation cell in the yz-plane, for which a suitable equation of motion is derived involving the instantaneous average normal stress $(\sigma_{yy}+\sigma_{zz})/2$ in the two lateral directions y and z, respectively. This quantity remains constant on average and equal to - P_{ext} throughout the simulation.

The formulation for deriving the equations of motion is described in details by Yang *et al.* [69]. Consider a system consisting of N atoms with $\mathbf{r}_{ik}$ the position of i atom belonging to k polymer chain. The bond lengths are kept fixed with $\mathbf{g}_{ik}$ the constraint forces acting on atom i. The Lagrangian is written as a function of the "extended" variables $\{\tilde{\mathbf{R}}_k, \mathbf{x}_{i\kappa}, A, s\}$ where $\tilde{\mathbf{R}}_k$ is the scaled (with respect to the box edge lengths) position of the center of mass of every chain κ, and $\mathbf{x}_{i\kappa}$ is the position of atom i in chain κ measured relative to the chain center of mass. These variables are "extended" in the sense that they invoke a scaled coordinate system and their time derivatives are always with respect to a "virtual" time t'.

The equations of motion derived from the extended Lagrangian with the same procedure followed for the other statistical ensembles. The final equations are easily recast in terms of real coordinates and real time and have the following form:

$$m_i\ddot{r}_{xia} = f_{xia} + g_{xia} - \frac{\dot{s}}{s}p_{xia}, \tag{E.1}$$

$$m_i\ddot{r}_{yia} = f_{yia} + g_{yia} - \frac{\dot{s}}{s}p_{yia} + \frac{m_iR_{ya}}{2A}\left(\ddot{A} - \frac{\dot{A}^2}{2A}\right), \tag{E.2}$$

$$m_i\ddot{r}_{zia} = f_{zia} + g_{zia} - \frac{\dot{s}}{s}p_{zia} + \frac{m_iR_{za}}{2A}\left(\ddot{A} - \frac{\dot{A}^2}{2A}\right), \tag{E.3}$$

$$Q\ddot{s} = Q\frac{\dot{s}^2}{s} + s\left[\sum_a\sum_i\frac{p^2_{xia} + p^2_{yia} + p^2_{zia}}{m_i} - (g+1)k_BT\right], \tag{E.4}$$

$$W\ddot{A} = W\frac{\dot{s}\dot{A}}{s} + s^2L_x\left[\frac{1}{2}(P_{yy} + P_{zz}) - P_{ext}\right], \tag{E.5}$$

where the forces with two indices indicate center of mass forces, while those of three indicate forces on atoms within a particular polymer chain. $\mathbf{R}_\alpha$ are the center of mass of molecules, while Q and W are constants associated with the temperature fluctuations and of the normal stresses σ_{yy} and σ_{zz} respectively.

The total Hamiltonian of the system, derived from the Lagrangian, has the following form

$$
\begin{aligned}
H_{NTL_x\sigma_{yy}\sigma_{zz}} = \sum_i \frac{p_i^2}{2m_i} + V(\mathbf{r}) - \frac{1}{2}\sum_\kappa\sum_i \lambda_i^\kappa \left(\left(\mathbf{r}_{i+1,\alpha} - \mathbf{r}_{i,\alpha}\right)^2 - l^2\right) \\
+ \frac{Q}{2}\left(\frac{\dot{s}}{s}\right)^2 + (g+1)\frac{\ln s}{\beta} + \frac{W}{2}\left(\frac{\dot{A}}{s}\right)^2 + P_{ext}L_x A
\end{aligned}
\tag{E.6}
$$

The first term on the right hand side represents the kinetic energy, the second term is the potential energy, the third term is the contribution to the Hamiltonian due to constraint bond lengths with λ_i^κ being the Lagrange multiplier for the i-th bond of chain κ [..] and the last four terms are the contributions due to the thermostat and the fluctuating box cross-sectional area in the plane yz.

For the solution of equations of motion we follow a modification of the velocity-Verlet algorithm proposed by Palmer [..] for a system with bond length constraints. In Palmer's approach, formulated in the *NVE* ensemble, the velocity Verlet algorithm is recast in a form in which the bond length constraint is applied two time steps beyond the current one in order to calculate the constraint force one time step ahead.

Then Palmer's approach [139] is employed in the *NTL$_x\sigma_{yy}\sigma_{zz}$* ensemble MD simulations. The equations of motion are integrated through a modified procedure described in details elsewhere [69].

BIBLIOGRAPHY

[1]   K. Binder, Editor, *Monte Carlo and Molecular Dynamics Simulations in Polymer Science*; Oxford University Press: New York, 1995.

[2]   J.D. Ferry, *Viscoelastic Properties of Polymers*, J. Wiley & sons, New York, 1980.

[3]   J. Mark, Editor, *Physical Properties of Polymers*, American Chemical Society, Washington, 1984.

[4]   M.P. Allen and D.J. Tildesley, *Computer Simulation of Liquids*; Oxford University Press: Oxford, 1987.

[5]   D. Frenkel and B. Smith, *Understanding Molecular Simulations: From Algorithms to Applications*; Academic Press: New York, 1996.

[6]   M. Doi and S.F. Edwards, *The Theory of Polymer Dynamics*, Claredon: Oxford, 1986.

[7]   N. Metropolis, A.W. Rosenbluth, M.N. Rosenbluth, A.H. Teller, and E. Teller, *J. Chem. Phys.* **1953**, *21*, 1087.

[8]   B.J. Alder and T.E. Wainwright, *J. Chem. Phys.* **1957**, *27*, 1208.

[9]   G.. Ciccoti and W.,G. Hoover, Editors, *Molecular Synamics Simulations of Statistical Mechanics Systems*, Proceedings of the 97th Int. "Enrico Fermi" School of Physics, North Hooland, Amsterdam, 1986.

[10]   H. Goldstein, *Classical Mechanics*, Addison-Wesley, MA, 1980.

[11]   W.C. Swope, H.C. Andersen, P.H. Berens, and K.R. Wilson, *J. Chem. Phys.*, **1982**, *76*, 637.

[12]   S. Nosé, *Mol. Phys.* **1984**, *52*, 255.

[13]   W.G. Hoover, *Phys. Rev. A* **1985**, *31*, 1695.

[14]   H.C. Andersen, *J. Chem. Phys.*, **1980**, *72*, 2384.

[15]   M. Parinello and A. Rahman, *Phys. Rev. Lett.*, **1980**, *45*, 1196.

[16]   H.J.C. Berendsen, J.P.M. Postma, W.F. van Gunsteren, A. DiNola, and J.R. Haak, *J.Chem.Phys.* **1984**, *81*, 3684.

[17]   M. Tuckerman, B. J. Berne, and G. J. Martyna, *J. Chem. Phys.* **1992**, *97*, 1990.

[18]   G. J. Martyna, M. E. Tuckerman, D. J. Tobias, and M. L. Klein, *Mol. Phys.* **1996**, *87*, 1117.

[19]   H.F. Trotter, *Proc. Am .Math Soc.*, **1959**, *10*, 545.

[20]   R. Edberg, D.J. Evans, and G.P. Morriss, *J. Chem. Phys.* **1986**, *84*, 6933.

[21]   J. P. Ryckaert, G. Ciccoti, and H. J.C. Berendsen, *J. Comp. Phys.* **1977**, *101*, 327.

[22]   H. C. Andersen, *J. Comp. Phys.* **1983**, *52*, 24.

[23]   K. Kremer and J. Grest, *J. Chem. Phys.* **1990**, *92*, 5057.

[24]   M. Pütz, K. Kremer, and G.S. Grest, *Europhys. Lett.* **2000**, *49*, 735.

[25]   M. Kröger and S. Hess, *Phys. Rev. Lett.* **2000**, *85*, 1128.

[26]   W. Tshöp, K. Kremer, J. Batoulis, T. Bürger, and O. Hahn, *Acta Polymer*, **1998**, *49*, 61; **1998**, *49*, 75.

[27]   R.L.C. Akkerman and W.J. Briels, *J. Chem. Phys.*, **2000**, *113*, 6409; **2001**, *114*, 1020.

[28]   J.T. Padding and W.J. Briels, *J. Chem. Phys.*, **2001**, *114*, 8685.

[29]   J. T. Padding and W. J. Briels, *J. Chem. Phys.* **2001**, *114*, 19.

[30]   P.J. Hoogebrugge and J.M.V.A. Koelman, *Europhys. Lett.*, **1992**, *19*, 155; **1993**, *21*, 363.

[31]   Y. Kong, C.W. Manke, W.G. Madden, and A.G. Schlijper, *Int. J. Thermophys.*, **1994**, *15*, 1093.

[32]   A.G. Schlijper, P.J. Hoogebrugge, and C.W. Manke, *J. Rheol.*, **1995**, *30*, 191.

[33]   R.D. Groot and P.B. Warren, *J. Chem. Phys.*, **1997**, *107*, 4423.

[34]   B.R. Bird, C.F. Curtiss, R.C. Armstrong, and O. Hassager, *Dynamics of Polymer Liquids*; Volume 1: Fluid Mechanics, 2nd ed.; Wiley: New York, 1987.

[35]   B.R. Bird, C.F. Curtiss, R.C. Armstrong, and O. Hassager, *Dynamics of Polymer Liquids*; Volume 2: Kinetic Theory, 2nd ed.; Wiley: New York, 1987.

[36]   L.R.G. Treloar, *The Physics of Rubber Elasticity*, 3rd ed.; Claredon Press, Oxford, 1975.

[37]   G.C. Berry, T.G. Fox, *Adv. Polym. Sci.* **1968,** *5*, 261.

[38]   A.N. Beris and B.J. Edwards, *Thermodynamics of Flowing Systems*, Oxford University press, Oxford, 1994.

[39]   H.C. Öttinger and M. Grmela, *Phys. Rew. E*, **1997**, *56*, 6620; **1997**, *56*, 6633.

[40]   V.G. Mavrantzas and H.C. Öttinger, *submitted to Phys . Rev. Lett.*

[41]   P.E. Rouse, *J. Chem. Phys.* **1953**, *21*, 1272.

[42]   P.H. Verdier, *J. Chem. Phys.* **1966**, *45*, 2118.

[43]   B.H. Zimm, *J. Chem. Phys.* **1956**, *24*, 269.

[44]   G. Smith and D.Y. Yoon, *J. Chem. Phys.* **1994**, *100*, 649.

[45]   G. Smith and D.Y. Yoon, *J. Chem. Phys.* **1995**, *103*, 1702.

[46]   J. Han, R.L. Jaffe, and D.Y. Yoon, *Macromolecules* **1997**, *30*, 7245.

[47]   W. Paul, G.D. Smith, and D.Y. Yoon, *Macromolecules* **1997**, *30*, 7772.

[48]   D. Richter, B. Ewen, B. Farago, and T. Wagner, *Phys. Rev. Lett.* **1989**, *62*, 2140.

[49]   D. Richter, L. Willner, A. Zirkel, B. Farago, L.J. Fetters, and J.S. Huang, *Macromolecules* **1994**, *27*, 7437.

[50]   M. Mondello and G. Grest, *J. Chem. Phys.* **1995**, *103*, 7156; **1997**, *106*, 9327.

[51]   P.G. de Gennes, *J. Chem. Phys.*, **1971**, *55*, 572.

[52]   T.T. Perkins, D.E. Smith, and S. Chu, *Science* **1994,** *264*, 819.

[53]   P. Schleger, B. Farago, C. Lartigue, A. Kollmar, and D. Richter, *Phys. Rev. Lett.* **1998,** *81*, 124.

[54]   D. Richter, L. Willner, A. Zirkel, B. Farago, L.J. Fetters and J.S. Huang, *Phys. Rev. Lett.* **1993**, *71*, 4158.

[55]   D. Richter, L. Willner, A. Zirkel, B. Farago, L.J. Fetters, and J.S. Huang, *Macromolecules* **1994**, *27*, 7437.

[56]   D. Richter, B. Farago, L.J. Fetters, J.S. Huang, B. Ewen, and C. Lartigue, *Phys. Rev. Lett.* **1990**, *64*, 1389.

[57]   W. Paul, G.D. Smith, D.Y. Yoon, B. Farago, S. Rathgeber, A. Zirkel, L. Willner, and D. Richter, *Phys. Rev. Lett.* **1998**, *80*, 2346.

[58]   R. Graft, A. Heuer, and H.W. Spiess, *Phys. Rev. Lett.* **1998**, *80*, 5738.

[59]   L.J. Fetters, W.W Graessley, R. Krishnamoorti, and D.J. Lohse, *Macromolecules* **1997**, *30*, 4973.

[60]   M. Doi, *J. Pol. Sci.*, **1983**, *21*, 265.

[61]   A.L. Frischeknecht and S.T. Milner, *Macromolecules* **2000**, *33*, 5273.

[62]   S.T. Milner and T.C.B. McLeish, *Phys. Rev. Lett.* **1998**, *81*, 725.

[63]   D.N. Theodorou and U.W. Suter, *Macromolecules* **1986**, *19*, 139.

[64]   A.S. Argon, P.H. Mott, and U.W. Suter, *Phys. Status Solid B* **1992** *172*, 193.

[65]   J. Gao and J.H. Weiner, *Macromolecules* **1992**, *25*, 1348.

[66]   J. Gao and J.H. Weiner, *J. Chem. Phys.* **1992**, *97*, 8628.

[67]   J. Gao and J.H. Weiner, *Macromolecules* **1994,** *27*, 1201.

[68]   D. Brown and J.H. Clarke, *Macromolecules* **1991**, *24*, 2075.

[69]   L. Yang, D.J. Srolovitz, and A.F. Yee, *J. Chem. Phys.* **1997,** *107*, 4396.

[70]   L. Yang, D.J. Srolovitz, and A.F. Yee, *J. Chem. Phys.* **1999**, *110*, 7058.

[71]   P.V.K. Pant and D.N. Theodorou, *Macromolecules* **1995**, *28*, 7224.

[72]   V.G. Mavrantzas and D.N. Theodorou, *Macromolecules* **1998**, *31*, 6310

[73]   V.G. Mavrantzas, T.D. Boone, E. Zervopoulou, and D.N. Theodorou, *Macromolecules* **1999**, *32*, 5072.

[74]   P. Van der Ploeg and H.J.C. Berendsen, *J. Chem. Phys.* **1982**, *76*, 3271.

[75]   V.A. Harmandaris, M. Doxastakis, V.G. Mavrantzas, and D.N. Theodorou, *J. Chem. Phys.* in press, 2001.

[76]   J.P. Ryckaert and A. Bellemans, *Chem. Phys. Lett.* **1975**, *30*, 123.

[77]   N. Gō and H.A. Scheraga, *Macromolecules* **1976**, *9*, 535.

[78]   M. Fixman, *Proc. Nat. Acad. Sci.* **1974**, *71*, 3050.

[79]   J.C. Horton, G.L. Squires, A.T. Boothroyd, L.J. Fetters, R.J. Rennie, C.J. Glinka, and R.A. Robinson, *Macromolecules* **1989**, *22*, 681.

[80]   D.S. Pearson, G. Ver Strate, E. Von Meerwall, and F.C. Schilling, *Macromolecules* **1987**, *20*, 1133.

[81]   V.A. Harmandaris, V.G. Mavrantzas, D.N. Theodorou, M. Kröger, J. Ramírez, H.C. Öttinger, and D. Vlassopoulos, *J. Chem. Phys.*, submitted.

[82]   V.A. Harmandaris, V.G. Mavrantzas, and D.N. Theodorou, *Macromolecules* **1998**, *31*, 7934.

[83]   M. Kröger, J. Ramírez, and H.C. Öttinger, *Comp. Theor. Polym. Sci.* in press (2001).

[84]   T.P. Lodge, *Phys. Rev. Lett.* **1999**, *83*, 3218.

[85]   H. Tao, T.P. Lodge, and E.D. von Meerwall, *Macromolecules* **2000**, *33*, 1747.

[86]   L. Harnau, R.G. Winkler, and P. Reineker, *J. Chem. Phys.* **1995,** *102*, 7750.

[87]   L. Harnau, R.G. Winkler, and P. Reineker, *J. Chem. Phys.* **1996,** *104*, 6355.

[88]   L.R. Dodd and D.N. Theodorou, *Adv. Polym. Sci.* **1994**, *116*, 249.

[89]   V.A. Harmandaris, V.G. Mavrantzas, and D.N. Theodorou, *Macromolecules* **2000**, *33*, 8062.

[90]   G.D. Smith, W. Paul, M. Monkenbush, and D. Richter, *J. Chem. Phys.* **2001**, *114*, 4285.

[91]   G.D. Smith, W. Paul, M. Monkenbush, L. Willner, D. Richter, X.H. Qiou and M.D. Ediger, *Macromolecules* **1999**, *32*, 8857.

[92]   P.G. De Gennes, *J. Physique* **1981**, *42*, 735.

[93]   E. von Meerwall, S. Beckman, J. Jang, and W.L. Mattice, *J. Chem. Phys.* **1998**, *108*, 4299.

[94]   F. Bueche, *Physical Properties of Polymers* (Interscience, New York, 1962).

[95]   E. von Meerwall and R.D. Ferguson, *J. Chem. Phys.* **1980**, *72*, 2861.

[96]   E. von Meerwall, J. Grisby, D. Tomich, and R. van Antwerp, *J. Polym. Sci., Polym. Phys. Ed.* **1982**, *20*, 1037.

[97]   M.L. Greenfield and D.N. Theodorou, *Macromolecules* **1998**, *31*, 7068.

[98]   M.L. Greenfield and D.N. Theodorou, *Macromolecules* **1993**, *26*, 5461.

[99]   H. Ertl, R.K. Ghai, and F.A. Dullien, *AIChE 1974*, *20*, 1.

[100] G. Fleischer and M. Appel, *Macromolecules* **1995**, *28*, 7281.

[101] M.H. Cohen and D. Turnbull, *J. Chem. Phys.* **1959**, *31*, 1164.

[102] P.B. Macedo and T.A. Litovitz, *J. Chem. Phys.* **1965**, *42*, 245.

[103] J.S. Vrentas and J.L. Duda, *J. Polyn. Sci., Phys. Ed.* **1977**, *15*, 403 ; **1977**, *15*, 417.

[104] J.S. Vrentas, C.M. Vrentas, and J.L. Duda, *Polymer Journal* **1993**, *25*, 99.

[105] V.A. Harmandaris, D. Aggelopoulou, V.G. Mavrantzas, and D.N. Theodorou, *J. Chem. Phys.*, submitted.

[106] M. Mondello, G.S. Grest, E.B. Webb III, and P. Peczak, *J. Chem. Phys.* **1998**, *109*, 798.

[107] Neogi, P., Editor, *Diffusion in Polymers,* University of Missouri-Rolla, Rolla, Missouri, 1996.

[108] J.L. Duda and J.M. Zielinski in Neogi, P., *Diffusion in Polymers,* chapter 3, pp. 143 –171, University of Missouri-Rolla, Rolla, Missouri, 1996.

[109] R. A. Waggoner, F. D. Blum and J. M. D. MacElroy, *Macromolecules* **1993**, *26*, 6841.

[110] E. von Meerwall, E. J. Feick, R. Ozisik and W. L. Mattice, *J. Chem. Phys.* **1999**, *111*, 750.

[111] E. von Meerwall and R. D. Ferguson, *J. Appl. Pol. Sc.* **1979**, *23*, 3657.

[112] S. K. Nath, F. A. Escobedo, J. J. de Pablo, *J. Chem. Phys.*, **1998**, *198*, 9905.

[113] E. Zervopoulou, V.G. Mavrantzas, and D.N. Theodorou, *J. Chem. Phys.*, **2001**, *115*, 2860.

[114] J. S. Vrentas, C. M. Vrentas and J. L. Duda, *Polymer Journal* **1993**, *25*, 99.

[115] J. S. Vrentas and C. M. Vrentas, *Macromolecules* **1993**, *26*, 1277.

[116] J. C. Vrentas and C. M. Vrentas, *Macromolecules* **1994**, *27*, 4684.

[117] J. C. Vrentas and C. M. Vrentas, *Macromolecules* **1995**, *28*, 4740.

[118] J. C. Vrentas, C. M. Vrentas and N. Faridi, *Macromolecules* **1996**, *29*, 3272.

[119] R. N. Haward, J. Macromol. Sci., *Rev. Macromol. Chem.* **1970**, *C4(2)*, 191.

[120] F. A. L. Dullien, *ALChE J.* **1972**, *18*, 62.

[121] P. J. Flory, R. A. Orwoll and A. Vrij, *J. Am. Chem. Soc.*, **1964**, *86*, 3507.

[122] D.J. Evans and G.P. Morris, *Statistical Mechanics of Nonequilibrium Liquids* (Academic Press, London, 1990).

[123] G.P. Morris and D.J. Evans, *Mol. Phys.* **1985**, *54*, 629; *Phys. Rev. A* **1987**, *35*, 792.

[124] D.J. Evans and G.P. Morris, *Mol. Phys.* **1987**, *61*, 1151; *Phys. Rev. A* **1988**, *38*, 4142.

[125] B.D. Todd, *Phys. Rev. E* **1997**, *56*, 6723; *ibid.* **1998**, *58*, 4587.

[126] S.T. Cui, P.T. Cummings, and H.D. Cochran, *J. Chem. Phys.* **1996**, *104*, 255.

[127] J. D. Moore, S.T. Cui, H.D. Cochran, and P.T. Cummings, *J. Non-Newt. Fluid Mech.* **2000**, *93*, 83.

[128] J.D Moore, S.T. Cui, H.D. Cohram, P.T. Cummings, *Phys. Rev. E* **1999**, *60*, 6956.

[129] B.D. Todd and D.J. Daivis, *J. Chem. Phys.* **1997**, *107*, 1617.

[130] B.D. Todd and D.J. Daivis, *Int. J. Thermop.* **1998**, *19*, 1063.

[131] B.D. Todd and D.J. Daivis, *Phys. Rev. Lett.* **1998**, *81*, 1118.

[132] V.G. Mavrantzas and D.N. Theodorou, *Comp. Theor. Polym. Sci.* **2000**, *10*, 1-13.

[133] J.P. Ryckaert, M. Klein, *J. Chem. Phys.* **1986**, *85*, 1613.

[134] D.N. Theodorou, T.D. Boone, L.R. Dodd, and K.F. Mansfield, *Makromol. Chem. Theory Sim.*, **1993**, *2*, 191.

[135] M.P. Allen, *Mol.Phys.* **1984**, *52*, 705.

[136] V.A. Harmandaris, V.G. Mavrantzas, and D.N. Theodorou, Manuscript in preparation.

[137] Exact values of the number of Kuhn segments making up a C_{24} or a C_{78} chain are given in Ref. [72]. Also, the relaxation time of a chain segment equal to one Kuhn segment was calculated from a) the relaxation time of the C_{24} PE melt, reported in Ref. [82], and b) the number of monomers making up the Kuhn segment, by using that in the unentangled regime this time varies inversely proportionally with the square of the segment length.

[138] J.P. Hansen and I.R. McDonald, *Theory of Simple Liquids*, Academic Press, 1990.

[139] B.J. Palmer, *J. Comp. Phys.*, **1993**, *104*, 472.